

Energy Transfer in Polyatomic-Rare Gas Collisions and van der Waals Molecule Dissociation

by

Jason Robert Gascooke BSc (Hons)

A Thesis submitted for the award of the degree of Doctor of Philosophy

School of Chemistry, Physics and Earth Sciences
Flinders University of South Australia

Submitted March, 2000

Table of Contents

| | |
|------------------------------|----|
| <i>Abstract</i> _____ | vi |
| <i>Declaration</i> _____ | ix |
| <i>Acknowledgments</i> _____ | x |

Chapter 1

Introduction

| | |
|-----------------------------------|---|
| <i>1.1 Overview</i> _____ | 1 |
| <i>1.2 Thesis Structure</i> _____ | 5 |

Chapter 2

The S₁-S₀ (¹B₂-¹A₁) transition of jet-cooled toluene. Excitation and dispersed fluorescence spectra, fluorescence lifetimes, and IVR.

| | |
|---------------------------------------------------------------------------------------------|----|
| <i>2.1 Introduction</i> _____ | 8 |
| <i>2.2 Experimental Details</i> _____ | 12 |
| <i>2.3 S₀ Vibrational Frequencies and Mode Numbering</i> _____ | 13 |
| <i>2.4 Fluorescence Excitation Spectrum</i> _____ | 19 |
| <i>2.5 Dispersed Fluorescence Spectra</i> _____ | 23 |
| 2.5.1 0 ⁰ Spectrum _____ | 24 |
| 2.5.2 0 ⁰ + 332 cm ⁻¹ _____ | 27 |
| 2.5.3 0 ⁰ + 372 cm ⁻¹ _____ | 29 |
| 2.5.4 0 ⁰ + 457 cm ⁻¹ and 0 ⁰ + 462 cm ⁻¹ _____ | 30 |
| 2.5.5 0 ⁰ + 532 cm ⁻¹ _____ | 32 |

| | |
|-------------------------------------------------------------------|-----------|
| 2.5.6 $0^0 + 736 \text{ cm}^{-1}$ and $0^0 + 754 \text{ cm}^{-1}$ | 32 |
| 2.5.7 $0^0 + 809 \text{ cm}^{-1}$ and $0^0 + 864 \text{ cm}^{-1}$ | 39 |
| 2.5.8 $0^0 + 915 \text{ cm}^{-1}$ | 39 |
| 2.5.9 $0^0 + 935 \text{ cm}^{-1}$ and $0^0 + 966 \text{ cm}^{-1}$ | 40 |
| 2.5.10 $0^0 + 1193 \text{ cm}^{-1}$ | 44 |
| 2.5.11 Levels above $0^0 + 1193 \text{ cm}^{-1}$ | 46 |
| 2.6. Sequence Structure | 46 |
| 2.7 Intramolecular Vibrational Energy Redistribution (IVR) | 48 |
| 2.8 Fluorescence Lifetime Measurements | 49 |
| 2.9 Conclusion | 52 |

Chapter 3

Vibrational Deactivation of Highly Excited Hexafluorobenzene

| | |
|----------------------------------------------------------------------------------------|-----------|
| 3.1 Introduction | 55 |
| 3.2 Experimental Details | 58 |
| 3.3 Data Analysis | 62 |
| 3.3.1. Variation of internal energy with time | 62 |
| 3.3.2. Extraction of energy transferred per collision as a function of internal energy | 65 |
| 3.4 Comparison Between IRMPA and UV-IC Excitation | 67 |
| 3.4.1. IRMPA-IRF experiments | 67 |
| 3.4.2. UV excitation (IC-IRF) experiments | 73 |
| 3.4.3. Comparison between IRMPA and UV-IC results | 74 |
| 3.5 Collision Partner Dependence | 75 |
| 3.6 Discussion | 77 |
| 3.6.1 Direct comparison with previous UV-IC excitation work. | 77 |
| 3.6.2 Comparison of collision partner dependence | 80 |
| 3.7 Conclusions | 85 |

Chapter 4

Design and Development of an Ion Imaging Apparatus for the study of Energy Transfer

| | |
|---------------------------------------------------------------------|-----|
| 4.1 Introduction | 87 |
| 4.2 The Ion Imaging Technique | 91 |
| 4.2.1 Concepts and mathematical formalism | 91 |
| 4.2.2 Velocity Mapping | 96 |
| 4.3 Computational Aspects | 99 |
| 4.3.1 Abel and Inverse Abel Transform Algorithm | 99 |
| 4.3.2 Generation of the Three Dimensional Radial Distribution | 100 |
| 4.3.3 Calculation of Energy Distributions - General Method | 101 |
| 4.3.4 Calculation of Energy Distributions - Isotropic Distributions | 103 |
| 4.3.5 Calculation of the Anisotropy Parameter β | 104 |
| 4.4 Experimental Design | 107 |
| 4.4.1 Vacuum Chamber Design | 109 |
| 4.4.2 Design of the Time of Flight spectrometer for Ion Imaging | 112 |
| 4.4.3 Ion and Electron Detectors | 116 |
| 4.4.4 High Voltage Power Supplies | 120 |
| 4.4.5 Supersonic expansion | 122 |
| 4.4.6 Laser System | 123 |
| 4.4.7 Camera System | 123 |
| 4.4.8 Ion Counting Algorithm | 124 |
| 4.4.9 Timing System | 125 |
| 4.4.10 Data Collection and Analysis System | 127 |
| 4.5 Discussion | 130 |
| 4.5.1 The Velocity Mapping Technique | 130 |
| 4.5.2 Circularising distorted photoelectron images. | 133 |
| 4.5.3 Ion Counting versus CCD Integration | 140 |
| 4.5.4 Resolution in photoelectron imaging | 143 |
| 4.5.5 Anisotropy Parameters | 148 |
| 4.6 Conclusion | 149 |

Chapter 5

Photoionisation of Benzene: Photoelectron Spectra and Angular Distributions

| | |
|----------------------------------------------|-----|
| <i>5.1 Introduction</i> | 151 |
| 5.1.1 Overview of Photoelectron Spectroscopy | 151 |
| 5.1.2 Benzene Ionic Spectroscopy | 156 |
| <i>5.2 Experimental Details</i> | 158 |
| <i>5.3 Results and Discussion</i> | 159 |
| 5.3.1 Photoelectron Spectra | 159 |
| 5.3.2 Photoelectron Angular Distributions | 172 |
| <i>5.4 Conclusion</i> | 183 |

Chapter 6

Photodissociation of benzene cation - argon_n (*n*=1,2) van der Waals clusters

| | |
|-----------------------------------------------------------------------------------------------------------------------------------------------------------------------------|-----|
| <i>6.1 Introduction</i> | 186 |
| <i>6.2 Previous Studies of van der Waals Molecule Dissociation</i> | 188 |
| <i>6.3 C₆H₆···Ar_n: Summary of Previous Work</i> | 192 |
| 6.3.1 S ₁ ↔S ₀ Spectroscopy of C ₆ H ₆ ···Ar | 193 |
| 6.3.2 Van der Waals vibrational modes of C ₆ H ₆ ···Ar | 195 |
| 6.3.3 Structure of C ₆ H ₆ ···Ar | 196 |
| 6.3.4 Dissociation Energy of C ₆ H ₆ ···Ar | 197 |
| 6.3.5 Dissociation Dynamics of C ₆ H ₆ ···Ar in 1+1 REMPI | 199 |
| 6.3.6 S ₁ ↔S ₀ Spectroscopy and Structure of C ₆ H ₆ ···Ar ₂ | 200 |
| 6.3.7 Dissociation Dynamics of C ₆ H ₆ ···Ar ₂ in 1+1 REMPI | 202 |
| 6.3.8 Knowledge of the (C ₆ H ₆ ···Ar _n) ⁺ van der Waals ions. | 203 |
| 6.3.9 Dissociation energy of the (C ₆ H ₆ ···Ar) ⁺ and (C ₆ H ₆ ···Ar ₂) ⁺ van der Waals ions | 204 |
| <i>6.4 Experimental Details</i> | 206 |

| | |
|-----------------------------------------------------|-----|
| 6.5 Data Analysis | 209 |
| 6.6 Results | 211 |
| 6.7 Discussion | 219 |
| 6.7.1 Population distribution following ionisation. | 219 |
| 6.7.2 Distribution of total energy released | 224 |
| 6.7.3 Dissociation of $(C_6H_6\cdots Ar)^+$ | 226 |
| 6.7.4 Dissociation of $(C_6H_6\cdots Ar_2)^+$ | 229 |
| 6.7.5 Comparison with energy transfer experiments | 231 |
| 6.8 Conclusion | 234 |

Chapter 7

| | |
|---------------------------------------|-----|
| Thesis Summary and Concluding Remarks | 236 |
|---------------------------------------|-----|

Appendix 1

| | |
|----------------------------------------------|-----|
| Forward and Inverse Abel Transform Algorithm | 244 |
|----------------------------------------------|-----|

| | |
|------------|-----|
| References | 249 |
|------------|-----|

Abstract

This thesis describes investigations in a number of areas linked by their relevance to the field of collision induced energy transfer. The $S_1 \leftarrow S_0$ ($^1B_2 - ^1A_1$) absorption spectrum of jet cooled toluene was studied using laser induced fluorescence and dispersed fluorescence spectroscopy. Assignments were determined for most of the features seen in the excitation spectrum up to 2000 cm^{-1} above the origin band. This has led to the determination of all vibrational frequencies for modes with S_0 frequencies less than $\sim 730\text{ cm}^{-1}$. To alleviate the ambiguities that exist in the labelling of vibrational modes, a numbering system based on the systematic scheme suggested Mulliken [*J. Chem. Phys.* **23**, 1997, (1955)] is proposed. Intramolecular vibrational redistribution (IVR) was found to start occurring at a relatively low energy. This is attributed to the methyl rotor accelerating the vibrational mode mixings. The rates of IVR are also dependent on the particular vibrational mode that is excited. Fluorescence lifetimes were measured for the majority of bands observed in the excitation spectrum. The lifetimes display a steady decrease as the level of vibrational excitation increases.

We also present an investigation into the vibrational relaxation of highly vibrationally excited hexafluorobenzene (HFB). Using both infrared multiphoton absorption (initial energy $\sim 16\,000\text{ cm}^{-1}$) and ultraviolet absorption followed by rapid internal conversion (initial energy $\sim 40\,000\text{ cm}^{-1}$), we have studied the deactivation of highly excited HFB using argon as the collision partner. The energy content of the excited HFB was monitored by measuring the infrared emission from the excited molecules as they collide with the argon bath gas. Although the two preparative methods produce distinctly different initial energy distributions, we have found that within experimental

error the average energy transferred per collision $\langle\langle\Delta E\rangle\rangle$ is the same for the two different techniques. $\langle\langle\Delta E\rangle\rangle$ was found to vary linearly with internal energy.

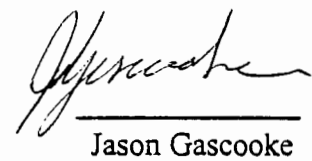
The energy transfer experiments utilising highly excited HFB prepared by infrared multiphoton absorption were extended to measuring $\langle\langle\Delta E\rangle\rangle$ values for all the monatomics collision partners. It was found that over the energy range accessed by the experiment $\langle\langle\Delta E\rangle\rangle$ varied linearly with energy for all the monatomics. $\langle\langle\Delta E\rangle\rangle$ was found to increase from helium to neon to argon but then decreased from argon to krypton before levelling off for xenon. The values of $\langle\langle\Delta E\rangle\rangle$ were found to be much larger for the deactivation of hexafluorobenzene than those found for other aromatic molecules.

We have designed and built an ion imaging apparatus for use in future energy transfer experiments. With the addition of magnetic shielding we were able to also record photoelectron images. The photoelectron image allows the photoelectron spectrum and the photoelectron angular distribution to be measured simultaneously. Using the apparatus we have recorded the photoelectron spectra resulting from the one colour - two photon resonance enhanced multiphoton ionisation (REMPI) of benzene via four different resonance transitions. Unlike previous methods of recording photoelectron spectra, the entire range of electron energies is able to be measured with this technique. The average photoelectron angular distributions produced from the four REMPI transitions have been determined. The anisotropy parameter, β , was found to vary between -0.21 and -0.35, indicating that the electrons are preferentially ejected perpendicular to the laser polarisation. The angular distribution for each individual band in the photoelectron spectra was determined and found to depend on the energy of the ejected electron.

Using the imaging apparatus we have measured the kinetic energy released during the removal of an argon atom from $(C_6H_6 \cdots Ar)^+$ and $(C_6H_6 \cdots Ar_2)^+(1|1)$ van der Waals clusters. The average kinetic energy released for the dissociation of $(C_6H_6 \cdots Ar)^+$ and

$(C_6H_6\cdots Ar_2)^+$ clusters was found to be 92 ± 4 and $78 \pm 5 \text{ cm}^{-1}$ respectively. The photoelectron spectra of benzene recorded earlier on the same instrument were used to determine the internal energy distribution prior to dissociation. For the case of $(C_6H_6\cdots Ar)^+$ the average initial energy was $\sim 1800 \text{ cm}^{-1}$. In the case of $(C_6H_6\cdots Ar_2)^+$ we argue that the initial energy was a lower value, $\sim 860 \text{ cm}^{-1}$, since higher internal energies lead to removal of both argon atoms. We attribute the difference in the average energy released to the difference in the initial average internal energy.

I certify that this thesis does not incorporate without acknowledgment any material previously submitted for a degree or diploma in any university; and that to the best of my knowledge and belief it does not contain any material previously published or written by another person except where due reference is made in the text.



Jason Gascooke

Acknowledgments

Firstly, thanks must go to my supervisor Professor Warren D. Lawrence who supported and encouraged me throughout this work. I appreciated the trust that he showed in me.

I would also like to thank all past and present lab members. They all provided a friendly and intellectual (and often silly) atmosphere which made life in the lab most enjoyable. Thanks to Joanne Nicholson and Eric Waclawik for their help and many whiteboard discussions/arguments throughout the years. Many thanks for the friendship provided by the current lab inhabitants: Heather Mackenzie-Ross, Rebecca von Stieglitz and especially Susan Bellm who would have to have the best sense of humour in the department.

This work would not be possible without the expert involvement of the mechanical, electrical and glass blowing workshops. I would especially like to thank Bill Drury and Peter Mariner for their electronics expertise. They were consistently present in our lab attending to up non-cooperative equipment.

The support and understanding given my parents was much appreciated.

Most of all I would like to thank Ula Alexander for her encouragement and just being there for me. Our lives together have been very enjoyable. Thankyou for the many adventures that we have shared together.

Chapter 1

Introduction

1.1 Overview

The transfer of energy between colliding molecules is central to our understanding of the dynamics involved in gas phase chemical reactions [Levine 1987]. Knowledge of energy transfer is necessary, for example, for calculations of the master equation to predict rates of unimolecular and recombination reactions [Gilbert 1990]. The energy transfer term required in the master equation is denoted as $P(E,E')$, which represents the probability of a molecule having energy E' undergoing a collision resulting in a final energy E . It has long been a goal of experimentalists to directly measure $P(E,E')$ distributions.

In the regime of low state densities, molecules can be prepared in a well defined vibrational state. After a single collision, the molecule can be probed to determine the final populated states, allowing the energy transfer pathways $P(E,E')$ to be mapped on a state-to-state basis. These types of experiments require a detailed knowledge of the molecular spectroscopy and internal energy levels of the molecule for complete analysis.

State-to-state energy transfer experiments on large polyatomic molecules usually are performed using aromatic compounds in the excited electronic state due to the

fortuitous spectroscopic properties of these systems. Strong $S_1 \leftarrow S_0$ vibronic absorption transitions allow the excitation of specific vibrational modes, while the high fluorescence quantum yields facilitate detection of the collisionally populated vibrational levels. Studies of aromatic molecules have allowed the observation of vibrational energy transfer at various initial internal energies and a range of different types of vibrations [Krajnovich 1987; Waclawik 1995].

Previous state-to-state experiments in our laboratory have included vibrational energy transfer from the 6^1 level of both benzene and benzene-d₆ [Waclawik 1993, 1995; Borg 1994], and from various vibronic levels in *p*-difluorobenzene [Mudjijono 1994a, 1994b, 1996a, 1996b, 1996c, 1998a, 1998b]. These experiments were performed using a variety of collision partners, and revealed the very different energy transfer pathways followed by different partners. It has been noted at a recent workshop on energy transfer that it is desirable to extend studies of energy transfer from aromatics to other classes of molecules [King 1996]. In this context, a logical extension to this state-to-state work is to study vibrational energy transfer from toluene as this would allow the effect of the methyl rotor on energy transfer pathways to be probed. Unfortunately, for toluene much of the spectroscopic data required to perform such experiments is either not known or speculative. In order to provide the required data we have undertaken a comprehensive study of the $S_1 \leftarrow S_0$ electronic transition of toluene, including assignment of the majority of absorption transitions, and of many low lying levels in the S_1 manifold. This work is presented in chapter two. Interestingly, the analysis of toluene data relied on collision experiments to aid in the assignments of some excited state vibrational frequencies. The results of the spectroscopic investigation have been subsequently used for an energy transfer study [Waclawik 1996].

Although $P(E,E')$ distributions can be found exactly at low state density, it becomes extremely difficult to measure these distributions for molecules containing chemically

significant amounts of energy. At high internal energies where bond breaking and bond formation occur, the density of states is extremely high, making state-to-state energy transfer experiments impossible. At these high energies it is the functional form of $P(E,E')$ that is desired. Generally, only the average of the $P(E,E')$ distribution can be determined, and is denoted as $\langle\langle\Delta E\rangle\rangle$, the average energy transferred per collision at an average energy of E . The manner in which $\langle\langle\Delta E\rangle\rangle$ varies with the internal energy is also measured and is of much interest. Barker *et al.* have extended these types of experiments to show that it is possible to also measure the second moment (or width) of the distribution using a two colour infrared fluorescence technique [Brenner 1993].

Studies of energy transfer from highly excited polyatomics all require a preparatory technique for creating the initially excited species, and a means of monitoring the amount of internal energy left in the molecule. There are a myriad of ways to perform both these tasks, yet key comparisons between the different techniques have not been performed. For the excitation process, two common techniques are UV absorption followed by rapid internal conversion and infrared multiphoton absorption (IRMPA). The former produces an ensemble of molecules having a narrow initial distribution of energies, while IRMPA produces a much broader distribution due to the somewhat random nature of the multiphoton absorption process. Chapter three compares the two techniques by measuring energy transfer parameters for the collisional relaxation of highly excited hexafluorobenzene by argon. Also presented in chapter three is the determination of $\langle\langle\Delta E\rangle\rangle$ values for the deactivation of highly excited hexafluorobenzene by each of the noble gases.

Only recently has some direct measurement of $P(E,E')$ at high internal energies been possible [Michaels 1997a]. Flynn *et al.* have measured a set of final rotational-vibrational states and translational energies (by measuring the Doppler profile) of CO₂ after collisions with highly excited hexafluorobenzene and pyrazine [Michaels 1997a]. By monitoring the final states of the collision partner, information on the $P(E,E')$

distribution for the highly excited molecules was inferred for the first time. Unfortunately it was not possible to measure the entire distribution, but still some very interesting results were obtained. The importance of experimentally determining $P(E,E')$ distributions has lead us to develop techniques aimed at directly measuring this quantity.

The success of Flynn *et al.*'s work shows the usefulness of monitoring the collision partner after collisions with a highly excited polyatomic. While the highly excited molecule is difficult to probe spectroscopically, the partner, which contains a comparatively small amount of energy, remains amenable to spectroscopic characterisation. A longer term goal of research in our group is to perform similar experiments using crossed molecular beams with ion imaging to measure the translation energy gained by the collision partner after the collision. Our first step towards this goal is to measure the recoiling velocities from the dissociation of van der Waals complexes. This is a simpler experiment since it can be performed using only one laser and a single molecular beam. It utilises the detection techniques and equipment necessary for full collision studies. Moreover, the results have implications for understanding energy transfer. Dissociation of van der Waals molecules has been described in the literature as a *half collision* [Rice 1986]. It can be thought of as the final step in a collision where the colliding molecule leaves the target molecule after transferring energy.

We have chosen to use the relatively new technique of ion imaging to measure the kinetic energy distribution of the recoiling fragment after van der Waals dissociation. Ion imaging has become an important tool in the last few years to study the fragmentation of polyatomic molecules [Chandler 1999; Heck 1995]. The basic idea behind this technique is to record the velocity distribution of dissociating fragments onto a two dimensional detector. After appropriate mathematical manipulation, it is

possible to convert the two dimensional image into the full three dimensional velocity, and hence kinetic energy, distribution of the probed fragment.

We have constructed an ion imaging apparatus designed to measure recoiling velocities in van der Waals molecule dissociation. The apparatus design is discussed in detail in chapter four. With the constructed apparatus, photoelectron spectra and angular distributions from the (1+1) resonance enhanced photoionisation (REMPI) of benzene were recorded and are presented in chapter five. Van der Waals dissociation studies are presented in chapter six for the dissociation of ionic benzene-argon clusters.

1.2 Thesis Structure

As described in the overview above, this thesis describes investigations in three areas related by the theme of energy transfer. Chapter two presents an investigation into the $S_1 \leftarrow S_0$ electronic transition of toluene, required as a background to studies of collision-induced energy transfer in this molecule. The text is a reprint of the paper which has since been published [Hickman 1996]. The experimental data were previously recorded by a co-worker (C. G. Hickman), so it is the analysis of the spectral data which is of interest. Only brief details of the experimental arrangement is presented here, but more detailed information can be found in earlier publications [Waclawik 1995]. As we have noted, this study was driven by the need to have good quality spectroscopic data on toluene for future energy transfer work. A majority of the vibronic transitions up to 2000 cm^{-1} above the origin was determined, along with all S_1 vibrational modes whose S_0 frequencies lie beneath 730 cm^{-1} . After reviewing all the previous spectroscopic work on toluene, it became obvious that the numbering system used to describe the vibrational modes needed updating. Previous authors used a numbering scheme based on the normal modes of benzene known as Wilson's notation [Wilson 1934]. We

suggest the more systematic approach of Mulliken [Mulliken 1955] to alleviate the problems associated with the current scheme. The new numbering system has already been adopted in a study on the photoelectron spectra of toluene [Shaw 1998]. Results from our study have assisted in determining the pathways for energy transfer from the 37^1 ($6b^1$ in Wilson's numbering) vibrational level in S_1 toluene [Waclawik 1996].

Chapter three contains experimental results for the deactivation of highly excited hexafluorobenzene by monatomic colliders, and is a merging of two recently published papers [Gascooke 1998a; Gascooke 1998b]. Different excitation techniques were examined by performing collisional relaxation experiments using argon as the collider. Hexafluorobenzene was prepared in a highly excited state using both UV absorption followed by rapid internal conversion ($\sim 40\ 300\ \text{cm}^{-1}$) and IRMPA ($\sim 16\ 000\ \text{cm}^{-1}$). The energy content of the relaxing molecule was monitored by measuring the infrared fluorescence emission as a function of the collision number. Results for the relaxation using the two different populating methods indicate that within experimental error the final energy transfer parameters obtained are the same. The study was extended to measure collisional relaxation by all of the noble gasses using IRMPA. The dependence of $\langle\langle\Delta E\rangle\rangle$ on the internal energy of the highly excited hexafluorobenzene and the effect of different mass colliders are discussed.

Construction of an ion imaging apparatus designed for use in energy transfer experiments is presented in chapter four. In addition to detecting cations, the device can also be operated to detect anions and electrons. In chapter five we discuss the application of imaging to photoelectron spectroscopy. Photoelectron velocity distributions from the (1+1) REMPI of benzene were recorded. These images contained information on both the high resolution photoelectron spectrum and the angular distribution of the ejected electrons. The high resolution photoelectron spectrum contains the full range of electron energies, from those with zero energy to electrons escaping with the maximum possible energy. This is unlike previous high resolution

photoelectron spectra of benzene. The angular distribution allowed anisotropy parameters to be extracted.

The ion imaging apparatus was subsequently used to measure the recoiling velocities of the benzene and benzene-argon cation fragments after the dissociation of the van der Waals ions $(C_6H_6 \cdots Ar)^+$ and $(C_6H_6 \cdots Ar_2)^+$ respectively. This energy transfer study is presented in chapter six. The ions were formed by (1+1) REMPI through the 6^1 intermediate state of the neutral complex. The distribution of translational energy released in the dissociation of each cluster was calculated.

Chapter 2

The S₁-S₀ (¹B₂-¹A₁) transition of jet-cooled toluene. Excitation and dispersed fluorescence spectra, fluorescence lifetimes, and IVR.

2.1 Introduction

Aromatic molecules form a class that has a special place in the study of molecular dynamical processes in excited electronic states. This arises because of fortuitous spectroscopic characteristics: their S₁-S₀ absorption usually lies in a region of the UV that is readily accessible with commercial dye lasers and doubling crystals and they generally have high fluorescence quantum yields from these electronic states. As a consequence they have been used to elucidate such diverse processes as collision-induced vibrational energy transfer [Rice 1986; Krajnovich 1987], intramolecular vibrational energy redistribution (IVR) [Knight 1988a; Parmenter 1982; Smalley 1983], and the behaviour of van der Waal's molecules [Gotch 1990; Bieske 1990, 1991a, 1991b; Garrett 1992].

Given the widespread use of aromatics in such studies, it is understandable that there is an extensive literature devoted to the electronic spectroscopy of such molecules. Surprisingly, however, much of the spectroscopy of one of the most commonly available aromatics, toluene, remains speculative. This is an interesting situation given that this molecule has been instrumental in the early elucidation of IVR mechanisms [Smalley 1983], has been studied with regard to the behaviour of the methyl rotor in the

S_0 and S_1 electronic states [Murakami 1981; Breen 1987; Philis 1990], and has been the subject of a study of collision-induced vibrational energy transfer within the S_1 state [Kincaid 1991].

It is the aim of this chapter is to improve our understanding of the vibrational structure associated with the S_1 - S_0 transition in toluene. This study was originally motivated by our interest in collision-induced vibrational energy transfer (VET) in aromatic molecules. To perform these experiments and analyse the results a considerable body of spectroscopic data is required concerning the polyatomic molecule under study, and in the case of toluene the data are insufficient for this purpose. VET studies of toluene in a supersonic expansion have been performed by us and was the subject of a recent publication [Waclawik 1996]. Toluene has been the subject of a recent VET study at room temperature, however the analysis was compromised in this work by a lack of knowledge of the vibrational level structure in the lower reaches of the S_1 vibrational manifold [Kincaid 1991].

There is an extensive literature devoted to studies of the S_0 vibrations of toluene using infrared and Raman spectroscopy [Pitzer 1943; Wilmshurst 1957; Fuson 1960; La Lau 1971; Varsanyi 1974]. Theoretical calculations of the S_0 vibrational frequencies have also been performed by a number of groups [Bogomolov 1960; La Lau 1971; Draeger 1985; Tasumi 1986]. While these various experimental and theoretical studies have provided assignments for all of the S_0 vibrational frequencies, there are a number of modes for which there is a lack of agreement concerning the frequency. A discussion of our choice of S_0 vibrational frequencies, gleaned by evaluation of, and comparison between, the values reported in references [Pitzer 1943; Wilmshurst 1957; Bogomolov 1960; Fuson 1960; La Lau 1971; Sverdlov 1973; Varsanyi 1974; Draeger 1985; Tasumi 1986] is included in the body of this chapter.

Early studies of the S₁-S₀ absorption spectrum began with work by Savard [Savard 1929], Spomer [Spomer 1942] and Masaki [Masaki 1936], and culminated with the report by Ginsburg *et al.* [Ginsburg 1946] of the spectrum at high resolution. Six of the S₁ vibrational frequencies were assigned in this period, with a further frequency tentatively assigned based on a sequence transition. Kahane-Paillois and Leach [Kahane-Paillois 1958] suggested a further two tentative S₁ frequencies. Elucidation of further S₁ vibrational frequencies had to await the development of laser and supersonic jet techniques.

Two reports of the two photon spectrum of a room temperature sample appeared in 1979, one by Vasudev and Brand [Vasudev 1979] and the other by Krogh-Jespersen *et al.* [Krogh-Jespersen 1979]. This established v'₁₄ in the excited state; as is the case in benzene, this mode dominates the two photon spectrum. Both groups gave tentative assignments for v_{9a} which are in reasonable agreement. Vasudev and Brand noted that both v₁ and v₁₂ appeared to be split by Fermi resonance. Krogh-Jespersen *et al.* provided the first assignments for v₁₁ and v_{16b} and for the five sequences recognised in the spectrum. This group has subsequently examined quantitatively the intensities in the two photon spectrum [Goodman 1981].

The one photon excitation spectrum has been reported by Smalley and co-workers in a molecular beam [Hopkins 1980a] as part of a study of a series of alkylbenzenes. Due to limitations of the doubling crystals used, this spectrum was restricted to the first 1000 cm⁻¹ of the S₁ vibrational manifold. These authors reported dispersed fluorescence spectra from the 4 prominent bands in the excitation spectrum [Hopkins 1980b], thereby confirming the original assignments of Ginsburg *et al.* [Ginsburg 1946]. Earlier dispersed fluorescence spectra had been reported from 3 levels in a room temperature sample by Blondeau and Stockburger [Blondeau 1971] as part of a general investigation of single vibronic level fluorescence of aromatics. The jet cooled spectrum up to 1000 cm⁻¹ showed five weak transitions, including two Fermi

resonance components, that were not assigned. Later jet-cooled (1+1) MPI spectra recorded by Murakami *et al.* [Murakami 1981] showed other weak transitions in this region which, apart from the methyl rotor transitions, they did not assign. Subsequent work has suggested that one of these methyl rotor assignments is incorrect [Breen 1987].

There has been a recent surge of interest in the behaviour of the methyl rotor. Leugers, Seliskar and co-workers have reported a high resolution study of the rotational contour of the origin band at room temperature [Leugers 1982a] and in a free jet expansion [Leugers 1982b, 1983]. This established that there is little change in the methyl rotor geometry between the ground and excited electronic states. Estimated values were reported for the change in the rotational constants for the phenyl frame. The methyl rotor levels associated with the 0_0^0 band have been examined by Breen *et al.* [Breen 1987] using a combination of REMPI-TOFMS and dispersed fluorescence spectroscopy. Only short sections of the excitation and dispersed fluorescence spectra were investigated by these authors.

In this paper we present the fluorescence excitation spectrum of toluene recorded in a supersonic free jet expansion up to *ca.* 2000 cm⁻¹ above the origin band. This spectrum is analysed with the aid of dispersed fluorescence spectra in a collision-free environment. This work confirms many of the tentative assignments reported by previous workers, and provides a number of new S₁ frequencies. The dispersed fluorescence spectra provide an opportunity to comment on the role of the methyl rotor in intramolecular vibrational energy redistribution (IVR) within the excited electronic state. Fluorescence lifetimes are also reported for the majority of the excited state levels.

A new numbering scheme for the vibrational modes, based on the convention suggested by Mulliken [Mulliken 1955], is introduced in this analysis in a bid to overcome the

confusion that currently exists. Previous workers have primarily used a numbering scheme based upon the normal modes of benzene, as described by Wilson [Wilson 1934]. The changes in the normal modes can be sufficiently large when a hydrogen atom is replaced by a methyl group that the choice of which benzene mode best fits a toluene mode can, in some cases, become a matter of personal preference. The literature on toluene spectroscopy is complicated by the ambiguities that arise through different choices by various authors.

2.2 Experimental Details

The experimental apparatus has been described in detail elsewhere [Waclawik 1995], and only a brief summary is provided here. The third harmonic of a Nd:YAG laser (Spectra Physics GCR12) was used to pump a dye laser (Lambda Physik LPD3002) operating with Coumarin 503 dye. The resulting tunable radiation (535 nm - 485 nm, 10 mJ) was frequency doubled in a BBO crystal. The redundant visible radiation was removed by a glass filter (Schott UG5) and the remaining UV light focussed to a diameter of 2mm at its crossing point with the molecular beam. For excitation spectra the fluorescence was imaged onto a photomultiplier tube (EMI 9813QB) with an iodine/cyclohexane filter used to block scattered laser light. For dispersed fluorescence spectra the fluorescence was imaged onto the slits of a 4.2 m Czerny-Turner spectrometer, with the photomultiplier tube now placed at the exit slit. The spectral resolution was typically $5\text{-}10 \text{ cm}^{-1}$. The spectrometer was calibrated in the spectral region of interest using the known lines of the 6^1 fluorescence spectrum of benzene and *p*-difluorobenzene [Bullock 1995].

Toluene (Univar grade, Ajax Chemicals) at ambient temperature was entrained in a flow of argon (99.99%, CIG) at a total pressure of 80 kPa. The gas mixture was expanded through a pulsed nozzle (General Valve Corporation, 1 mm orifice) into the

vacuum chamber and was interrogated by the laser radiation at $X/D = 7$. For collisional experiments the value of X/D was reduced to 3 and the stagnation temperature of the toluene was lowered to 245 K to prevent contributions from toluene-toluene collisions.

Fluorescence signals from the photomultiplier tube were integrated by a boxcar averager (Stanford Research Systems SR250, gate width 150 ns), digitised by a 12 bit A/D converter and stored on a personal computer (386DX33). Signals from between 10 and 25 laser shots were averaged at each point, depending on the signal to noise ratio.

The fluorescence lifetime of each feature in the excitation spectrum was determined from measurements of the fluorescence decay. Fluorescence decay curves were acquired directly using a digitising oscilloscope (Hewlett Packard HP54510A, 1 GSa/s) set to 256 averages.

2.3 S₀ Vibrational Frequencies and Mode Numbering

The numbering of the vibrational modes of toluene is problematic. Previous workers have used a variety of numbering schemes including a numerical scheme from 1 to 38 [Sverdlov 1973] similar to Mulliken's convention [Mulliken 1955], a complicated scheme describing the type of mode using a combination of superscripts and subscripts [Tasumi 1986], and, most commonly, a scheme relating the phenyl modes to those of benzene, as described by Wilson [Wilson 1934]. This latter approach is prone to complications arising from the changes in certain normal modes when a hydrogen atom is replaced by a methyl group. The changes in the normal modes can be sufficiently large that the choice of which benzene mode best fits a toluene mode can be somewhat arbitrary. The literature on toluene spectroscopy is complicated by the different choices made by various authors. It is further complicated by different choices for the symmetry labelling.

The problem arises because the early spectroscopy of toluene was carried out prior to the existence of a convention for an axis system and mode numbering scheme for polyatomic molecules. This lack of standardisation was dealt with by Mulliken [Mulliken 1955], who proposed a set of rules for the choice of molecular axes and for vibrational mode numbering. These rules have since been used to remove ambiguities in the vibrational mode numbering and symmetry assignments in various molecular systems, for example the difluorobenzenes [Knight 1988b]. Given the existence of Mulliken's convention, we suggest that the confusion currently surrounding the mode numbering in toluene be obviated by introducing a new numbering scheme based on this convention.

The proposed numbering scheme allocates the vibrational mode numbers by arranging the vibrational frequencies in decreasing order within each irreducible representation. In common with previous work, toluene is assumed to have C_{2v} symmetry, the methyl rotor being treated as a point mass. The axis system for this assignment is that prescribed by Mulliken [Mulliken 1955], the z axis being coincident with the C_2 axis and the y axis in the plane of the phenyl ring. Under these circumstances thirty vibrational modes are obtained. Inclusion of the remaining vibrational modes, *i.e.* those involving the intramethyl group motions, adds a further 8 modes (the methyl rotation is not included). The correlation between the existing and proposed systems is given in table 2.1.

The literature regarding toluene is further complicated by different choices regarding the symmetry labelling of the normal modes which transform as b_1 and b_2 . The symmetry labelling given in table 2.1 is opposite to that of previous authors reporting the results of spectroscopic work, although those undertaking calculations have used the present convention [La Lau 1971; Draeger 1985; Tasumi 1986]. This is a result of previous experimentalists using a labelling system based on a different axis system [Pitzer 1943] or an older version of the C_{2v} character table in which the symmetry

Table 2.1 Comparison between the existing and the suggested nomenclatures for the mode numbering in toluene (continued on next page).

| Symmetry | ν / cm^{-1} (S ₀) | Current Work | Pitzer and Scott [Pitzer 1943] | Fuson <i>et al.</i> [Fuson 1960] | Sverdlov <i>et al.</i> [Sverdlov 1973] | Varsanyi [Varsanyi 1974] |
|----------------|---------------------------------------------|-----------------|--------------------------------------|-------------------------------------|-----------------------------------------------|--------------------------------|
| A ₁ | 3087 | 1 | 20a | 7a | 20a | 20a |
| | 3063 | 2 | 2 | 20a | 13 | 2 |
| | 3055 | 3 | 13 | 2 | 7a | 7a |
| | 2921 | 4 | M1 | ν_s | | ν_s |
| | 1605 | 5 | 8a | 8a | 8a | 8a |
| | 1494 | 6 | 19a | 19a | 19a | 19a |
| | 1379 | 7 | M3 | δ_s | | δ_s |
| | 1210 | 8 | 7a | 13 | 2 | 13 |
| | 1175 | 9 | 9a | 9a | 9a | 9a |
| | 1030 | 10 | 18a | 18a | 18a | 18a |
| | 1003 | 11 | 1 | 12 | 12 | 12 |
| | 785 | 12 | 12 | 1 | 1 | 1 |
| | 521 | 13 | 6a | 6a | 6a | 6a |
| A ₂ | 964 | 14 | 17a | 17a | 17a | 17a |
| | 843 | 15 | 10a | 10a | 10a | 10a |
| | 407 | 16 | 16a | 16a | 16a | 16a |
| B ₁ | 2979 | 17 | M2 | ν_a'' | | ν_{as} |
| | 1450 | 18 | M4 | δ_a'' | | δ_{as}^+ |
| | 1040 | 19 | M6 | r" | | δ_{as}^- |
| | 978 | 20 | 5 | 5 | 5 | 5 |
| | 895 | 21 | 17b | 17b | 17b | 17b |
| | 728 | 22 | 10b | 11 | 10b | 11 |
| | 695 | 23 | 4 | 4 | 4 | 4 |
| | 464 | 24 | 16b | 16b | 11 | 16b |
| | 216 | 25 | 11 | 10b | 16b | 10b |
| B ₂ | 3039 | 26 | 20b | 7b | 20b | 7b |
| | 3029 | 27 | 7b | 20b | 7b | 20b |
| | 2952 | 28 | M2 | ν_a' | | ν_{as} |
| | 1586 | 29 | 8b | 8b | 8b | 8b |
| | 1463 | 30 | M4 | δ_a' | | δ_{as}^+ |
| | 1445 | 31 | - | 19b | 19b | 19b |

Table 2.1 (continued)

| Symmetry | ν / cm^{-1} (S_0) | Current Work | Pitzer and Scott [Pitzer 1943] | Fuson <i>et al.</i> [Fuson 1960] | Sverdlov <i>et al.</i> [Sverdlov 1973] | Varsanyi [Varsanyi 1974] |
|----------------------|-------------------------------------|-----------------|--------------------------------------|-------------------------------------|-----------------------------------------------|--------------------------------|
| B_2 (continued) | 1312 | 32 | 19b | 3 | 14 | 14 |
| | 1280 | 33 | 3 | - | 3 | - |
| | 1155 | 34 | 9b | 9b | 9b | 9b |
| | 1080 | 35 | 15 | 18b | 18b | 18b |
| | 1040 | 36 | M6 | r' | | δ_{as}^- |
| | 623 | 37 | 6b | 6b | 6b | 6b |
| | 342 | 38 | 18b | 15 | 15 | 15 |

species of the x and y axes are reversed [Ginsburg 1946]. The convention for C_{2v} shown in Mulliken's paper is for the y axis to be of symmetry type b_2 with the x axis b_1 [Mulliken 1955]. Sverdlov *et al.* [Sverdlov 1973] introduced a similar mode numbering scheme to that suggested here; the difference between this scheme and ours lies in the interchange of the vibrations of b_1 and b_2 symmetry, which results in a different numbering of the vibrational modes.

Table 2.1 shows the S_0 vibrational frequencies, listed in descending order within each symmetry species, and the new mode numbers. Because Mulliken's convention assigns the mode numbering on the basis of the vibrations ordered by frequency within each symmetry type, it is important to ensure as far as possible that the choice of S_0 frequencies places the modes in the correct order. The listed frequencies have been gleaned by evaluation of the values reported by various authors [Pitzer 1943; Wilmshurst 1957; Bogomolov 1960; Fuson 1960; La Lau 1971; Sverdlov 1973 Varsanyi 1974; Draeger 1985; Tasumi 1986;]. Our approach in compiling the values listed in Table 2.1 has been to compare the experimentally determined values reported, and where there is close agreement among the various authors we have taken the most

common, or in some circumstances average, value. This value has then been compared with the values reported by groups performing theoretical calculations to ensure that there is consistency. With the exception of three regions, the frequencies reported here agree with those tabulated by Varsanyi [Varsanyi 1974]. For these three regions there are significant differences between values reported by various authors, as follows:

Region 1: There are discrepancies concerning the CH stretch frequencies. There are four a_1 , one b_1 and three b_2 CH stretches. There is disagreement concerning the frequencies for the five CH stretches associated with the phenyl and one of the three associated with the methyl (the b_1). (3 of the 4 a_1 and 2 of the 3 b_2 CH stretches are associated with the phenyl; 1 each of the a_1 , b_1 and b_2 CH stretches are associated with the methyl.) The problem arises because of the similarity of the CH stretch frequencies. Varsanyi has pointed out that the exact assignment of the CH stretching modes in substituted benzenes is extremely difficult [Varsanyi 1974].

The three a_1 phenyl CH stretches have been assigned to almost equivalent frequencies near 3060 cm^{-1} [Pitzer 1943; Bogomolov 1960; Fuson 1960; La Lau 1971; Sverdlov 1973; Draeger 1985], or as two frequencies in that region and a third near 3000 cm^{-1} [Wilmshurst 1957; Varsanyi 1974]. Normal mode calculations consistently show these stretches being very similar in energy [La Lau 1971; Draeger 1985]. Consequently we believe that the former is correct and suggest the phenyl a_1 CH stretches as 3087 cm^{-1} , 3063 cm^{-1} and 3055 cm^{-1} , based on the frequencies given by Fuson *et al.* [Fuson 1960]. There is a report of local mode calculations which have the CH stretch fundamentals in the latter configuration [Ghosh 1988]. These authors point out that the local mode approximation may not be ideal for the fundamental region, and consequently we base our assessment on the results of the normal mode calculations.

The b_1 methyl CH stretch has been reported at frequencies of *ca.* 2930 , 2950 and 2980 cm^{-1} . Calculated frequencies span a similar range. We have, somewhat

arbitrarily, chosen the value of 2979 cm^{-1} , as reported by Fuson *et al.* [Fuson 1960]. This is also very close to the value of 2976 cm^{-1} reported by Sverdlov *et al.* [Sverdlov 1973]. The remaining CH stretch frequencies in dispute are the two b_2 phenyl modes. Calculations suggest that these two modes are close in frequency [La Lau 1971; Draeger 1985], whereas a number of authors report experimental values that are widely spaced [Pitzer 1943; Bogomolov 1960; Sverdlov 1973]. We have taken the values reported by Fuson *et al.* because they are reasonably close to those predicted, but we remain in doubt concerning the validity of these values.

Region 2: There is ambiguity concerning the b_2 modes between 1250 and 1500 cm^{-1} . In this region there are four fundamentals, three associated with the phenyl ring and one with the methyl group. There is considerable discrepancy among different authors as to the values of the fundamental frequencies in this region. Unfortunately, there are also substantial differences among the calculated frequencies in this region. It appears that there are two bands in the vicinity of 1450 cm^{-1} and also two bands in the $1260 - 1330\text{ cm}^{-1}$ region. A large majority of authors place the methyl vibration as the highest frequency mode, and there is some consensus for its frequency being $\sim 1463\text{ cm}^{-1}$. Fuson *et al.* [Fuson 1960] observe a band at 1460 cm^{-1} that shifts on deuteration of the methyl group, adding confirmation to this assignment. With this assignment for the methyl band, the phenyl mode in this region would appear to be at 1445 cm^{-1} .

The two fundamentals in the region near 1300 cm^{-1} are less easily decided. One of these two modes is the analogue of ν_{14} in benzene and is the active mode in the two photon spectrum. The ν_{14} hot band has been reported from the two photon spectrum of toluene in perfluoro-*n*-hexane [Faidas 1988]. This spectrum gave a frequency of ν_{14} of 1251 cm^{-1} . The solution and gas phase frequencies for other modes seen in this solution spectrum show very close agreement. Thus the gas phase value of ν_{14} should be very near 1251 cm^{-1} . Three frequencies are commonly reported in gas phase studies, 1330 cm^{-1} , 1312 cm^{-1} and 1280 cm^{-1} . It is tentatively suggested that the 1280 cm^{-1}

band corresponds to ν_{14} , although if this is correct then the frequency shift from solution to gas phase is larger than expected. Theoretical calculations support the value of 1280 cm^{-1} [La Lau 1971; Draeger 1985] and it is adopted here. The value of the remaining fundamental in this region is taken to be 1312 cm^{-1} as this appears to be the most consistently reported value. We note that SVL fluorescence following two photon excitation of ν_{14} in S_1 would provide confirmation of the ground state frequency of this mode. This experiment was attempted but the signal level was insufficient to obtain a spectrum.

Region 3: The b_2 methyl asymmetric bend near 1000 cm^{-1} is variously reported between 967 and 1060 cm^{-1} [Pitzer 1943; Wilmshurst 1957; Bogomolov 1960; Fuson 1960; La Lau 1971; Sverdlov 1973; Varsanyi 1974; Draeger 1985; Tasumi 1986]. Calculations suggest the former value [Bogomolov 1960; Draeger 1985; Tasumi 1986]. At the same time our investigations were being performed, Balfour *et al.* made spectral measurements on a number of deuterated toluenes [Balfour 1994a; Balfour 1994b]. Based on the variation of vibrational frequencies upon deuteration, a value of 1040 cm^{-1} for the b_2 methyl asymmetric bend was determined, and it is adopted here.

2.4 Fluorescence Excitation Spectrum

Jet-cooled excitation spectra of toluene have been reported previously by Smalley and co-workers [Hopkins 1980a], Murakami *et al.* [Murakami 1981] and Breen *et al.* [Breen 1987]. The two latter groups were primarily interested in the methyl rotor features. Breen *et al.* did not study any bands more than 150 cm^{-1} above the origin band, and while Murakami *et al.* recorded the spectrum up to $\sim 600\text{ cm}^{-1}$ above the origin band they did not make any assignments of non-methyl rotor features. The excitation spectrum published by Smalley's group extended 1000 cm^{-1} above the origin

band and was limited to this range by the 90^0 phase matching angle of their KDP doubling crystal. A high resolution spectrum (0.1 cm^{-1} resolution) has been reported for the origin band using a jet-cooled sample [Leugers 1983].

Figure 2.1 shows the excitation spectrum measured in this work, which extends to *ca.* 2000 cm^{-1} above the origin band. The observed lines are listed in table 2.2, together with their assignments. The assignments, which are based largely on the analysis of dispersed fluorescence spectra, are discussed below. Comparison of the initial 1000 cm^{-1} of our spectrum with that of Smalley *et al.* shows that they are broadly similar, but there are a number of important differences. Firstly, we observe a number of weak bands which were not reported by Smalley. These bands are also seen in the spectrum reported by Murakami *et al.*, although the intensities appear to be considerably larger than those observed here. This may be due to the use of REMPI detection by these authors. Secondly, the positions of previously reported bands are in excellent agreement with those obtained here, with the sole exception of the Fermi resonance components *ca.* 460 cm^{-1} above the origin band. Smalley and coworkers report the two components at $+441\text{ cm}^{-1}$ and $+461\text{ cm}^{-1}$ relative to the origin band. This is inconsistent with our spectra, which reveal the bands to be at $+457\text{ cm}^{-1}$ and $+462\text{ cm}^{-1}$ respectively. We have made multiple, consistent measurements of these bands and believe our values to be correct. Our spectrum appears to be consistent with the spectrum of Murakami *et al.* in this region; unfortunately frequencies were not listed in Murakami's work. The hot bands at $+16\text{ cm}^{-1}$ and $+77\text{ cm}^{-1}$ are due to uncooled methyl rotor levels having different nuclear spin states. They have previously been observed by Murakami [Murakami 1981] and by Breen [Breen 1987].

Assignment of the prominent features of the spectrum is straightforward, and follows directly from the assignments of Ginsburg *et al.* [Ginsburg 1946] and Smalley and co-workers [Hopkins 1980a]. The spectrum is dominated by short progressions in the totally symmetric vibrations v_{10} , v_{11} and v_{12} . v_{37} (B_2), which is analogous to one of

Table 2.2 Assignment of bands observed in the fluorescence excitation spectrum of toluene.

| Position ^a /cm ⁻¹ | Relative Intensity | Assignment ^b | Position /cm ⁻¹ | Relative Intensity | Assignment |
|--------------------------------------------|-----------------------|------------------------------------|-------------------------------|-----------------------|-------------------------------------|
| 0 | 1000 | $0_0^0 (0a'_1 \rightarrow 0a'_1)$ | +988 | 72 | $37_0^1 (13_0^1 / 24_0^1 25_0^1) *$ |
| +55 | 76 | $0_0^0 (0a'_1 \rightarrow 3a''_1)$ | +997 | 103 | $37_0^1 (13_0^1 / 24_0^1 25_0^1) *$ |
| +332 | 113 | 38_0^1 | +1193 | 138 | 8_0^1 |
| +372 | 21 | $16_0^1 25_0^1$ | +1263 | 68 | $37_0^1 (12_0^1 / 23_0^1 24_0^1) *$ |
| +457 | 189 | $13_0^1 / 24_0^1 25_0^1$ | +1284 | 80 | $37_0^1 (12_0^1 / 23_0^1 24_0^1) *$ |
| +462 | 120 | $13_0^1 / 24_0^1 25_0^1$ | +1371 | 74 | - |
| +532 | 594 | 37_0^1 | +1390 | 73 | $10_0^1 (13_0^1 / 24_0^1 25_0^1) *$ |
| +613 | 78 | - | +1426 | 97 | $11_0^1 (13_0^1 / 24_0^1 25_0^1) *$ |
| +736 | 42 | $12_0^1 / 23_0^1 24_0^1$ | +1466 | 202 | $10_0^1 37_0^1$ |
| +754 | 134 | $12_0^1 / 23_0^1 24_0^1$ | +1494 | 183 | $11_0^1 37_0^1 *$ |
| +809 | 34 | - | +1575 | 33 | - |
| +864 | 32 | $37_0^1 38_0^1 *$ | +1727 | 33 | $8_0^1 37_0^1 *$ |
| +915 | 77 | $14_0^1 16_0^1$ | +1868 | 61 | $10_0^2 *$ |
| +935 | 715 | 10_0^1 | +1900 | 97 | $10_0^1 11_0^1 *$ |
| +966 | 541 | 11_0^1 | +1929 | 53 | $11_0^2 *$ |
| +1929 | 0.050 | - | | | |

a. Band positions are given relative to the 0_0^0 band at 37477.4 cm⁻¹.

b. Assignments marked by asterisks have not been confirmed by dispersed fluorescence spectroscopy.

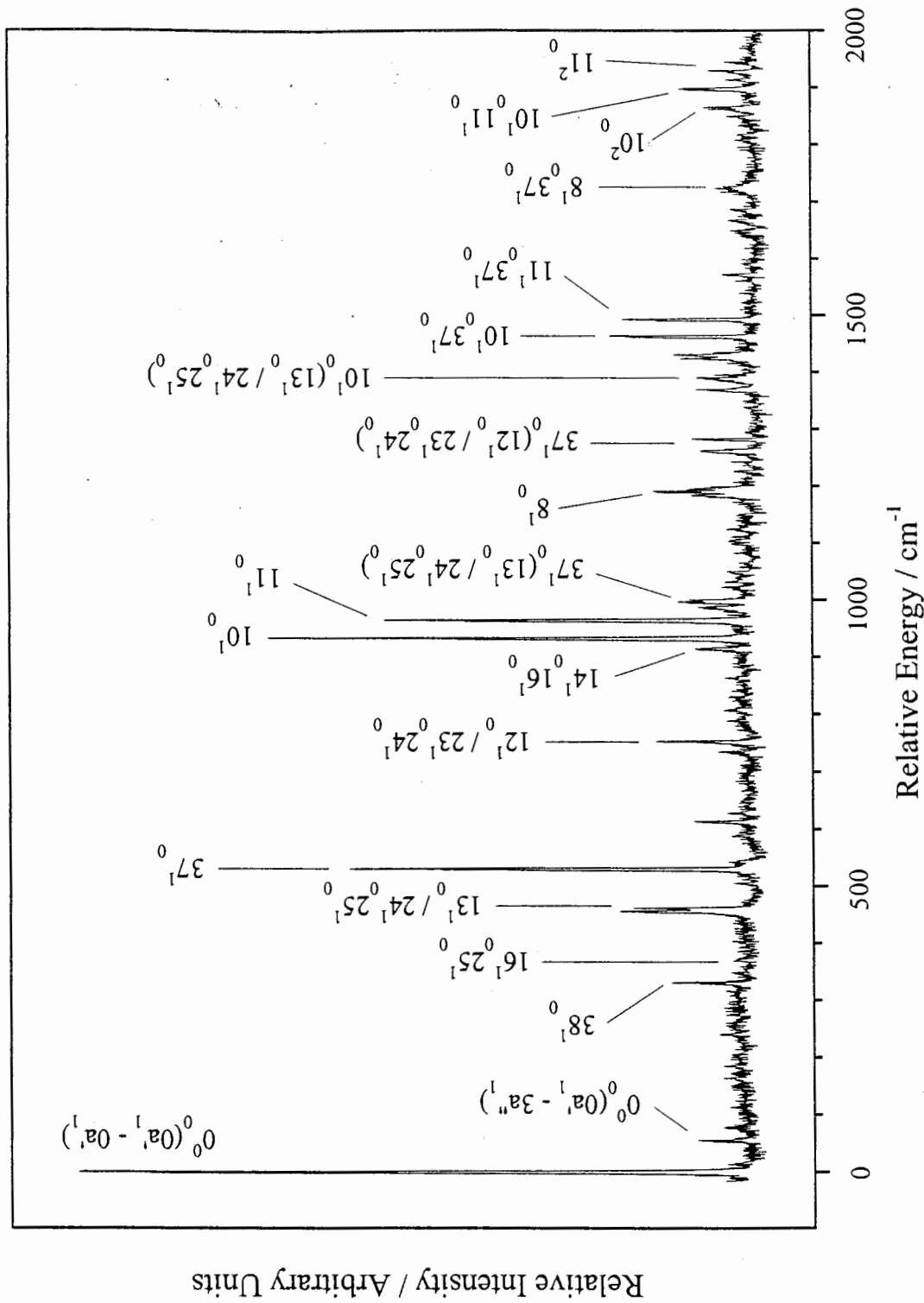


Figure 2.1 Fluorescence excitation spectrum of toluene in the region of the S₁-S₀ (¹B₂-¹A₁) band. The x-axis is relative to the origin transition at 37477.4 cm⁻¹.

the degenerate components of the dominant vibronically inducing mode v_6 in benzene, acts as an intense vibronic origin, being approximately 60% as intense as the origin band. Weak, second order vibronic features are also seen in the spectrum. It is clear that, while being formally allowed, the transition retains a significant vibronically allowed component.

Assignment of the weaker features is less straightforward. In order to provide definitive assignments, dispersed fluorescence spectra (single vibronic level (SVL) fluorescence) were obtained from the majority of the spectral features. The emitting level is assigned based on the terminating S_0 frequencies. It was found that the dispersed fluorescence spectra rapidly become congested with increasing vibrational energy in the emitting level, due no doubt to intramolecular couplings associated with intramolecular vibrational energy redistribution (IVR). For this reason a number of the higher lying vibrations have not had their identity confirmed by dispersed fluorescence spectra, and their assignment is based solely on combinations of S_1 frequencies established in the lower reaches of the vibrational manifold. These transitions are marked by asterisks in table 2.2. The dispersed fluorescence spectra are discussed below. Previous assignments for bands are discussed when presenting the SVL fluorescence spectra.

2.5 Dispersed Fluorescence Spectra

The dispersed fluorescence spectra of non-totally symmetric modes consist of a 0^0 -like spectrum shifted by the ground state frequency of the emitting S_1 level. From the known S_0 frequencies the emitting level can be identified, and with it the excited state frequency. This technique is well established as a method for assigning excited state fundamentals [Knight 1975]. The spectra and the levels with which they are associated will be discussed in order of increasing excitation energy, starting with the origin band. For compactness, tables of assigned features are only provided for those spectra arising

from totally symmetric modes, since the vibrational structure is altered in such cases from that seen in the 0^0 emission. This alteration is a consequence of a change in the Franck-Condon pattern.

2.5.1 0^0 Spectrum

The 0^0 spectrum, recorded at a resolution of 5 cm^{-1} , is illustrated in figure 2.2. This spectrum has been reported previously at lower resolution, and the gross features assigned [Blondeau 1971; Hopkins 1980b]. The major bands are listed in table 2.3 and are noted to be principally short progressions and combinations involving the low lying A_1 modes in S_0 . The non-totally symmetric mode v_{37} (B_2) is also seen to be very strong. These observations are consistent with the vibrational activity seen in the excitation spectrum. A number of weak features are observed which cannot be assigned to any combination of the known ground state frequencies. A number of these appear as weak bands or shoulders to the blue of a prominent fluorescence band, and they may be due to resonances in S_0 involving levels with methyl rotor excitation. The unassigned lines are a small fraction of those observed, and are all of low intensity. The weak lines at -50, -81 and -112 cm^{-1} correspond with the methyl rotor transitions reported by Breen *et al.* [Breen 1987], although there is a discrepancy in the latter frequency (Breen *et al.* report 128 cm^{-1}).

To identify the vibrational levels seen in the excitation spectrum, their SVL fluorescence spectra were assigned using the strongest bands in the 0^0 spectrum as a "fingerprint". The SVL fluorescence spectra from higher S_1 vibrational levels should exhibit the lines seen in the 0^0 spectrum shifted by an amount corresponding to an S_0 fundamental, combination or overtone frequency. For a_1 modes the intensity distribution of these bands may change due to changes in the Franck Condon factors.

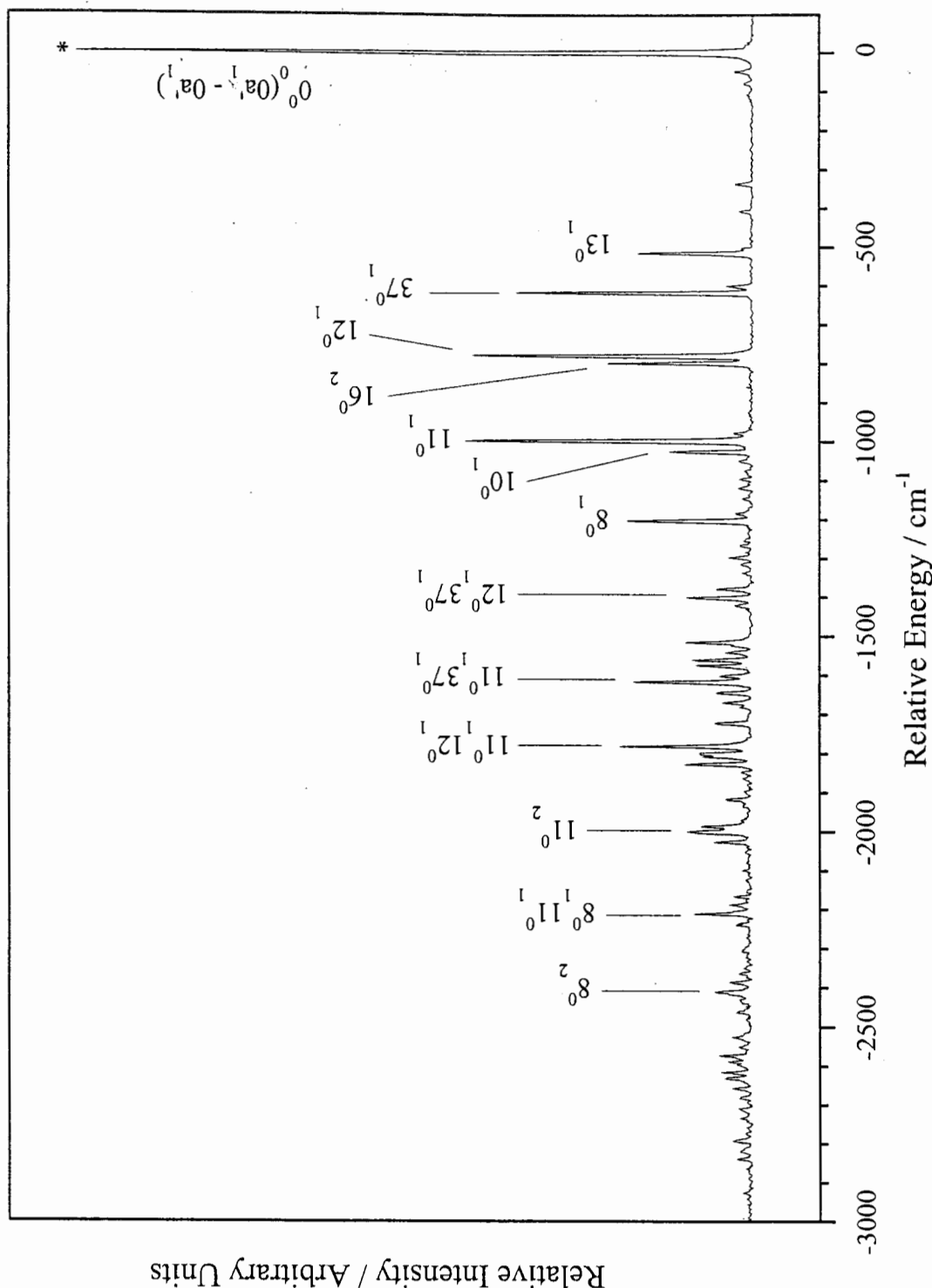


Figure 2.2 Dispersed fluorescence spectrum of toluene from the $0^0(0a'_1)$ level (0 cm^{-1}) at $37\,477.4 \text{ cm}^{-1}$, recorded with a resolution of 5 cm^{-1} . The asterisk indicates the excitation position which is contaminated by scattered laser light.

Table 2.3 Transitions observed in the dispersed fluorescence spectrum of toluene excited to the $0^0(0a'_1)$ level.

| Position ^a / cm ⁻¹ | Relative Intensity | Assignment | Position / cm ⁻¹ | Relative Intensity | Assignment |
|---------------------------------------------|-----------------------|-----------------------------------|--------------------------------|-----------------------|------------------------|
| 0 | 1000 | $0_0^0(0a'_1 \rightarrow 0a'_1)$ | -1560 | 88 | 12_2^0 |
| -50 | 26 | $0_0^0(0a'_1 \rightarrow 3a''_1)$ | -1575 | 83 | $12_1^0 16_2^0$ |
| -81 | 12 | $0_0^0(1e'' \rightarrow 4e')$ | -1601 | 48 | 5_1^0 |
| -112 | 8 | $0_0^0(1e'' \rightarrow 5e'')$ | -1616 | 175 | $11_1^0 37_1^0$ |
| -342 | 24 | 38_1^0 | -1644 | 53 | $10_1^0 37_1^0$ |
| -411 | 18 | $16_1^0, 25_2^0$ | -1668 | 43 | ? |
| -521 | 169 | 13_1^0 | -1720 | 55 | $8_1^0 13_1^0$ |
| -605 | 38 | $16_1^0 25_1^0$ | -1779 | 195 | $11_1^0 12_1^0$ |
| -623 | 348 | 37_1^0 | -1797 | 78 | $11_1^0 16_2^0$ |
| -785 | 413 | 12_1^0 | -1804 | 73 | $10_1^0 12_1^0$ |
| -804 | 213 | 16_2^0 | -1825 | 100 | $8_1^0 37_1^0$ |
| -1003 | 424 | 11_1^0 | | | $10_1^0 16_2^0$ |
| -1030 | 122 | 10_1^0 | -1913 | 39 | ? |
| -1206 | 185 | 8_1^0 | -1981 | 76 | $8_1^0 12_1^0$ |
| -1300 | 35 | $12_1^0 13_1^0$ | -1994 | 96 | 11_2^0 |
| -1317 | 17 | $13_1^0 16_2^0$ | -2020 | 56 | $10_1^0 11_1^0$ |
| -1380 | 53 | $14_1^0 16_1^0$ | -2157 | 27 | $12_1^0 14_1^0 16_1^0$ |
| -1403 | 97 | $12_1^0 37_1^0$ | -2178 | 34 | $12_2^0 37_1^0$ |
| -1422 | 26 | $16_2^0 37_1^0$ | | | $14_1^0 16_3^0$ |
| -1516 | 99 | $11_1^0 13_1^0$ | -2201 | 86 | $8_1^0 11_1^0$ |
| -1540 | 39 | $10_1^0 13_1^0$ | | | $12_1^0 16_2^0 37_1^0$ |

^a Band Positions are given relative to the 0_0^0 band at 37477.4 cm⁻¹.

Table 2.3 (continued)

| Position ^a / cm ⁻¹ | Relative Intensity | Assignment | Position / cm ⁻¹ | Relative Intensity | Assignment |
|---------------------------------------------|-----------------------|---------------------------------------------|--------------------------------|-----------------------|------------------------|
| -2227 | 24 | $8_1^0 10_1^0$ | -2598 | 46 | $11_2^0 37_1^0$ |
| -2396 | 56 | 8_2^0 , $11_1^0 12_1^0 37_1^0$ | -2612 | 41 | $10_1^0 11_1^0 37_1^0$ |
| -2556 | 49 | $11_1^0 12_2^0$ | -2770 | 29 | $11_2^0 12_1^0$ |
| -2571 | 36 | $10_1^0 12_2^0$, $11_1^0 12_1^0 16_2^0$ | -2794 | 18 | $10_1^0 11_1^0 12_1^0$ |

^a Band Positions are given relative to the 0_0^0 band at 37477.4 cm⁻¹.

2.5.2 $\theta\theta + 332 \text{ cm}^{-1}$

The weak band 332 cm⁻¹ to the blue of the origin band can be tentatively assigned as 38_0^1 based on assignments for the -12 cm⁻¹ sequence band reported by Krogh-Jespersen *et al.* [Krogh-Jespersen 1979] and by Leugers and Seliskar [Leugers 1982a]. However Kahane-Paillois [Kahane-Paillois 1958] proposed ν_{38}^1 as 281 cm⁻¹. The dispersed fluorescence spectrum can be assigned to that of 0^0 transposed to lower frequencies by 344 cm⁻¹, as shown in figure 2.3. This shift corresponds to the S₀ level 38₁, identifying the originally excited level in S₁ as 38¹, and confirming the assignment proposed by Krogh-Jespersen *et al.* and Leugers and Seliskar. The assignment of Kahane-Paillois of ν_{38}^1 as 281 cm⁻¹ is seen to be incorrect.

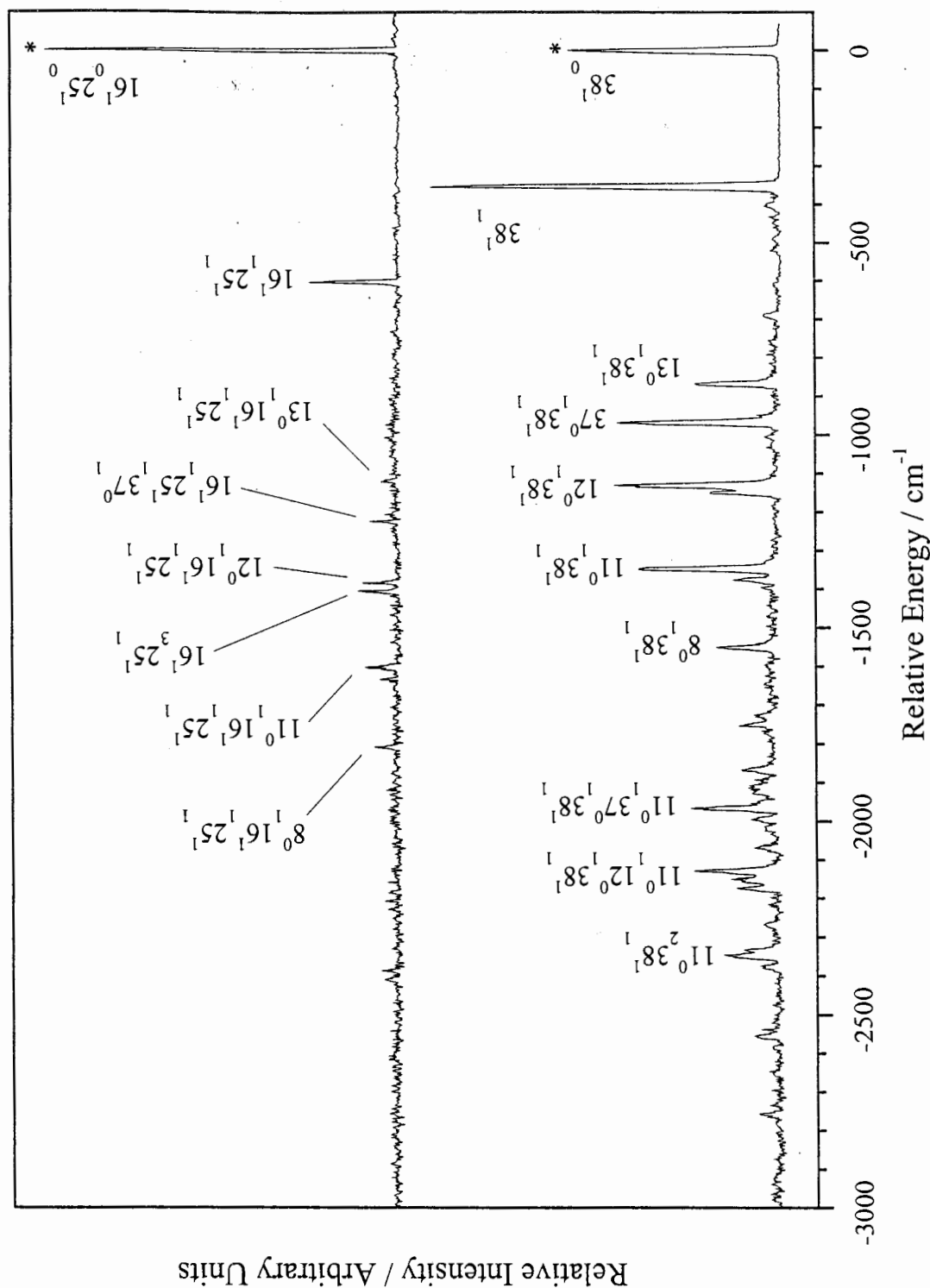


Figure 2.3 Dispersed fluorescence spectra of toluene from the 38^1 (lower) and 16^125^1 (upper) levels at 0^0+332 cm^{-1} and 0^0+372 cm^{-1} respectively, recorded with a resolution of 10 cm^{-1} . Asterisks indicate the excitation positions which are contaminated by scattered laser light.

2.5.3 $\theta^0 + 372 \text{ cm}^{-1}$

The weak excitation feature that we observe 372 cm^{-1} above the origin band was not reported by Smalley *et al.* [Hopkins 1980a], presumably because of its extremely low intensity, however it is seen in the spectrum of Murakami *et al.* [Murakami 1981]. Its dispersed fluorescence spectrum is assigned as a 0^0 spectrum shifted 604 cm^{-1} to the red, as displayed in figure 2.3. There is only one S_0 state in this region, $16_1 25_1$, which is calculated to be at 623 cm^{-1} . Thus we assign the emitting level as $16^1 25^1$, with a frequency of 372 cm^{-1} . This combination has B_2 symmetry, which is vibronically allowed. The transition is thus an example of a second order vibronic band. Although there is some ambiguity concerning the benzene analogue of ν_{25} in toluene (see table 2.1), it has been associated with ν_{11} . This places the $16_0^1 25_0^1$ band in toluene as the analogue of the $11_0^1 16_0^1$ band in benzene. The latter is a strong second order transition [Nicholson 1995; Fischer 1981].

This assignment agrees with previous work which assigned $\nu'_{16} = 228 \text{ cm}^{-1}$ and $\nu'_{25} = 157 \text{ cm}^{-1}$ based on the sequence structure. A weak sequence band, $16_1^1 25_1^1$, should appear at -232 cm^{-1} , and such a band was reported by Ginsburg [Ginsburg 1946]. The sequence bands at 179 cm^{-1} and 61 cm^{-1} are assigned to 16_1^1 and 25_1^1 respectively.

A feature of the $16^1 25^1$ spectrum is the odd intensity ratio of the lines at $-1\ 384 \text{ cm}^{-1}$ and $-1\ 405 \text{ cm}^{-1}$. These correspond to transitions in the 0^0 spectrum terminating in the levels 12_1 and 16_2 , with the transition to the former being stronger than the latter. The opposite is true in this case. We find throughout the toluene fluorescence spectra that emission from levels assigned to involve ν_{16} show this intensity change. 12_1 and 16_2 are both of A_1 symmetry, and are close-lying ($\Delta E \sim 20 \text{ cm}^{-1}$). The 16_2^0 transition should have very little intensity, yet is reasonably strong, and we speculate that this is due to 16_2 borrowing intensity from 12_1 via a Fermi resonance interaction. The intensity changes associated with emission from levels involving excitation of ν_{16} are

suggested to arise as a consequence of the change in the Fermi resonance, which now involves $12_1 16_1$ and 16_3 , and the altered Franck-Condon contribution to each component. The intensity measured may indicate a switching, due to diagonal anharmonicity, in the energy ordering of $12_1 16_1$ and 16_3 .

2.5.4 $0^0 + 457 \text{ cm}^{-1}$ and $0^0 + 462 \text{ cm}^{-1}$

These overlapping transitions have been assigned by Smalley *et al.* [Hopkins 1980a] to a Fermi resonance between ν'_{13} and another, unidentified a_1 combination or overtone.

The dispersed fluorescence spectra are given in figure 2.4. The progression origins for each component are indicated on this figure. Comparison of the two spectra shows that both can be assigned as two overlayed 0^0 spectra. The relative intensities of the two overlayed spectra differ for the two excitation features. Such spectra are characteristic of Fermi resonance. One would expect the relative intensities of the two overlayed spectra to be reversed between the two fluorescence spectra. While the relative intensities clearly change, there is not quite the expected reversal. This is most likely a consequence of our inability to cleanly excite each excitation band, due to overlap of the rotational contours.

The lines at *ca.* -520 cm^{-1} and -664 cm^{-1} form the origins of each of the overlayed 0^0 -like spectra, and hence can be assigned to the vibrational levels involved in the Fermi resonance. The first of these components can be assigned to ν'_{13} , whilst the latter must be due to an overtone or combination band with the correct symmetry (a_1) and appropriate S_0 frequency. The only possibility is $24_1 25_1$, which is predicted to be at -680 cm^{-1} . This assignment confirms previously proposed frequencies for ν'_{24} and ν'_{25} . The value for ν'_{25} has been discussed above. Krogh-Jespersen *et al.* [Krogh-Jespersen 1979] suggest that ν'_{24} may be 320 cm^{-1} based on a weak band seen in the hot band region of the two-photon spectrum. The observed position of the

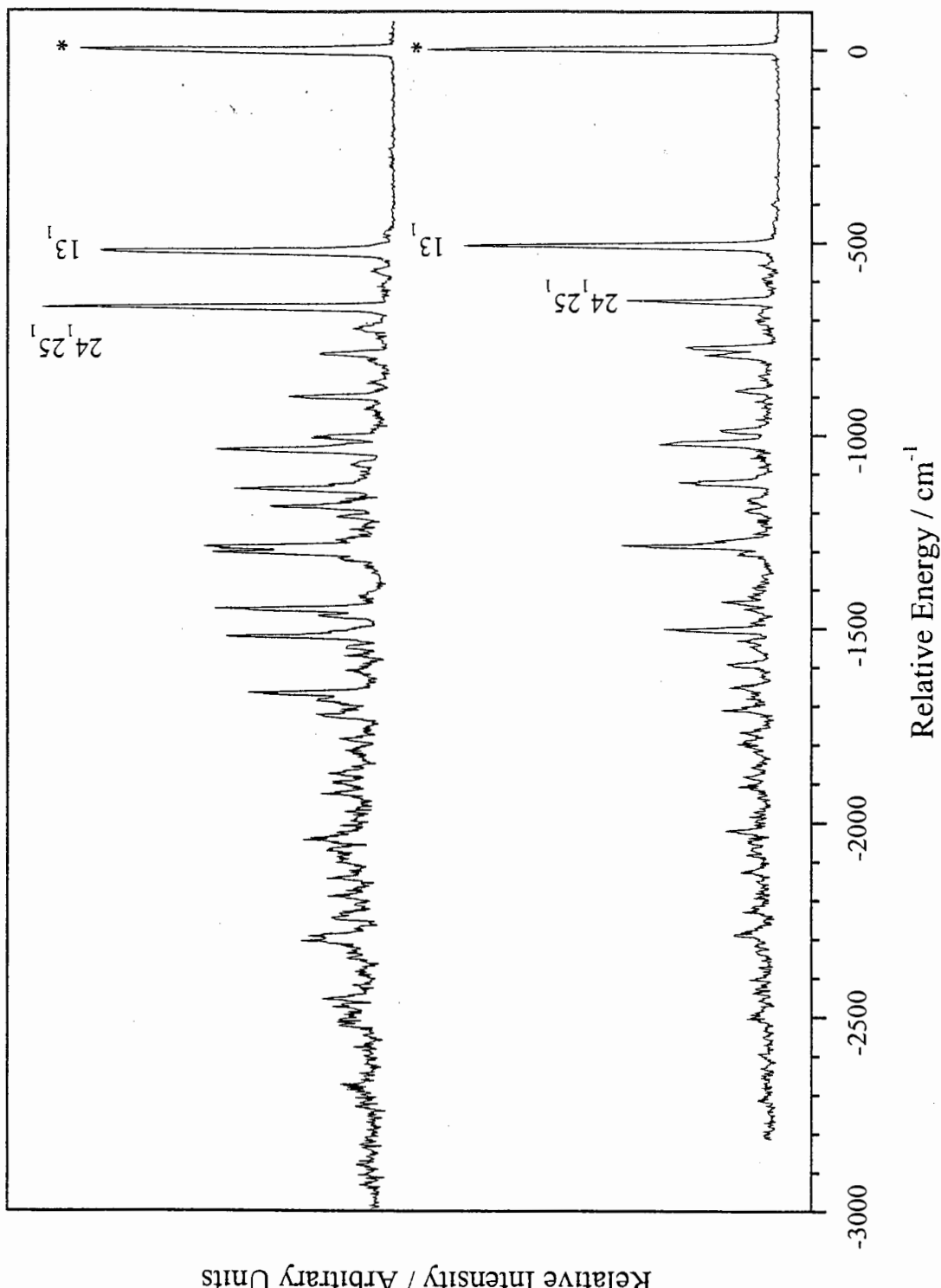


Figure 2.4 Dispersed fluorescence spectra of toluene from the Fermi Resonance components 13^1 and 24^125^1 at $0^0 + 457\text{ cm}^{-1}$ (lower) and $0^0 + 462\text{ cm}^{-1}$ (upper), recorded with a resolution of 10 cm^{-1} . Asterisks indicate the excitation positions which are contaminated by scattered laser light. The terminating S_0 levels are indicated on the progression origins corresponding to the two Fermi Resonance components.

combination band in the LIF spectrum suggests $\nu'_{24} = 302 \text{ cm}^{-1}$. The difference between the calculated and observed positions of the $24_1 25_1$ combination band is 16 cm^{-1} , most probably due to anharmonicity. Assuming a similar shift in S_1 , the frequency of ν'_{24} would be $\sim 320 \text{ cm}^{-1}$, consistent with the band observed by Krogh-Jespersen *et al.*

2.5.5 $0^0 + 532 \text{ cm}^{-1}$

The next feature seen in excitation is the strong band at $0^0 + 532 \text{ cm}^{-1}$. This has been assigned to the transition 37_0^1 by Ginsburg *et al.* [Ginsburg 1946], Kahane-Paillois [Kahane-Paillois 1958] and also Smalley and co-workers [Hopkins 1980a]. Smalley and co-workers [Hopkins 1980b] and Blondeau and Stockburger [Blondeau 1971] have presented assignments for the strong features observed in dispersed fluorescence from this level. We have examined this spectrum afresh to provide a more complete assignment. This analysis is shown in table 2.4 with the 37^1 spectrum presented in figure 2.5. Analysis of the dispersed fluorescence spectrum shows three series of lines corresponding to 0^0 spectra, two based upon transitions to the levels $37_{0,2}$ and the other to 37_1 . This is what is expected for a transition from a non-totally symmetric mode that has both an allowed ($\Delta\nu = 0$) and vibronically active ($\Delta\nu = \pm 1$) component.

2.5.6 $0^0 + 736 \text{ cm}^{-1}$ and $0^0 + 754 \text{ cm}^{-1}$

The band at $\sim 754 \text{ cm}^{-1}$ has been assigned as ν'_{12} by many previous workers, however it is only recently that the lower energy band has been observed [Vasudev 1979; Hopkins 1980a]. This pair of lines has been assigned to a Fermi resonance involving ν'_{12} and another, unidentified a_1 combination or overtone [Vasudev 1979; Hopkins 1980a]. The SVL fluorescence spectra from these two levels, reproduced in figure 2.6, confirm that the emitting levels form a Fermi resonance pair. The spectra

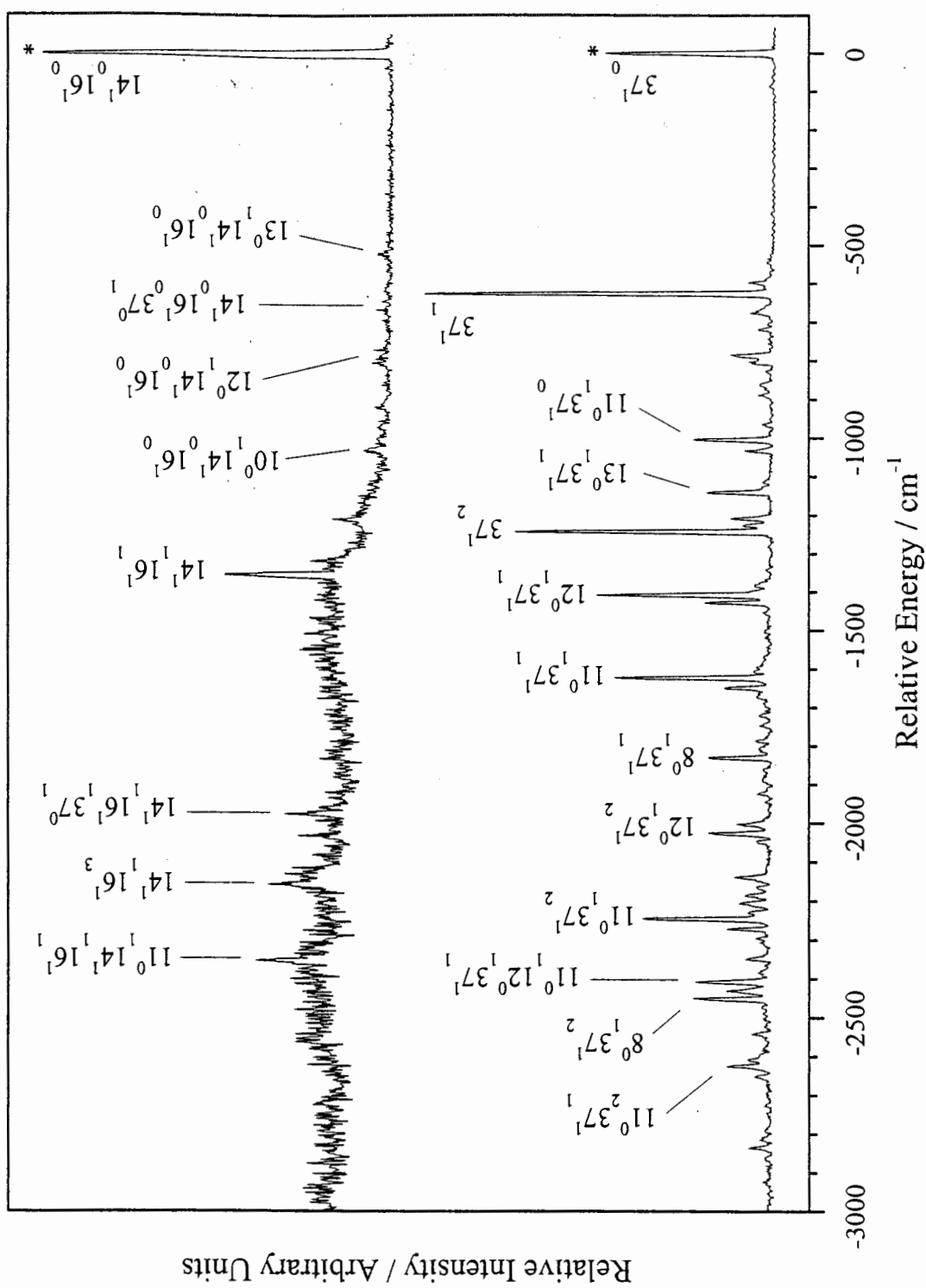


Figure 2.5 Dispersed fluorescence spectra of toluene from the 37^1 (lower) and 14^116^1 (upper) levels at 0^0+532 cm^{-1} and 0^0+915 cm^{-1} , recorded with a resolution of 10 cm^{-1} . Asterisks indicate the excitation positions which are contaminated by scattered laser light.

Table 2.4 Transitions observed in the dispersed fluorescence spectrum of toluene excited to the 37^1 level ($0^0 + 532 \text{ cm}^{-1}$).

| Position ^a / cm^{-1} | Relative Intensity | Assignment | Position / cm^{-1} | Relative Intensity | Assignment |
|---------------------------------------------|-----------------------|---------------------------------------------|--------------------------------|-----------------------|------------------------|
| 0 | 484 | 37_0^1 | -2022 | 189 | $12_1^0 37_2^1$ |
| -623 | 1000 | 37_1^1 | -2043 | 51 | $16_2^0 37_2^1$ |
| -671 | 68 | $37_1^1 (0a'_1 \rightarrow 3a''_1)$ | -2133 | 113 | $11_1^0 13_1^0 37_1^1$ |
| -717 | 46 | $37_1^1 (1e'' \rightarrow 4e')$ | -2159 | 51 | $10_1^0 13_1^0 37_1^1$ |
| -785 | 124 | $12_1^0 37_0^1$ | -2180 | 84 | $12_2^0 37_1^1$ |
| -803 | 72 | $16_2^0 37_0^1$ | -2197 | 100 | $12_1^0 16_2^0 37_1^1$ |
| -1004 | 232 | $11_1^0 37_0^1$ | -2221 | 76 | $5_1^0 37_1^1$ |
| -1032 | 84 | $10_1^0 37_0^1$ | -2238 | 377 | $11_1^0 37_2^1$ |
| -1141 | 194 | $13_1^0 37_1^1$ | -2263 | 135 | $10_1^0 37_2^1$ |
| -1208 | 124 | $8_1^0 37_0^1$ | -2286 | 53 | ? |
| -1225 | 93 | ? | -2339 | 82 | $8_1^0 13_1^0 37_1^1$ |
| -1242 | 741 | 37_2^1 | -2398 | 227 | $11_1^0 12_1^0 37_1^1$ |
| -1380 | 57 | $14_1^0 16_1^0 37_0^1$ | -2421 | 137 | $10_1^0 12_1^0 37_1^1$ |
| -1407 | 508 | $12_1^0 37_1^1$ | | | $11_1^0 16_2^0 37_1^1$ |
| -1427 | 200 | $16_2^0 37_1^1$ | -2441 | 233 | $8_1^0 37_2^1$ |
| -1605 | 59 | $5_1^0 37_0^1$ | | | $10_1^0 16_2^0 37_1^1$ |
| -1620 | 457 | $11_1^0 37_1^1$ | -2530 | 65 | ? |
| -1647 | 144 | $10_1^0 37_1^1$ | -2595 | 76 | $8_1^0 12_1^0 37_1^1$ |
| -1783 | 53 | $11_1^0 12_1^0 37_0^1$ | -2610 | 135 | $11_2^0 37_1^1$ |
| -1827 | 190 | $8_1^0 37_1^1$ | -2637 | 57 | $10_1^0 11_1^0 37_1^1$ |
| -1919 | 48 | $12_1^0 13_1^0 37_1^1$ | -2818 | 74 | $8_1^0 11_1^0 37_1^1$ |
| -1999 | 107 | $11_2^0 37_0^1$, $14_1^0 16_1^0 37_1^1$ | -2846 | 30 | $8_1^0 10_1^0 37_1^1$ |

^a Positions are measured relative to the 37_0^1 band at 38009.4 cm^{-1} .

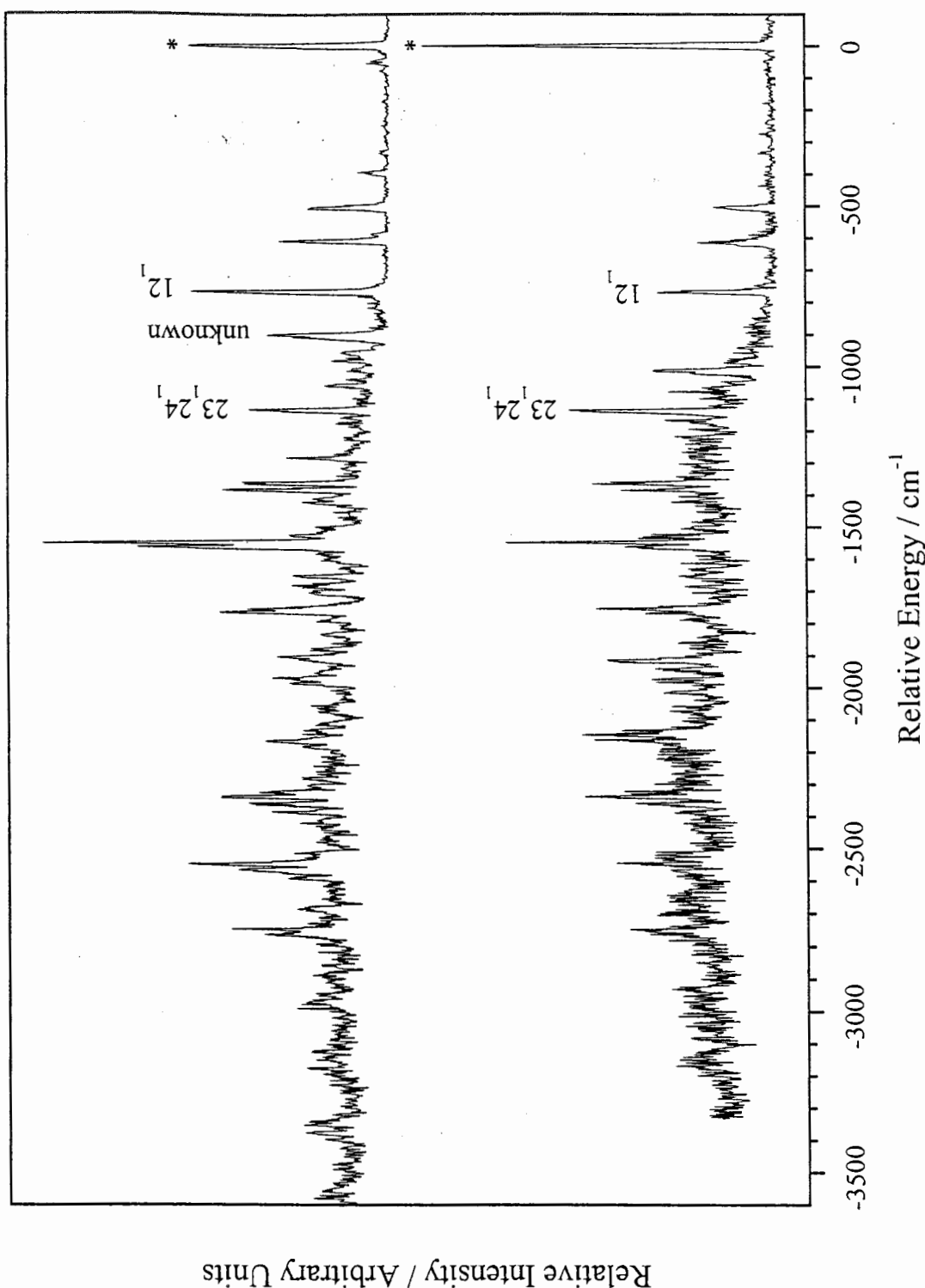


Figure 2.6 Dispersed fluorescence spectra of toluene from the Fermi Resonance components 12^1 and 23^124^1 at $0^0 + 736\text{ cm}^{-1}$ (lower) and $0^0 + 754\text{ cm}^{-1}$ (upper), recorded with a resolution of 10 cm^{-1} . Asterisks indicate the excitation positions which are contaminated by scattered laser light. The terminating S_0 levels are indicated on the progression origins corresponding to the two Fermi Resonance components. The upper spectrum shows a strong unassigned peak at -904 cm^{-1} .

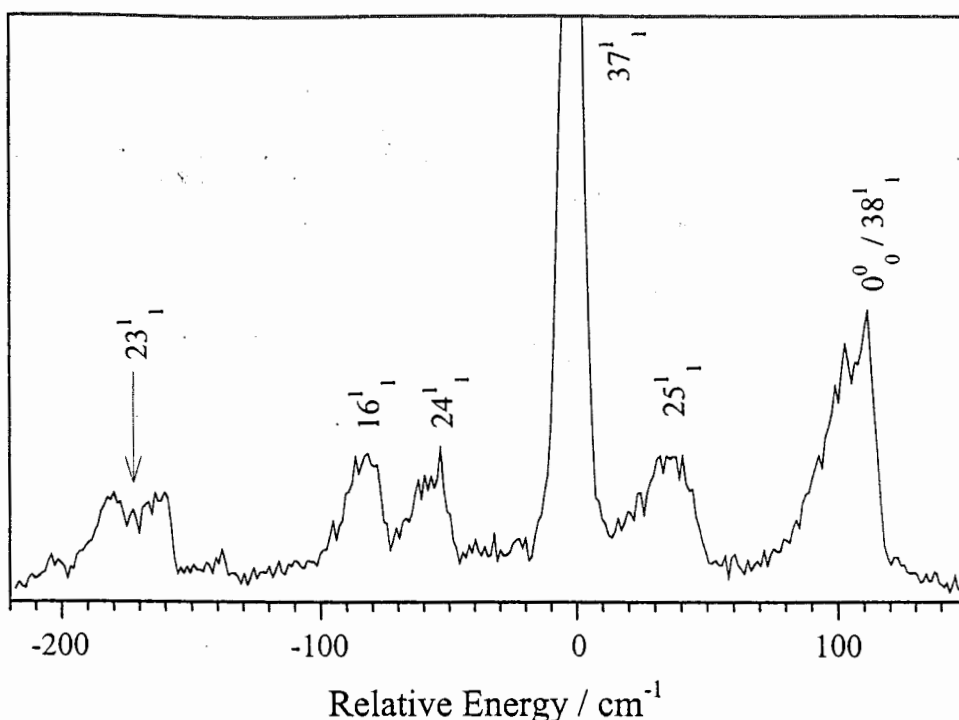
identify one of the modes involved as ν_{12} while the other has an S_0 frequency of 1157 cm^{-1} . On this basis the other state is almost certainly 23^124^1 which has a calculated S_0 frequency of 1159 cm^{-1} . The nearest other possibility is 22^124^1 , which at 1192 cm^{-1} , some 35 cm^{-1} away, is too far removed to be likely.

By deconvoluting the observed resonance, we deduce unperturbed S_1 frequencies for the two coupled levels of 748 and 743 cm^{-1} , and a coupling matrix element of 8.4 cm^{-1} . This implies a frequency for ν'_{23} of 423 cm^{-1} . The deperturbed frequency of ν'_{12} is 748 cm^{-1} . The large frequency change between S_0 and S_1 for ν_{23} (60% reduction) is consistent with the behaviour of the analogous mode in benzene [Knight 1975] (ν_4 ; 52% reduction), adding support for this assignment.

Further evidence for this assignment comes from our studies of collision-induced vibrational energy transfer. Collisions offer a means of populating vibrational levels in S_1 toluene that cannot be populated by direct optical excitation. Collision-induced vibrational energy transfer in supersonic expansions leads overwhelmingly to population of levels lying below the initial level [Moss 1983; Rice 1986; Waclawik 1993; Waclawik 1995]. We have undertaken experiments in which collision-induced transfer from the optically prepared state 37^1 is used to access vibrational levels that lie below this initial state. ν'_{23} lies below 37^1 , and hence the observation of a feature at a sequence position of $\nu'_{23} - \nu''_{23} = 272\text{ cm}^{-1}$ would add significant weight to the assignment of ν'_{23} .

The collision-induced transfer experiments were undertaken in the collision region of the supersonic expansion ($X/D=3$). The vibrational relaxation was measured using time resolved dispersed fluorescence spectroscopy. The details of this type of experiment have been given in a previous publication [Waclawik 1995]. Two fluorescence spectra, corresponding to different times after excitation, are presented in figure 2.7. The spectrum is scanned over the region surrounding the 37^1 band, which is where any

Relative Intensity / Arbitrary Units



Relative Intensity / Arbitrary Units

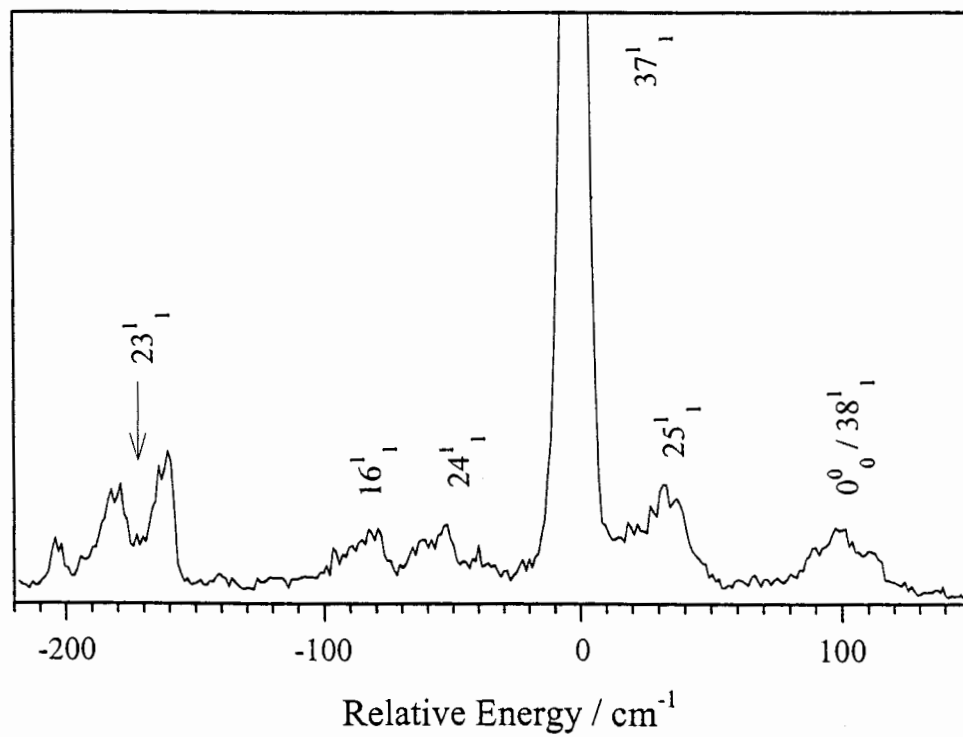


Figure 2.7 TRDF spectra of toluene in the region of the 37_1^1 band with nitrogen as collision partner. The data is obtained by integrating the regions between 10 ns and 60 ns (lower) and 60 ns and 110 ns (upper) in the fluorescence decay trace. The wavenumber scale is relative to the 37_1^1 band position.

bands due to emission from collisionally populated levels will appear (so-called growth bands). The spectrum corresponding to the longer delay time shows a number of growth bands. All can be assigned to known vibrational levels. In particular, there is growth at the position expected for transfer to v'_{23} based on our assignment. The evidence strongly supports v'_{23} being 423 cm^{-1} .

There are extra bands in the 0^0+754 cm^{-1} spectrum beyond those expected from the Fermi resonance, the most prominent of which is indicated in figure 2.6. This suggests that this level is further mixed with a near lying level, and, since these extra bands are not seen in the 0^0+736 cm^{-1} spectrum, that this mixing arises because the energy shift associated with the Fermi resonance brings the states into resonance. There is no additional band observed in the excitation spectrum that can be assigned to the other component of this resonance. We suggest that the other component is hidden beneath the rotational contour of the 0^0+754 cm^{-1} band, as this is consistent with this resonance arising from weak coupling between two very close levels. The other component of the resonance has not been identified.

The spectra also reveal a number of lines involving transitions built on 10_1^0 and 11_1^0 . This suggests that in the excited electronic state the normal coordinates are changed from those of the ground electronic state such that the modes labelled v'_{10} , v'_{11} and v'_{12} in S_1 are each mixtures of v''_{10} , v''_{11} and v''_{12} as they occur in S_0 . In other words, the normal coordinates are rotated in the excited electronic state. Further evidence for this has been observed in the spectra of v'_{10} and v'_{11} which are discussed below.

These spectra are the first to reveal the spectroscopic signature of intramolecular vibrational energy redistribution (IVR) in the excited electronic state. A noisy, featureless "hump" underlies the sharp spectrum assigned to the feature excited. This hump begins *ca.* 1000 cm^{-1} from the excitation position. This behaviour is a usual

feature of emission spectra from high lying levels in excited electronic states, and has been taken to indicate the onset of IVR [Parmenter 1982; Smalley 1983]. This effect appears in the dispersed fluorescence spectra from all higher lying vibrational levels. Its presence causes difficulties in assigning some of the spectra from higher lying levels. IVR is discussed in a separate section below.

2.5.7 $0^0 + 809 \text{ cm}^{-1}$ and $0^0 + 864 \text{ cm}^{-1}$

The weak bands at $0^0 + 809 \text{ cm}^{-1}$ and $0^0 + 864 \text{ cm}^{-1}$ have not been previously reported. Dispersed fluorescence spectra from these bands are dominated by the broad featureless emission discussed above to such an extent that they are unassignable on the basis of these spectra. However, based on the frequencies of 37^1 and 38^1 deduced from spectra of lower lying bands, the level at $0^0 + 864 \text{ cm}^{-1}$ can be assigned as $37^1 38^1$. Both the position and intensity of the band agree with those expected based on this assignment. There is no obvious assignment for the level at $0^0 + 809 \text{ cm}^{-1}$ and this band remains unidentified.

2.5.8 $0^0 + 915 \text{ cm}^{-1}$

The band at $0^0 + 915 \text{ cm}^{-1}$ was observed by Smalley and coworkers [Hopkins 1980a] and by Vasudev and Brand [Vasudev 1979] (observed at 922 cm^{-1}), who associated it with a Fermi resonance involving ν'_{11} . Fluorescence from this excitation feature is close to being unusable for assignment due to the extensive background emission above 1200 cm^{-1} which almost swamps the residual structure. Under close inspection the spectrum does, however, show evidence for a 0^0 spectrum shifted by 1355 cm^{-1} , as illustrated in figure 2.5. The spectrum does not show structure consistent with a Fermi resonance involving ν'_{11} .

There are three candidates for the terminating level at 1355 cm^{-1} , chosen by virtue of their possessing the correct symmetry and having a predicted S_0 frequency within the range $\pm 20\text{ cm}^{-1}$ from the observed band. These three possibilities are 21^124^1 (1359 cm^{-1}), 14^116^1 (1371 cm^{-1}) and 10^138^1 (1372 cm^{-1}). Assignment is aided by the observation that there is an anomalous intensity ratio for the lines at -2130 cm^{-1} and -2157 cm^{-1} , corresponding to fluorescence terminating in levels involving combinations of the emitting level with 12_1 and 16_2 . In the 0^0 spectrum the transition 12_1^0 is approximately twice as intense as 16_2^0 . However the opposite is true for the spectrum at hand and also for that obtained from the level at 0^0+372 cm^{-1} , which was assigned to 16^125^1 . Similar, less pronounced effects can also be seen in spectra that are assigned to v'_{12} or combinations thereof. In these cases the intensity ratio is generally between two and one. As we have discussed when presenting the 0^0+372 cm^{-1} assignment, 12_1 and 16_2 are believed to be in Fermi resonance, and disturbed intensity ratios of the type seen here are observed for emitting levels involving combinations with v'_{16} and also with v'_{12} . This suggests that the excitation level observed at 0^0+915 cm^{-1} may be assigned to 14^116^1 rather than to either 21^124^1 or 10^138^1 . v'_{14} is therefore deduced to be 687 cm^{-1} .

2.5.9 $0^0 + 935\text{ cm}^{-1}$ and $0^0 + 966\text{ cm}^{-1}$

The bands at 0^0+935 cm^{-1} and 0^0+966 cm^{-1} have been assigned by previous workers as 11_0^1 and 10_0^1 respectively [Ginsburg 1946; Kahane-Paillous 1958; Vasudev 1979; Krogh-Jespersen 1979; Hopkins 1980a]. The dispersed fluorescence spectra from these two bands are illustrated in figure 2.8 and detailed assignments for the latter level are listed in table 2.5. Smalley and co-workers [Hopkins 1980b] have given assignments for the most prominent bands in these spectra. Blondeau and Stockburger [Blondeau 1971] have reported the room temperature dispersed fluorescence spectrum from the $0^0 + 935\text{ cm}^{-1}$ feature which shows little structure due to the overwhelming

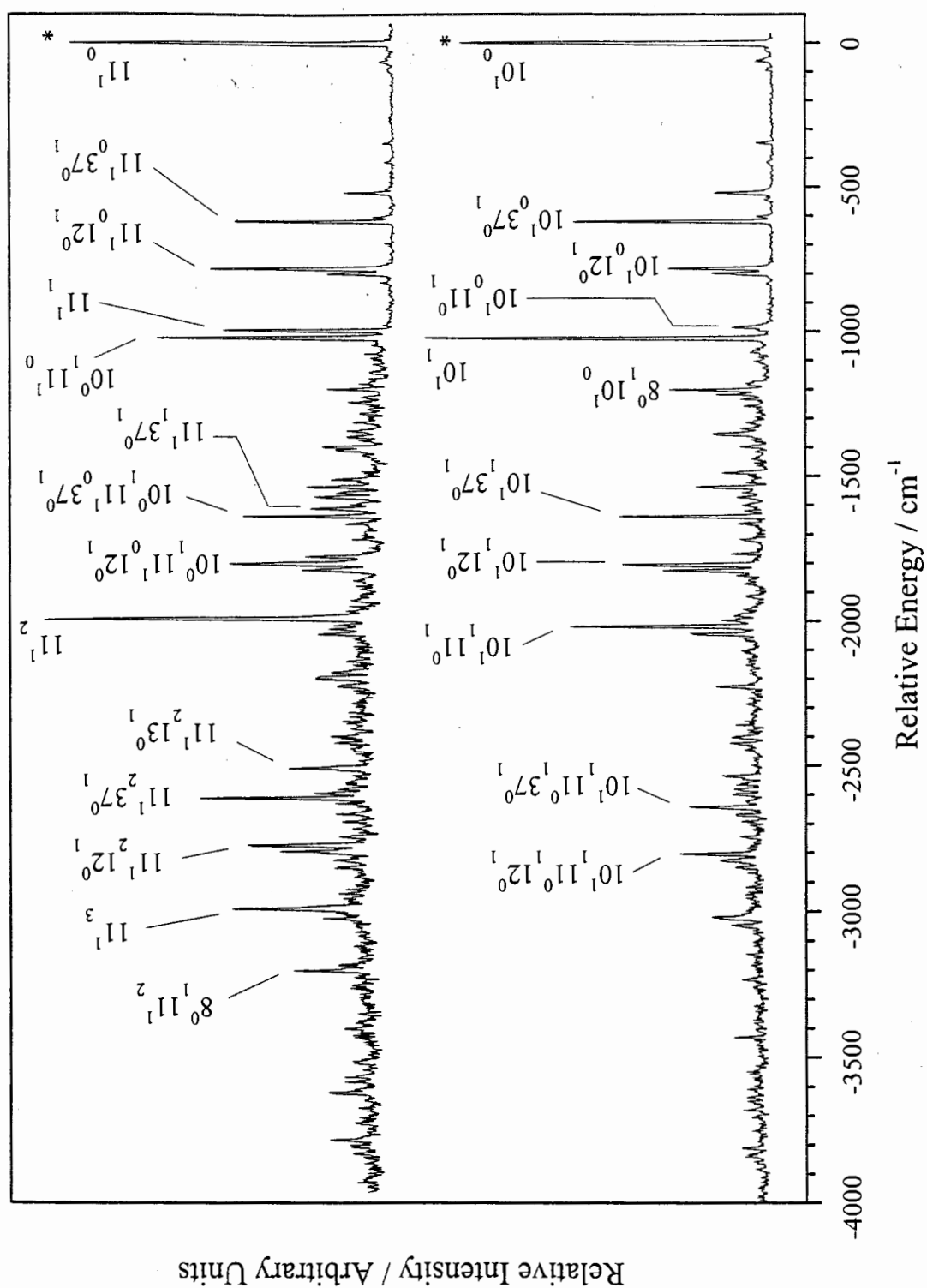


Figure 2.8 Dispersed fluorescence spectra of toluene from the 10^1 (lower) and 11^1 (upper) levels at $0^0 + 935 \text{ cm}^{-1}$ and $0^0 + 966 \text{ cm}^{-1}$ respectively, recorded with a resolution of 5 cm^{-1} . Asterisks indicate the excitation positions which are contaminated by scattered laser light.

Table 2.5 Transitions observed in the dispersed fluorescence spectrum of toluene excited to the 11^1 level ($0^0 + 966 \text{ cm}^{-1}$) (continued on next page).

| Position ^a / cm^{-1} | Relative Intensity | Assignment | Position / cm^{-1} | Relative Intensity | Assignment |
|---------------------------------------------|-----------------------|--------------------------------------|--------------------------------|-----------------------|--------------------------|
| 0 | 926 | 11_0^1 | -1651 | 428 | $10_1^0 11_0^1 37_1^0$ |
| -347 | 24 | $11_0^1 38_1^0$ | -1674 | 131 | ? |
| -414 | 17 | $11_0^1 16_1^0$, $11_0^1 25_2^0$ | -1728 | 113 | $8_1^0 11_0^1 13_1^0$ |
| -522 | 135 | $11_0^1 13_1^0$ | -1788 | 248 | $11_1^1 12_1^0$ |
| -607 | 54 | $11_0^1 16_1^0 25_1^0$ | -1813 | 468 | $10_1^0 11_0^1 12_1^0$, |
| -623 | 452 | $11_0^1 37_1^0$ | -1833 | 257 | $11_1^1 16_2^0$ |
| -788 | 522 | $11_0^1 12_1^0$ | | | $8_1^0 11_0^1 37_1^0$ |
| -805 | 183 | $11_0^1 16_2^0$ | -2001 | 1000 | 11_2^1 |
| -1004 | 486 | 11_1^1 | -2023 | 164 | $10_1^0 11_1^1$ |
| -1030 | 677 | $10_1^0 11_0^1$ | -2037 | 181 | ? |
| -1209 | 184 | $8_1^0 11_0^1$ | -2054 | 212 | $10_2^0 11_0^1$ |
| -1256 | 123 | ? | -2188 | 174 | $11_0^1 12_2^0 37_1^0$ |
| -1294 | 90 | $11_0^1 12_1^0 13_1^0$ | -2203 | 202 | $8_1^0 11_1^1$, |
| -1325 | 109 | $11_0^1 13_1^0 16_2^0$ | | | $11_0^1 12_1^0 16_2^0$ |
| -1354 | 128 | $11_1^1 38_1^0$ (?) | -2234 | 157 | $8_1^0 10_1^0 11_0^1$ |
| -1374 | 128 | $10_1^0 11_0^1 38_1^0$ (?) | -2407 | 176 | $11_1^1 12_1^0 37_1^0$, |
| -1388 | 95 | $11_0^1 14_1^0 16_1^0$ | | | $8_2^0 11_0^1$ |
| -1409 | 198 | $11_0^1 12_1^0 37_1^0$ | -2428 | 163 | $10_1^0 11_0^1 12_1^0$ |
| -1421 | 139 | $11_0^1 16_2^0 37_1^0$ | | | $11_1^1 16_2^0 37_1^0$ |
| -1522 | 173 | $11_1^1 13_1^0$ | -2513 | 297 | $11_2^1 13_1^0$ |
| -1549 | 243 | $10_1^0 11_0^1 13_1^0$ | -2563 | 135 | $11_1^1 12_2^0$ |
| -1568 | 158 | $11_0^1 12_2^0$ | -2585 | 157 | $10_1^0 11_0^1 12_2^0$, |
| -1583 | 221 | $11_0^1 12_1^0 16_2^0$ | | | $11_1^1 12_1^0 16_2^0$ |
| -1623 | 233 | $11_1^1 37_1^0$ | -2599 | 225 | $11_1^1 5_1^0$ |

^a Positions are measured relative to the 11_0^1 band at 38443.7 cm^{-1} .

Table 2.5 (continued):

| Position a / cm ⁻¹ | Relative Intensity | Assignment | Position / cm ⁻¹ | Relative Intensity | Assignment |
|----------------------------------|-----------------------|-------------------------------------------------------------------------------------------------------------------------------------------------------------------------------------------------------------------------------------------------------------------------------|--------------------------------|-----------------------|--------------------------------------------------------------------------------------------------------------------|
| -2616 | 552 | 11 ₂ ¹ 37 ₁ ⁰ | -2851 | 126 | 8 ₁ ⁰ 10 ₁ ⁰ 11 ₀ ¹ 37 ₁ ⁰ |
| -2633 | 162 | 10 ₁ ⁰ 11 ₁ ¹ 37 ₁ ⁰ | | | 10 ₂ ⁰ 11 ₀ ¹ 16 ₂ ⁰ |
| -2669 | 161 | 10 ₂ ⁰ 11 ₀ ¹ 37 ₁ ⁰ | -2991 | 461 | 11 ₃ ¹ |
| -2697 | 143 | ? | -3023 | 197 | 10 ₁ ⁰ 11 ₂ ¹ |
| -2747 | 150 | 8 ₁ ⁰ 10 ₁ ⁰ 11 ₀ ¹ 13 ₁ ⁰ | -3199 | 283 | 8 ₁ ⁰ 11 ₂ ¹ |
| -2779 | 417 | 11 ₂ ¹ 12 ₁ ⁰ | -3393 | 137 | 11 ₂ ¹ 12 ₁ ⁰ 37 ₁ ⁰ |
| -2799 | 322 | 11 ₂ ¹ 16 ₂ ⁰ , 10 ₁ ⁰ 11 ₁ ¹ 12 ₁ ⁰ | -3506 | 96 | 11 ₃ ¹ 13 ₁ ⁰ |
| | | | -3553 | 137 | 11 ₂ ¹ 12 ₂ ⁰ |
| -2828 | 168 | 8 ₁ ⁰ 11 ₁ ¹ 37 ₁ ⁰ , 10 ₂ ⁰ 11 ₀ ¹ 12 ₁ ⁰ , 10 ₁ ⁰ 11 ₁ ¹ 16 ₂ ⁰ | -3571 | 136 | 11 ₂ ¹ 12 ₁ ⁰ 16 ₂ ⁰ |
| | | | -3608 | 183 | 11 ₃ ¹ 37 ₁ ⁰ |
| | | | -3767 | 179 | 11 ₃ ¹ 12 ₁ ⁰ |

a Positions are measured relative to the 11₀¹ band at 38443.7 cm⁻¹.

contribution of IVR. The free jet spectrum is less influenced by IVR, revealing a role for rotational coupling mechanisms in the state mixing.

As can be seen from the figure, the structure in both spectra is very similar, and the assignments shown in table 2.5 can be readily extrapolated to yield those for the 0⁰+935 cm⁻¹ level. Both spectra exhibit a large number of lines terminating in levels built upon 11₁ and 10₁, suggesting that the S₁ normal coordinates for these vibrations are best described as a mixture of the motions of v₁₀ and v₁₁ in the ground electronic state. This strong mixing was noted by Smalley and co-workers. In addition, our spectra show evidence for a weaker mixing on the part of v₁₂. The appearance of v₁₀

and ν_{11} in the 12^1 emission has been noted earlier. Thus it appears that the change in vibrational potential between the ground and excited electronic states leads to an alteration in the normal coordinates for ν'_{10} , ν'_{11} and ν'_{12} .

Based on the relative intensities of the two bands terminating in ν_{10} and ν_{11} in S_0 , we assign the band at $0^0 + 935 \text{ cm}^{-1}$ to 10_0^1 and the band at $0^0 + 966 \text{ cm}^{-1}$ to 11_0^1 .

However it is clear that the mixing is substantial and the assignment to individual modes is a gross approximation. Its primary use is to simplify the notation used to label the fluorescence transitions.

2.5.10 $0^0 + 1193 \text{ cm}^{-1}$

The feature at $0^0 + 1193 \text{ cm}^{-1}$ appears to be two or three overlapped transitions, and this probably explains the different frequencies reported by various authors [Ginsburg 1946; Kahane-Paillois 1958; Krogh-Jespersen 1979; Vasudev 1979]. Ginsburg *et al.* [Ginsburg 1946] report a diffuse band in this region which they assign to ν'_8 , with a frequency of 1189 cm^{-1} . Vasudev and Brand [Vasudev 1979] and Krogh-Jespersen *et al.* [Krogh-Jespersen 1979] also assign it to ν'_8 , however they report frequencies of 1193 and 1194 cm^{-1} respectively. Because of the poor quality of the dispersed fluorescence spectra (principally due to IVR as outlined above) only the central component of the LIF feature was investigated. The spectrum, illustrated in figure 2.9, shows a band at a displacement from excitation consistent with the emitting being level is ν'_8 .

Analysis of this spectrum was hindered not only by the background due to IVR, but by a number of unassignable lines, suggesting that the other components of the excitation line may also be contributing. Furthermore, there are anomalous intensities in the bands close to excitation: the 0^0 -like structure built on 8_0^1 does not show the expected band intensities. We do not know the reason for this anomalous intensity pattern.

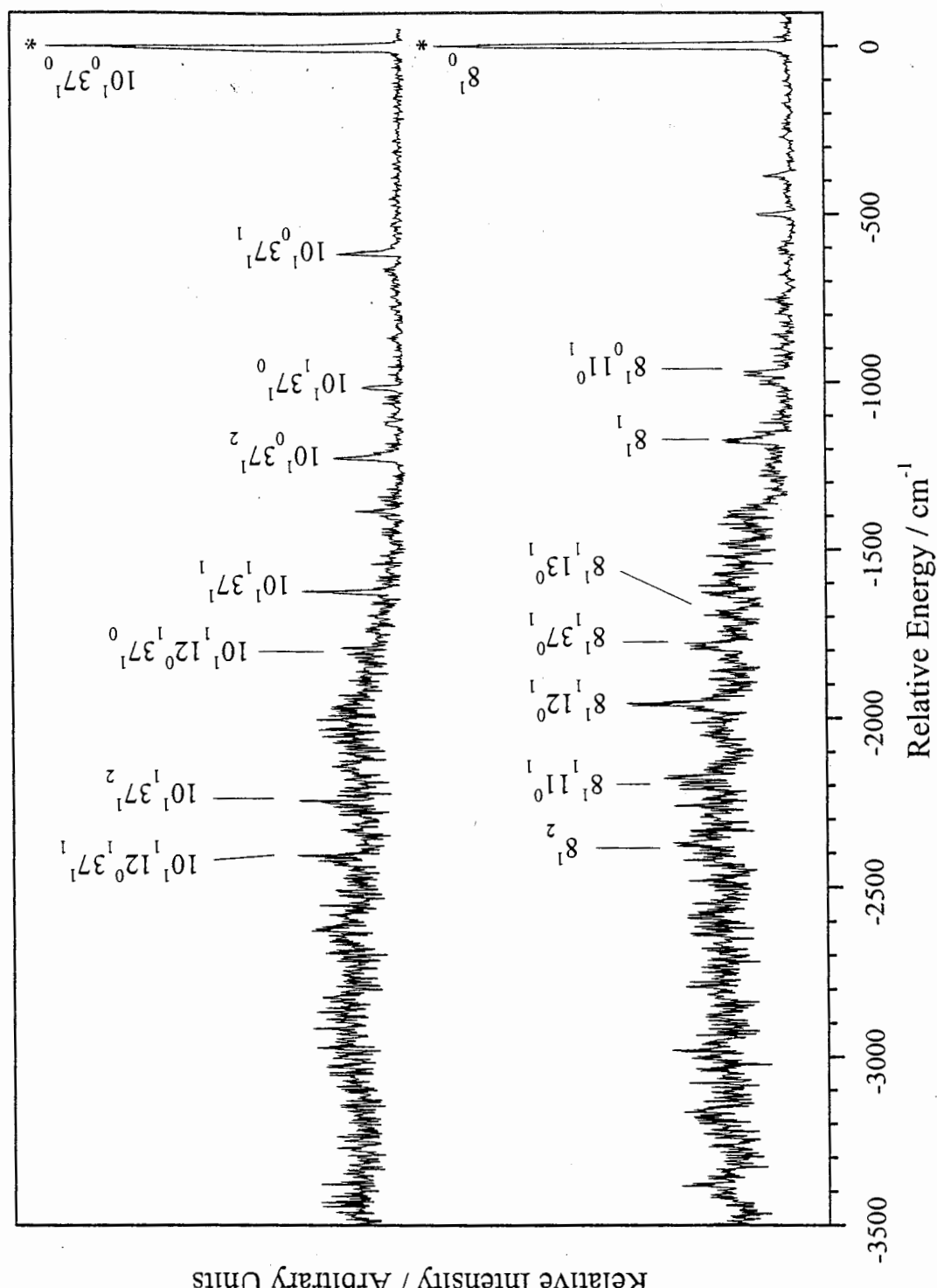


Figure 2.9 Dispersed fluorescence spectra of toluene from the 8^1 (lower) and 10^137^1 (upper) levels at 0^0+1193 cm^{-1} and 0^0+1466 cm^{-1} respectively, recorded with a resolution of 10 cm^{-1} . Asterisks indicate the excitation positions which are contaminated by scattered laser light.

2.5.11 Levels above $0^0 + 1193 \text{ cm}^{-1}$

The stronger vibrational activity seen above 1193 cm^{-1} can be assigned as higher progression members of modes that have already been identified. In particular, one should see progressions in the two intense totally symmetric modes ν_{10} and ν_{11} built on ν_{37} . Assignments made in this fashion, without recourse to confirmation via dispersed fluorescence, are shown in table 2.2 marked with an asterisk. It is clear from our experience at lower energies that the states are becoming significantly mixed and that this is causing the dispersed fluorescence spectra to become diffuse and of limited value in aiding assignment. This is particularly the case with weaker excitation features, which seem to be more severely affected. The fluorescence spectrum from the excitation line at $0^0 + 1263 \text{ cm}^{-1}$ is too diffuse to provide an assignment. Consequently it was felt that no use would be served by measuring fluorescence spectra from any of the higher lying weak features. However, fluorescence from the strong line at $0^0 + 1466 \text{ cm}^{-1}$ was obtained, and although the spectrum is very congested, it confirmed assignment of this level as ν_{37} added to the $0^0 + 935 \text{ cm}^{-1}$ band. It is thus assigned 10^{1371} ; the spectrum is shown in figure 2.9. (Recall, however that the ν'_{10} , ν'_{11} and ν'_{12} normal modes are mixed relative to the S_0 values.)

2.6. Sequence Structure

From the dispersed fluorescence spectra we have assignments for the S_1 frequencies for all of the modes with S_0 frequencies below 728 cm^{-1} . These confirm the assignments of the sequence structure reported by Krogh-Jespersen *et al.* [Krogh-Jespersen 1979]. The sequence bands observed in the two photon spectrum are listed in table 2.6, along with assignments in the new numbering scheme.

Table 2.6 Sequence transitions observed in the room temperature two photon excitation spectrum of toluene [Krogh-Jespersen 1979]. Band positions are measured relative to the origin transition.

| Band position ^a / cm ⁻¹ | Assignment |
|--------------------------------------------------|------------------------------|
| -12 | 38 ₁ ¹ |
| -61 | 25 ₁ ¹ |
| -95 | 37 ₁ ¹ |
| -151 | 24 ₁ ¹ |
| -179 | 16 ₁ ¹ |

^a Band positions are measured relative to the 0₀⁰ band at 37477.4 cm⁻¹.

The sequence structure reported by Krogh-Jespersen *et al.* is consistent with that seen by other workers. The only exception comes from the high resolution study of the origin band by Leugers and Seliskar [Leugers 1982a, 1982b, 1983]. These authors report that a feature at -7.32 cm⁻¹ is due to a sequence band. Our assignments of S₁ frequencies fail to predict any sequences closer than -10 cm⁻¹. Based on the calculated methyl rotor levels [Breen 1987], the methyl rotor will have significant population in levels with many quanta in the internal rotation. Examination of the calculated S₁ and S₀ rotor levels reveals that there will be a large number of rotor sequence transitions that will stack up around the parent band. These are the most likely candidates for the near lying sequences reported by Leugers and Seliskar.

2.7 Intramolecular Vibrational Energy Redistribution (IVR)

Toluene featured early in studies of IVR. Blondeau and Stockburger drew attention to the loss of structure in single vibronic level fluorescence spectra from high vibrational energies as early as 1971 [Blondeau 1971], and proposed that it was due to what is now known as IVR. Later, toluene was the first in a series of alkyl benzenes investigated in an elegant set of experiments by Smalley and coworkers [Hopkins 1980b]. The main thrust of this work involved observing dispersed fluorescence from selected ring modes and deducing the influence of the state density on IVR from the changes associated with increasing length of the alkyl side-chain. The IVR behaviour of S_1 toluene itself was not specifically investigated. The behaviour of toluene with respect to IVR is of specific interest because the presence of a methyl rotor has been shown to accelerate IVR in related molecules such as *p*-fluorotoluene [Parmenter 1986]. We thus offer comment on aspects of IVR in S_1 toluene that emerge from the dispersed fluorescence spectra measured.

A precursor to IVR is mixing among the vibrational states such that a new set of close-lying molecular eigenstates are generated that will beat together when excited coherently, giving rise to time dependence in the vibrational motion. As discussed above in relation to the dispersed fluorescence spectra, a spectral signature of extensive vibrational mixing is the appearance of a broad hump underlying the sharp structure expected. This broad, featureless hump arises from emission by many zero-order components in the mixed molecular state. It is important to recognise that this feature does not allow one to deduce the range over which the states are coupled, *i.e.* it is not necessarily associated with mixing amongst close-lying vibrational states. In the context of our experiments we simply note the behaviour of the spectra with respect to the appearance of this hump, and the degree to which there is residual structure from the zero-order level excited.

The hump first appears in fluorescence from the Fermi resonance pair at *ca.* 750 cm⁻¹. At this point structure is readily observed on top of this hump. Fluorescence from weak features above this show little structure, suggesting that they are extensively mixed. However, the strong A₁ fundamentals ν_{10} and ν_{11} , which lie above some bands that show little structure, show only a weak hump with a strong structured component. There thus appears to be a mode dependence to the mixing. All spectra from levels probed above ν'_{10} and ν'_{11} are dominated by broad, structureless emission.

In comparison with similar molecules that lack a methyl rotor, the onset of extensive vibrational state mixing in toluene is certainly occurring at low energies, consistent with this mixing being enhanced by the presence of the methyl rotor. Furthermore, a comparison between the room temperature spectra reported by Blondeau and Stockburger [Blondeau 1971] and the spectra reported here reveals that the IVR features are much more pronounced in the room temperature spectra. This behaviour is typical, and is widely acknowledged to be a consequence of rotational coupling mechanisms (Coriolis and centrifugal coupling) being enhanced in the room temperature spectra because of the larger J,K states accessed [Lawrance 1988]. In the case of toluene, there is in addition to these mechanisms the possible influence of high excitation in the methyl rotor at room temperature.

2.8 Fluorescence Lifetime Measurements

As we noted in the Introduction, a motivation for this work was to establish the frequencies of the low-lying vibrational modes, as a prelude to studies of vibrational energy transfer in this molecule. In addition to a knowledge of vibrational frequencies, an analysis of state-to-state vibrational energy transfer requires a knowledge of fluorescence lifetimes. Consequently we have also taken the opportunity to measure the fluorescence lifetimes of most of the bands observed in the excitation spectra. The

Table 2.7 Fluorescence lifetimes of S₁ vibrational levels. Errors indicate $\pm 3\sigma$.

| Assignment | Position ^a / cm ⁻¹ | Lifetime / ns |
|--------------------------------------------------------------------------------------------------------------------------|---------------------------------------------|---------------|
| 0 ₀ ⁰ (0a' ₁ → 0a' ₁) | 0 | 86.4 ± 0.7 |
| 0 ₀ ⁰ (0a' ₁ → 3a" ₁) | +55 | 82.1 ± 2.1 |
| 38 ₀ ¹ | +332 | 77.4 ± 1.4 |
| 13 ₀ ¹ / 24 ₀ ¹ 25 ₀ ¹ | +457 | 69.6 ± 0.9 |
| 13 ₀ ¹ / 24 ₀ ¹ 25 ₀ ¹ | +462 | 72.6 ± 1.2 |
| 37 ₀ ¹ | +532 | 72.2 ± 0.4 |
| 12 ₀ ¹ / 23 ₀ ¹ 24 ₀ ¹ | +736 | 61.5 ± 3.3 |
| 12 ₀ ¹ / 23 ₀ ¹ 24 ₀ ¹ | +754 | 69.9 ± 1.1 |
| 10 ₀ ¹ | +935 | 76.4 ± 0.5 |
| 11 ₀ ¹ | +966 | 74.9 ± 0.8 |
| 8 ₀ ¹ | +1193 | 56.6 ± 0.7 |
| 37 ₀ ¹ (12 ₀ ¹ / 23 ₀ ¹ 24 ₀ ¹) | +1263 | 53.9 ± 1.4 |
| 37 ₀ ¹ (12 ₀ ¹ / 23 ₀ ¹ 24 ₀ ¹) | +1284 | 57.3 ± 0.9 |
| 10 ₀ ¹ 37 ₀ ¹ | +1466 | 56.3 ± 0.9 |
| 11 ₀ ¹ 37 ₀ ¹ | +1494 | 53.0 ± 1.1 |
| 10 ₀ ² | +1868 | 49.7 ± 1.8 |
| 10 ₀ ¹ 11 ₀ ¹ | +1900 | 48.2 ± 0.8 |

^a Band positions are measured relative to the 0₀⁰ band at 37477.4 cm⁻¹.

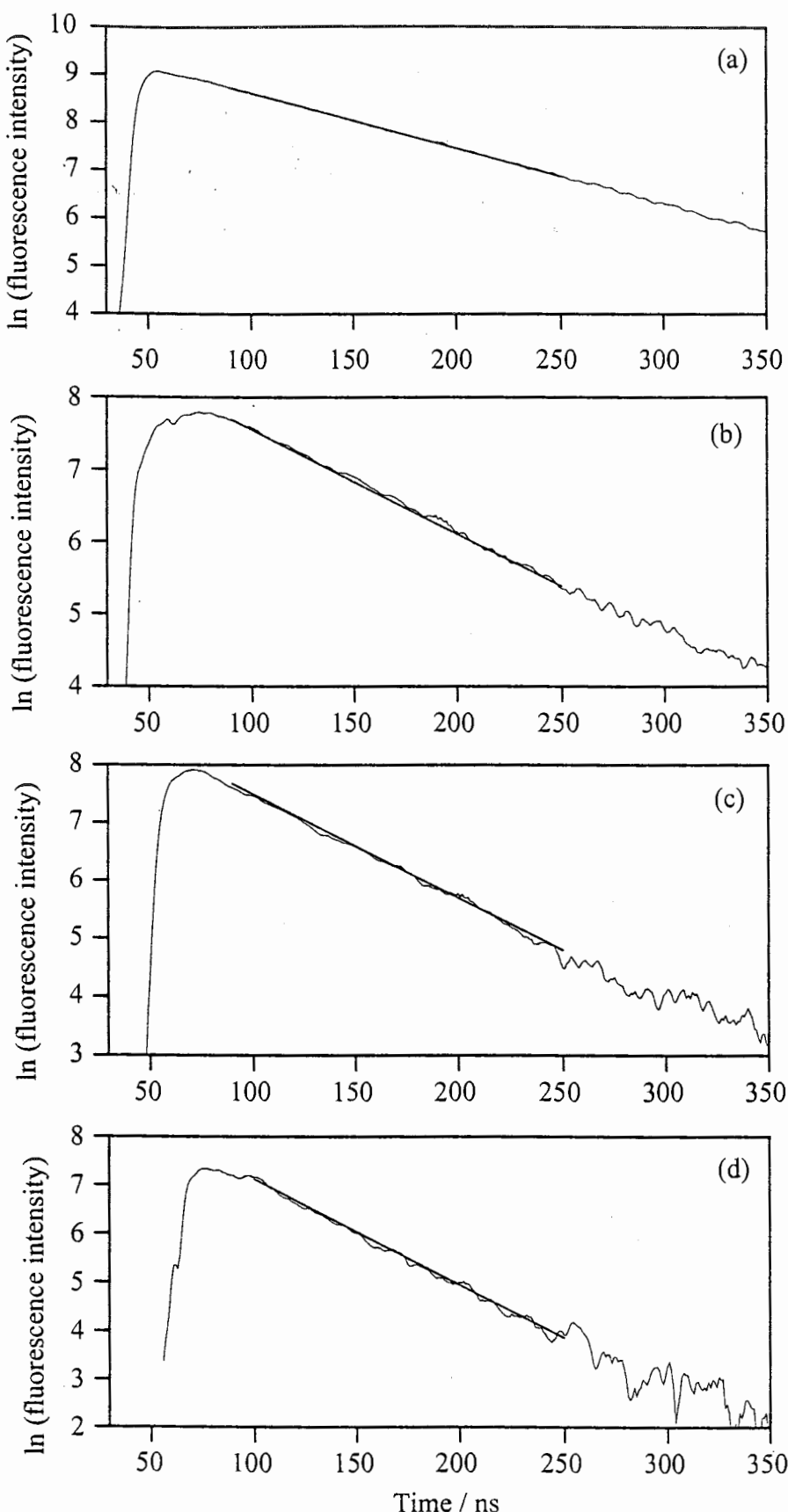


Figure 2.10 Plots of the natural logarithm of the fluorescence intensity versus time for a number of S_1 levels; (a) 0^0 (0 cm^{-1}), (b) $13^1/24^125^1$ (0^0+462 cm^{-1}), (c) 8^1 (0^0+1193 cm^{-1}), (d) 10^111^1 (0^0+1900 cm^{-1}).

results are collated in table 2.7. The lifetimes were evaluated by performing a linear least squares fit to a graph of $\ln(I)$ versus t . Representative traces, with their fits, are illustrated in figure 2.10.

Lifetimes have been reported previously by two groups using room temperature samples. Jacon *et al.* report lifetimes for 10 levels up to 3080 cm^{-1} [Jacon 1977] while Kincaid *et al.* have reported lifetimes for the 0^0 , 11^1 and 29^1 levels [Kincaid 1991]. Where there is overlap in the bands studied, the lifetimes obtained by us tend to be longer. In the case of the data of Jacon *et al.* the difference lies well outside of the reported uncertainty, while for the data of Kincaid *et al.* our lifetimes overlap within the reported uncertainty. The differences most probably have their origin in the selectivity of the excitation process. Because previous work was undertaken using a room temperature sample, the measurements will have unavoidably included excitation of sequence transitions, particularly those involving the methyl rotor internal rotation. It is probable that the lifetimes of these rotor levels are shorter than those of the cold band, and that this is responsible for the trend observed. In general we find a decrease in the lifetimes with increasing energy. Such behaviour is typical of that observed for a molecule in the statistical limit of radiationless transitions.

2.9 Conclusion

With the aid of dispersed fluorescence spectra we have assigned the majority of the features seen in the excitation spectrum of jet-cooled toluene up to 2000 cm^{-1} above the origin band. The presence of Fermi resonances has enabled the assignment of a number of otherwise inactive fundamentals. Collisional transfer to optically inaccessible states has also been used to confirm assignments. The S_1 vibrational frequencies of all modes with S_0 frequencies up to *ca.* 730 cm^{-1} are now known. The S_0 and S_1 fundamental frequencies are summarised in table 2.8.

Table 2.8 Values of the S₀ and S₁ frequencies for the toluene vibrational modes.

| Symmetry | Mode | v (S ₀) / cm ⁻¹ | v (S ₁) / cm ⁻¹ | Symmetry | Mode | v (S ₀) / cm ⁻¹ | v (S ₁) / cm ⁻¹ |
|----------------|------|----------------------------------------|----------------------------------------|----------------|------|----------------------------------------|----------------------------------------|
| A ₁ | 1 | 3087 | | B ₁ | 17 | 2979 | |
| | 2 | 3063 | | | 18 | 1450 | |
| | 3 | 3055 | | | 19 | 1040 | |
| | 4 | 2921 | | | 20 | 978 | |
| | 5 | 1605 | | | 21 | 895 | |
| | 6 | 1494 | | | 22 | 728 | |
| | 7 | 1379 | | | 23 | 695 | 423 |
| | 8 | 1210 | 1193 | | 24 | 464 | 320 |
| | 9 | 1175 | 1021 ^a | | 25 | 216 | 157 |
| | 10 | 1030 | 935 | | 26 | 3039 | |
| | 11 | 1003 | 966 | | 27 | 3029 | |
| | 12 | 785 | 736/754 | | 28 | 2952 | |
| | 13 | 521 | 457/462 | | 29 | 1586 | |
| A ₂ | 14 | 964 | 687 ^b | B ₂ | 30 | 1463 | |
| | 15 | 843 | | | 31 | 1445 | |
| | 16 | 407 | 228 | | 32 | 1312 | |
| | | | | | 33 | 1280 | |
| | | | | | 34 | 1155 | |
| | | | | | 35 | 1080 | |
| | | | | | 36 | 1040 | |
| | | | | | 37 | 623 | 532 |
| | | | | | 38 | 342 | 332 |

^a This assignment is tentative, see Krogh-Jespersen *et al.* [Krogh-Jespersen 1979].

^b This assignment is tentative, see text.

The dispersed fluorescence spectra reveal a low energy onset for IVR, consistent with the methyl rotor accelerating vibrational mode mixings. Fluorescence lifetimes have been measured for the majority of bands observed in the excitation spectrum. These display a steady decrease as the level of vibrational excitation increases.

Chapter 3

Vibrational Deactivation of Highly Excited Hexafluorobenzene

3.1 Introduction

Collision-induced energy transfer between molecules containing significant amounts of vibrational energy is an essential excitation and de-excitation mechanism in many gas phase reactions [Oref 1990]. Despite its importance, there is a paucity of knowledge concerning collisional deactivation from highly excited molecules and many important questions await definitive answers. Two key questions are (i) what is the form of the collision energy step size distribution function $P(E,E')$, and (ii) what is the dependence of the average energy transferred per collision on the internal energy of the excited molecule? For example, the energy dependence has been shown to be constant [Oref 1990], linear [Oref 1990]; linear but rolling off at higher energies [Barker 1993; 1995], and linear above a certain threshold energy [Hartland 1997]. In this chapter we report the results of experiments that provide insights into the second of these questions. The excitation in these experiments is provided by infrared multiphoton absorption (IRMPA).

Direct measurements of collisional energy transfer from highly excited molecules have usually relied on ultraviolet (UV) pumping of a molecule to an excited electronic state, followed by non-radiative intramolecular transfer to high-lying vibrational levels in the

ground electronic state as the means of state preparation [Oref 1990; Barker 1993, 1995]. Producing an ensemble of excited molecules through rapid internal conversion has the advantage that the initial energy distribution is extremely narrow and defined, centred about the excitation wavelength of the light source used. This technique, however, is limited to molecules possessing an electronic transition which will undergo rapid internal conversion at wavelengths accessible by conventional lasers. Consequently, the types of molecules and the range of initial internal energies that can be studied are severely restricted by the energy of the electronic transitions.

Infrared multiphoton absorption (IRMPA), generally using a high power CO₂ laser, provides an alternative method for initial preparation of large populations of highly excited molecules in the ground electronic state with various initial internal energies [Brown 1985; Zellweger 1985a, 1985b, 1986; Barker 1988; Abel 1992a, 1992b; Coronado 1997]. In contrast with studies utilising UV pumping followed by internal conversion (IC), IRMPA remains a poor cousin. This arises because there is uncertainty in the initial energy distribution associated with the IRMPA process [Brown 1985; Zellweger 1985a]. Nevertheless, it has been shown theoretically that under appropriate conditions the results extracted from the data depend solely on the *average* excitation energy, i.e. they are independent of the initial distribution [Coronado 1994, 1996]. The average internal energy the excited molecule initially reaches after IRMPA is controlled by varying the fluence of the excitation laser.

IRMPA is potentially a very useful technique for studying different types of molecular systems from those studied using IC as the state preparation technique. IC following visible/UV excitation has generally been used with cyclic ring systems, usually aromatics, because these molecules possess the required photophysical properties. In contrast, molecules studied using IRMPA are halogenated hydrocarbons, for example 1,1,2-trifluoroethane [Zellweger 1986], *cis*-ClFC=CFCl [Coronado 1997] and CDCl₃ [Rinaldi 1996]. It is clear that the types of molecules for which direct energy transfer

data are available need to encompass a broader range of systems, and this is not possible using the IC technique for state preparation. IRMPA offers a versatile alternative.

The work presented here is in two parts. First, in order to demonstrate that the drawbacks of IRMPA identified above are no impediment to obtaining high quality data, we have undertaken a study of energy transfer in hexafluorobenzene (HFB), for which it is possible to use both IRMPA and IC as methods of excitation. Argon was used as the collision partner. By comparing the results of these studies we demonstrate the reliability of results obtained with IRMPA. Second, energy transfer between highly excited HFB and a series of monatomic partners is investigated in order to obtain insight into the energy dependence of the average energy transferred per collision.

In the direct studies of large molecule collisional energy transfer, time-resolved monitoring of the energy content of the highly vibrationally excited molecules has been carried out using IRF or hot-band UV absorption spectroscopy [Oref 1990]. IRF has generally been used to probe molecules excited by the internal conversion technique (hereafter referred to as IC-IRF), as has UV absorption spectroscopy (hereafter referred to as IC-UVA). There have been very few studies using the combination of IRMPA coupled with time-resolved IRF (hereafter referred to as IRMPA-IRF) [Brown 1985; Zellweger 1986; Rinaldi 1996; Coronado 1997].

HFB has excellent attributes for energy transfer studies. It is a large molecule that undergoes rapid internal conversion after UV excitation with near unit quantum efficiency [Phillips 1967; Ichimura 1984, 1985]. This allows initial state preparation using an excimer laser at either 193 or 248 nm. HFB is very stable, requiring >1700 K to initiate any thermal decomposition [Damm 1990] and >60 000 cm⁻¹ for photochemical decomposition [Watanabe 1990]. Because of these photophysical properties, collisional deactivation of highly excited HFB has previously been the

subject of experimental [Ichimura 1985, 1987; Damm 1990] and complementary theoretical studies [Lenzer 1995, 1997]. Previous workers have used the IC-UVA technique with excitation at 193 nm. Ichimura *et al.* carried out measurements for the colliders Ar, N₂, O₂ and HFB [Ichimura 1985, 1987], while Damm *et al.* investigated the colliders He, Ar, N₂, O₂, C₃H₈, *n*-C₈H₁₈, and *n*-C₈F₁₈ [Damm 1990].

HFB has two very strong infrared (IR) absorption bands at 1007 and 1530 cm⁻¹, [Eaton 1973; Pearce 1973] the former being coincident with CO₂ laser output, thus making it a suitable candidate for IRMPA-IRF studies and allowing direct comparison between the IRMPA-IRF and IC-IRF techniques. In this chapter we compare results for the collisional relaxation of highly excited HFB by Ar using both URMPA and UV-IC preparatory techniques. Experimental results were also obtained for the other monatomic collision partners He, Ne, Kr and Xe using the IRMPA-IRF technique. The analysis of the IRF decays leads to insights into the variation of the bulk average energy transferred per collision, $\langle\langle\Delta E\rangle\rangle$ with internal energy of the HFB molecules. Our results are compared with previous experimental work [Ichimura 1987; Damm 1990] and with recent quasiclassical trajectory calculations on the deactivation of highly excited HFB by He, Ar and Xe. [Lenzer 1995, 1997]

3.2 Experimental Details

As mentioned in the preceding section, HFB has two very strong infrared absorption bands centred around 1007 and 1530 cm⁻¹. The 1007 cm⁻¹ band is coincident with CO₂ laser output. We use time-resolved infrared fluorescence (IRF) near 1500 cm⁻¹ to monitor energy loss from highly vibrationally excited HFB prepared by IRMPA with CO₂ laser pumping using the P(38) line at 1029.43 cm⁻¹. The IC-IRF experiments

utilised 248 nm ($\sim 40\ 300\ \text{cm}^{-1}$) excitation. Due to it providing superior signals, the band near $1000\ \text{cm}^{-1}$ was monitored in these UV excitation experiments.

The experimental system for the excitation of HFB via IRMPA coupled with time-resolved IRF monitoring is a more elaborate version of the experimental design used for recent studies of the collisional deactivation of vibrationally excited CO₂ and N₂O [Poel 1995, 1996, 1997]. A schematic diagram of the experimental arrangement is shown in figure 3.1. Infrared laser radiation from a tunable CO₂ laser (Lumonics TEA 103-2) is directed through a Galilean telescope and then into a cylindrical fluorescence cell constructed from stainless steel and fitted with NaCl end windows. A mercury-free gas handling line can evacuate the cell to $\sim 10^{-4}\ \text{Torr}$. The pressure in the cell was monitored with a 0–1 Torr capacitance manometer (MKS Baratron). The IRF from the excited HFB molecules was observed perpendicular to the laser beam axis through a MgF₂ side window and a bandpass interference filter centred at $1486\ \text{cm}^{-1}$ with a bandwidth of $167\ \text{cm}^{-1}$. The IRF is detected with a liquid nitrogen cooled HgCdTe detector (Infrared Associates) equipped with a matched preamplifier (combined rise time $\sim 400\ \text{ns}$). The detector/preamplifier output was captured by a digital storage oscilloscope (LeCroy 9310) and transferred to a laboratory computer for analysis. The detector/preamplifier was shielded by a copper cage to prevent electrical interference from the firing of the laser.

A photon drag detector (Rofin 7415) was used to monitor the CO₂ laser pulse temporal profile and to trigger the oscilloscope. The oscilloscope was used to average decay curves for ~ 200 pulses at a laser pulse repetition frequency of $\sim 1\ \text{Hz}$, in order to achieve adequate signal to noise ratios.

Extreme care was taken in the measurements of the average number of IR photons absorbed per HFB molecule. The conventional method involves averaging the energy of the CO₂ laser before and after the sample [Bagratashvili 1985]. In our experiments,

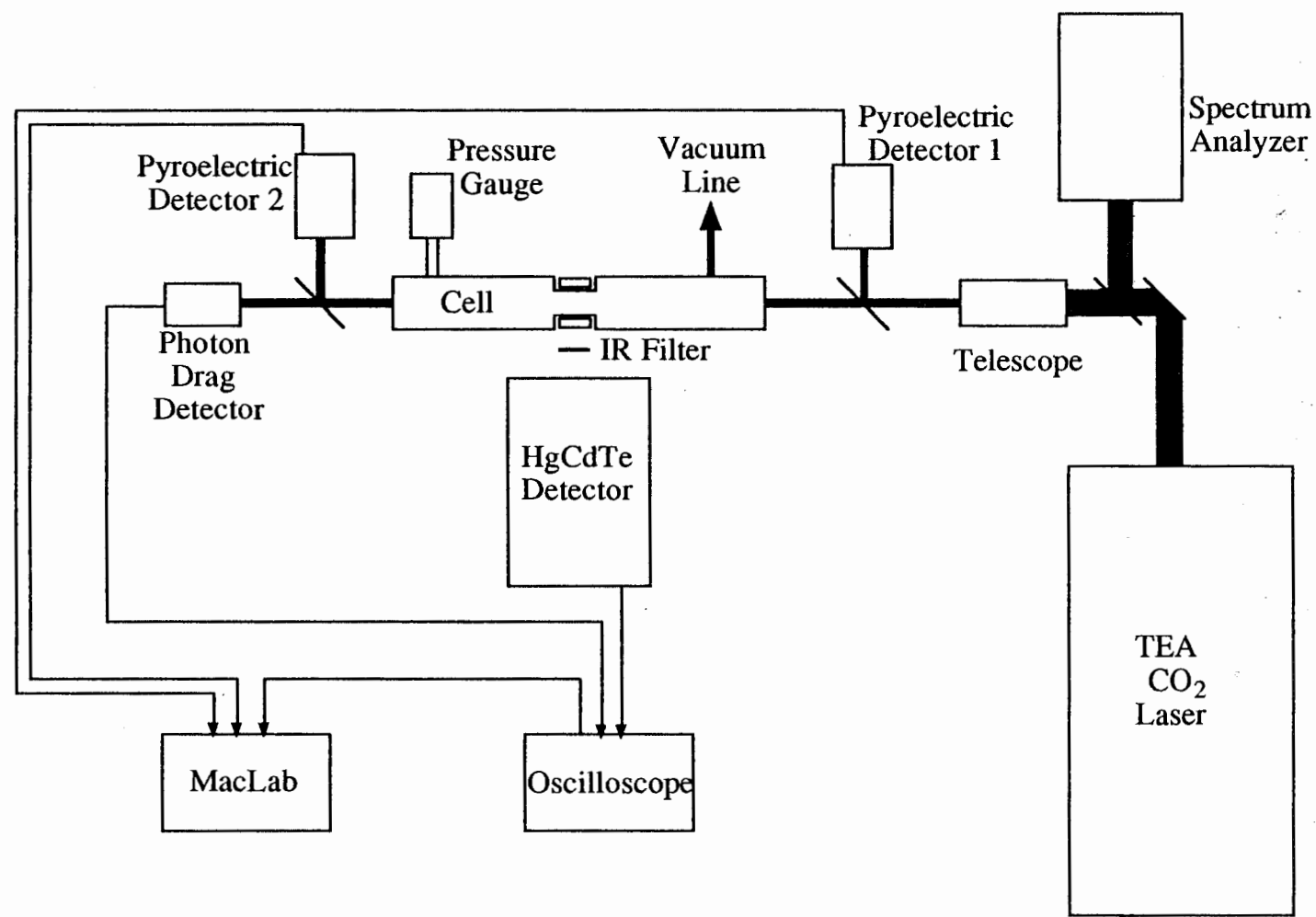


Figure 3.1 Schematic diagram of the experimental system.

the energy of each pulse before and after the cell was recorded simultaneously using two pyroelectric joulemeters (Molelectron J25). The signal from these joulemeters were captured using a data acquisition system (MacLab /4) allowing every shot to be recorded. This allows the energy absorbed, and hence the average number of photons absorbed per molecule, to be determined for every pulse. This is then repeated over a number of pulses to obtain the average number of photons absorbed per molecule and also an indication of the spread in initial excitation energies. Furthermore, the CO₂ laser was optimised for pulse-to-pulse stability and the triggering system of the IR detection system was set-up so that it accepted signal only when the laser fluence was above a preset threshold. This results in optimum pulse to pulse stability and a narrow distribution of the energy input. The laser beam was checked regularly for uniformity to ensure no hot spots were present. Consequently the initial excitation energy does not vary significantly from shot to shot.

In the experiments using UV excitation coupled with time-resolved IRF monitoring, the HFB was irradiated by an excimer laser (Questek Model 2220) at $\lambda = 248$ nm (KrF) operating at 10 Hz. The cell was fitted with quartz end windows to allow the transmission of the UV laser. The excimer pulses had an average fluence of ~ 4 mJ cm⁻² and a full width at half the maximum (FWHM) of 10 ns. Low laser power was necessary to prevent the deposition of polymer products on the cell windows which lead to large amounts of scattered light. IRF from HFB near 1000 cm⁻¹ was monitored through a NaCl window and appropriate bandpass interference filter with the HgCdTe detector coupled to a digital storage oscilloscope (Hewlett-Packard 54510A). Approximately 1000 laser shots were averaged for each run to obtain adequate signal to noise.

He (BOC, 99.999%), Ne (Spectra Gases, 99.996%), Ar (BOC, 99.999%), Kr (Spectra Gases 99.995%), and Xe (Spectra Gases 99.999%) were used directly as supplied. C₆F₆ (Aldrich, 99.9%) was degassed using several freeze-pump-thaw cycles prior to use.

3.3 Data Analysis

3.3.1. Variation of internal energy with time

The experiments measure infrared intensity as a function of time. From these data one wishes to extract the variation of the internal energy with time. The usual methods for doing this have been described by Barker *et al.* [Miller 1996a; Toselli 1991]. They involve extrapolating the experimental intensity versus time traces to time zero where the initial energy is known. The changes in IR fluorescence intensity with time can then be associated with changes in internal energy with time using calculated calibration curves (see below). The accuracy of this method relies on the accuracy of the back-extrapolation, and ignores problems such as the finite detector response.

Our experience with the back extrapolation approach has been that it can lead to larger uncertainties than the data warrant. For this reason we have chosen a different approach that overcomes the limitations of back-extrapolation and allows effects such as the finite detector response to be incorporated in the analysis. The method involves fitting the internal energy versus time behaviour directly to the data.

The internal energy is assumed to follow the general functional form

$$E(t) = E_0 \exp[-k_{t1}(t - t_0) - k_{t2}(t - t_0)^2] \quad 3.1$$

where E_0 is the initial excitation energy, k_{t1} , k_{t2} , and t_0 are variable parameters in the fitting procedure. t_0 is an adjustable parameter necessary for the automated fitting procedure to overlay the experimental and fitted decay traces. In practice the fitted value of t_0 is identical for each set. It should be noted that this functional form is only a

mathematical representation of the energy decay profile used for fitting purposes and there is no physical meaning associated with the parameters k_{t1} and k_{t2} . This functional form was chosen since an exponential is the most widely used form for modeling energy decay and, through the presence of a second, t^2 , term, the expression additionally allows for the roll-off in the average energy transferred per collision as reported by previous workers [Damm 1990; Miller 1996a; Toselli 1991]. The procedure involves the following five steps:

1. An initial set of k_{t1} , k_{t2} , and t_0 parameters is used to generate an $E(t)$ function, as per equation 3.1.
2. This $E(t)$ function is converted to an infrared fluorescence intensity versus time function, $IRF(t)$, using the relationship between relative IRF intensity of the n th mode, $I_n(E)$, and internal energy, first derived by Durana and McDonald [Durana 1977]

$$I_n(E) = \sum_{\nu=1}^{\nu_{\max}} \nu \frac{\rho_{s-1}(E - \nu h\nu_n)}{\rho_s(E)} \quad 3.2$$

and

$$IRF(t) = A_{IRF} I_n[E(t)] \quad 3.3$$

Here $h\nu_n$ is the energy of the n th mode, $\rho_s(E)$ is the vibrational density of states at energy E , $\rho_{s-1}(E)$ is the vibrational density of states calculated by excluding the mode that is being monitored and A_{IRF} is a fitted scaling factor. The applicability of the above relationship has been extensively tested and no occurrences have been found where the relationship has failed to hold [Barker 1993]. The density of states were calculated using an exact counting algorithm [Beyer 1973] and the vibrational frequencies listed by Steele and co-workers. [Eaton 1973; Pearce 1973].

3. An infrared emission versus time curve is generated from the IR fluorescence intensity versus time function calculated at step 2, $IRF(t)$, and a function used to describe black body radiation. This is necessary as in general the infrared emission signal contains components from both IRF and black body radiation (present due to the generation of heat during the collisional relaxation process). Thus the experimental decays consist of a superposition of an IRF decay curve and a black body radiation rise. The black body radiation, $BBR(t)$, was represented by an expression which is derived from the standard black body radiation formulae [Atkins 1997]

$$BBR(t) = A_{BBR} \exp\left(-\frac{hv}{kT(t)}\right) \quad 3.4$$

and

$$T(t) = T_0 + \Delta T \left(1 - \frac{E(t)}{E_0}\right) \quad 3.5$$

where A_{BBR} is an intensity constant, T_0 is the initial temperature, ΔT is the temperature rise after relaxation, and E_0 is the initial vibrational energy. The short timescales used throughout these experiments precluded the need to consider the slow decay of heat to the cell walls. The infrared emission intensity, $IR(t)$, is thus

$$IR(t) = IRF(t) + BBR(t) \quad 3.6$$

In principle, A_{BBR} and ΔT are both adjustable parameters introduced by the addition of black body radiation. However in practice A_{BBR} is the only adjustable parameter required as the calculations were found to be insensitive to ΔT over a wide range of values (i.e. ~20-200 K rise in our results).

4. The calculated infrared emission signal, $IR(t)$, is convoluted with the experimentally determined detector response function, $SRF(t)$

$$I(t) = SRF(t) * IR(t)$$

3.7

$I(t)$ is thus a calculated function that can be compared directly with the observed IR emission traces.

5. $I(t)$ is compared with the experimental trace, the parameters k_{t1} , k_{t2} , t_0 , A_{BBR} and A_{IRF} are adjusted, and the process repeated until the calculated and experimental traces converge. In practice the entire process is automated. We used the Levenberg-Marquardt method of non-linear least squares fitting to match an $E(t)$ function to an observed IR emission trace [Press 1992].

3.3.2. Extraction of energy transferred per collision as a function of internal energy

The decay curves are measured at a range of HFB dilutions in the collider gas. For each curve, i.e. each dilution, values of k_{t1} and k_{t2} are determined as discussed in the preceding section, giving an $E(t)$ function. This expression for $E(t)$ is converted to $E(z)$, where z is the collision number determined using Lennard-Jones collision frequencies [Lenzer 1995]. The values for the Lennard-Jones parameters and collision frequencies, k_{LJ} , used in this study are shown in table 3.1. The parameters for He, Ar and HFB were taken from Damm *et al.* [Damm 1990] and those for Ne, Kr and Xe were taken from Mourits and Rummens [Mourits 1977]. The values for k_{LJ} were calculated using the empirical equation of Neufeld *et al.* [Neufeld 1972] for the collision integral.

The form of $E(z)$ obtained is analytic (since $E(t)$ is analytic from equation 3.1), and an expression is readily derived for the average energy transferred per collision, $\langle\langle\Delta E\rangle\rangle = dE(z)/dz$. Using equation 3.1, the functional form for the average energy transferred per collision is given by

Table 3.1 Lennard-Jones parameter used in this study.

| Collider | σ / nm | $\epsilon/k_B / \text{K}$ | $10^{10}k_{LJ} / \text{cm}^3\text{s}^{-1}$ |
|----------|----------------------|---------------------------|--------------------------------------------|
| He | 0.255 | 10.22 | 6.98 |
| Ne | 0.282 | 32.0 | 3.92 |
| Ar | 0.347 | 113.5 | 4.15 |
| Kr | 0.366 | 178 | 3.60 |
| Xe | 0.405 | 230 | 3.59 |
| HFB | 0.619 | 323 | 5.21 |

$$\langle\langle\Delta E\rangle\rangle = -\langle\langle E\rangle\rangle [k_{z1}^2 - 4k_{z2} \ln(\langle\langle E\rangle\rangle / E_0)]^{1/2} \quad 3.8$$

where k_{z1} and k_{z2} are related to k_{t1} and k_{t2} via the transformation from time to collision number. These $\langle\langle\Delta E\rangle\rangle$ functions refer to particular mixtures of HFB and collision partner and thus include both HFB-HFB collisions and HFB-collision partner collisions. To extract the HFB-collision partner value alone, these $\langle\langle\Delta E\rangle\rangle$ functions must be extrapolated to the case of infinite dilution of HFB in the collision partner. This is achieved by plotting $\langle\langle\Delta E\rangle\rangle$ as a function of the collision fraction, F_c , for a series of energy values (typically every 250 cm⁻¹). The collision fraction is given by

$$F_c = \frac{k_c^{LJ} N_c}{k_c^{LJ} N_c + k_p^{LJ} N_p} \quad 3.9$$

where k_c^{LJ} and k_p^{LJ} are the Lennard Jones collision frequencies of the HFB-collision partner and HFB-HFB pair respectively, and N_c and N_p are the number of collider and parent molecules respectively. By extrapolating each $\langle\langle\Delta E\rangle\rangle$ versus F_c plot to $F_c = 1$, a $\langle\langle\Delta E\rangle\rangle$ value corresponding solely to HFB-collision partner transfer is obtained

at each energy, $\langle\langle \Delta E \rangle\rangle$. These points obtained using this method were fitted using the following functional form to obtain the final $\langle\langle \Delta E \rangle\rangle$ vs $\langle\langle E \rangle\rangle$ curve

$$\langle\langle \Delta E \rangle\rangle = -\langle\langle E \rangle\rangle [k_1^2 - 4k_2 \ln(\langle\langle E \rangle\rangle / E_0)]^{1/2} \quad 3.10$$

The energy range for the applicability of equation 3.10 is from the initial average energy down to, in our case, $\sim 5000 \text{ cm}^{-1}$.

3.4 Comparison Between IRMPA and UV-IC Excitation

3.4.1. *IRMPA-IRF experiments*

While IRMPA is an extremely useful method for preparing an initial ensemble of highly excited molecules at variable initial internal energies, it leads to a range of initial energies since molecules within the sample can absorb an integer number of photons, ranging from zero up. Various workers have either calculated this distribution [Brown 1985; Zellweger 1985a] or it has been inferred using experimental techniques such as Raman spectroscopy [Bagratashvili 1980, 1981]. Problems arise as the distribution can be bimodal, resulting from a near thermal population of those molecules that did not absorb, and a higher energy distribution of molecules that absorbed many photons [Bagratashvili 1985]. The average number of photons absorbed per molecule, \bar{n} , is determined from the total energy absorbed by the molecules, and the number of absorbing molecules. In the case of the bimodal distribution just discussed, a calculation of \bar{n} , and hence the average initial vibrational energy, requires a knowledge of the fraction of molecules that underwent the IRMPA process.

In general the fraction of molecules excited increases with increasing laser fluence [Bagratashvili 1985]. To produce significant levels of internal excitation, high fluences are required so that many photons are absorbed. Thus energy transfer experiments typically operate under conditions in which the molecules remaining in the unexcited thermal fraction constitute a small component. Indeed, for large molecules where the quasi-continuum is reached easily, the fraction of molecules left in the thermal component can be negligible.

In the case of HFB there are two previous experimental measurements suggesting that essentially all of the molecules are excited by the CO₂ laser [Speiser 1980; Chen 1984]. The evidence consists of UV absorption spectra measured before and after CO₂ laser pumping. In the region 230-300 nm, the peak of the UV absorption spectrum for a 300 K thermal sample of HFB is at 230 nm. Following IRMPA the UV absorption is shifted to longer wavelength and is zero at 230 nm [Speiser 1980; Chen 1984]. These measurements have been made at pressures of 30 Torr [Speiser 1980] and 2 Torr [Chen 1984] of HFB. In the latter case the laser fluence was 0.18 J cm⁻²; in the other it was not reported. Our measurements have been made at lower total pressures (<1 Torr) and a higher fluence of ~0.8 J cm⁻². We expect that under our experimental conditions all HFB molecules will absorb.

We have proceeded by analysing our IRMPA-IRF data on the basis of this assumption. This leads to a particular value of \bar{n} , and hence average initial energy, that determines the slope of the $\langle\langle\Delta E\rangle\rangle$ versus $\langle\langle E\rangle\rangle$ curve. By comparing the $\langle\langle\Delta E\rangle\rangle$ versus $\langle\langle E\rangle\rangle$ curve obtained from the IRMPA-IRF experiments for Ar with that obtained from the IC-IRF experiments we have a check on the validity of this assumption.

From measurements of the laser fluence before, Φ_{in} , and after, Φ_{out} , the cell (with corrections for attenuation from cell windows), the average energy absorbed, $\langle\langle Q\rangle\rangle$, can be calculated via the relationship [Bagratashvili 1985]

$$\langle\langle Q \rangle\rangle = \frac{\Phi_{in}}{NL} \ln\left(\frac{\Phi_{in}}{\Phi_{out}}\right) \quad 3.11$$

where N is the concentration of the molecule of interest in the cell, and L is the cell length. This equation is valid for a collimated laser beam and an absorption of <10% [Bagratashvili 1985]. When all molecules are excited, as assumed in this study (see above), then $\langle\langle Q \rangle\rangle$ is equal to $\langle\langle E \rangle\rangle$ at time zero. For the range of laser fluences measured during our experiments, the distribution of average initial excitation energies for HFB is shown in figure 3.2. This figure shows the average excitation energy to be $16\,000 \pm 1\,500\text{ cm}^{-1}$.

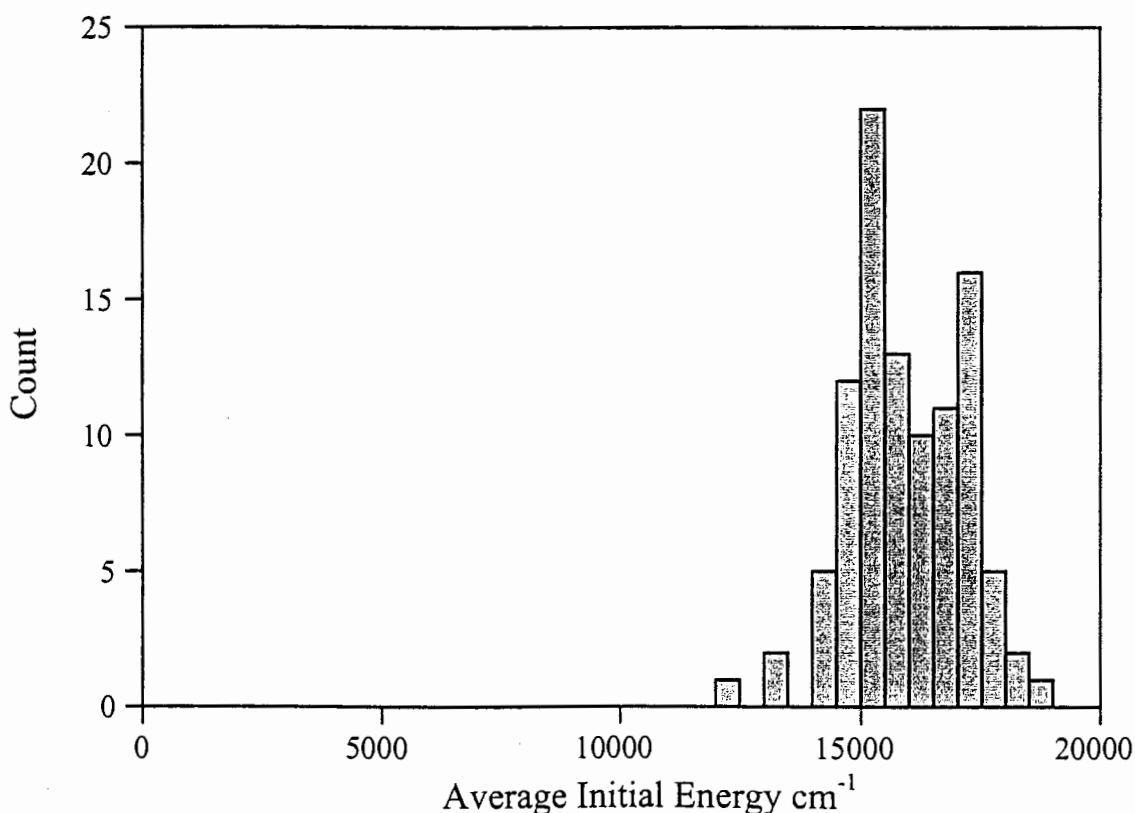


Figure 3.2 Histogram of average energy absorbed per molecule recorded for 100 pulses of the CO₂ laser.

Decay traces at various bath gas pressures were recorded with a constant HFB pressure of 2.5 mTorr. This very low pressure was necessary to minimise black body radiation and to avoid any errors associated with large temperature rises within the cell. Higher pressures also led to shock waves in the cell. The low HFB pressures used increase the accuracy of the data analysis, which involves an extrapolation to zero collision fraction of HFB. IRF traces typical of those observed in the IRMPA experiments are shown in figure 3.3 (a fitted curve is shown on one of the decay traces). Simple random walk simulations show that at the total pressures and timescale of the experiments, wall collisions are insignificant. Plots of $\langle\langle\Delta E\rangle\rangle$ versus collision fraction, F_c , at selected energies are shown in figure 3.4. From the $\langle\langle\Delta E\rangle\rangle$ values determined from the extrapolation of these plots, the functional form of how $\langle\langle\Delta E\rangle\rangle$ depends on internal energy $\langle\langle E\rangle\rangle$ is determined. Fitting this data to equation 3.10 allows the parameters k_1 and k_2 to be determined. These parameters are presented in table 3.2 along with the value of $\langle\langle\Delta E\rangle\rangle$ calculated at $15\ 000\ \text{cm}^{-1}$. The uncertainty is the standard error resulting largely from the extrapolation in the collision fraction plot (figure 3.4), .

The magnitude of the nonlinear term compared with the linear term, illustrated through a comparison of the ratios of these two terms when the average energy has fallen to half its initial value, is less than 5%. Thus for small values of k_2 , equation 3.10 reduces to

$$\langle\langle\Delta E\rangle\rangle = -k\langle\langle E\rangle\rangle \quad 3.12$$

The k value found by fitting the $\langle\langle\Delta E\rangle\rangle$ vs $\langle\langle E\rangle\rangle$ plot to this linear form is also shown in table 3.2.

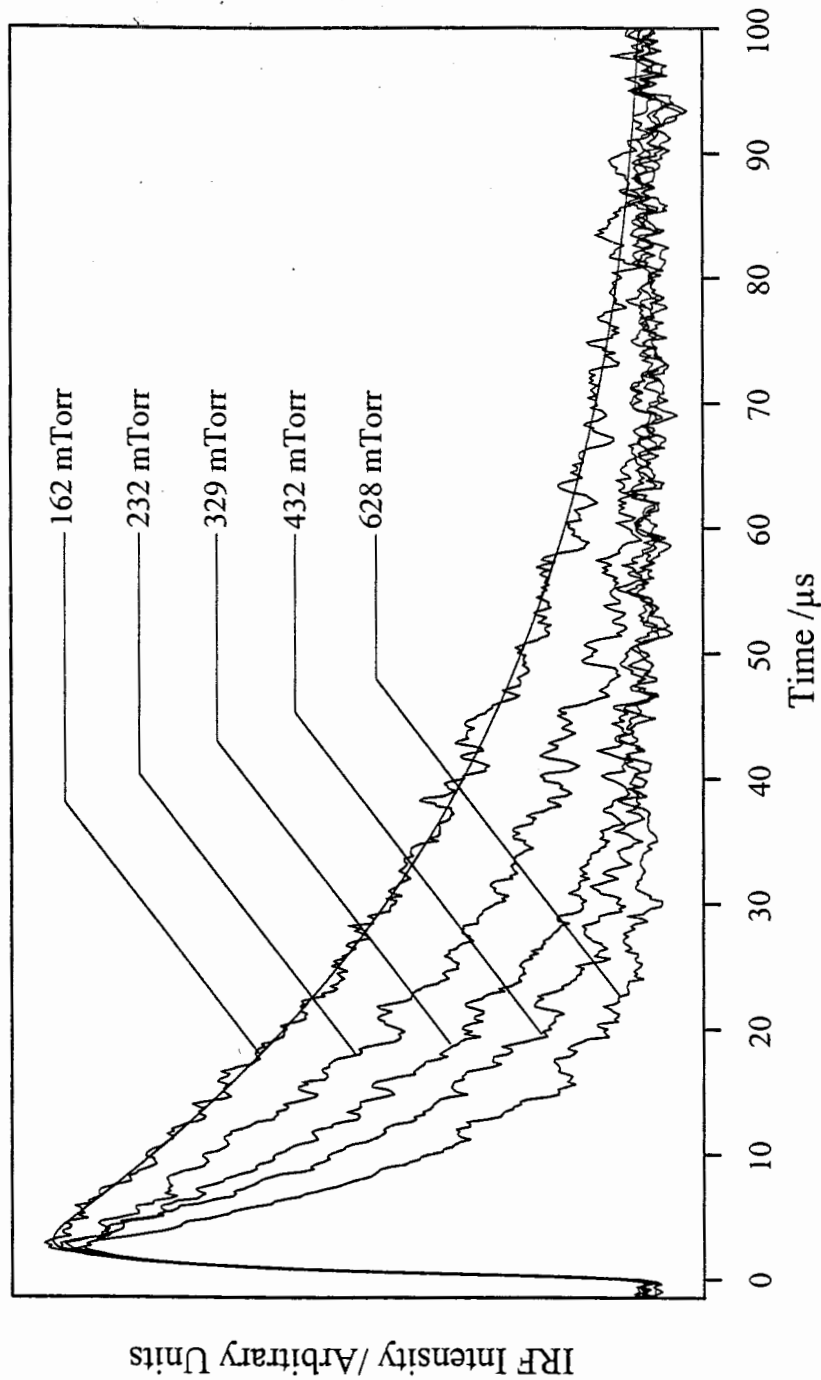


Figure 3.3 Infrared fluorescence decay curves for excited HFB prepared by CO_2 laser radiation in the presence of the indicated pressures of Argon collider gas. $P_{\text{HFB}} = 2.5 \text{ mTorr}$.

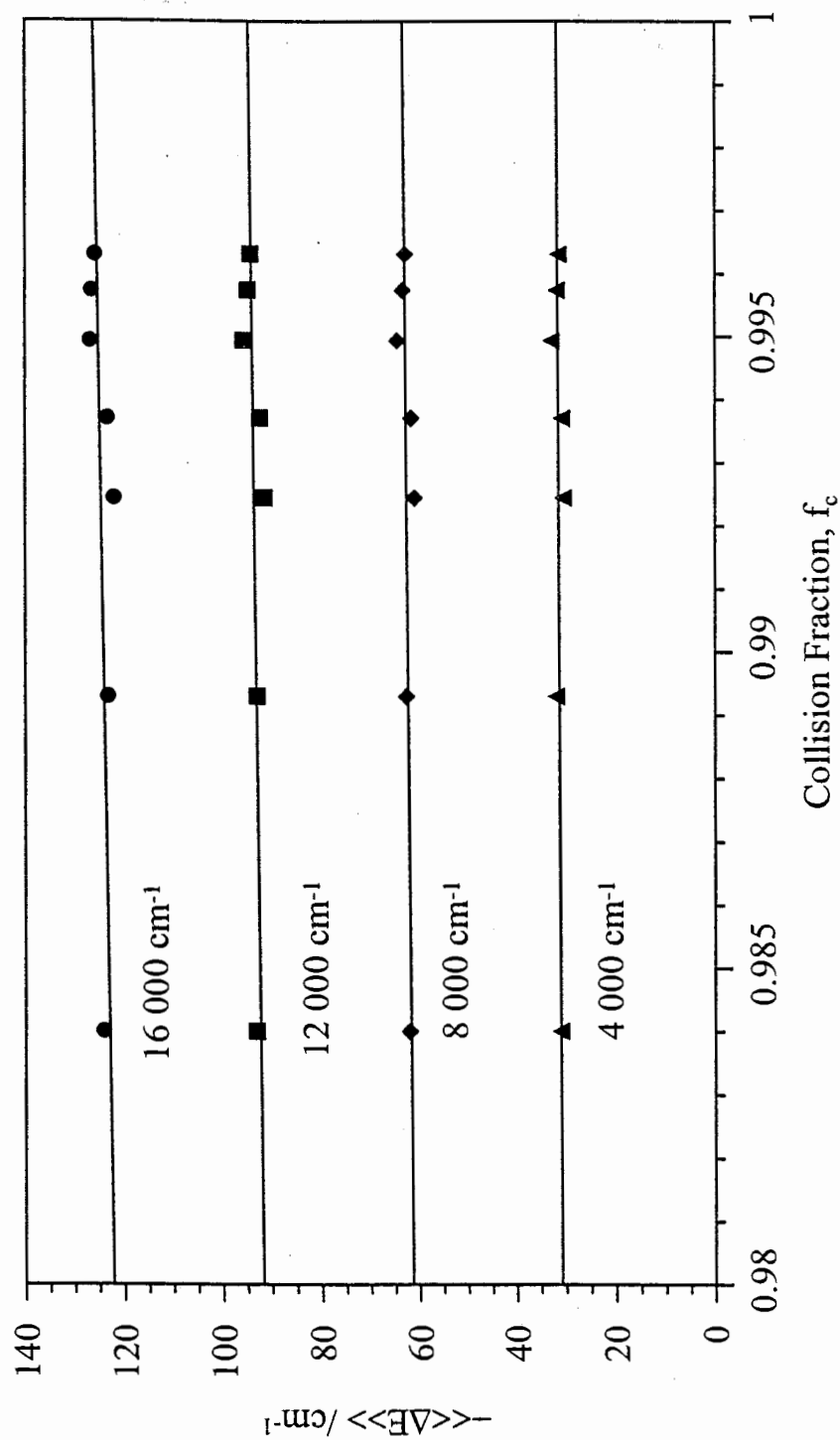


Figure 3.4 Average energy transferred per collision as a function of collision fraction for indicated internal energies.

Table 3.2 Energy dependence of the average energy transferred per collision for highly excited HFB deactivated by argon

| Excitation | Curved fit ^a | | Linear fit ^b k | - $\langle\langle\Delta E\rangle\rangle^c$ |
|------------|-------------------------|-----------------------|--------------------------------|--------------------------------------------|
| | Method | k_1 | k_2 | |
| IRMPA | | 8.13×10^{-3} | 4.29×10^{-7} | 8.20×10^{-3} |
| UV-IC | | 8.11×10^{-3} | 1.13×10^{-6} | 126 ± 9 |

^a Fit to equation 3.10.^b Fit to linear function $\langle\langle\Delta E\rangle\rangle = -k\langle\langle E\rangle\rangle$ ^c Evaluated at 15 000 cm⁻¹

3.4.2. UV excitation (IC-IRF) experiments

The UV photophysics of HFB has been investigated by many authors [Phillips 1967; Ichimura 1984]. After excitation with an excimer laser at both 193 nm (ArF) and 248 nm (KrF) hexafluorobenzene undergoes rapid internal conversion to the electronic ground state with almost unit quantum efficiency to produce an ensemble of highly vibrationally excited molecules. This method of initial state preparation has been used previously to excited HFB for collisional energy transfer studies [Damm 1990; Ichimura 1985, 1987; Michaels 1997b].

Decay traces at various Ar pressures were recorded with a constant HFB pressure of 50 mTorr. These traces were analysed to obtain $\langle\langle\Delta E\rangle\rangle$ as discussed in section 3.3 above. The parameters k_1 and k_2 for the $\langle\langle\Delta E\rangle\rangle$ function obtained are shown in table 3.2 along with the value of $\langle\langle\Delta E\rangle\rangle$ calculated at 15 000 cm⁻¹. Also shown is the k value determined by fitting to equation 3.12.

3.4.3. Comparison between IRMPA and UV-IC results

$\langle\langle\Delta E\rangle\rangle$ vs $\langle\langle E\rangle\rangle$ curves for both the IRMPA and UV-IC preparative methods are shown in figure 3.5. Errors on the plot represent standard deviations determined from the extrapolation of $\langle\langle\Delta E\rangle\rangle$ vs F_c curves and errors observed between runs. Figure 3.5 clearly shows the two experimental results agree well with each other.

UV excitation followed by rapid internal conversion results in an initial energy distribution similar to that of a thermal vibrational Boltzmann distribution shifted by the excitation wavelength ($\sim 40\ 300\ \text{cm}^{-1}$). On the other hand, IRMPA produces a broader distribution since a HFB molecule can absorb an integer number of photons centred around the average number of photons absorbed per molecule. Although the two

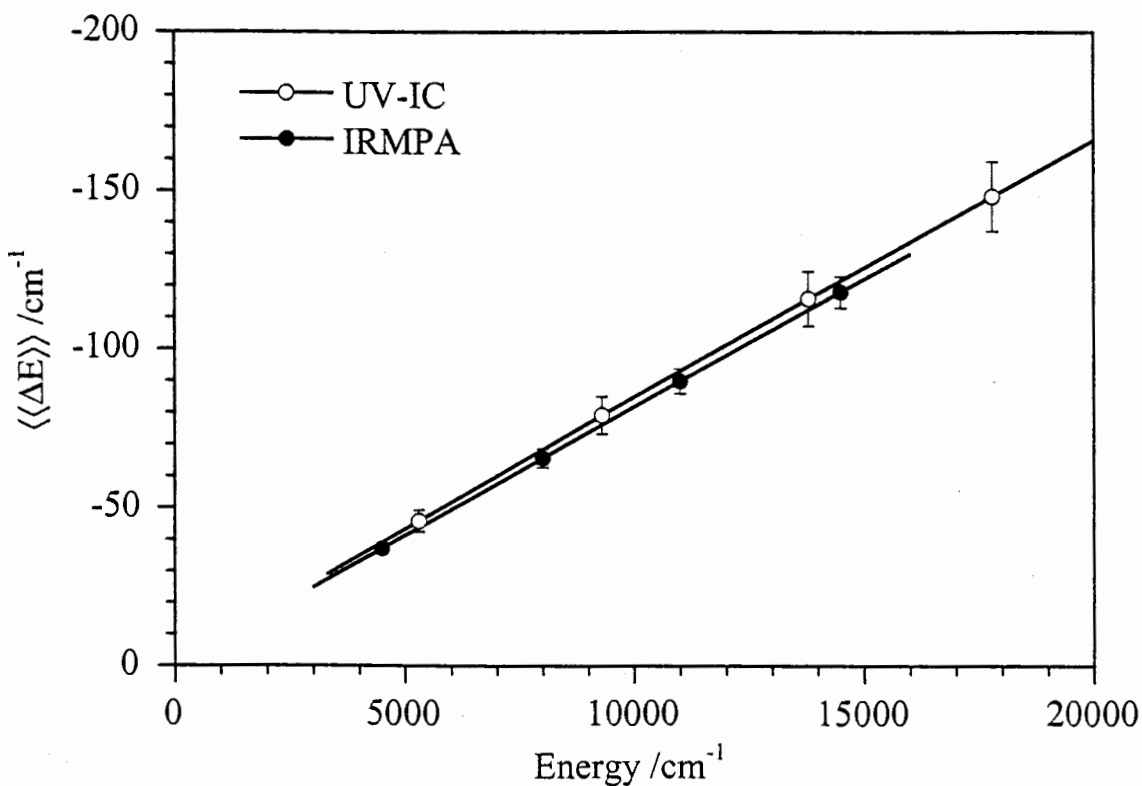


Figure 3.5 $\langle\langle\Delta E\rangle\rangle$ vs $\langle\langle E\rangle\rangle$ curves for the two different methods of initial state preparation used in this study.

methods of initial state preparation produce substantially different initial distributions, the energy transfer parameters obtained by our study are identical within experimental error. This result has previously been postulated from theoretical calculations [Coronado 1994; 1996], but until now no experimental work has substantiated this claim. This is the first direct experimental comparison between the two methods of initial excitation, and demonstrates that IRMPA is a viable method for energy transfer studies.

3.5 Collision Partner Dependence

With the knowledge that IRMPA is a successful technique for producing highly excited HFB molecules suitable for use in energy transfer experiments, we have extended our study to include all the monatomic partners. Using IRMPA as the excitation method, HFB was excited to an initial average energy of $16\ 000\ \text{cm}^{-1}$. The procedures outlined in section 3.4.1 were followed to determine the average energy transferred per collision for each of the remaining monatomics.

Figure 3.6 shows the average energy transferred per collision as a function of the average internal energy for each monatomic. Also included in the graph are the results from the IC-IRF data for Ar as the collision partner. The values for $\langle\langle\Delta E\rangle\rangle$ obtained from the data analysis are given in table 3.3. For all collision partners the parameters reveal $\langle\langle\Delta E\rangle\rangle$ to be essentially linear with energy (see figure 3.6). After fitting each data set to equation 3.10, we can again compare the magnitude of the non-linear term with the linear term when the average energy has fallen to half its initial value. We find that the ratio is typically a few percent. Thus we have fitted our data to the simple linear equation given by equation 3.12. The values of k determined for each of the colliders used in this study is also shown in table 3.3.

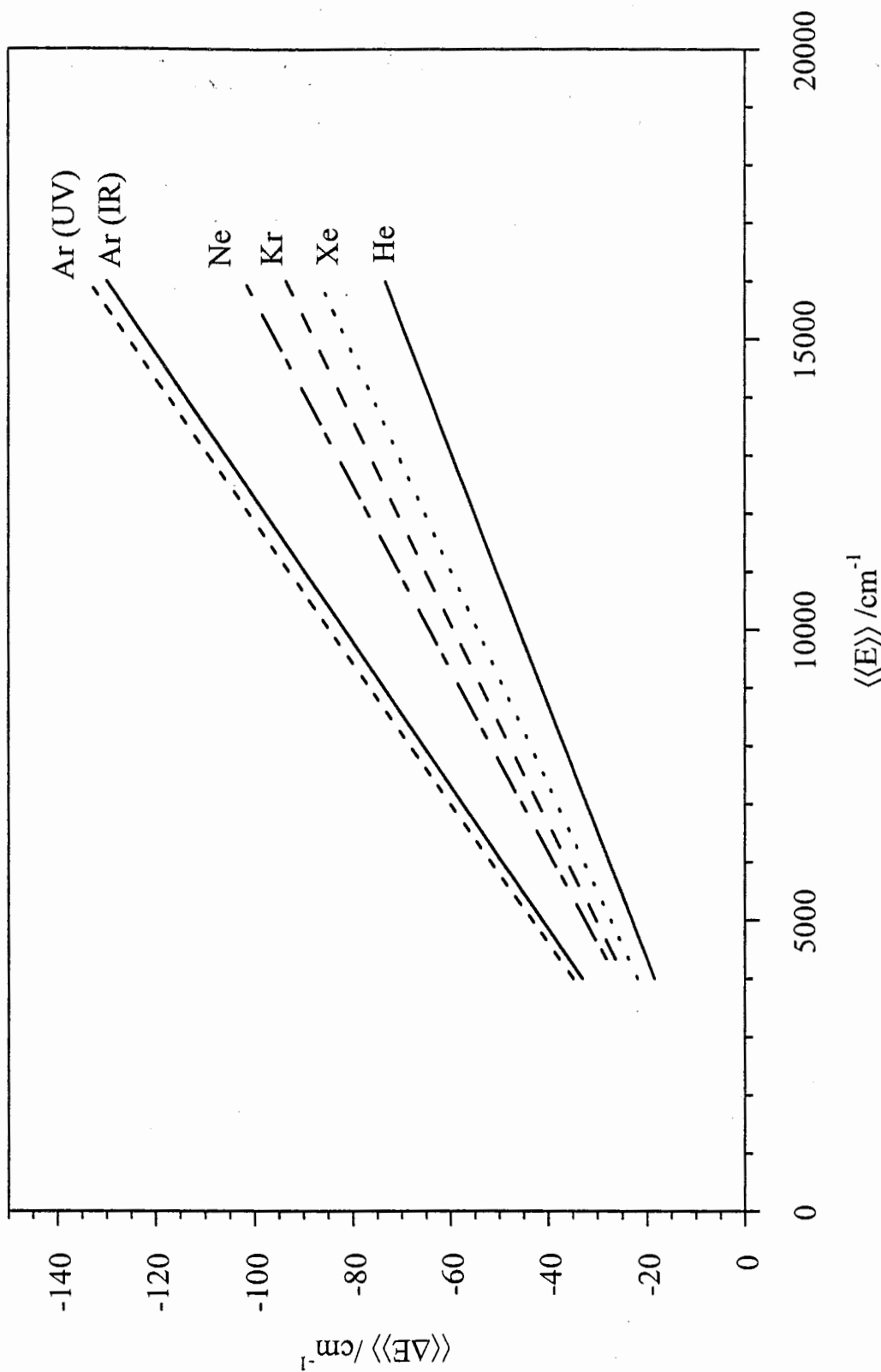


Figure 3.6 Average energy transferred per collision for each collision partner as a function of average internal energy.

Table 3.3 Energy dependence of the average energy transferred per collision, $\langle\langle\Delta E\rangle\rangle$ according to equation 3.12.

| Collider | k^a | $-\langle\langle\Delta E\rangle\rangle^b / \text{cm}^{-1}$ |
|----------|----------------------------------|------------------------------------------------------------|
| He | $(4.60 \pm 0.14) \times 10^{-3}$ | 69 ± 2 |
| Ne | $(6.42 \pm 0.17) \times 10^{-3}$ | 96 ± 3 |
| Ar | $(8.16 \pm 0.36) \times 10^{-3}$ | 122 ± 5 |
| Ar(UV) | $(8.20 \pm 0.60) \times 10^{-3}$ | 126 ± 9 |
| Kr | $(5.92 \pm 0.15) \times 10^{-3}$ | 88 ± 3 |
| Xe | $(5.44 \pm 0.12) \times 10^{-3}$ | 82 ± 1 |

^a Fit to linear function $\langle\langle\Delta E\rangle\rangle = -k\langle\langle E\rangle\rangle$ ^b Evaluated at 15 000 cm⁻¹

3.6 Discussion

3.6.1 Direct comparison with previous UV-IC excitation work.

The energy transfer parameters, determined from our UV-IC preparation of highly excited HFB, can be directly compared with previous studies using the same preparation technique [Damm 1990; Ichimura 1987] and also theoretical calculations [Lenzer 1995]. Since our IC-IRF experiments were limited to Ar, this is the only partner for which we can make direct comparisons of the results from UV-IC experiments. Comparisons for other collision partners will be made in the following section.

A summary of $\langle\langle\Delta E\rangle\rangle$ values obtained from the studies above, along with our values, is shown in table 3.4. Figure 3.7 shows the $\langle\langle\Delta E\rangle\rangle$ vs $\langle\langle E\rangle\rangle$ curves for the present work

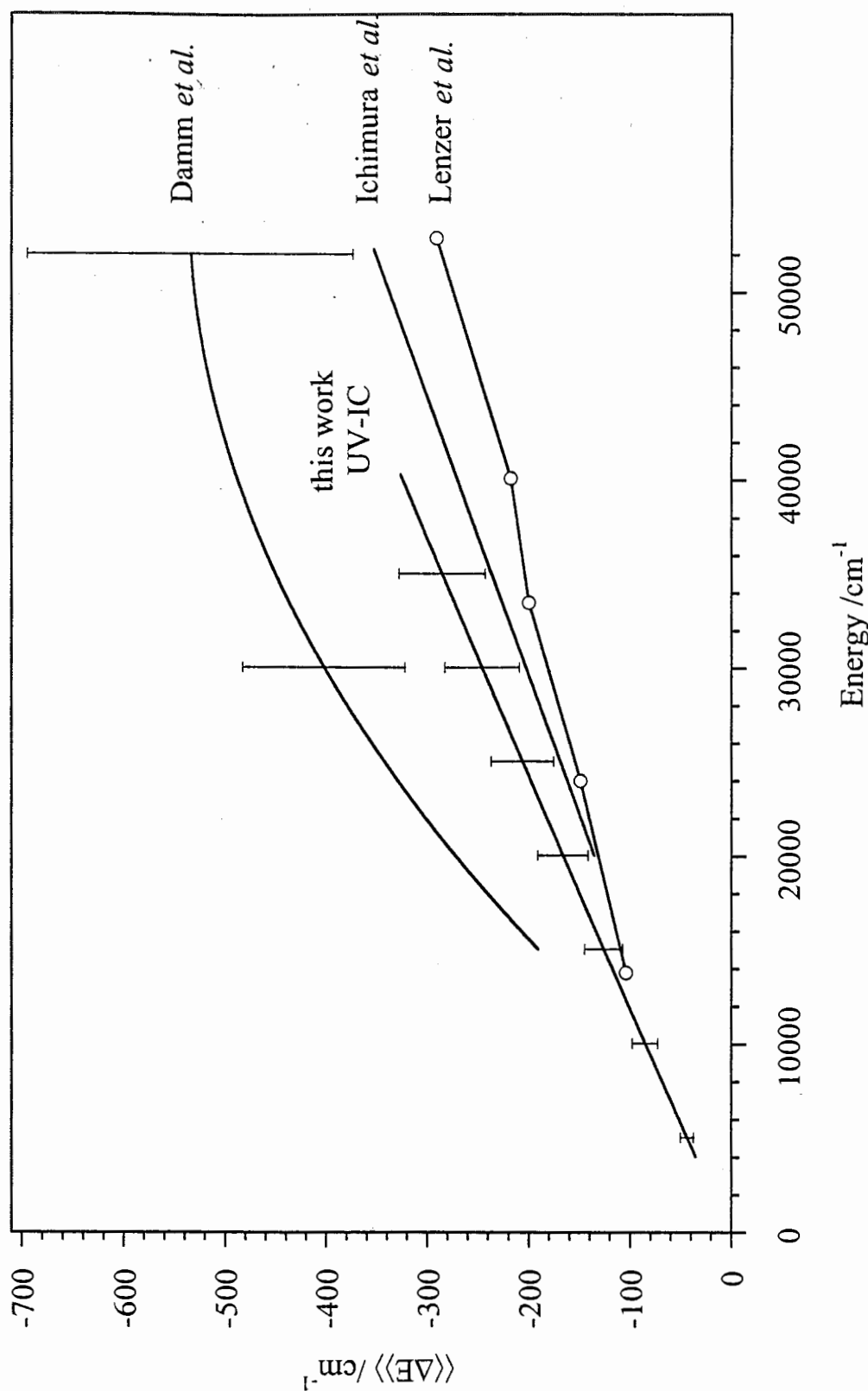


Figure 3.7 Summary of $\langle\Delta E\rangle$ vs $\langle E \rangle$ curves for the deactivation of highly excited HFB by Ar collider gas.

Table 3.4 Average energy transferred per collision, $-\langle\langle\Delta E\rangle\rangle$, for deactivation of HFB by argon.

| Excitation Method | Ref. | $-\langle\langle\Delta E\rangle\rangle / \text{cm}^{-1}$ | | | |
|-------------------------|-----------------|-----------------------------------------------------------------------------|-----------------------|-----------------------|-----------------------|
| | | Average internal energy, $\langle\langle E \rangle\rangle / \text{cm}^{-1}$ | | | |
| | | 51 800 ^a | 40 300 ^b | 24 000 | 15 000 |
| UV-193 nm | [Ichimura 1987] | 196 | 153 | 91 | 61 |
| UV-193 nm | [Damm 1990] | 540 | $\sim 476^{\text{c}}$ | $\sim 333^{\text{c}}$ | $\sim 190^{\text{c}}$ |
| UV-248 nm | this work | | 327 | 198 | 126 |
| theory-QCT ^d | [Lenzer 1995] | | | 149 | |

^a Photon energy at 193 nm.^b Photon energy at 248 nm.^c Estimated from Figure 9 of Damm *et al.* [Damm 1990].^d Quasiclassical trajectory calculations.

along with other experimental and theoretical studies based on the deactivation of highly excited HFB by Argon. The error bars on our UV-IC data indicate two standard errors, determined from the error in the extrapolation of the $\langle\langle\Delta E\rangle\rangle$ vs F_c curves (see above) and the error determined between different runs. The $\langle\langle\Delta E\rangle\rangle$ vs $\langle\langle\Delta E\rangle\rangle$ curve for Damm *et al.* was estimated from their figure 9 [Damm 1990], while the data points for the theoretical curve were estimated from figure 4 of Lenzer *et al.* [Lenzer 1995]. The theoretical points of Lenzer *et al.* have been joined by a line for illustrative purposes. Although the work of Ichimura *et al.* was assessed by Damm *et al.* to be obsolete due to an incorrect calibration curve, it has been included for completeness.

As evidenced by figure 3.7, our $\langle\langle\Delta E\rangle\rangle$ vs $\langle\langle E \rangle\rangle$ curve is lower than that of Damm *et al.* [Damm 1990], but larger than that of Ichimura *et al.* [Ichimura 1987]. The theoretical calculations by Lenzer *et al.* are in close agreement with our data [Lenzer 1995].

Considerable debate exists over the functional form of the $\langle\langle\Delta E\rangle\rangle$ vs $\langle\langle E\rangle\rangle$ curves. The results of Damm *et al.* indicate that there is a definite roll-off with increasing energy [Damm 1990]. Other authors have even seen these $\langle\langle\Delta E\rangle\rangle$ curves to completely roll over ($\langle\langle\Delta E\rangle\rangle$ values decrease with increasing energy) [Toselli 1991]. Our assumed functional form for $\langle\langle\Delta E\rangle\rangle$ consists of two parameters, k_1 describing the linear term and k_2 describing any curvature. The UV-IC data obtained in this study show k_2 to be insignificant in comparison with k_1 (see table 3.2). Although fitting parameters have been used which will model any roll-off that possibly exists, the experimental data suggests $\langle\langle\Delta E\rangle\rangle$ to be essentially linear with energy. The magnitude of the non-linear term compared with the linear term, obtained in this study, is illustrated through a comparison of the ratios of these two terms. The value of this ratio was found to be <5% (calculated when the average energy has fallen to half its initial value). Hence, these parameters reveal $\langle\langle\Delta E\rangle\rangle$ to be essentially linear with energy.

3.6.2 Comparison of collision partner dependence

From the functional form for $\langle\langle\Delta E\rangle\rangle$ obtained from our data, we can extrapolate to regions where we can compare our values of $\langle\langle\Delta E\rangle\rangle$ with those measured in previous studies which have used initial excitation at 193 nm [Ichimura 1987; Damm 1990]. The results for Ar with IRMPA-IRF and IC-IRF show that this approach is valid. All results for HFB with noble gas colliders are shown in table 3.5. To aid comparisons with quasiclassical trajectory calculations, this table also shows our data calculated at an internal energy of $24\,000\text{ cm}^{-1}$. Since the initial energy of the highly excited HFB molecule in our experiment is $16\,000\text{ cm}^{-1}$, the higher energy values are an extrapolation of our data assuming that $\langle\langle\Delta E\rangle\rangle$ is linear with energy. This extrapolation is valid for the case of argon since the IC-IRF experiments show that $\langle\langle\Delta E\rangle\rangle$ is linear with energy up to $\sim 40\,000\text{ cm}^{-1}$. For the purpose of comparisons, we assume that this is also true for all the other monatomic collision partners. By comparing the results

Table 3.5 Average energy transferred per collision, $\langle\langle\Delta E\rangle\rangle$, for the deactivation of HFB by noble gases.

| Collider | $-\langle\langle\Delta E\rangle\rangle / \text{cm}^{-1}$ | | | | Excitation Method | Reference | | |
|----------|-----------------------------------------------------------------------------|-------------------------------------|-------------------------------------|-------------------------------------|------------------------------------------------------------|----------------------------|--|--|
| | Average internal energy, $\langle\langle E \rangle\rangle / \text{cm}^{-1}$ | | | | | | | |
| | 51 800 ^a | 40 300 ^b | 24 000 | 15 000 | | | | |
| He | 300 | $\sim 286^{\text{c}}$ 110 200 | $\sim 162^{\text{c}}$ 110 200 | $\sim 57^{\text{c}}$ 69 | UV-193 nm IRMPA theory-QCT ^d | [Damm 1990] | | |
| | | | | | | this work | | |
| | | | | | | [Lenzer 1995] | | |
| Ne | | | 154 | 96 | IRMPA | this work | | |
| Ar | 196 | 153 | 91 | 61 | UV-193 nm | [Ichimura 1987] | | |
| | 540 | $\sim 476^{\text{c}}$ 327 | $\sim 333^{\text{c}}$ 198 194 | $\sim 190^{\text{c}}$ 126 122 | UV-193 nm UV-248 nm IRMPA theory-QCT ^d | [Damm 1990] | | |
| | | | | | | this work | | |
| | | | | | | this work | | |
| | | | | | | [Lenzer 1995] | | |
| Kr | | | 139 | 88 | IRMPA | this work | | |
| Xe | | | 130 | 82 | IRMPA theory-QCT ^d | this work [Lenzer 1995] | | |

^a Photon energy at 193 nm.^b Photon energy at 248 nm.^c Estimated from Figure 9 of Damm *et al.* [Damm 1990]^d Quasiclassical trajectory calculations.

obtained from IC-IRF and IRMPA-IRF for the case of argon as collider (see section 3.4.3), we have demonstrated that the two techniques produce identical results within experimental error. Our IRMPA results can thus be compared with previous IC results.

In the previous section we have compared our results with those of Ichimura *et al.* and Damm *et al.* for the deactivation of highly excited HFB by argon. Damm *et al.* also present results using helium as the collision partner. Allowing for extrapolation of their studies into our energy regime, comparison of our $\langle\langle\Delta E\rangle\rangle$ values for He with those of Damm *et al.* show reasonable agreement.

Our results for a full series of five noble gas colliders facilitate the establishment of a trend within the series. The average energy transferred per collision for these colliders was found to increase from He through to Ar, however it subsequently decreased from Ar through to Xe.

The maximum $\langle\langle\Delta E\rangle\rangle$ observed for Ar collider suggests that there is a preferred deactivate mass in the noble gas series. It is worth noting that the trend observed in our study is very similar to that observed by Tardy who used the technique of IRMPA coupled with time-resolved optoacoustics to investigate the deactivation of C_6F_{14} and C_8F_{18} by the same series of five noble gases as used in our work [Tardy 1993]. Tardy found that the relative collision efficiency (the deactivation rate constant relative to the hard sphere collision rate constant) increased from He to Ne to Ar and then decreased to Kr followed by a slight levelling off for Xe. While the absolute values of this relative collision efficiency may have uncertainties, the observed trends for a series of similar colliders with a given excited species should be reliable for comparative purposes. Tardy carried out a satisfactory analysis of his results in terms of the simple billiard ball model (impulsive collision) by treating the excited polyatomic as a *pseudo*-diatomic molecule and using the equation presented by Benson [Benson 1982].

Lenzer *et al.* [Lenzer 1995, 1997] have carried out quasiclassical trajectory calculations on the deactivation of excited HFB (and benzene) by some mono- and polyatomic colliders, including the noble gases He, Ar and Xe. The calculations were carried out for initial energies of 14 000, 24 000, 34 000, 40 700 and 53 270 cm⁻¹ but the authors used the results at 24 000 cm⁻¹ for detailed comparisons between input parameters in the calculations and between calculations and experimental results. Their calculations for HFB at 24 000 cm⁻¹ are shown in table 3.6. As pointed out by Lenzer *et al.* [Lenzer 1995, 1997], the agreement between their trajectory calculations and experiment is excellent for benzene but less satisfying when compared with the experimental results of Damm *et al.* for HFB [Damm 1990]. While the trajectory calculations for the magnitudes of $\langle\langle\Delta E\rangle\rangle$ are in reasonable agreement with our experiments for Ar collider, they are somewhat higher than experiment for He and lower than experiment for Xe. Also, the trend predicted by the trajectory calculations is a continuous decrease in the average energy transferred per collision from He to Ar to Xe, in contrast to our experiments which show a maximum for Ar in the noble gas series. Lenzer and Luther [Lenzer 1997] suggest that inadequacies in the trajectory calculations for HFB are probably due to an insufficient representation of the intermolecular potential between F and Ar atoms.

There is considerable debate concerning the variation in the average energy transferred per collision with internal energy. Figure 3.6 shows the linear energy dependence of $\langle\langle\Delta E\rangle\rangle$ for each monatomic over the energy range studied. This is consistent with trends observed in earlier work based on IC-IRF and IC-UVA studies when extrapolated to low energies [Barker 1988; Ichimura 1987; Damm 1990]. Also, despite the differences in absolute values of $\langle\langle\Delta E\rangle\rangle$ between trajectory calculations and experiment, the energy dependence of $\langle\langle\Delta E\rangle\rangle$ predicted by the trajectory calculations is essentially linear [Lenzer 1995, 1997]

Table 3.6 Average energy transferred per collision, $-\langle\langle\Delta E\rangle\rangle$, for deactivation of excited aromatics by noble gases.

| Excited molecule | $-\langle\langle\Delta E\rangle\rangle / \text{cm}^{-1}$ at $\langle\langle E \rangle\rangle = 24\ 000 \text{ cm}^{-1}$ | | | | | Reference | |
|------------------|-------------------------------------------------------------------------------------------------------------------------|-----|--------------------------|-----|-----|-----------------------|--|
| | Collider | | | | | | |
| | He | Ne | Ar | Kr | Xe | | |
| HFB | ~162 110 | 154 | ~333 91 198 194 | 139 | 130 | [Damm 1990] | |
| | | | | | | [Ichimura 1987] | |
| | | | | | | this work (UV-IC) | |
| | | | | | | this work (IRMPA) | |
| benzene | 23 | 20 | 30 | 34 | 36 | [Barker 1993, 1995] | |
| toluene | 62 | 77 | 112 | 110 | 124 | [Barker 1993, 1995] | |
| pyrazine | 22 | 33 | 32 | 51 | 52 | [Miller 1996a, 1996b] | |

The results obtained here for HFB may be compared with data on aromatics of similar size (eg. benzene, toluene, pyrazine) [Barker 1993, 1995; Miller 1996a, 1996b]. For convenience of qualitative comparison, the values for $\langle\langle\Delta E\rangle\rangle$ at $24\ 000 \text{ cm}^{-1}$ are shown in table 3.6 but the relativities are essentially the same at $15\ 000 \text{ cm}^{-1}$. The collisional deactivation of HFB show much higher $\langle\langle\Delta E\rangle\rangle$ values (between three and ten times larger) when compared to these aromatics. The large difference in the energy dependence and absolute values of $\langle\langle\Delta E\rangle\rangle$ between HFB and toluene deactivated by Ar has been highlighted by Damm *et al.* [Damm 1990]. This much more efficient collisional deactivation of HFB has been suggested by Damm *et al.* as probably due to

the increased number of low frequency modes. The increased efficiency of collisional energy transfer of HFB relative to these other aromatics is also supported by the trajectory calculations (at least for HFB versus benzene) [Lenzer 1995, 1997] despite the differences in absolute values of $\langle\langle\Delta E\rangle\rangle$ between theory and experiment. The trajectory calculations show that the lower the vibrational frequencies the more efficient is the collisional energy transfer, as was suggested by Damm *et al.* [Damm 1990].

3.7 Conclusions

Studies of the deactivation of highly excited polyatomic molecules require a method to initially prepare the excited molecule. Two common methods are infrared multiphoton absorption (IRMPA) and UV absorption followed by rapid internal conversion (UV-IC). These two methods, however, produce distinctly different initial energy distributions. Although these two methods, and others, have been used for energy transfer studies, no comparison between any of the methods for initial state preparation has been performed.

We have used both the IRMPA and UV-IC methods to produce highly excited hexafluorobenzene and by monitoring the infrared fluorescence, the collisional deactivation of hexafluorobenzene was measured. Using argon as the collision partner, it was found that within experimental error the average energy transferred per collision, $\langle\langle\Delta E\rangle\rangle$, was the same in both cases. That is, the energy transfer parameters were found to be the same for the two different initial energy distributions. This is the first experimental comparison between two different excitation methods, and demonstrates that IRMPA is an acceptable method to produce highly excited molecules for the use in energy transfer studies.

The success of using IRMPA to determine energy transfer parameters has enabled us to extend the study of collisional deactivation of highly excited HFB to all the noble gas colliders He, Ne, Ar, Kr and Xe using the IRF detection technique. The magnitude of the average energy transferred per collision was found to increase from He through to Ar, however it subsequently decreased from Ar through to Xe. The average energy transferred per collision is a linear function of energy. For the same colliders, the $\langle\langle\Delta E\rangle\rangle$ values for HFB are much greater than those for the closely related aromatics, benzene, toluene and pyrazine.

Chapter 4

Design and Development of an Ion Imaging Apparatus for the study of Energy Transfer

4.1 Introduction

Measuring the energy content within molecules after they collide with highly excited molecules was shown by Flynn's group to be a successful way to monitor energy transfer from highly excited molecules such as benzene [Sedlacek 1991], hexafluorobenzene [Sedlacek 1991; Michaels 1997b], and pyrazine [Mullin 1995; Michaels 1995, 1998]. Using a very high resolution diode laser system they were able to measure the Doppler profile of the rovibrational transitions of CO₂ after it had undergone collisions with a highly excited polyatomic. This allowed the recording of all the degrees of freedom (translation, rotation and vibration) excited after a collision. Precise details concerning the energy transfer process could thus be extracted. For example, two distinctly different types of collisions were observed. When the CO₂ molecule was vibrationally excited in the collision, very little excitation of the rotational or translational degrees of freedom occurred. The probability of vibrational excitation was also found to increase with decreasing temperature. The authors attribute these effects to a long range energy transfer process (occurring on the attractive part of the intermolecular potential). The other type of collision, involving a short range repulsive force mechanism, was responsible for large energy transfers to CO₂ rotational and translational degrees of freedom, without any vibrational excitation.

Flynn's group went on to describe how the state resolved data recorded in their experiments could be converted into a $P(E,E')$ distribution [Michaels 1997a]. This was the first time that a $P(E,E')$ distribution was experimentally determined for energy transfer from a highly excited molecule. Even though only the tail of the distribution could be calculated ($\Delta E > 2000 \text{ cm}^{-1}$), it was nevertheless a significant achievement in energy transfer studies. There were a number of factors which limited knowledge of the distribution to large energy transfers. Most of the limitations are due to the room temperature environment in which the experiments are performed. Transfer to low rotational states in the vibrationless ground state become very difficult to measure because these states are already highly populated at room temperature. It is difficult to measure the collisionally induced Doppler widths of the rotational transitions from these levels. It is also difficult to determine from which initial rotational levels the final rotational state is populated. This is unfortunate since small transfers of energy into rotations and translations are highly efficient processes, and are therefore expected to be of significant importance. Monitoring transfer to, and within, the bending mode of CO₂ was also difficult because ~8% of the room temperature population lies in that state. A technique which overcomes these difficulties will be necessary to gain more information on the exact form of $P(E,E')$.

The idea of extracting energy transfer information by observing changes in the collision partner has prompted us to perform similar experiments using the relatively new technique of ion imaging. Ion imaging has become an important tool in the last few years to study the fragmentation of polyatomic molecules [Heck 1995; Chandler 1999]. This technique was first employed by Chandler and Houston to show that it is possible to measure both the kinetic energy and the angular distribution of CH₃ fragments released after the photodissociation of CH₃I [Chandler 1987]. Since then, ion imaging techniques have been employed in a wide variety of chemical systems to elucidate the processes involved in unimolecular dissociations (see for example [Samartzis 1997; Droz-Georget 1997; Suzuki 1996; Rogers 1996]), inelastic scattering [Bontuyan 1993],

and bimolecular reactions [Kitsopoulos 1993]. Recently the technique has been extended to measure the energy and angular distributions of electrons ejected in photoionisation [Parker 1997; Jung 1997; Wang 1999]. The first report of ion imaging to determine the translational energy released in van der Waals complex dissociation also appeared recently [Yoder 1999].

Ion imaging is an experimental technique that effectively allows one to obtain the speed and direction of either dissociating fragments or photoejected electrons. This is achieved by projecting the three dimensional velocity distribution of the dissociating fragment (or photoelectron) onto a two dimensional detector. The projection requires the use of an electric field which is used to accelerate ions or electrons onto a two dimensional detector. To project dissociating neutral fragments, they must be immediately ionised following the dissociation process. Performing the dissociation in a time of flight mass spectrometer allows only the fragment of interest to be detected, eliminating background from other species. Detailed information describing the technique will be presented below, along with the mathematical description necessary for the analysis of the resulting images.

Returning to our goal of measuring energy transfer from highly excited polyatomics, we believe that it is possible to use ion imaging to monitor the energy transferred to the collision partner. Ion imaging has been shown to be successful in studying state resolved differential cross sections for energy transfer in the Ar-NO system [Bontuyan 1993]. In our case, the desired polyatomic and collision partner under investigation would be seeded in separate supersonic expansions resulting in a significant cooling of their vibrational, rotational, and translational distributions. Formation of the highly excited species is easily achievable using standard methods such as UV absorption followed by rapid internal conversion back into the electronic ground state. After collisions with the collision partner at the intersection of the crossed beams, any energy that was transferred will result in the excitation of rotational, vibrational or

translational states or a combination of these. Rotational and vibrational states of the collision partner could be probed by simply ionising the species using a laser wavelength corresponding to an absorption transition from the rovibrational level under investigation. Using the ion imaging technique, translational energies would be determined, thus giving information on all degrees of freedom.

Measurement of the transferred kinetic energy using ion imaging has a number of advantages over the Doppler profile technique used by Flynn's group. Firstly, the shape of the kinetic energy distribution can be found exactly, unlike that obtained from the Doppler measurements where the linewidth is fitted to a temperature, thus assuming a Boltzmann distribution. Secondly, the molecular beam environment allows observation of transfer to much lower rotational and translational energies than is possible in room temperature experiments. Thus ion imaging allows the observation of transfer to a much broader range of translational energies. Finally, the crossed beam environment constrains the collision energy between the target molecule and collider to a narrow, well defined range. This is in contrast to room temperature experiments where the collision energy is averaged over the entire Maxwell-Boltzmann distribution of molecular velocities.

We are approaching the development of a crossed beam apparatus with ion imaging in a step-wise fashion. Since our group has no experience in ion imaging experiments, the first step is to construct a simpler, one beam apparatus with an ion imaging detection system. This has been the goal of the system described here. The lessons learned in the use of this system will inform the development of the crossed beam system.

In this chapter the ion imaging technique is presented with the design and development of a single molecular beam ion imaging apparatus. The apparatus was designed to work both for ion imaging and as a standard time of flight instrument for spectroscopic investigations. The apparatus has been used in the ion imaging configuration to study

the energy released in van der Waals cluster dissociation, specifically the dissociation of benzene-argon ionic van der Waals clusters formed by (1+1) resonance enhanced multiphoton ionisation (REMPI).

Prior to the van der Waals dissociation experiments on benzene, it was realised that the vibrational distribution that benzene ions are formed through photoionisation is not accurately known. To overcome this problem, the apparatus was modified so that it could be used to also measure photoelectron spectra. Since the instrument was not initially designed for the recording of electron images, the standard design protocols used for designing electron spectrometers were not considered, and consequently the images observed contain small distortions. We present a method which corrects for these distortions, greatly improving the energy resolution of spectra extracted from the images.

4.2 The Ion Imaging Technique

4.2.1 *Concepts and mathematical formalism*

Consider a simple dissociation where the fragments dissociate from a point source with only a single kinetic energy. This is shown diagrammatically in figure 4.1. After excitation of a parallel transition by linearly polarised laser light, the molecule becomes aligned along the direction defined by the polarisation direction. Any dissociation will therefore occur with cylindrical symmetry around the axis parallel to the laser's electric field vector. After dissociation, the fragments expand spherically around the point of dissociation. The actual angular dependence of the dissociating fragments will depend on the molecular dynamics of the dissociation process. The fragments are subsequently

ionised with a laser, which can be either the same laser pulse as used for the dissociation or a second laser pulse of different wavelength. Importantly, the ionisation process has negligible influence on the fragment's velocity. When this expanding ionic sphere is placed in an electric field, such as that present in a time of flight mass spectrometer, the spherical expansion is accelerated in the direction of the electric field and towards a detector. The expanding sphere will eventually hit the ion detector, forming on it a two dimensional image representing the initial three dimensional dissociation distribution. The size of the resulting image depends on the velocity of the fragments, and the time it takes them to arrive at the detector. Moreover, since the flight time in a time of flight mass spectrometer is proportional to the square root of the mass, then it turns out that the radius of the expanding sphere only depends on the kinetic energy of the fragment ($r \propto \sqrt{E_{kinetic}}$) and is fully independent of the fragment's mass. Knowledge of the flight time allows the ion energies to be calculated, and if there is sufficient information regarding energy levels within the products, then the final populated states can be determined. Since the expansion occurs in a time of flight mass spectrometer it is possible to only monitor the fragment of interest by activating the detector at the time at which the desired fragment mass arrives.

Since the images obtained are two dimensional, the actual three dimensional description of the dissociation process needs to be extracted. The parameters necessary for the calculation of these distributions are included in figure 4.1. The three dimensional distribution is given by $F(E_k, \theta)$ where E_k is the kinetic energy of the fragment and θ is the angle between the laser polarisation and the velocity vector. During the time the fragment ions take to reach the detector, they will have expanded by a distance R , determined by the fragment's mass and kinetic energy. This radial distribution is denoted as $F(R, \theta)$.

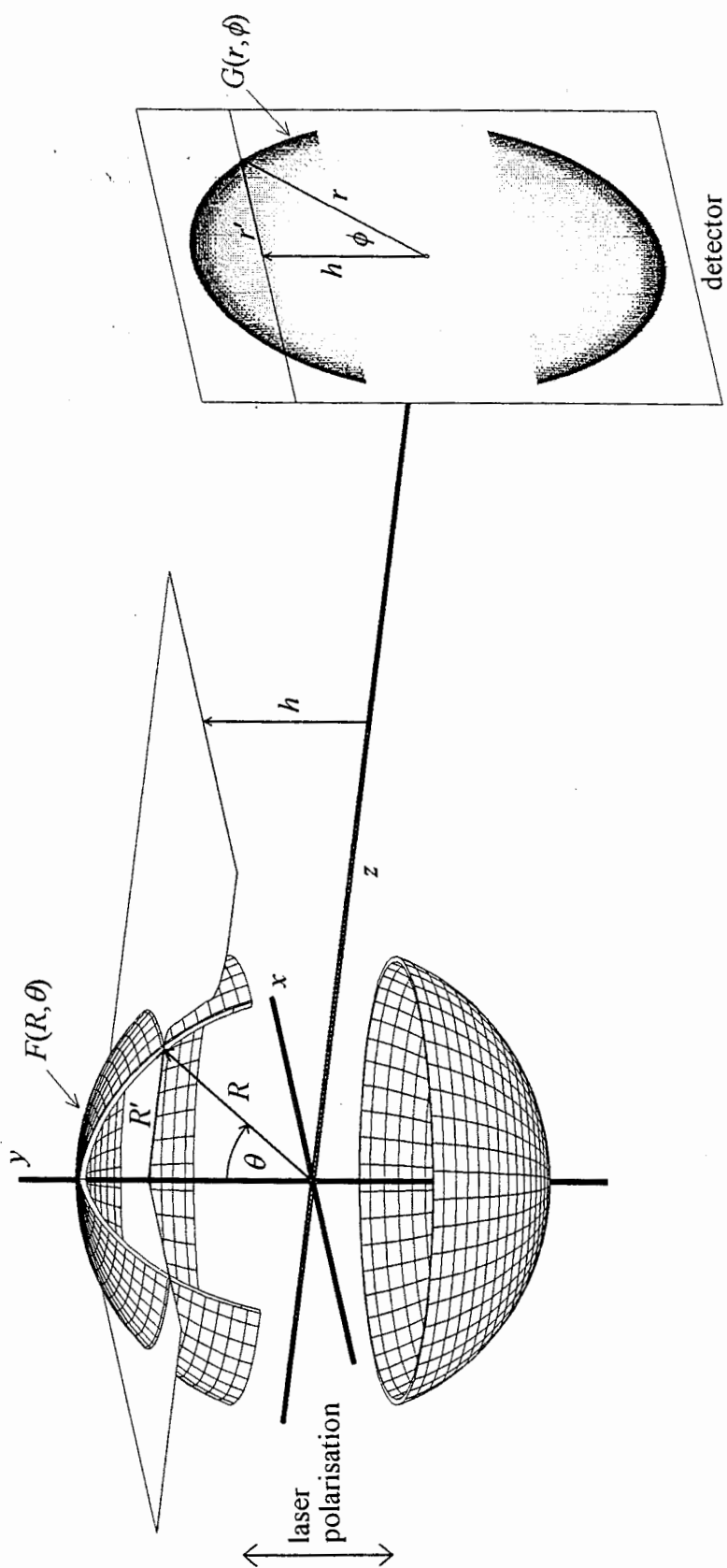


Figure 4.1 Diagrammatic representation of the ion imaging technique. The parameters used to describe the Abel transform are also included. These parameters are described in the text.

First we consider what happens to a plane orthogonal to the laser polarisation as shown in figure 4.1. The plane sits at a height h above the z -axis, so the plane cuts through the dissociation distribution, and has a radial intensity given by $f(R', h)$ where R' is the radial distance from the cylindrical axis. The projection of this plane onto the detector results in a line a distance h above the x -axis, and symmetrical about the y -axis. It is an easy task to show that the line projection $g(r', h)$ is given by

$$g(r', h) = 2 \int_{r'}^{\infty} \frac{f(R', h) R'}{\sqrt{R'^2 - r'^2}} dR' \quad 4.1$$

where r' is the perpendicular distance from the y -axis [Heck 1995]. This projection is known as the Abel transform. When this transform is applied for every height h , the final two dimensional image $G(r, \phi)$ is realised.

Recovery of the original three dimensional function from the two dimensional image is given by the reverse process, where each line of the two dimensional image is taken and the inverse Abel transform applied. The inverse Abel transform is given by [Bracewell 1977]

$$f(R', h) = -\frac{1}{\pi} \int_{R'}^{\infty} \frac{g'(r', h)}{\sqrt{(r'^2 - R'^2)}} dr' \quad 4.2$$

We note that it has recently been shown through simulations that the inverse Abel transform does not give the best image reconstruction in ion imaging experiments under conditions of high kinetic energies, or more correctly, high values of the ratio between the ion kinetic energy and the potential energy gained in the accelerating region [Winterhalter 1999]. However, since we are working with sufficient field strengths to be far removed from those extreme conditions, the inverse Abel method is appropriate for the treatment of our data.

The radial and angular variables describing the dissociation are separable. Thus the probability distribution $F(R, \theta)$ can be expressed as the product of a radial part $F_R(R)$ and an angular part $F_A(\theta)$. The angular dependence of the dissociating fragments is determined by a number of factors, such as the molecular alignment, the angle between the fragmenting bond and the transition dipole moment, and the speed of dissociation with respect to the rotational period. In general, the angular dependence is given by a linear combination of Legendre polynomials $P_n(x)$

$$F(\theta) \propto \sum_n \beta_n P_n(\cos \theta) \quad 4.3$$

where β_n are the Legendre coefficients. For excitation of randomly orientated molecules the odd terms vanish leaving only the even terms. For simple one photon dissociations only the first two terms $P_0(x)$ and $P_2(x)$ are required, so $F_A(\theta)$ reduces to

$$F_\theta(\theta) = \frac{1}{4\pi} [1 + \beta P_2(\cos \theta)] \quad 4.4$$

where β is the parameter defining the degree of alignment. β can vary between -1 and +2 with a value of zero indicating an isotropic distribution. The second order Legendre polynomial is given by

$$P_2(\cos \theta) = \frac{1}{2} [3 \cos^2(\theta) - 1] \quad 4.5$$

Thus a value for β of -1 leads to a $\sin^2 \theta$ distribution, while a value of +2 produces a $\cos^2 \theta$ distribution. These two limiting cases represent instantaneous fragmentation where the dissociation is either parallel ($\beta = 2$) or perpendicular ($\beta = -1$) to the transition dipole moment. However, in general the value of β lies somewhere in between these two extremes.

In order to illustrate the type of behaviour that can be observed, example images of the three dimensional dissociation distribution and their corresponding two dimensional projections have been calculated and are shown in figure 4.2. Using a velocity distribution consisting of a single Gaussian centred far from the origin (figure 4.2a), the three dimensional velocity distributions are calculated for the two extremes, $\beta = -1$ and $\beta = +2$, using the procedure detailed later (section 4.3). These distributions are shown in figures 4.2b and 4.2c respectively. These images (and all other three dimensional velocity distributions presented in this thesis) require rotation about the centre y -axis to realise the full three dimensional distribution. The Abel transform is applied to both calculated velocity distributions to give the example two dimensional images shown in figures 4.2d and 4.2e. The method used for calculating Abel transforms and their inverses is given in the section 4.3.

For photoionisation, the mathematical description of the angular dependence for ejected photoelectrons is identical to that discussed for fragmentation. However, particular angular distributions arise as a result of the interference between the partial waves which constitute the outgoing photoelectron wavefunction. This is discussed in more detail by Ried *et al.* in a recent review [Ried 1995]. When using resonance enhanced multiphoton ionisation to produce the photoelectrons, it may be necessary to include the next order Legendre polynomial since absorption of the first photon can introduce some alignment into the system [Ried 1995].

4.2.2 Velocity Mapping

The original method of ion imaging utilised the same electrode arrangements as those used in time of flight mass spectrometers [Chandler 1989]. The acceleration regions and field free regions were kept as uniform as possible by using high transmission

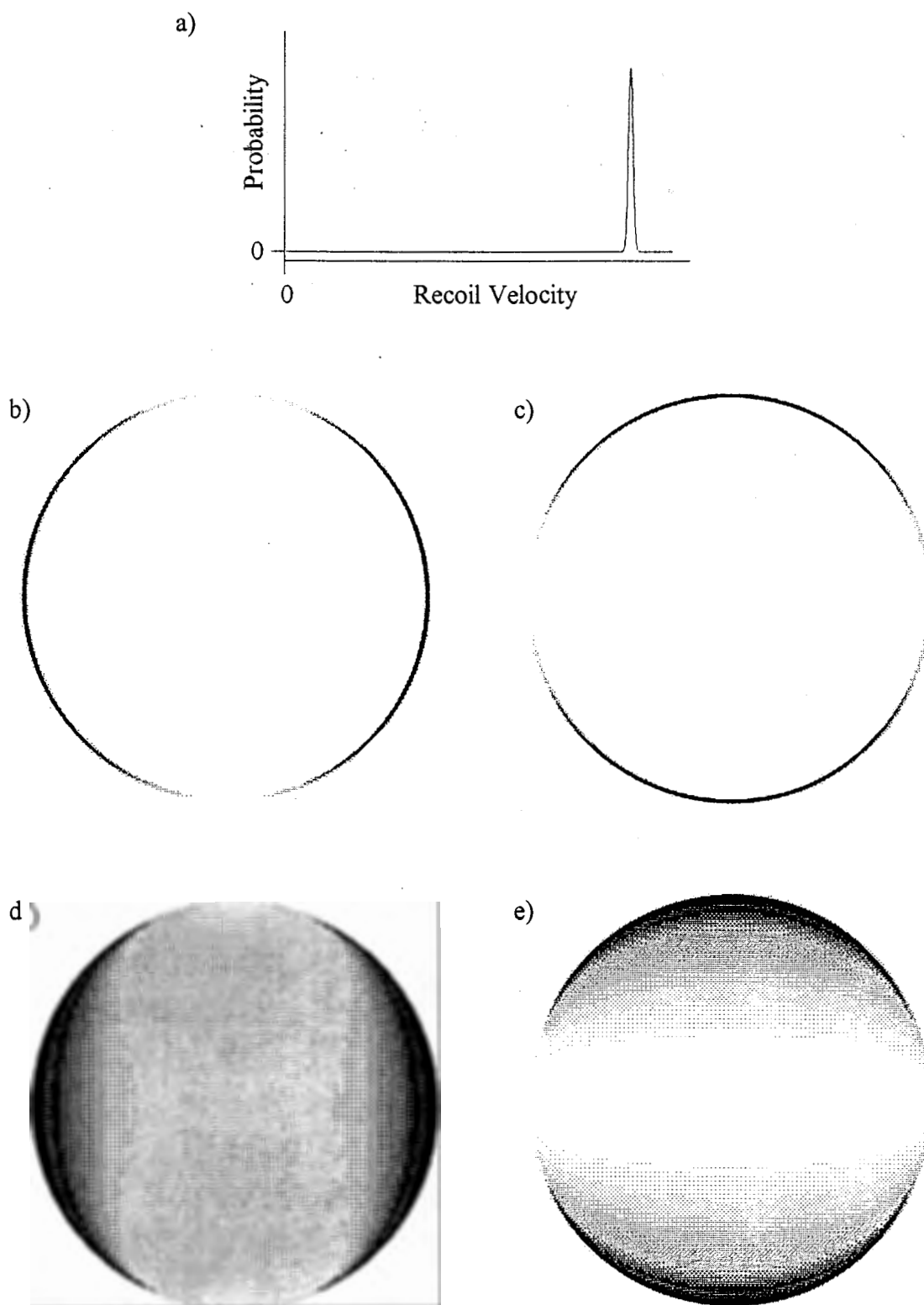


Figure 4.2 Example images showing the two extremes of the angular distribution of fragments: a) shows the radial function (distribution of velocities) used to calculate the three dimensional velocity distribution for b) $\beta = -1$ and c) $\beta = +2$. The two dimensional images resulting from these three dimensional distributions are shown in d) $\beta = -1$ and e) $\beta = +2$. Laser polarisation is vertical in the images.

metallic mesh to separate each region, allowing the passage of ions between sections of the spectrometer. This suffered from a resolution problem due to the finite volume of the intersection between the molecular beam and the laser beam. This intersection, which is cylindrical in shape, will be convoluted with the three dimensional dissociation distribution, resulting in a blurred image along the same direction as the laser beam. Methods of deconvolution were necessarily developed to obtain the true three dimensional dissociation distribution [Strickland 1991]. The presence of mesh also affects the image since ions can not pass through the metallic wires of the grid, leaving a grid pattern superimposed on any image observed at the detector.

Eppink and Parker have recently shown that both of the above mentioned problems can be overcome by simply removing the mesh between acceleration regions [Eppink 1997]. This distorts the electric field around the holes and makes them act as lenses. By selecting appropriate voltages, this lens action causes ions having the same velocity (ie speed and direction) to hit the detector at the same spot, irrespective of their initial starting position along the laser beam. In other words, although ions might start at different locations along the laser beam, they will strike the detector at the same location when they have the same initial velocities. This technique has been dubbed “velocity map imaging” by its originators. With velocity map imaging the problem of initial starting positions is overcome and, unlike the original method, no deconvolution is necessary. The lack of mesh also means that no ions are lost during transit, so no mesh shadow will be seen in the recorded images. There is a down side to the method of velocity mapping, however, since the voltages required for successful imaging are slightly different to those necessary for maximum mass resolution. This leads to a slight degradation of the mass resolution under best imaging conditions and so a velocity map imaging instrument may not be able to discern between species that are close in mass. This will be discussed further when the design of the time of flight mass spectrometer is presented. The lensing system used in velocity map imaging also leads to a magnification of the image and so images must be calibrated.

4.3 Computational Aspects

4.3.1 Abel and Inverse Abel Transform Algorithm

As discussed above, computations of the Abel transform and its inverse are central to the analysis of our results. Direct computation of these transforms is not a simple task because of the singularity when R' approaches r' (see equation 4.1 and 4.2). A common method to calculate the inverse Abel transform is to take the Fourier transform of the image and then apply the inverse Hankel transform [Strickland 1991]. The Fourier transform is generally calculated using fast Fourier transform (FFT) methods which rely on the data being of length 2^n and evenly spaced along the x -axis.

An alternative approach, derived by Hansen *et al.*, gives a simpler way of calculating the forward and inverse Abel transforms [Hansen 1985]. It has the advantage that it can be used on arbitrary length data, and the data do not have to have constant spacing along the x -axis, although the method is simplified if this is the case. We use this method as the basis of our calculations. While Hansen *et al.* presented the general method in their paper, they went on to focus on the specific case of constant x -axis spacing and also made assumptions about the data to be analysed that we have found do not apply in our case. It has thus been necessary to modify their procedure for our situation.

In their original derivation, Hansen *et al.* assume that the function to be transformed is constant over the x interval, thereby greatly simplifying the required mathematics. For the inverse case they calculate the derivative using forward difference. These two simplifications tend to cancel each other out for functions which monotonically decrease with increasing radius. We find, however, that calculations of the inverse

function are slightly in error for arbitrary functions having both positive and negative derivatives. By assuming the function to vary linearly over the interval and using central derivatives we found the inverse transform to give more accurate results. We have also allowed for irregular spacing along the x -axis, since we require this for calculating photoelectron spectra and β values in photoelectron distributions. The formula used to calculate the forward and reverse transforms is given in appendix A. The program code for the forward and inverse Abel transforms was rigorously tested in two ways. Firstly, many of the Abel transform pairs given by Bracewell [Bracewell 1977] were computed and compared with the true analytical function. Secondly, by applying the forward and inverse transform a number of times in succession to arbitrary functions, we confirmed that the original function was returned.

The derivative in the integrand of the inverse Abel transform is particularly nasty since it amplifies any noise present in the raw data [Heck 1995]. Therefore high quality images must be acquired to successfully perform the inverse Abel transform. Methods have been developed or suggested to reduce this problem, and include smoothing the data prior to differentiation, applying filters [Hansen 1985] and convolution techniques [Strickland 1991]. We, however, use no enhancements unless explicitly stated. When performing the inverse Abel transform on real data, the transform becomes unstable near the origin due to noise in the data. In the two dimensional images, this manifests itself as a vertical stripe in the centre of each transformed image. The stripe is a well known artefact of calculating the inverse Abel transform [Chang 1998], and is ignored in subsequent data analysis.

4.3.2 Generation of the Three Dimensional Radial Distribution

As outlined above, calculation of the three dimensional distribution $F(R, \theta)$ function requires the two dimensional image to be transformed through use of the inverse Abel

transform. This process required the centre of each image to be first determined. For all images recorded in this work this was straightforward since they all showed a peak in centre of the image. This was the case even for photoelectron spectra where there were always some electrons ejected with near zero kinetic energy. The peak was fitted to a two dimensional Gaussian function using the Levenberg-Marquardt algorithm for non-linear least squares fitting [Press 1992], allowing the central coordinate to be found. Rounding the central coordinates to the nearest half pixel, and using the fact that the images are symmetrical about the x and y axes, allowed the image to be averaged over the four quadrants prior to the application of the inverse Abel transform. This improved the signal to noise ratio in the transformed image. Each row of the image was transformed using the inverse Abel transform algorithm discussed above (section 4.3.1 and appendix A) to generate the final $F(R, \theta)$ image. Since the two dimensional image was averaged over the four quadrants before the transformation procedure, the final transformed image is identical in each quadrant, and only one quadrant needs to be displayed. We, however, display the entire image as we find it aids visualisation of the dissociation and photoionisation events.

4.3.3 Calculation of Energy Distributions - General Method

Once the inverse Abel transform has been applied to obtain the three dimensional distribution $F(R, \theta)$, the function describing the probability that a particle will have a particular energy, $P(E)$, needs to be calculated. For the case of photoelectrons, this is the photoelectron spectrum. We calculate the energy spectrum by first generating a radial plot representing the angle averaged intensity of the $F(R, \theta)$ distribution at a radius R . This is done by taking each pixel of the transformed image (ignoring the centre stripe as discussed above) and calculating the distance from the image centre. The intensity value at that pixel is added to a histogram based on the radial distance. Since the radius will be later converted to energy values, the bin sizes in the radial

histogram were constructed so that the bin sizes were of constant width after conversion to the energy scale (i.e. decreasing width as R increases). Since the number of pixels at low R is small, this is not practical in this region, and so in practice a region of fixed radial increments remains at low R . The process involved keeping the radial histogram bin sizes, $\Delta(R)$, constant (Δ_{const} was typically set to one pixel) up to a critical radius R_c . When the radius exceeded R_c , the step size decreased by amounts of $\Delta(R) = (R_c/R) \times \Delta_{\text{const}}$ as the radius R increased. This meant that the number of data points in each bin was constant for radii above R_0 . The critical radius can be calculated from the user defined number of counts per bin at the plateau, C_{max} by the relation $R_c = C_{\text{max}} / (2\pi\Delta_{\text{const}})$. It was found that 100 data points per bin was sufficient for adequate signal to noise while retaining sufficient points over each peak in the energy spectrum. Once the binning was complete the bins were averaged (the intensity value in each bin divided by the number of pixels for that bin) resulting in a plot of average intensity versus the radius. We refer to this plot as the radial plot. It is used to calculate the population distributions and for fitting anisotropy values (see the next section).

To find the total radial distribution, $P(R)$, the intensity of the radial plots require integrating over all polar and azimuthal angles (i.e. over the entire spherical shell at radius R) to get the total number of ions or electrons at a radius R . Since the surface area of the shell is proportional to the square of the radius, the intensity values in the radial plot need multiplying by R^2 to give a radial population distribution. The radius scale was converted to energy units by calibrating with a known kinetic energy release and dividing the intensity values in the radial distribution by $\sqrt{E_{\text{kinetic}}}$. This adjustment factor is required to correct the probability distribution function when transforming from velocity space into energy space (the Jacobian for the transformation is $dv = \sqrt{1/(2mE)} dE$). Therefore the intensities in the radial plots, $F(R)$, require multiplication only by R to transform the radial plots into the energy space population distribution. Since the maximum energy released is governed by the known laser wavelength and known ionisation potential, the photoelectron images were used for

calibration. Photoelectron images were calibrated by setting the maximum of the highest energy peak to the excess energy in the ion prior to ionisation. After normalisation, so the integrated probability was equal to unity, the final energy distributions (eg. photoelectron spectra) were determined.

Since the radial plot, $F(R)$, is multiplied by R to obtain the final energy population distribution, $P(E)$, one may expect the noise in the distribution to increase with increasing energy. Although this is true for a two dimensional image having uniform noise covering the entire image, the ion and photoelectron images that we obtain have decreasing noise levels as the radial distance increases. This is attributed to increased signal towards the centre of the images resulting in greater statistical noise. After applying the inverse Abel transform, the radial plots, $F(R)$, appear to have decreasing noise as R is increased. Therefore, after multiplying $F(R)$ by R the noise level appears constant in the final energy distributions. If we had used a constant bin size in the histogram to determine the radial plots, then the energy distributions would have noise levels that decrease with increasing energy (at the expense of lower energy resolution).

4.3.4 Calculation of Energy Distributions - Isotropic Distributions

For isotropic distributions ($\beta=0$), such as those we observe in the van der Waals molecule dissociation work presented in chapter 6, a different approach can be used to calculate the energy spectrum. The approach, based on that used by Yoder *et al.* [Yoder 1999], does not involve taking the inverse Abel transform of the two dimensional image, but instead relies on producing a radial plot of the image and then applying the inverse Abel transform. Without going into a rigorous mathematical derivation, one can intuitively see that this is true by realising that an isotropic distribution removes the unique cylindrical axis. Thus the Abel transform can be performed with the cylindrical axis rotated at any angle in the x - y plane. This means

that the two dimensional projection must have circular symmetry about the origin. Since the projection can be calculated at any angle, a convenient choice is when $\theta = 90^\circ$ ($h = 0$), implying that $R' = R$ and $r' = r$. Thus the inverse Abel transform (equation 4.2) reduces to a one dimensional form

$$F(R) = -\frac{1}{\pi} \int_R^{\infty} \frac{G'(r)}{\sqrt{(r^2 - R^2)}} dr \quad 4.6$$

The function $G(r)$ is obtained by calculating the radial plot of the two dimensional image using the histogram technique described above (section 4.3.3). The inverse Abel transform can then be applied directly to this one dimensional function. Since the histogram process produces data having variable step sizes, it was necessary to use the modified inverse Abel transform algorithm described in section 4.3.1. An alternative approach to directly compute the inverse Abel transform is to fit the data to a functional form for which the inverse Abel transform is known, and then analytically determine the function $F(R)$. This is the approach taken by Yoder *et al.*, who fitted their $G(r)$ to a sum of Gaussians [Yoder 1999]. After calculating the transformed radial plot $F(R)$, the energy spectrum is calculated by multiplying intensities by R and converting radius to energy as described in the previous section.

4.3.5 Calculation of the Anisotropy Parameter β

As discussed earlier, ion and electron images contain information on the anisotropy of the process being measured. The anisotropy is usually reported as a value of β , as shown in equation 4.4. β values are generally calculated by plotting the average intensity of pixels on the population distribution image $F(R, \theta)$ as a function of the angle θ . We achieve this by calculating the angle of each pixel in the image, and adding

the intensity value to a histogram. The step size of the histogram was set to 2° wedges. The anisotropy parameter β was then determined by fitting the histogram using the function

$$F_\theta(\theta) = A \left[1 + \frac{\beta}{2} [3 \cos^2(\theta) - 1] \right] \quad 4.7$$

where A is a fitted parameter used to scale the function onto the data. For the photoelectron spectra we found it necessary to obtain values for β for different values of the electron energy. In this case $F_\theta(\theta)$ functions were obtained by including only pixels between selected values of R (i.e. between R_1 and R_2).

We have also found it useful to obtain β values in a totally different manner. By using the radial plots obtained during the calculation of the energy spectra (see section 4.3.3) and assuming functional forms for β , synthetic two dimensional images can be constructed, and fitted to the raw image. This procedure occurs via a number of steps. Firstly, a blank image is created onto which the synthetic image will be prepared. For each row in the synthetic image, the function $f(R', h)$ is calculated. This is done by multiplying the average radial intensity function ($F(R, \theta)$ averaged over θ) by $F_\theta(\theta)$ as calculated by equation 4.4. At this point it should be noted that β need not be constant with respect to the radius. For example, it is possible to use different β values for different peaks that are seen in the spectrum, or one can assume that β has a functional form that varies with the radius. Since we are using the average radial intensity function, and not the ‘true’ radial function $F_R(R)$, we need to divide our data by the factor $(1 + \beta/4) / 4$. This factor comes from the integration of equation 4.4 over all θ and ensures that the total population at each radius remains constant when β is varied. Finally, the $f(R', h)$ function is obtained by transforming the coordinate R into R' using simple geometry.

After computation of $f(R', h)$, the forward Abel transform was applied to obtain the projection onto the detector. Since the average radial intensity function that was used in the initially step did not have a constant interval in R , it was necessary to use the modified Abel transform algorithm described in section 4.3.1. The procedure was repeated for every height h to construct the full two dimensional projection.

After the synthetic image is calculated, it is compared to the original image by calculating the χ^2 value given by

$$\chi^2 = \sum_i \sum_j (f(i, j)_{\text{exp}} - f(i, j)_{\text{fit}})^2 \quad 4.8$$

where the summation occurs over all the (i, j) pixels on which the fitting is performed, $f(i, j)_{\text{exp}}$ is the intensity at the (i, j) pixel for the experimental image and $f(i, j)_{\text{fit}}$ is the corresponding intensity of the current fit. β values were adjusted until the minimum χ^2 value was found. In the first instance this was achieved using the Levenberg-Marquardt algorithm for non-linear least squares fitting [Press 1992]. When calculating β values using assumed functions for the change of β with energy (i.e. letting β vary with energy) it was found that the Levenberg-Marquardt algorithm failed because of problems associated with β being restricted to values within the -1 to +2 range. In these cases a Monte Carlo method was used to determine the lowest χ^2 value, and thus the best fitted parameters.

It is noted that no scaling parameter is needed to match the synthetic data onto the real image since the data used to create the synthetic image came directly from the raw image. During the testing stages an adjustable scaler was included as a check and it was found that within the fitting error it was always unity.

The above fitting procedure was tested by assuming an average radial intensity function containing many peaks of varying widths, and assuming that β varied linearly with the

radius (β range from -0.8 to +1.8). The two dimensional projection was constructed and acted as the raw image for the trial fit. Using the procedure outlined above and allowing β to vary linearly with the radius in the fit, the best fitted parameters were determined. The fitted values were found to be accurate to better than 1%. The only discrepancy arose from narrow peaks, where it was difficult to calculate an accurate derivative function needed for the inverse Abel transform.

This fitting technique is not limited to angular distributions having a $P_2(\cos\theta)$ distribution, but can be modified to include higher order Legendre polynomials. Such fits were performed for photoelectron images of benzene (1+1) REMPI, but it was found that inclusion of the $P_4(\cos\theta)$ term did not improve the fit. This shows that under the experimental conditions used in this study negligible alignment occurs in the intermediate state

4.4 Experimental Design

Figure 4.3 shows diagrammatically the entire experimental layout necessary for the collection of ion images. Basically, a pulsed nozzle was used to form a supersonic expansion in the main chamber creating vibrationally, rotationally and translationally cooled molecules. These molecules passed through a skimmer into the ionisation region of a time of flight mass spectrometer. A UV pulse from a frequency doubled dye laser ionised the molecules in the centre of the first acceleration region. The ions or electrons (depending on the mode of operation) were accelerated in a two stage acceleration region, and then travelled along a field free region. During the flight time, the molecules separate out in time according to their masses, and then finally strike a position sensitive detector. The detector, consisting of an ion/electron amplifier and a phosphorescent screen, was only activated when the species of interest arrived. The

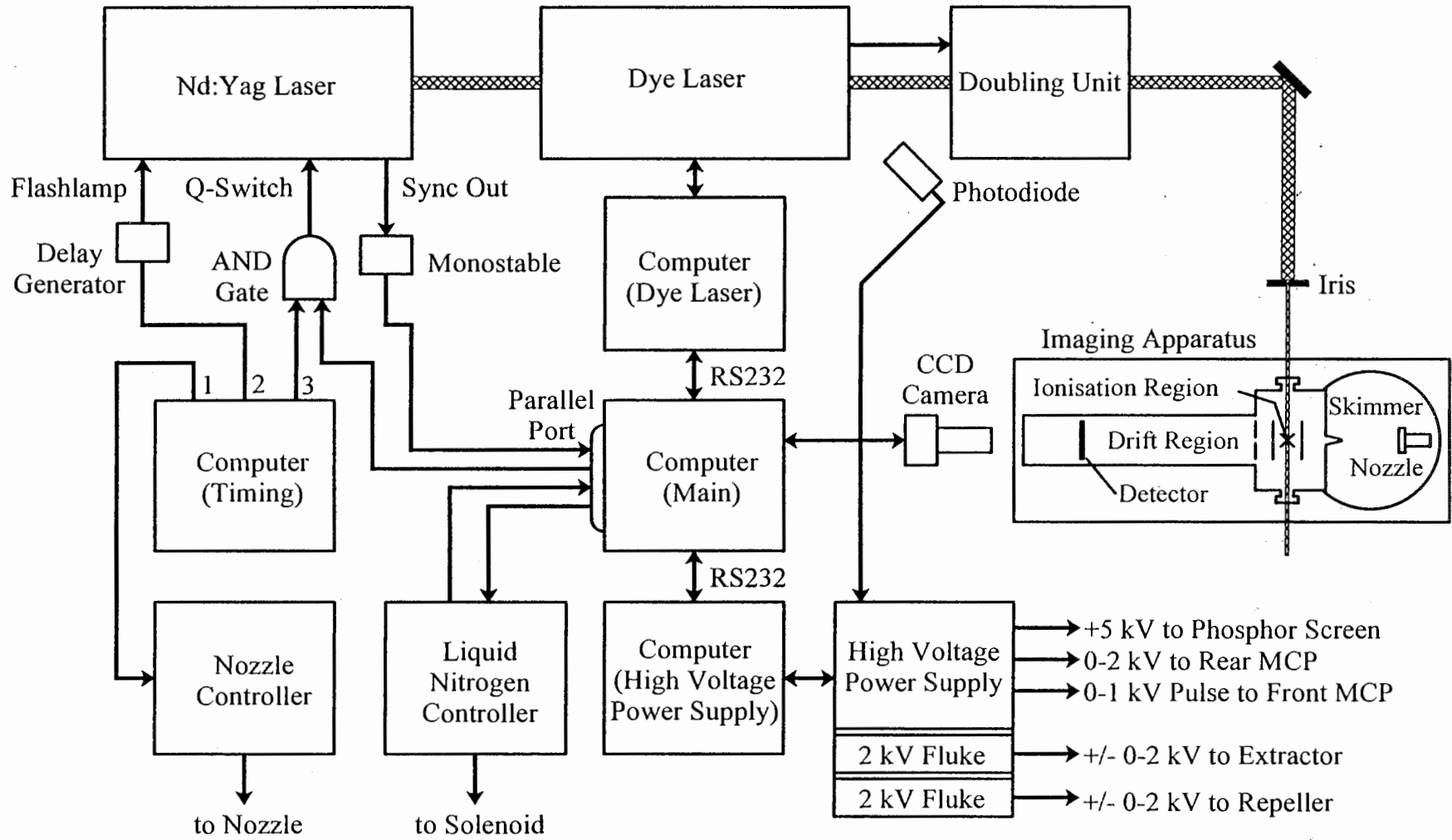


Figure 4.3 Overview of the experimental layout used for the collection of ion and electron images.

phosphor screen was viewed through a glass window using a cooled digital camera. Many images containing the positions of individual ions/electrons were collected and analysed to determine the two dimensional projection of the three dimensional dissociation or photoionisation event.

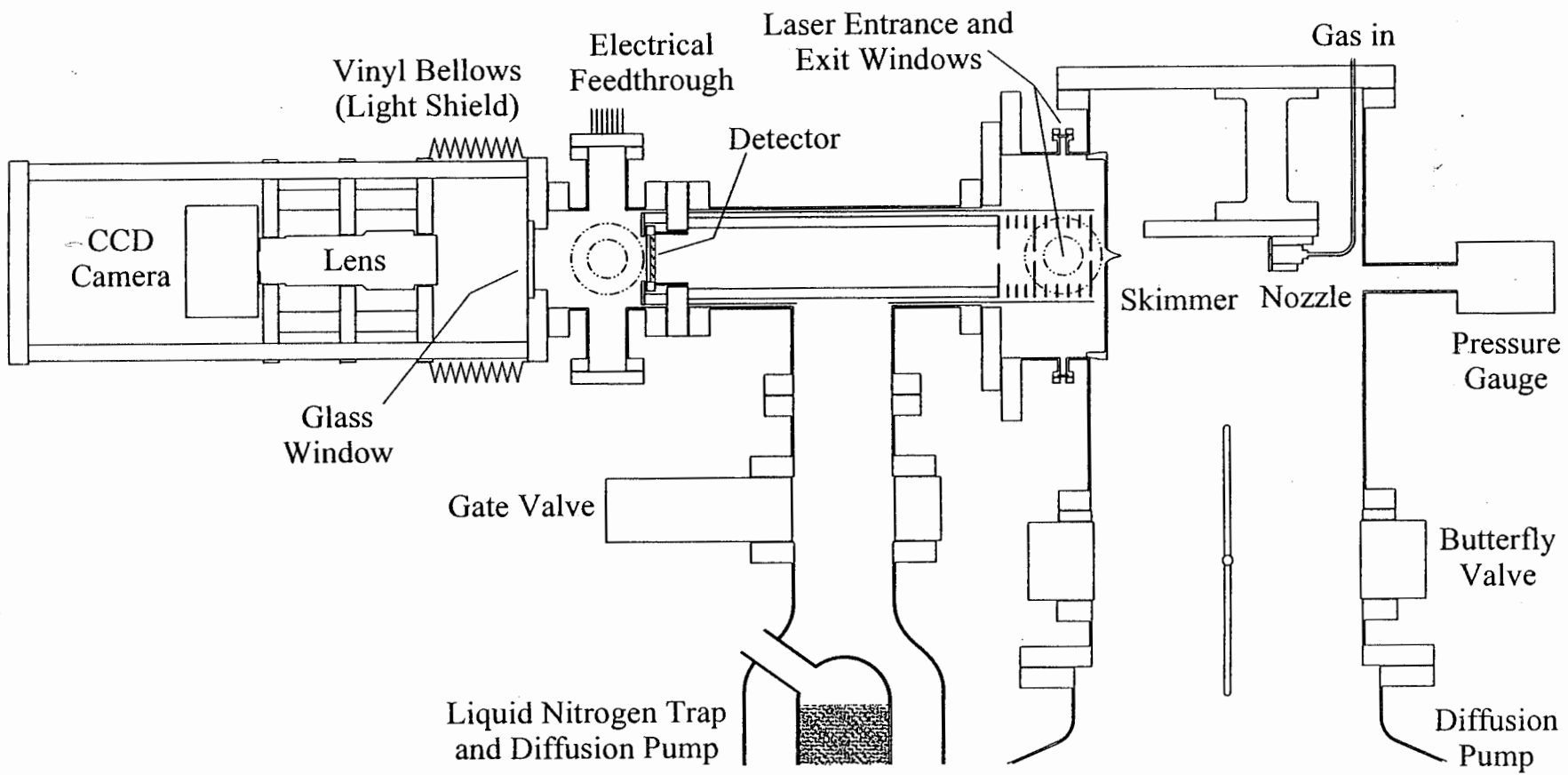
In the following sections, detailed information is given pertaining to each section of the experimental layout.

4.4.1 Vacuum Chamber Design

A scaled diagram showing the cross section through the entire apparatus is displayed in figure 4.4. The main constituents were a main vacuum chamber containing the nozzle assembly and a smaller vacuum chamber housing the actual time of flight instrument and detector. The two chambers were separated by a skimmer through which the molecular beam passed from the main chamber into the time of flight chamber. Separation of the chambers was necessary to keep the pressure inside the time of flight chamber low enough for detector operation, and to reduce the amount of residual gas present between nozzle pulses.

The main chamber was a stainless steel cylinder 270 mm in diameter and 269 mm tall with an aluminium top flange. A welded tee on one side held the skimmer assembly and contained two sets of laser entry and exit ports orthogonal to each other. A roughing port was also attached to the main chamber to allow initial evacuation of the chambers. Attached to the top flange were the nozzle assembly and gas and electrical feedthroughs. The pressure within the chamber was measured with a Penning gauge (Edwards AIM-S) connected to a home built gauge controller. Beneath the main chamber was a butterfly valve for isolation purposes and a ten inch diffusion pump (Torr Vacuum Products R-1020).

Figure 4.4 A cross section through the constructed ion imaging apparatus.



The smaller chamber was bolted to the tee of the main chamber and consisted of a 100 mm diameter tee piece and a six way cross, resulting in a total length of 525 mm. The entire time of flight assembly, including the detector, was mounted off a flange sandwiched between the tee piece and the cross. The acceleration region of the time of flight protruded into the welded tee of the main chamber so that the centre of the first acceleration region lined up with the laser entry and exit windows. The six way cross contained four small ports, three of which were used for delivering voltages to the time of flight and detector. The remaining port either had a Penning gauge (Edwards AIM-S) attached during testing or was left blank during experimental runs (see below). At the end of the chamber a glass window was located to view the images formed on the detector. This chamber was pumped from beneath through a gate valve, a liquid nitrogen trap equipped with a home built automatic filling system and a four inch diffusion pump (Dynavac F600).

The diffusion pumps for the two chambers were charged with synthetic diffusion pump oil (Santovac 5) and their outlets attached to a 38 mm diameter vacuum manifold which was pumped by two rotary backing pumps (Varian SD700). Differential pumping conditions were tested under pulsing conditions using Penning vacuum gauges connected to both chambers.

Once the pumping system had been characterised, the gauge in the time of flight chamber was removed before imaging studies commenced. This was necessary since the large permanent magnet in the Penning gauge was found to greatly distort the flight path for electrons. After several days of pumping the main chamber and time of flight chambers were typically evacuated to base pressures of 5×10^{-7} torr and 8×10^{-8} torr respectively. Under pulsing conditions the pressures in the main and time of flight chambers were typically 3×10^{-5} and 1×10^{-6} torr respectively.

4.4.2 *Design of the Time of Flight spectrometer for Ion Imaging*

The imaging apparatus described here utilises the velocity map imaging technique developed by Eppink and Parker [Eppink 1997] and discussed above (section 4.2.2). It was also desirable to design the instrument such that it could quickly be modified to record standard mass spectra with high mass resolution. To reduce costs, the vacuum chamber was constructed largely using components from several decommissioned apparatus. This placed a further constraint on the final design of the imaging apparatus.

The design process relied heavily on the use of computer simulation of ion and electron trajectories in electric fields. The commercial software package SIMION was used, allowing all aspects of the design to be thoroughly tested [Dahl 1995]. The inbuilt programming language in this package enabled software to be written to model our specific requirements, allowing the automated determination of the best parameters for ion imaging subject to certain constraints.

The time of flight mass spectrometer was designed around a standard Wiley-McLaren type spectrometer having two accelerating regions and a drift region [Wiley 1955]. Ions are created in the centre of two plates termed the repeller and the extractor, so named because the voltages are applied such that the ions are accelerated away from the repeller towards the extractor plate. After the ions pass through the extractor, they are further accelerated toward a field free region where ions separate into their different masses. The process of mass separation is simply due to the greater accelerations that lighter masses undergo in the acceleration region, resulting in these masses arriving at the detector first. Wiley-McLaren were to first to show that by choosing appropriate voltages, ions starting at different positions along the time of flight axis arrived (to a first order approximation) at the detector at the same time. Although ions which form closer to the detector enter the field free region first, the ions formed further away spend more time in the electric field and are consequently accelerated slightly more. There

exists a location in the drift tube, termed the space focus, where the faster ions will "catch up" to the slow ions. An ion detector is usually placed at the space focus allowing the recording of greatly improved mass resolved spectra.

In a review by Boesl *et al.* they show that for certain combination of distances and accelerating voltages one can improve the standard (first order) mass focussing of Wiley-McLaren spectrometers to give a second order space focus [Boesl 1992]. This review also discusses the resolution problems encountered in time of flight mass spectrometry. For small time of flight mass spectrometers second order space focusing becomes useful since the short flight times do not allow much time for adjacent masses to separate out. Thus second order space focussing can have a dramatic effect on the mass resolution of small spectrometers. We have designed our electrode arrangement around this second order space focusing concept to allow the best resolution possible in standard (non-imaging) time of flight operations.

As eluded to above, the total length of the mass spectrometer was constrained by the vacuum equipment that was available for use. Using ion simulations, many different configurations were tested and the final design with dimensions is shown in figure 4.5. The simulations suggested that the actual dimensions of the ionisation regions are not critical, so long as the second order space focussing formula for the distances [Boesl 1992] was adhered to. To provide uniform electric fields within the two acceleration stages, rings were added between the repeller, extractor and ground plates. High ohmic resistors joined the plates and rings to form a voltage divider, allowing the voltages on the repeller and extractor plates to be varied independently while always keeping a uniform electric field. For initial testing and characterisation, high transmission metallic mesh was glued over the holes using electrically conducting paint, thus eliminating any lensing effect caused by the holes. For subsequent ion imaging work this mesh was removed so the holes could form lenses, allowing the technique of velocity map imaging to be used. The field free drift region was surrounded by a layer

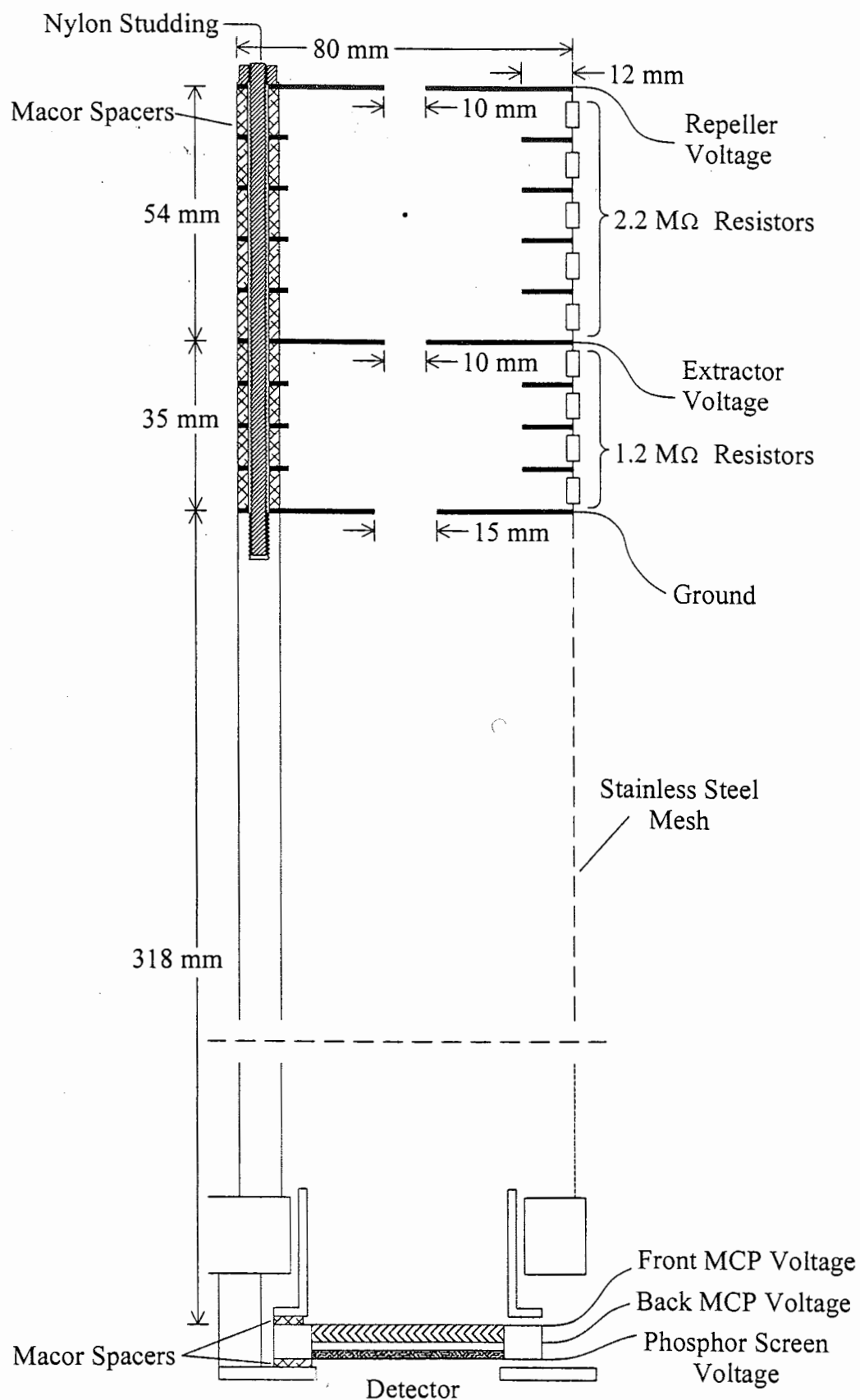


Figure 4.5 Diagram, including dimensions, of the time of flight mass spectrometer developed for ion imaging studies.

of fine stainless steel mesh to prevent any undesired external electric fields from penetrating into this region.

Although initially the time of flight apparatus was designed for the detection of ions, we found in later applications that it was desirable to record laser induced photoelectron spectra to determine vibrational distributions following ionisation. Eppink and Parker have shown that an apparatus designed for ion imaging will also work as an electron imaging device [Eppink 1997]. However, since electrons are much more susceptible to the influence of stray magnetic fields than are ions, it is necessary to shield the time of flight tube from magnetic fields. For this reason the entire time of flight tube was surrounded with magnetic shielding (Co-Netic, Magnetic Shield Corporation) (this was done inside the vacuum chamber with holes for the laser entry and exit). We found it necessary to also cover the outside of the time of flight vacuum chamber with Co-Netic shielding to further reduce the influence of magnetic fields. These two layers of shielding were found to be adequate for our purposes, so no attempt was made to nullify magnetic fields with the use of Helmholtz coils.

Computer simulations suggest that operating the spectrometer in standard mode (with mesh between accelerating regions) with a molecular beam (all molecules having the same velocity) will result in mass resolution which is limited by the pulse width of the laser. That is, since the laser has a finite width (~ 5 ns in our case) this will be convoluted with the true mass spectrum resulting in broader mass peaks and consequently lower mass resolution. This is indeed what we observed experimentally. When the spectrometer is operated in the imaging mode (no mesh covering the holes between acceleration regions), simulations suggest the mass resolution will be degraded slightly. For example, assuming a 1 mm wide laser beam the simulations show that the time of flight spectrum will have a width of ~ 3 ns for the benzene mass. This, however, is still less than the pulse width of our laser.

The biggest influence on the mass resolution, in both standard and imaging modes, is the presence of molecules having velocities parallel to the time of flight tube. For example, we can consider two ions that are formed at the same time with the same speed, but one is heading towards the detector while the other is moving away from it. The ion moving away from the detector is decelerated by the electric field, and then accelerated back towards the detector. After a time termed the 'turn around time' this ion will return back to its starting location having the same speed that it started out with, but now travelling towards the detector. During the turn around time, the ion initially moving towards the detector has already travelled some distance in the acceleration region. Consequently this ion will hit the detector first, followed by lagging ion separated in time by the turn around time. In our experiments the molecular beam is already travelling in the direction of the detector, so this effect is superimposed on top of the beam velocity. From simulations, it appears that ions having different initial velocities quantitatively affects the mass resolution of both the standard and ion imaging modes of operation in the same way.

For the experiments described in this thesis, we are observing recoil velocities from both ions and electrons. Consequently we need to take into consideration backward and forward recoils when determining the times at which our detector needs to be operational (see next section). For the case of detecting ions, this means that the detector is not only active when the species of interest arrives, but also over a small range of nearby masses. Fortunately, this is not a problem in the series of experiments presented here since other background ions are sufficiently different in mass.

4.4.3 *Ion and Electron Detectors*

Two different detectors were used with this time of flight mass spectrometer. To initially characterise the system, and to record high mass resolution spectra, a

microsphere plate detector (El-Mul EO25A) was used. A grounded mesh was placed approximately one millimetre above the front surface of the detector. The front detector surface was held at negative high voltage (up to -2.1 kV) so the ions would pass through the grounded grid and then accelerate rapidly into the detector, increasing the detector efficiency. After striking the active surface of the detector, electrons are ejected from the surface. Approximately -100 V was applied to the back of the detector which causes the collisionally ejected electrons to accelerate towards the back of the detector. The passage of the electron through the detector leads to a cascade of further electrons. In this manner, the input ion produces a current pulse at the back face of the detector. An anode at the back of the detector held near zero volts collects the electrons from the amplification process. The anode was terminated with a $50\ \Omega$ resistor as close as possible to the anode. The signal was carried via $50\ \Omega$ coaxial cable inside the chamber, through a $50\ \Omega$ SMA feedthrough and finally via coaxial cable to the oscilloscope. This eliminated most of the impedance mismatching responsible for the ringing problems associated with fast pulses.

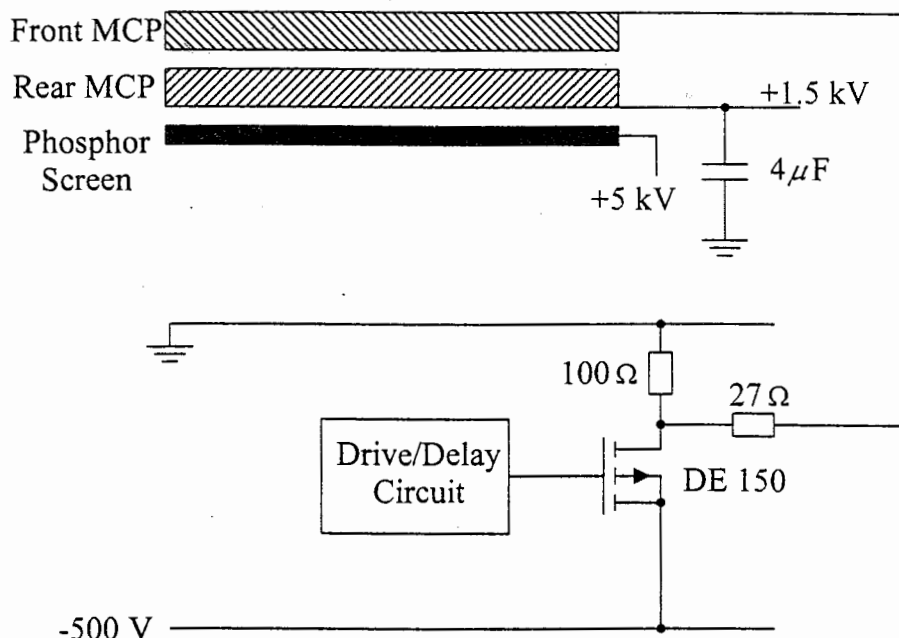
The ion imaging studies require the use of a position sensitive detector. A commercial device incorporating two microchannel plates placed in a chevron configuration followed by a phosphor screen (Galilio 3040-PS) was used. The operation of this detector is very similar to that described above for the microsphere plates. The notable differences are 1) that no mesh grid is placed in front of the detector, and 2) when the ejected electrons reach the back of the detector, they are accelerated onto the phosphor screen. On the reverse side of the phosphor screen a flash of light is seen when the ejected electrons hit the phosphor. Thus, by using a camera one can record the positions of these flashes, which give the positions at which the ions struck the detector.

Since we are only interested in one mass and need to avoid interference from other masses, the detector is only turned on when ions of the desired mass arrive. Because the amplification in the microchannel plates increases very rapidly with the applied

voltage, they effectively only give signal above 1.5 kV potential difference across the chevron pair. Thus the detector can be set at \sim 1.5 kV continuously and pulsed for short times to (typically) 2 kV to detect the ions of interest. This way a pulse of only 500 V is required to turn the detector “on”. The mass selection thus works by having the voltage applied to the detector deliberately kept below its working level, leaving the detector non-functioning. As the species of interest is about to hit the detector, a short voltage pulse is applied which allows the detector to become operational for only long enough to view the desired masses. In this way the images appearing on the phosphor screen only originate from that mass. The voltage schemes used for positive ion and electron imaging are shown in figure 4.6.

To detect positive ions, the back of the detector is held constant at +1.5 kV and the front is first grounded. As the mass of interest appears, the front of the detector is pulsed to -500 V. This pulse has two purposes. Firstly, it creates the 2 kV drop across the detector required to make it operational. Secondly, it accelerates the ion so that it hits the detector with increased kinetic energy. Since the efficiency of the detector increases with the ion’s translation energy, more intense phosphorescent images result with this configuration than if we used the alternative arrangement of pulsing the back of the detector up to 2 kV. The pulsing was controlled by a home built (Flinders University, School of Chemistry, Physics and Earth Sciences Electronics Workshop) high speed, high voltage pulsing unit based on a high speed, high voltage field effect transistor (FET) (DE-150, Directed Energy Inc). To achieve fast rise and fall times and a clean pulse shape the -500 V was pulsed across a $100\ \Omega$ terminating load and into a $27\ \Omega$ inline resistor and subsequently down a $50\ \Omega$ coaxial cable to the detector. This setup is schematically shown in figure 4.6. While operating without the detector attached, the pulsing unit was capable of producing pulses having a fall time (turn on time) of 6-7 ns and a rise time (turn off time) of \sim 40 ns. Since the detector has a non-negligible capacitance, pulsing with the detector attached results in the fall time increasing to \sim 40 ns and the rise time to \sim 90 ns. Pulse widths were typically around 300 ns, so no

a)



b)

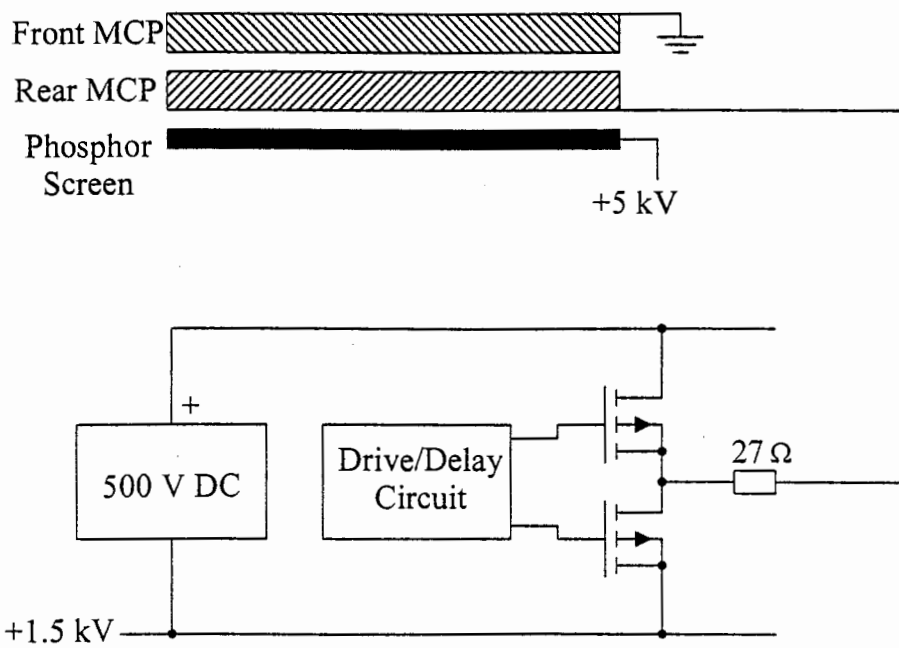


Figure 4.6 Voltage schemes for the detection of a) positive ions and b) electrons.

problems with power dissipation within the FET or across the terminating resistor were observed.

The detection of photoelectrons requires the front of the detector to remain at ground potential and the back to be pulsed. The back is kept at +1.5 kV until the photoelectrons arrive, at which time it is pulsed up to +2 kV, thus activating the detector. Electrons are detected much more efficiently than ions so the extra energy given to positive ions before hitting the detector in positive ion mode is not required here. Since all photoelectrons arrive at the same time, the rise and fall times of the pulse are not critical. Consequently the pulse was supplied by a home built pulsing unit (Flinders University, School of Chemistry, Physics and Earth Sciences Electronics Workshop) using standard high voltage FETs with rise and fall times of approximately 200 ns.

4.4.4 High Voltage Power Supplies

The high voltage supplies and pulses required for the phosphor screen detector were provided by a series of home built (Flinders University, School of Chemistry, Physics and Earth Sciences Electronics workshop) high voltage power supplies housed in a single box. The unit comprised a +7 kV power supply for the phosphor screen, a +2 kV supply for the back of the detector, and a -1 kV supply for pulsing the front of the detector.

The voltages were controlled and manipulated by a dedicated computer (386 clone) through two data acquisition cards using software written by the author. Analogue voltages from the computer were used to provide a reference to the power supplies, and the high voltage value (scaled) was read back into the computer which provided active feedback to maintain the desired voltage. The feedback program constantly adjusts the

reference voltage until the real high voltage value is the same as the desired value. This eliminates voltage drift as the ambient temperature varies.

The pulse delay and width applied to the detector to achieve gating about the desired mass gate was also controlled from the high voltage power supply computer by digitally entering the values into the pulse generator's circuitry. Course and fine delay generators were used within the pulsing unit which gave an overall jitter of approximately one nanosecond. During initial testing it was found that an undesired effect of pulsing the front of the detector was capacitive coupling with the back of the detector, causing the back voltage to drop by a similar amount to that being pulsed. To prevent this, a large value, high voltage capacitor ($4 \mu\text{F}$) was placed across the power supply for the back of the detector. The initial trigger for starting the delay count came from a photodiode monitoring the dye laser output.

In electron mode, pulsing the back of the detector may increase the voltage on the phosphor screen by a similar amount (as seen in the positive ion case), but this was not of concern since the only effect it would have is to slightly increase the amount of phosphorescence. No delay generators were necessary in the pulse generator used for electron imaging since the photoelectrons arrive within 50 ns after the laser pulse. The trigger to initiate the pulse was taken directly from the laser trigger.

Measuring photoelectron spectra requires the polarity of the voltages in the acceleration region to be reversed. Two commercial power supplies (Fluke 415B) were used for this purpose. The internal design of the Fluke power supplies is such that when changing between positive and negative polarity, only the zero reference changes, not the actual voltage difference. This means that when the polarity is changed the absolute value of the accelerating voltages remains the same. This provides security when using photoelectron images to calibrate the energy scale of positive ion images.

4.4.5 Supersonic expansion

Gas mixtures of 1% benzene (BDH 99.7%, freeze-pumped-thawed) in argon (BOC 99.997%) were prepared in a six litre stainless steel pressure vessel to a total pressure of approximately 600 kPa. The output was regulated to the desired backing pressure as measured by a bourdon gauge. For the van der Waals molecule dissociation experiments the pressure was set to 500 kPa to ensure an adequate number of clusters were produced. For electron imaging experiments the backing pressure was reduced to about 300 kPa. The delivery line passed into the chamber through gas fittings located on the top flange of the main chamber and continued on to the nozzle.

The pulsed nozzle (General Valve, 0.8mm orifice) was attached to a stage which was mounted to the top flange of the main chamber. The stage allowed the position of the nozzle to be moved along the entire length in 10 mm increments. The molecular beam passed through a skimmer (Beam Dynamics 1.5 mm) into the ionisation region of the time of flight mass spectrometer. For the experiments described in this thesis, the nozzle was placed to give a nozzle to skimmer distance of 145 mm. The distance between the nozzle and interaction region is 200 mm. The nozzle solenoid was driven from a home built pulsed nozzle driver (Flinders University, School of Chemistry, Physics and Earth Sciences Electronics Workshop) which delivered 300 V, 200 μ s square pulses. The electrical connections were made through feedthroughs attached to the top flange of the main chamber. Mounting the complete nozzle assembly on the top flange made maintenance of the nozzle and adjusting the nozzle's position a straight forward task.

4.4.6 *Laser System*

The 355nm output of a pulsed Nd:YAG laser (Continuum Surelite II) was used to pump a dye laser (Lambda Physik Scanmate 2E) fitted with a doubling unit utilising a BBO doubling crystal, compensating crystal and four Pellin-Broca prisms. The laser system thus delivers a tunable UV output without any change of beam position while changing wavelengths. This becomes critical for calibration purposes since it was found that the imaging technique was sensitive to the beam position in the ionisation region. A 10% beam splitter was placed between the dye laser and the doubling unit when the wavelength was to be measured. This allowed a small amount of laser light to be directed into the entrance aperture of a pulsed wavemeter (Burleigh WA-4500). The UV light was directed through a 1 mm iris and passed unfocussed through the chamber's UV grade fused silica windows. The polarisation of the beam was set parallel to the detector face. Laser powers were kept low to reduce Coulombic repulsion or space charge effects. Low power was also necessary for the success of ion counting (see section 4.4.8).

4.4.7 *Camera System*

Images of the phosphor screen were directly viewed through a glass window on the end of the time-of-flight chamber using a video zoom lens (Navitar Zoom 7000) and captured on a charge coupled device (CCD) camera (Spectrasource Teleris 2). The CCD chip (Kodak 0400 with Lumogen coating) comprised a 784×520 pixel array. The camera and lens assembly was mounted off the end flange using four aluminium rods on which it could be moved to achieve the lens to detector distance required for the magnification appropriate to the experiment being performed. To exclude outside light

from entering the camera, vinyl bellows encased the region between the camera lens and the end vacuum flange.

4.4.8 *Ion Counting Algorithm*

Data are collected by measuring the position of ions or electrons as they hit the detector and, over a number of laser shots, an image of where the ions land is built up. The original way of achieving this was to leave the camera shutter open and integrate the image for many laser shots [Chandler 1989]. Recently, however, the technique of ion counting has been introduced, firstly by Rogers *et al.* [Rogers 1996], but subsequently reported independently and discussed in considerably more detail by Chang *et al.* [Chang 1998]. Ion counting relies on taking a single image and determining the positions where individual ions landed. This information is added to a two dimensional histogram describing the number of ions that landed at each pixel in the image. This process is repeated many times until enough ions are counted to form an acceptable histogram image. A significant improvement in resolution is observed when using ion counting techniques [Chang 1998] because the large area of each ion in an image is effectively reduced to a single point (the central point of the spot produced by the ion).

We have used ion counting in our experiments. Typically an image is accumulated on the CCD camera for 5 laser shots. This image is downloaded to the controlling computer which then processes the image to determine the location of the ions and update the two dimensional histogram of counts versus pixel position. Unfortunately the download time of an image (400 ms) prevented this process being performed on a shot-by-shot basis.

The algorithm used by Chang *et al.* to determine each ion's location assumed that an ion event occurred where a pixel above a certain threshold is taller than its four nearest

neighbours [Chang 1998]. We use a different algorithm where each spot is found and rastered across to find the pixel with the maximum intensity. We define a spot to be a grouping of pixels that all have intensities greater than a pre-determined threshold. The most intense pixel in the spot is deemed to be the ion's location. To improve the analysis speed of large images, the software to search for pixels above the threshold was written in 32 bit assembly language (Intel 0x86). The threshold searching code consisted of only six instructions, each taking one clock cycle of the processor. Once a threshold pixel was found, highly optimised C⁺⁺ code was used to raster over the spot to determine the most intense pixel. An average image (784 x 520) pixels typically took 8-9 μ s to scan and detect the maxima of several ion spots.

A somewhat unfortunate problem with the experiments that we perform is that a significant number of the ions or electrons have low kinetic energy releases. This means that there is a build up of ions near the centre of the image, and if too many ions/electrons are present per image they may potentially overlap with each other causing inaccuracies with the ion counting method. This is a known problem with ion counting routines and has been dubbed spatial congestion by Chang *et al.* [Chang 1998]. To prevent spatial congestion, the laser power was reduced until the signal levels were such that ions appeared as single non-overlapping spots and could be counted correctly. It was important to check that this condition was fulfilled when preparing for an experimental run.

4.4.9 Timing System

The timing of events during an experiment was controlled from a computer equipped with a counter/timer card. Five volt pulses of 10 μ s duration and 10 Hz frequency were produced by the card with delay times adjustable in 10 μ s steps. The timing cycle starts with a pulse to trigger the home built pulsed nozzle driver. After a slight internal delay,

the nozzle driver delivers a 300 V pulse to the nozzle. Approximately 350 μ s before the molecular beam reaches the ionisation region, the flashlamp of the Nd:YAG laser is fired. The Q-switch of the Nd:YAG laser is triggered when the desired part of the molecular beam pulse is in the intersection region. Laser power was adjusted by varying the flashlamp delay either coarsely using the computer timing card, or by using a delay generator to interpolate between the 10 μ s step size. This way, the flashlamp to Q-switch time is varied, allowing the laser power to be altered, without disturbing the delay between nozzle opening and the laser firing.

During initial data collection, the camera was used in a standard operating mode where the electromechanical shutter was opened during collection of an image and closed while downloading the image. As we have discussed in the previous section, each complete image was constructed as a sum of individual images obtained using a few laser shots so that ion counting techniques could be used. This meant that the shutter was opened and closed more than once per second during data acquisition. As a consequence of the high usage of the shutter, after several months of use the shutter operated only intermittently. The high cost and long down time associated with having the unit shipped overseas for repair and the fact that this would be an ongoing problem led us to seek an alternative arrangement for data acquisition.

The operation of the readout of the CCD chip is such that the image becomes distorted if the CCD is exposed to light while an image is being read. The light generated by the arrival of ions during readout is enough to distort the images, as shown in figure 4.7. To overcome the problem, the shutter was left open during both data acquisition and download, and the laser was only fired when the camera was collecting an image. This was achieved by allowing the Q-switch to only fire while taking an image, while leaving the flashlamp firing at 10 Hz to maintain the correct thermal load on the laser cavity. This process was controlled through the computer program responsible for data

acquisition since this allowed precise determination of when the laser needed to be switched on and off.

4.4.10 Data Collection and Analysis System

The entire data collection process was controlled from a central computer (Pentium II). This computer needed to 1) communicate with the dye laser computer to facilitate scanning of wavelengths, 2) communicate with the computer controlling the high voltage power supply, 3) instruct the Nd:YAG laser to fire when collecting data, 4) monitor the firing of the laser in case of (frequent) malfunction, 5) pause the data collection while the liquid nitrogen filling system requests to fill (the electrical noise

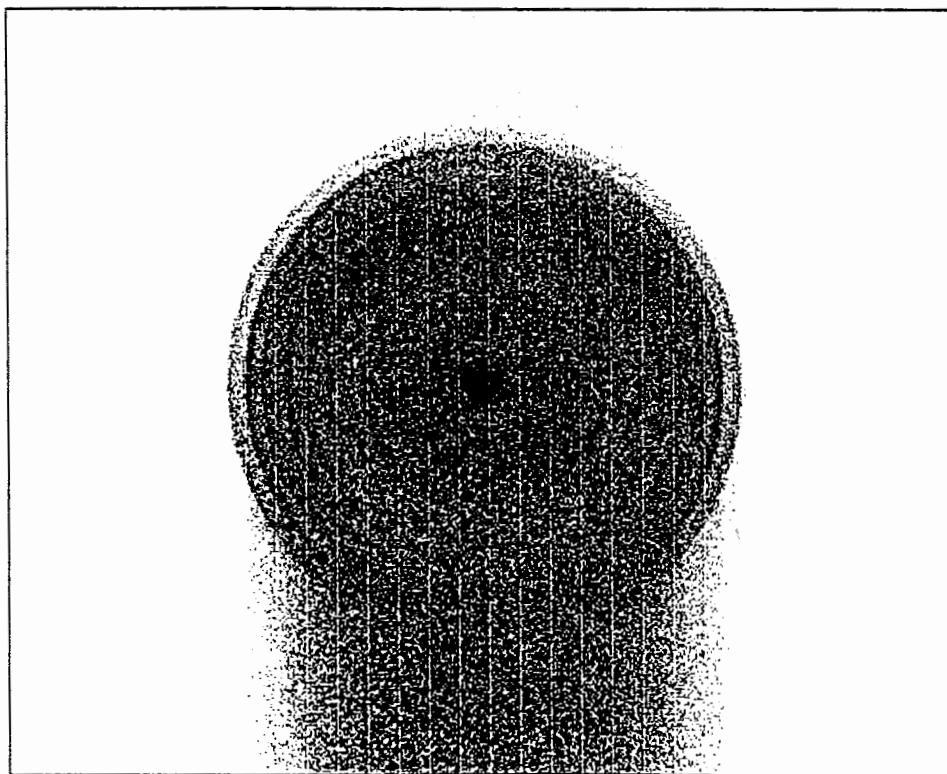


Figure 4.7 Photoelectron image collected with the CCD camera shutter left open. Note the distortion due to the appearance of ions as the image is read out.

generated during the switching of solenoids caused noise spikes in the images), 6) operate and transfer images from the CCD camera, and finally 7) process the downloaded image.

The program to control these processes was written by the author using the C⁺⁺ programming language (Borland C⁺⁺ 4.5; Borland C⁺⁺ Builder 3) to operate under the Windows 95/98 operating system. The software was written to take advantage of the multitasking environment of the operating system. This allowed data collection and data analysis to be performed simultaneously as discussed below.

The supplied dynamic link library (DLL) software for the controlling the CCD camera did not support overlapped operations, that is, collection and downloading of the image could not run as a background task whilst allowing the main program to continue. To overcome this limitation in data collection efficiency, we encapsulated all camera controlling software into a C⁺⁺ class allowing camera functions to run in a separate thread (task). This allowed new images to be integrated on the CCD chip whilst, in parallel, the time consuming procedure of refreshing large images on the computer screen can occur. Another feature of multitasking is that the user may continuously interact with the data collection software. This, for example, allows the user to vary viewing parameters at any time to enhance data visualisation and interpretation. Since our camera has a relatively slow download speed, there is not a significant advantage in processing an image in parallel with downloading the next image. Consequently we process images after they are downloaded and prior to collection of the next image. We, however, anticipate purchasing a camera with a much faster download rate, which would allow us to record images on a single shot basis. This would require the data processing to be conducted in parallel, which would be an easily implemented alteration to our existing software. Parallel processing for image collection has also been discussed by Chang *et al.* [Chang 1998]. At the completion of collecting the desired number of images, the final histogrammed image was saved for future analysis.

The images were saved in Flexible Image Transfer System (FITS) format [NOST 1995]. This was the file format used by the camera manufacturers with their proprietary camera controlling software, and we have also adopted it. The FITS format offers a number of distinct advantages. The main advantage is that data can be stored as either 8 bit integer, 16 bit integer, 32 bit integer, 32 bit real (single precision floating point) or 64 bit (double precision floating point) data. This was very useful since the camera values returned from the camera are 16 bit integer in nature, yet floating point numbers are beneficial for subsequent analysis. Another advantage is that the structure of the FITS file consists of a text header of arbitrary length. This header not only contains data relating to the size of the image, the number of dimensions, and type of data stored in it, but also allows the addition of user defined text. This can be used to record information pertaining to the image, such as the experimental conditions used when recording the image, or to keep a history of operations that were performed on the image.

A C⁺⁺ class was written to encapsulate the use of FITS file formats. The class allowed the manipulation of up to 999 dimensions (the maximum allowable in the FITS file format [NOST 1995]). Of course only two dimensions are required for storing the recorded images, but three dimensional data was also used to produce full three dimensional visualisations of the dissociation processes. The class was constructed such that the end user could easily produce *n*-dimensional images and access or store data within the image in a way that was similar to using arrays. The user does not need to know *a priori* the type of data contained in the image. A second C⁺⁺ class was written encapsulating the first class, and also routines specific to the operating system which allowed the conversion to, and displaying of coloured bitmaps, representing the two dimensional FITS file.

A general program was written to allow the ion images to be manipulated and analysed. This program included two dimensional non-linear least squares fitting of functions to

the image, calculating radial and angular plots from the image (as discussed above in sections 4.3.3 and 4.3.4), forward and reverse Abel transforms, fitting of anisotropy parameters, and many other useful tools. A screen shot of this software is shown in figure 4.8. The bitmap images produced by this program were able to be transferred to image processing software (PaintShop 5) for colour printing.

4.5 Discussion

4.5.1 *The Velocity Mapping Technique*

The best way to show the benefits of velocity map imaging is to compare images resulting from the old ion imaging technique and the new technique. Figure 4.9 shows an ion image from both techniques under similar experimental conditions. They were created by resonantly ionising benzene through the 6^1 vibronic level. In figure 4.9a (old method containing metallic grids), a line across the detector is observed. This line is produced by the intersection of the laser beam with the molecular beam and is a direct projection of this intersection region onto the detector. The line is also seen to contain bright and dark regions in a regular pattern. This is attributed to a shadow effect caused by the two metallic meshes placed in the acceleration region to ensure the constant electric field. Thus we can immediately see that the presence of grids in the acceleration regions distorts the image considerably.

Figure 4.9b shows the same system as figure 4.9a except that the grids have been removed, and the voltages adjusted to the optimal values for velocity map imaging. To achieve the optimal values we kept the repeller voltage fixed and varied the extractor voltage until a circular image is obtained. The image measured now represents the

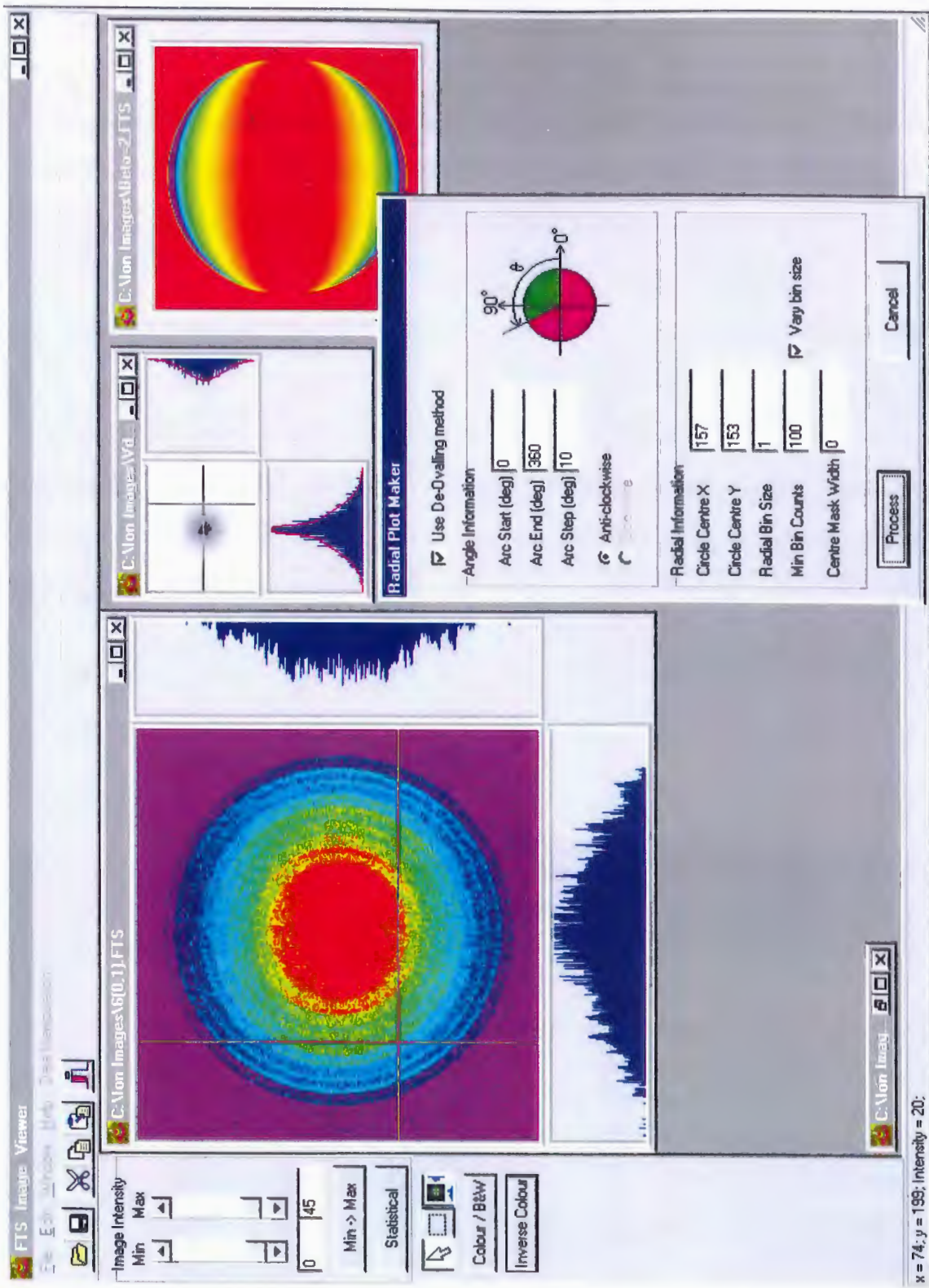


Figure 4.8 Screen capture of the software written to analyse the ion and electron images.

spread of molecular velocities in the molecular beam. It was found experimentally that the optimum extractor voltage were very close to those determined from ion trajectory simulations (± 5 V). As is clearly shown in the figure, the image is no longer a line, but instead a circular spot. The circular appearance was found to be constant over a ± 2 V volt range when 1400 V was applied to the repeller and 880 V applied to the extractor. Approaching this voltage range from the value used in standard operation, a horizontal line across the detector shrunk, becoming a horizontal oval, and finally becoming a circle at the optimum voltage. As the voltage is adjusted past the optimum, the spot again becomes a horizontal oval and eventually a horizontal line is again produced. This makes it straightforward to select the optimum value when setting the instrument for velocity map imaging. The lack of grids also ensures that all of the ions reach the detector so no shadows are produced.

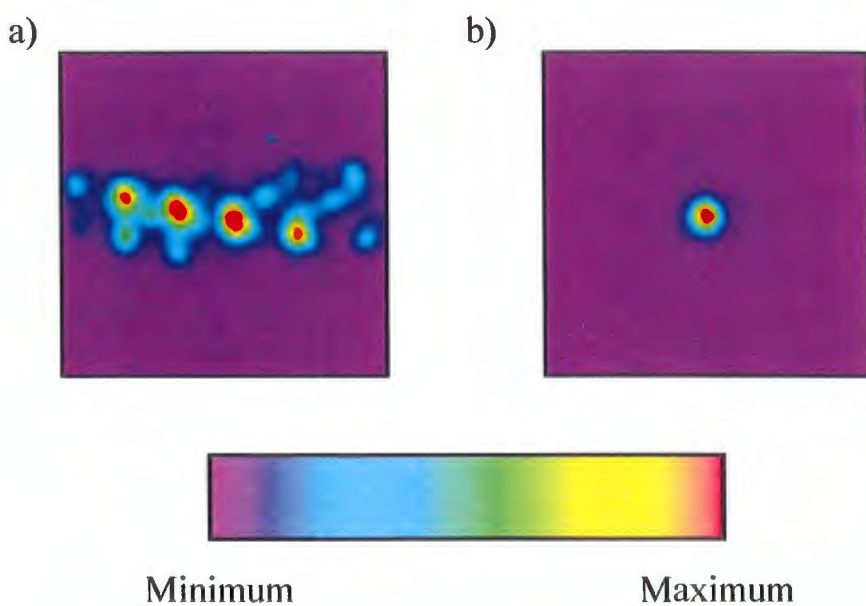


Figure 4.9 Images of cold benzene taken under similar experimental conditions. Image a) was produced with the standard method of ion imaging (i.e. using mesh grids in the time of flight electrodes, while image (b) was produced using the velocity mapping technique (mesh removed and extractor voltage adjusted to optimise ion focussing).

4.5.2 Circularising distorted photoelectron images.

Although our imaging apparatus was originally designed for observing positive ions, we have also successfully observed, with minor modifications to shield the time of flight tube from stray magnetic fields and to alter the detector voltages (see sections 4.4.2 and 4.4.3), the energies and direction of photoejected electrons from ionising benzene. The images obtained for photoelectrons exhibited non-circularity. Non-circular photoelectron images have been noted by previous authors [Parker 1997]. In this section we discuss a technique we have developed to circularise such distorted images.

The photoelectron imaging experiments were performed on benzene using REMPI. After resonantly ionising benzene through a S_1 vibrational state, the resulting ion is left in a number of vibrational states [Long 1983]. Since the total amount of energy available to the ion is constant (governed by the laser wavelength), the excess energy has to be taken away by the ejected electron, resulting in an energy distribution which is highly structured. As an example, an experimental image of the photoelectron distribution formed by ionising benzene through the 6_0^1 resonant transition is shown in figure 4.10.

At first glance, the rings on figure 4.10 appear circular. On closer inspection, however, it can be seen that the rings comprising the image are not quite circular, being distorted slightly into a slanted oval shape (for the outside ring the short radius is 2 pixels smaller than the large radius). This oval shape is produced because of the effect stray magnetic fields have on the photoelectron's trajectory. To determine the photoelectron spectrum the inverse Abel transform is performed and the resulting image converted to a plot of the intensity versus radius by integrating the intensity around the circle at fixed values of the radius (see section 4.3.2 and 4.3.3). Since the image is not perfectly circular, the subsequent photoelectron spectrum would result in the peaks having a width larger than

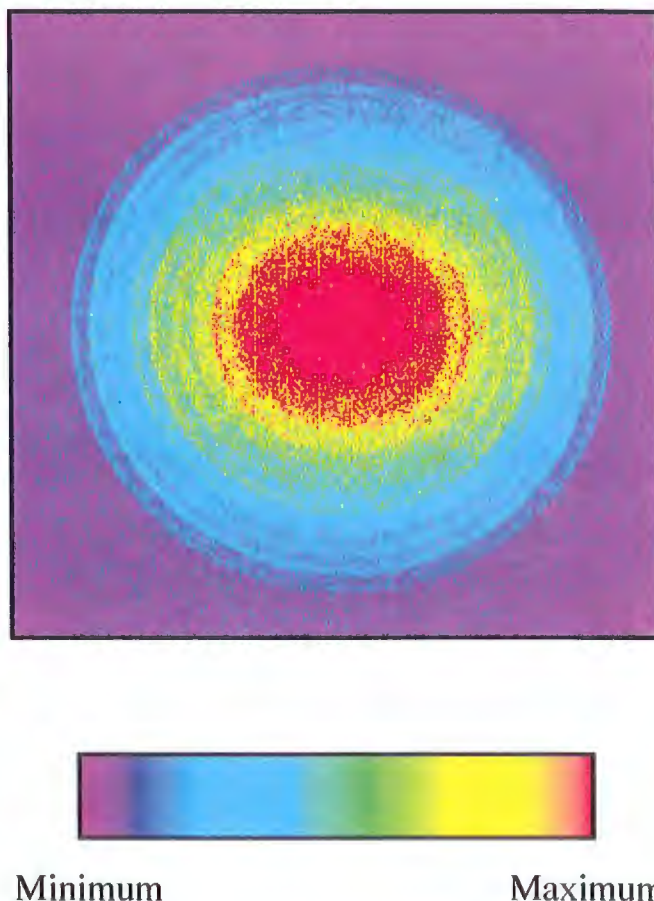


Figure 4.10 Experimental photoelectron image of the ejected electrons after (1+1) REMPI via the 6_0^1 transition in benzene. Laser polarisation is vertical in the image.

one may expect by just looking at the image. Non-circular images of photoelectron distributions due to the difficulties in shielding from magnetic fields have been noted by Parker and Eppink [Parker 1997]. They report that, as expected, better energy resolution was obtained if they only integrated over a small angular range. We find a similar effect with our photoelectron spectra.

While narrowing the integration to small angular sections improves the resolution, it is nevertheless an unsatisfactory solution. Such an approach discards much of the data, lowering the signal to noise ratio. Moreover, photoelectron distributions calculated from just the angular segments, or wedges, in general give only the peak positions, not the correct intensities because of anisotropy in the angular distributions. It is preferable to devise a method by which slight distortions can be “repaired” and the image returned to being circular prior to analysis.

We have developed a novel technique that will morph the original distorted image into a circular image. The circular image can then be operated on in standard ways to produce higher resolution photoelectron spectra. Basically, the method stretches or compresses wedges of the image until a circular image is formed. In order to apply the method we require the image to have a well defined ring structure.

Consider an image that is divided into a series of small wedges, analogous to cutting a pie. The average radial intensity for each wedge is denoted as $I_n(x)$ where x is the distance from the centre of the image. By applying a transformation F_n on the radial coordinate for the n th wedge, it will be possible to find a solution to the equation

$$A_n I_n(F_n(x)) = I_0(x) \quad 4.9$$

Here A_n is a constant for a particular wedge and is required to account for the fact that, due to photoelectron distributions being anisotropic in general, the absolute intensities

in different wedges are different. While equation 4.9 equates the two sides, in practice the relation is only approximate. This occurs because equation 4.9 assumes that the anisotropy is constant for all bands in the image, and hence the radial intensity distribution for each wedge is the same, but in fact we find that this is not always so (see section 5.3.2 in chapter 5). The key idea encapsulated in this formula is that all wedges are stretched or shrunk radially until the peak positions overlap with a reference wedge. This approach assumes that the distortion is radial. While this may not be the case in practice, provided the distortion is not significant, such an assumption will lead to little deviation from correct intensities in the circularised image. The improved resolution and ability to use the entire image more than compensates for the minor errors this assumption may introduce.

It is important to find the transformation function that results in the best radial overlap of each distribution. We find for our images that a linear transformation, $F_n(x) = k_n x$, is adequate to describe the deformation. The transformation is found by applying, in the first instance, a Levenberg-Marquardt algorithm for non-linear least squares fitting [Press 1992], and then fine tuning manually using the ‘chi-by-eye’ method to check the alignment of rings in the wedges being compared. In a situation in which there are a lot of clearly defined rings, it would be possible (although time consuming!) to generate an arbitrary function for each F_n by manually aligning all the peak positions.

Once the appropriate transformation function has been found for each wedge, the new wedge distribution $I'_n(x)$ is given by simply applying the transform, F_n , to each wedge and multiplying the intensity by an appropriate scaling factor $B_n(x)$,

$$I'_n(x) = B_n(x) I_n(F_n(x)) \quad 4.10$$

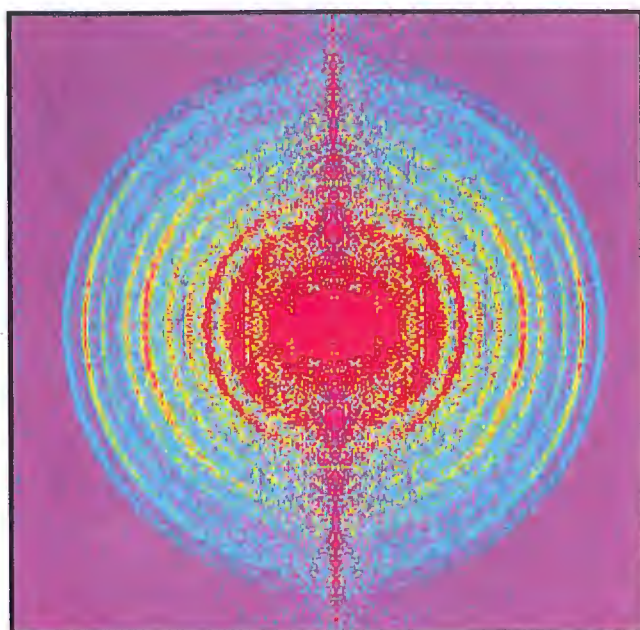
The scaling factor $B_n(x)$ is required to account for the conservation of signal and depends on the functional form of F_n . That is, the integral of $I_n(x)$ and $I'_n(x)$ must be

identical since the number of electrons that arrived in a wedge is not altered by the transformation. For the linear transformation that we have used, $B_n(x)$ is simply equal to k_n .

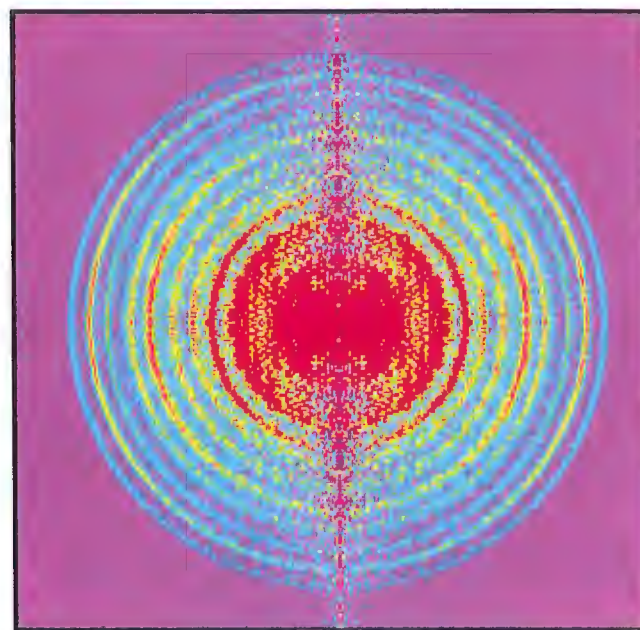
The best results from this technique will occur when the wedge size is small so that there are no distortions within each wedge. In practise, however, the image lies on a grid defined by the pixel positions of the CCD array. Consequently large wedges (in our case 10° wedges are used) are needed for sufficient signal for comparing peak positions. For this reason the practical realisation of the circularisation procedure worked as follows. The k_n values are calculated in the same way as discussed above but, to calculate the new image, each pixel of the new, transformed image is taken one at a time. At each pixel the angle is determined and a value of k appropriate to that angle is found by interpolating the series of k_n values (for the interpolation process, the angle associated with each k_n is taken to be the centre of the wedge that was used to determine that k_n). Using the determined k value, the radius of the pixel and its angle, this location in the new, transformed image can be correlated with a position in the raw (original) image. The raw image is interpolated (in two dimensions) to give a value corresponding to the calculated radius and the angle. The interpolated intensity is multiplied by the scaling factor and placed into the new image at the correct pixel location.

The success of this method can be seen when comparing the three dimensional population distribution images and corresponding photoelectron spectra calculated with and without the above procedure applied. Such images and photoelectron spectra are shown in figure 4.11 and figure 4.12 respectively, for benzene ionised using the 6^1O resonant transition. The improvement in the energy resolution that can be obtained by applying the simple procedure outlined above can be seen from inspection of these figures. The three dimensional population distribution image in figure 4.11a, clearly shows that the non-circularised image has 'blurred' rings at angles near 0° and 180° .

a)



b)

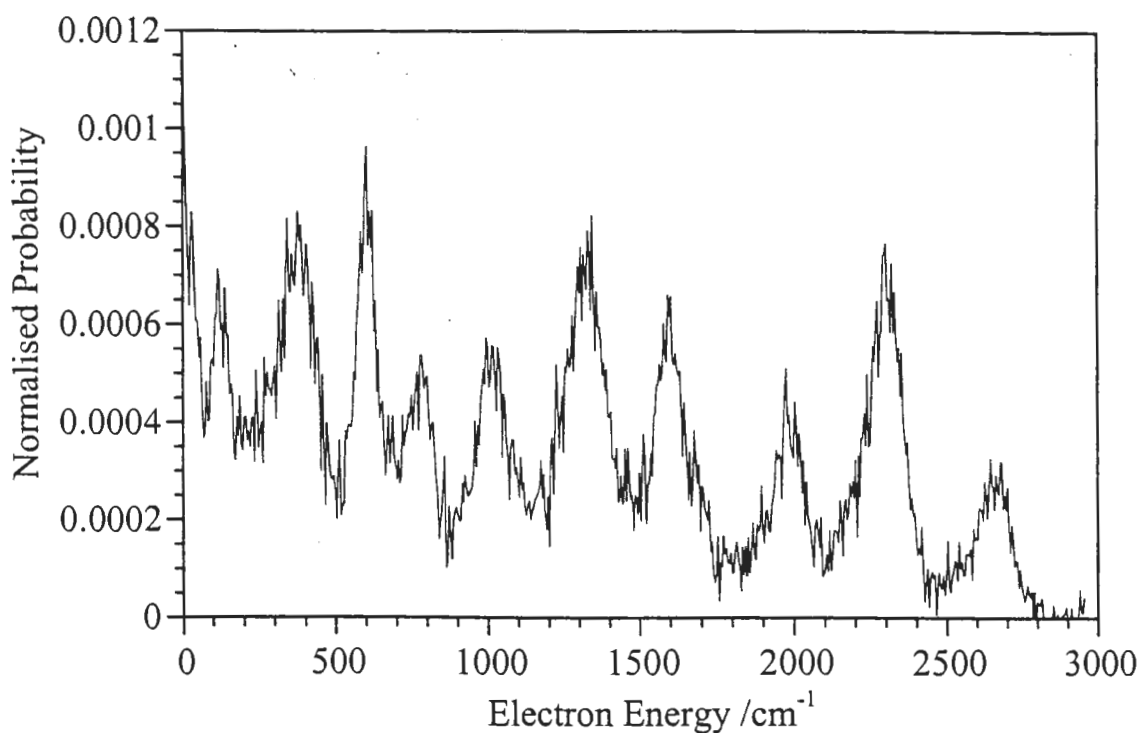


Minimum

Maximum

Figure 4.11 Comparison between the reconstructed three dimensional distribution of benzene ionised using the 6_0^1 resonant transition calculated a) without and b) with the application of the new circularising procedure. Note the improved resolution achieved with the circularising method. Laser polarisation is vertical in the images.

a)



b)

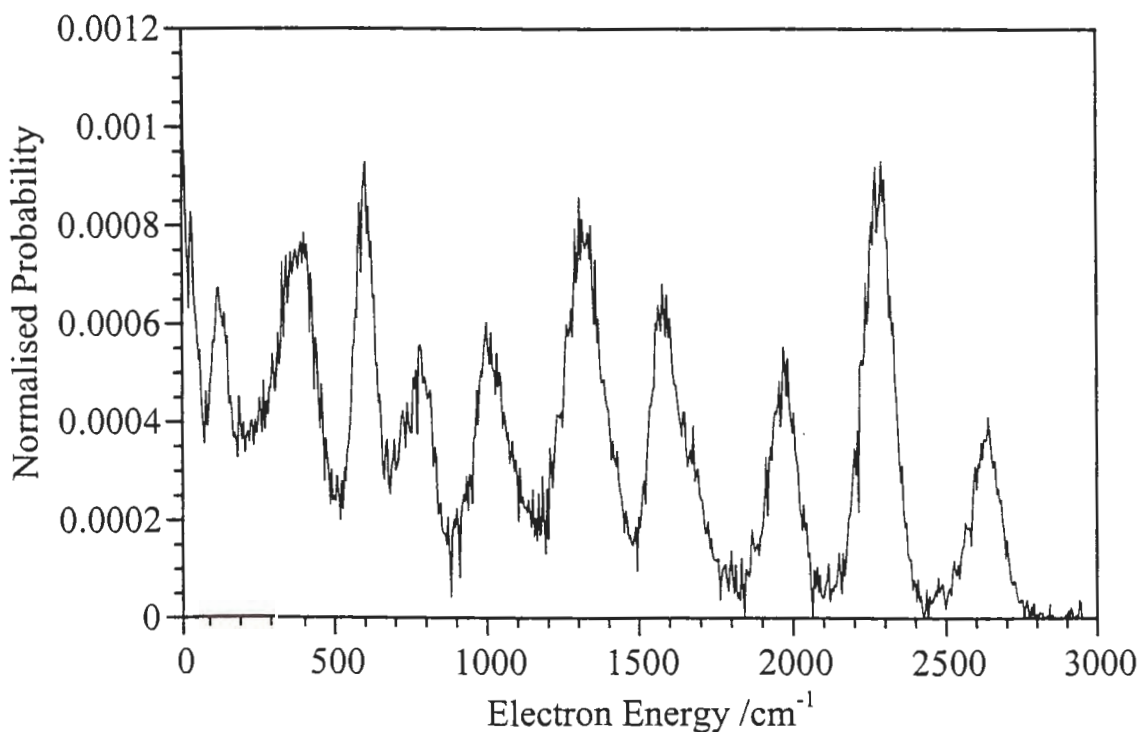


Figure 4.12 Comparison between photoelectron spectra of benzene ionised using the 6_0^1 resonant transition calculated a) without and b) with the application of the new circularising procedure. Note the improved resolution achieved with the circularising method.

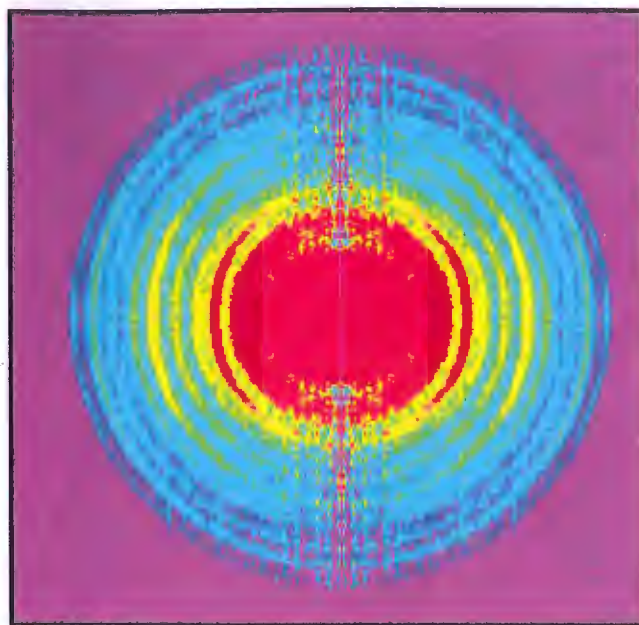
This is the area in which our deformations lie. By applying the circularisation method as described above, we generate an image (figure 4.11b) where the peaks are now considerably sharper in this region. The photoelectron spectra calculated from these images also show differences. After the circularisation algorithm has been applied, the peaks become narrower and now the photoelectron intensity almost returns to the baseline between the peaks at high electron energy. Thus the circularisation method improves the energy resolution in photoelectron images obtained through electron imaging. All photoelectron images presented here and in the next chapters have undergone the circularisation process unless explicitly stated.

4.5.3 Ion Counting versus CCD Integration

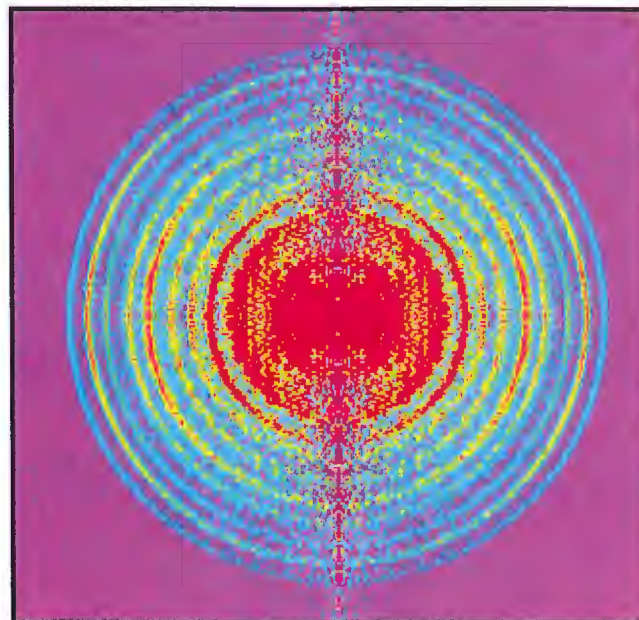
The rings observed in the electron images of the photoionisation of benzene are an ideal benchmark to discuss the increase in the energy resolution of the spectrometer associated with ion/electron counting compared with CCD integration. Figure 4.13 displays the reconstructed three dimensional photoelectron distribution and figure 4.14 the photoelectron spectra obtained by ionising benzene using the 6_0^1 resonant transition using both CCD integration and the ion/electron counting technique.

The integrated image was collected immediately after the electron counted image with no change in the experimental conditions. It is clearly seen that the counting algorithm results in considerably increased energy resolution. The improved resolution is attributed to reducing the finite size of the spot (which covers a number of pixels) down to a single pixel [Chang 1998]. If the true width of the rings in the image was infinitely small (ie composed of thin spherical shells), then the integration technique would produce a width equal to the width of a single electron spot. On the other hand, electron counting determines the location of the maximum of each the spot, which will lie on the ring, thus producing an image where the rings are only one pixel wide.

a)



b)

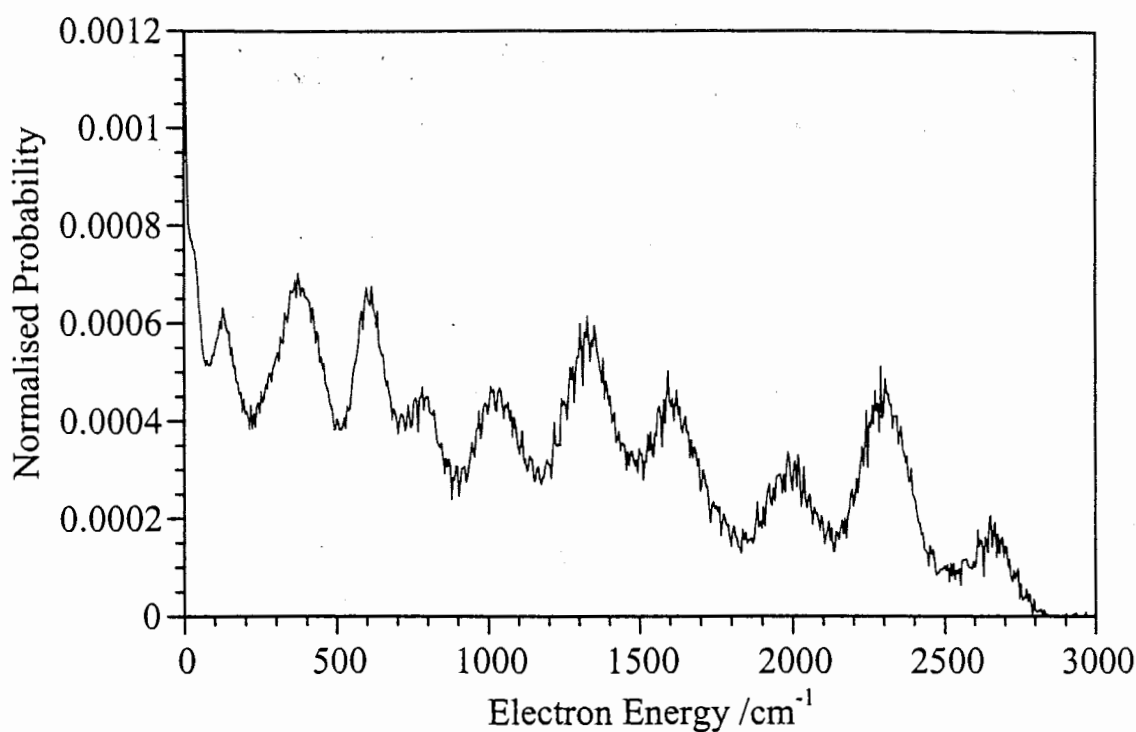


Minimum

Maximum

Figure 4.13 Three dimensional photoelectron population distribution images obtained by ionising benzene via the 6_0^1 resonant transition using both a) CCD integration and b) ion/electron counting technique. Laser polarisation is vertical in the images.

a)



b)

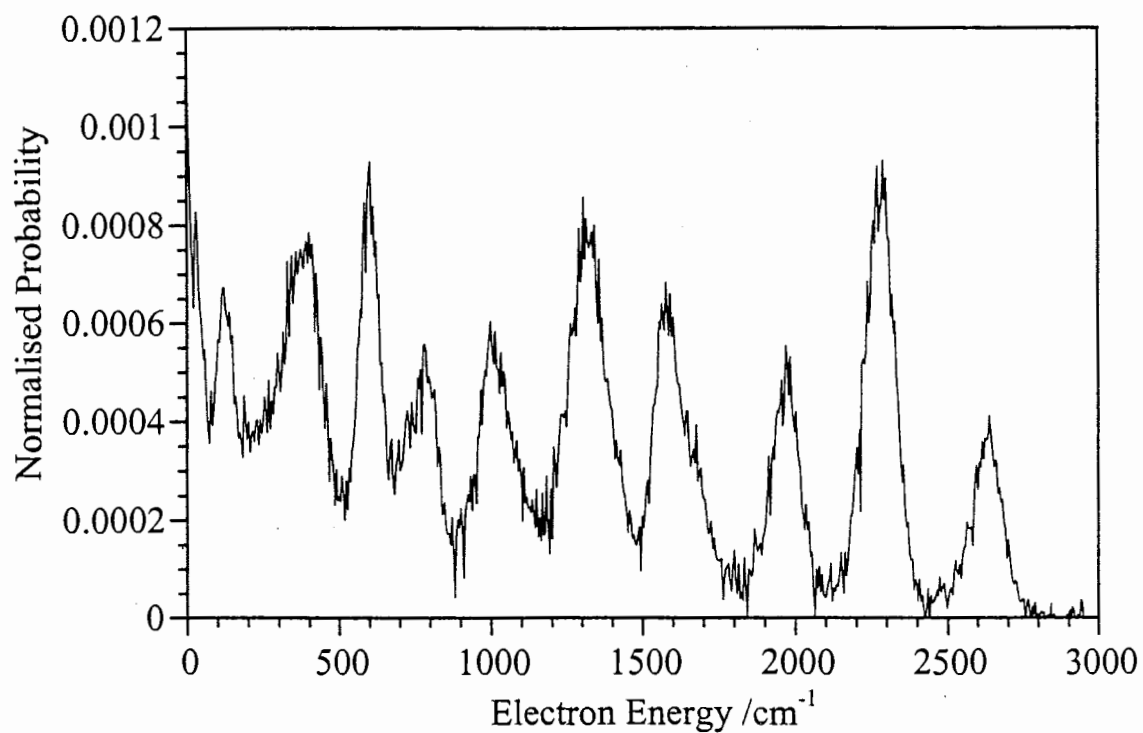


Figure 4.14 Photoelectron spectra obtained from the images in figure 4.13 a) CCD integration and b) ion/electron counting technique.

For the spectrum shown in figure 4.14, the width of the outside ring due to the rotational contour should be approximately 9 cm^{-1} [Krause 1992]. We see a value somewhat greater than this even using the counting technique. The reasons for this are discussed in more detail in the next section. The point to be made here is that the resolution obtained is not limited by the image processing technique when using ion counting, but it would be if we had used the integration technique.

4.5.4 Resolution in photoelectron imaging

Since electrons are highly susceptible to stray magnetic fields compared with ions, the photoelectron spectra serve as a “worst case” for determining the device’s resolution. For each spherical shell, one ideally would obtain an image of a circular ring. Unfortunately, electric and magnetic field distortions can cause the electron to wander slightly off course and not hit the detector in the correct location, resulting in distorted images. In the present apparatus, we believe that there is no interference from stray electric fields since simulations suggest the electrode arrangement is adequate, and we have not seen any distortions using the instrument in positive ion mode. However, we do see distortions in our electron images, which we attribute to interference from stray magnetic fields. We have already noted a distortion of the image from being precisely circular and discussed how images can be processed to overcome this level of distortion (see section 4.5.2). In addition to this overall image distortion, there are sections of the image which are very sharp and well focused, and also regions that appear somewhat blurred. These distortions are seen to change when metallic tools or electrical equipment is moved in the vicinity of the time of flight vacuum chamber, demonstrating the effect stray magnetic fields have on the image. This is not at all surprising since the only protection against external magnetic fields was the Co-Netic shielding around the time of flight tube and around the time of flight vacuum chamber. In fact, we were very surprised with the quality of the electron images when one considers the lack of effort

used to shield the instrument from magnetic interferences. The apparatus will soon be undergoing significant modifications in an attempt to eliminate all interferences from magnetic fields and this should improve the resolution. Significantly, as shown in the next chapter, our resolution is comparable to that obtained in a conventional photoelectron time of flight apparatus for electron energies less than 1000 cm^{-1} , even with the distortions seen in our images.

In an attempt to determine the best resolution currently attainable with our electron imaging apparatus, images of the 6_1^0 photoionisation were recorded with the repeller and extractor voltages at a quarter of their normal operating voltages. This results in a doubling of the image size. The laser power was increased so more photoelectrons were produced, allowing the larger image to be filled in the same amount of time as usual. Interestingly, no side-effects (such as a Coulomb explosion) were noticed when increasing the laser power. The best quarter of the image was taken, and reflected into the other three quadrants to obtain the raw image shown in figure 4.15a. Due to the increasing size of the image, the whole distribution no longer fits on the CCD chip, so just a small section of the outermost ring is visible in the corners. After applying the inverse Abel transform, the population distribution shown in figure 4.15b is calculated. It should be noted that since the entire image was not collected, then technically the inverse Abel transform cannot be applied. However, we are only interested in the peak widths and not the true peak intensities of the image. The *pseudo* photoelectron spectrum obtained from the image is shown in figure 4.16. The noisy signal to the low energy side of the highest energy peak is an artefact of performing the inverse Abel transform on an incomplete image.

Close examination of the raw data for the ‘high resolution image’ (figure 4.15) shows the inner most ring, which occurs at an energy of 40 cm^{-1} , to be a very broad image spanning quite a number of pixels. Given that this ring is quite broad, it is likely that is wider than the instrumental resolution. The photoelectron spectrum derived from the

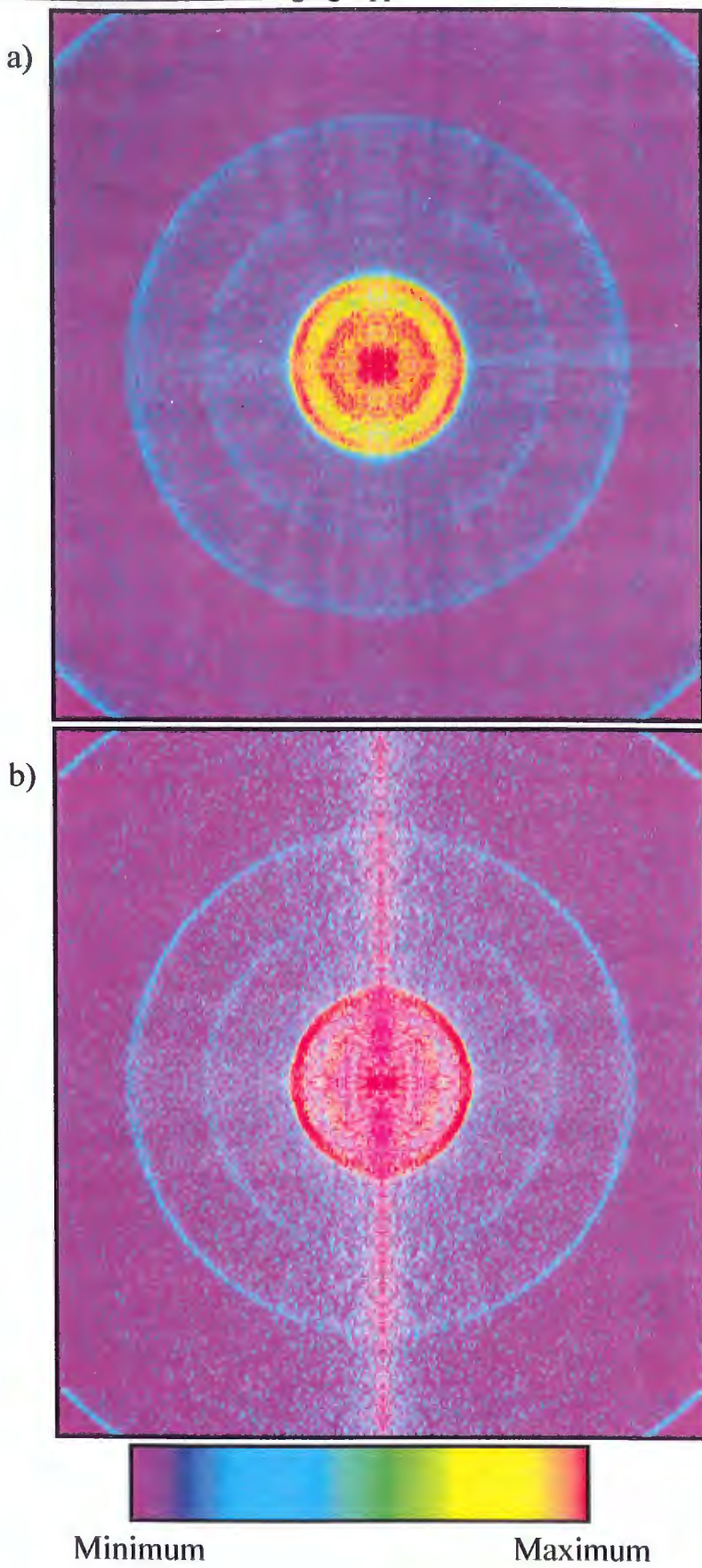


Figure 4.15 High resolution images of the photoelectrons arising from REMPI of benzene via the 6_1^0 transition (a) and the image after applying the inverse Abel transform (b). Laser polarisation is vertical in the images.

image gives a width of 10 cm^{-1} for this peak. This agrees very well with values obtained for bands of the benzene cation observed using mass analysed pulsed field ionisation spectroscopy (9 cm^{-1} [Krause 1992]; 8 cm^{-1} [Goode 1997]) using lasers of similar bandwidth to those used in our experiments. This width is associated with the rotational contour of the bands. The $S_1 \leftarrow S_0$ resonant step produces molecules in a range of rotational states. The ionisation step therefore starts from many different rotational levels, producing the observed widths [Krause 1992]. Chewter *et al.* recorded high resolution ZEKE photoelectron spectra of benzene by reducing the linewidth of the dye laser with an intracavity étalon [Chewter 1987a]. They were able to excite specific rotational states in the 6^1 vibrational level, greatly reducing the number of starting states for the ionisation step. The spectra showed smaller peak widths with assignable rotational fine structure. It is interesting to note however, that this structure occurred

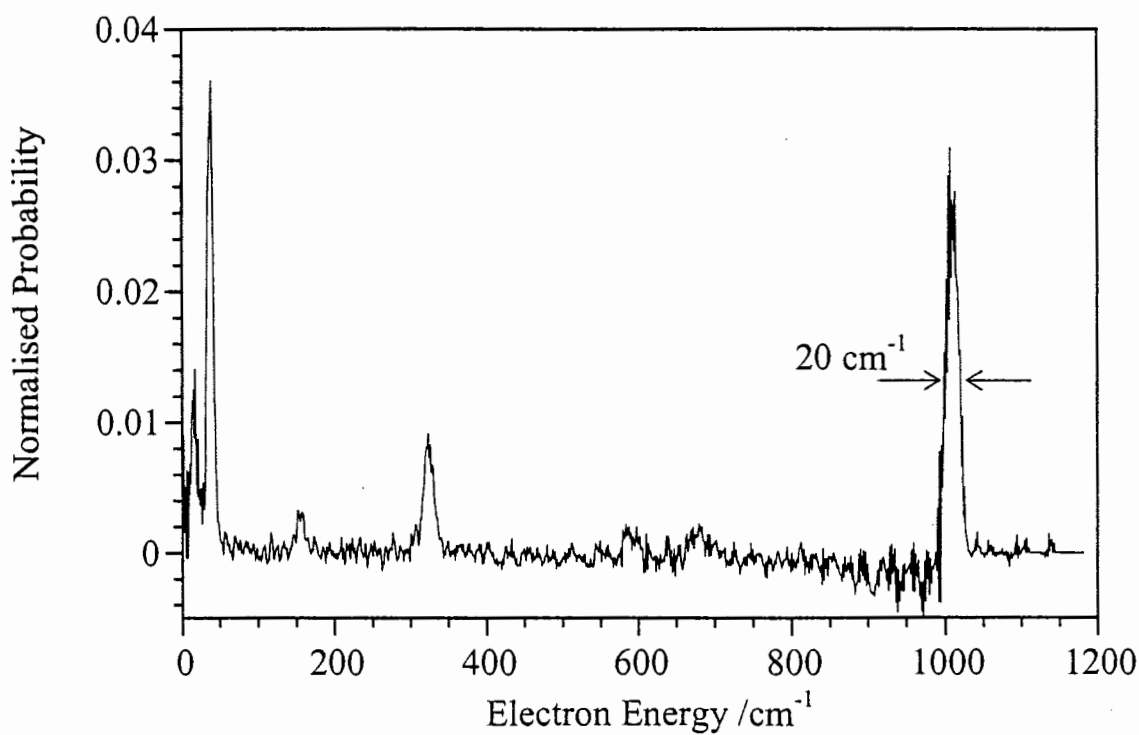


Figure 4.16 High resolution *pseudo*-photoelectron spectrum derived from the image shown in figure 4.15.

over a total energy range of approximately 7 cm^{-1} [Chewter 1987a; Müller-Dethlefs 1995]. Our experiments were performed without the use of an étalon, so we do not expect to see any structure in this ring. In fact, from the peak widths seen at higher electron energies (see next paragraph), we believe the instrumental resolution at this peak is $\sim 3\text{-}4\text{ cm}^{-1}$.

The outside ring shown in the corners of figure 4.15 is produced by ions formed in their vibrational ground state. This region of the image appears to be unaffected by distortions in that it gives particularly sharp rings so it can be used to test the resolution that would be possible under distortion free conditions. The *pseudo* photoelectron spectrum (figure 4.16) shows the peak to have a full width at half maximum of 20 cm^{-1} at an energy of 1011 cm^{-1} . We believe this to be an indication of the resolution we would expect to see in our modified spectrometer. Given that the rotational contour is $\sim 8\text{-}10\text{ cm}^{-1}$, a bandwidth of 20 cm^{-1} suggests an instrumental bandwidth of $\sim 18\text{ cm}^{-1}$ (the rotational contour and instrumental bandwidth have been assumed to be Gaussian for the purpose of this estimate). The instrumental resolution actually refers to velocity, as the image actually measures the ion/electron velocity distribution. A constant resolution in velocity corresponds to a resolution that decreases with increasing energy, since kinetic energy depends on velocity squared. The resolution, ΔE , at other energies, E , can be estimated from that for the 1011 cm^{-1} band via

$$\begin{aligned}\Delta E &\sim 18\sqrt{E/1011}\text{ cm}^{-1} \\ &\sim 0.57\sqrt{E}\text{ cm}^{-1}\end{aligned}\quad 4.10$$

The resolution obtainable in photoelectron spectra from electron imaging experiments has recently been discussed in detail by Chandler and Parker [Chandler 1999]. By recording the ion image created by ionising atomic oxygen following the dissociation of O_2 , peak widths in the O^+ energy spectrum were measured. They determined the peak width to follow the expression $\Delta E = 25\sqrt{E}$ where ΔE is calculated in units of meV and

E is given in eV. For non-overlapped peaks they suggest that a more realistic formula is $\Delta E \approx 20\sqrt{E}$. This is also the resolution stated by Wang *et al.* in their brief overview of different types of photoelectron spectrometers [Wang 1999]. By converting equation 4.10 into eV units, we find for our experimental arrangement that we have peak widths $\Delta E = 6.3\sqrt{E}$. Thus the resolution we have obtained is about 3 times better than that calculated by Chandler and Parker [Chandler 1999]. We have reviewed the current literature and have found, to the best of our knowledge, the resolution values presented by Chandler and Parker to be the best. Since our resolution is substantially better than theirs, we believe our results present the highest resolution obtained for ion/electron imaging experiments.

An attempt was made to measure ion images from the dissociation of a homonuclear diatomic since the dissociation will leave the atomic fragments with well defined kinetic energies. The dissociation of O₂ is known to produce ions with kinetic energies in the energy regime that we are working with (< 5000 cm⁻¹) [Parker 1997]. Although a reasonable attempt was made, inadequate laser powers near 225nm precluded us from obtaining any acceptable ion images of O⁺. However, given the insensitivity of ions to the stray magnetic fields, we expect the resolution to be comparable to the highest resolution obtained with the photoelectron images.

4.5.5 Anisotropy Parameters

As clearly evident in the photoelectron images (see for example figure 4.11), the distribution of intensity depends on the ejection angle. That is, for ionisation via the benzene resonant transition 6₀¹, more electrons are ejected perpendicular to the laser polarisation than parallel to it. An angular plot of the 6₀¹ photoelectron image is shown in figure 4.17. This plot shows the total integrated intensity at each angle for the three dimensional distribution image $F(R, \theta)$, as discussed in section 4.3.5. The solid line

represents a best fit to the equation 4.7. Although the $P_4(\cos\theta)$ term in equation 4.3 may be necessary because of the two photon process, it was found that adequate fits could be obtained with its omission. Anisotropy parameters arising from the (1+1) REMPI of benzene from various intermediate states are discussed in the next chapter.

4.6 Conclusion

We have designed and constructed an ion imaging apparatus to be used in future studies of energy transfer. Using the technique of ion imaging with velocity mapping, we were able to show that the apparatus works satisfactorily. With minor modifications it was

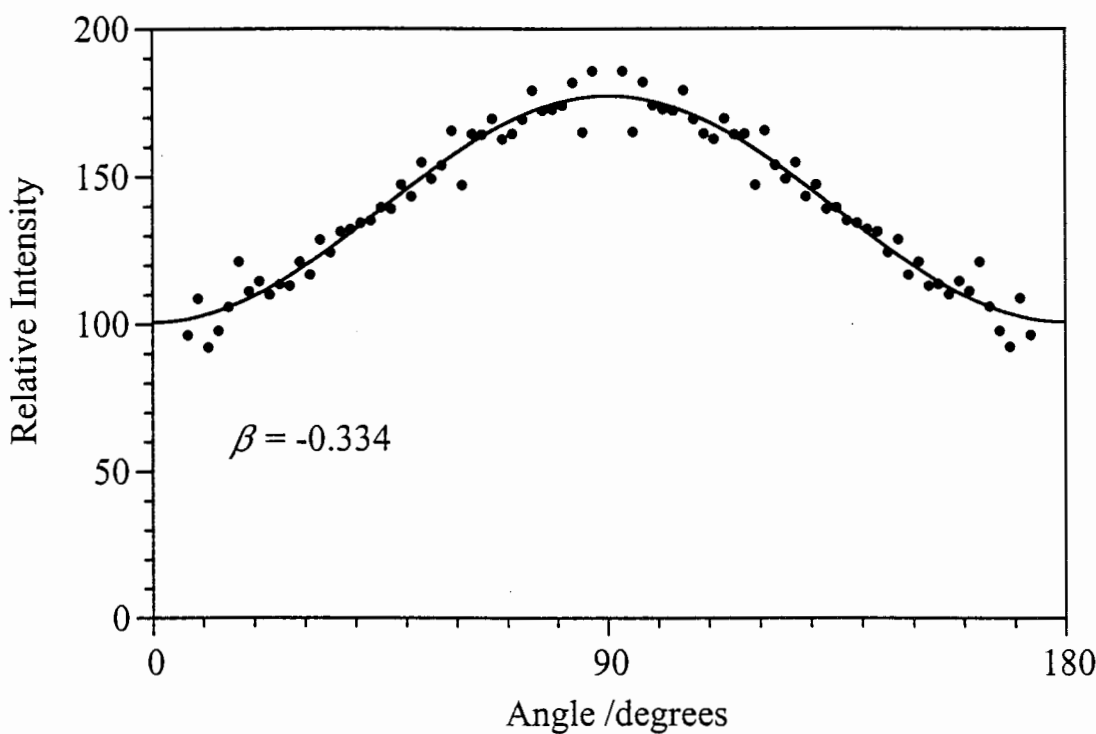


Figure 4.17 Plot of the photoelectron angular distribution formed by the REMPI of benzene via the 6_0^1 resonant state. The solid line is the best fit line to equation 4.7.

found that photoelectron images could also be recorded, allowing the determination of photoelectron spectra and anisotropy parameters.

Images obtained of photoelectrons show some deformity due to the presence of stray magnetic fields. Bearing in mind that the spectrometer was never intended for the recording of photoelectron spectra, deformations are not entirely unexpected. Two types of deformities were seen, the major being a slanted oval appearance of the image, and also blurring in some regions. We presented a technique to modify the image such that it returns to a circular shape, providing an improvement in the energy resolution in photoelectron spectra.

The spectrometer is clearly capable of imaging low energy electrons ($< 40 \text{ cm}^{-1}$ or 5 meV) and also has good resolution at higher energies. The resolution obtained in the spectrometer could be improved by better shielding of the electrons from stray magnetic fields. We have shown that under favourable conditions we produce peak widths of 20 cm^{-1} at an energy of 1011 cm^{-1} , which is approximately three times better than that previously reported.

In the following chapters we discuss two different sets of experiments performed with the apparatus. We have recorded photoelectron images from benzene using resonance enhanced multiphoton ionisation through various resonance transitions in the $S_1 \leftarrow S_0$ absorption spectrum. From these images, photoelectron spectra and anisotropy values were determined. This work is presented in the next chapter. Chapter six presents the results of experiments measuring energy transfer associated with the dissociation of benzene cation - argon van der Waals complexes.

Chapter 5

Photoionisation of Benzene: Photoelectron Spectra and Angular Distributions

5.1 Introduction

5.1.1 *Overview of Photoelectron Spectroscopy*

Measuring electron energies produced by the photoionisation of molecules has long been recognised as a technique to probe the electronic structure of molecules and the vibrational states of their ions. [Turner 1970; Brundle 1977]. Photoelectron spectra provide valuable information such as electron binding energies, molecular geometry, electronic effects produced by substituents or ligands, vibrational frequencies of the ion, and much more [Baker 1977].

Photoelectron spectroscopy requires the use of a monoenergetic light source. The majority of UV photoelectron spectroscopic studies utilise the He(I) line at 58.43nm (photon energy of 21.218 eV), although the number of publications using synchrotron radiation is becoming more common. An alternative technique for photoionisation is to ionise through an intermediate electronic state. This allows light of longer wavelength (such as that easily obtainable by doubling the output of dye lasers) to be used. This also allows greater flexibility in ionisation schemes since different intermediate levels can be populated.

More information about the ionic state can be gleaned by using resonant enhanced multiphoton ionisation (REMPI) rather than single photon ionisation. Firstly, since the ionisation occurs through an intermediate state then the Franck-Condon factors governing the finally populated ionic levels are those between the excited resonant state and the ground electronic state of the ion. Since most molecules exhibit some change in geometry in going from the ground state to the excited state, and further changes from the excited state to the ionic state, Franck-Condon factors are distinctly different between ionisation from the ground state and ionisation from an excited state. Thus ionisation from an excited electronic state (i.e. REMPI) allows the possibility of observing transitions that are not observable in one photon ionisation due to their unfavourable Franck-Condon factors.

Ionisation through a resonant state also allows, under certain circumstances, transitions which are forbidden in the one photon spectrum to be observed. In particular, ionisation of a molecule into a degenerate electronic state having Jahn-Teller active vibrations will impose different vibrational angular momentum constraints on the finally allowed ionic states (this is further discussed below).

Besides measuring the kinetic energy of the ejected electrons, the angle at which the electrons are ejected can be measured with respect to the polarisation of the excitation source. These photoelectron angular distributions are sensitive probes of the interaction of the departing photoelectron with the anisotropic ion core [Downie 1999]. This interaction is best described as a quantum mechanical scattering process characterised by amplitudes and phase differences between partial waves of the ejected electron [Reid 1995; Downie 1999]. Photoelectron angular distributions also depend on the alignment of the molecule prior to ionisation. Recently, it has been shown how these angular distributions can be used to probe the time evolution of the alignment of molecules [Reid 1999].

A number of techniques are available to analyse electron energies, most popular of which are electrostatic analysers (such as hemispherical mirror analyser), magnetic bottle spectrometers, and field free time of flight techniques. The method generally used for recording high resolution photoelectron spectra and angular distributions are based on time of flight techniques (see for example Reid *et al.* [Reid 1999]). An electron detector, such as a microchannel plate, is placed at a fixed distance from the point of ionisation. Following the ionising event, the electron continues to travel in the ejected direction, unperturbed by any acceleration regions. If the photoelectron is travelling toward the detector, then the time taken to hit the detector will be an indication of the electron's kinetic energy. Angular distributions are determined by recording photoelectron spectra at different angles between the polarisation vector and the detector. This is accomplished by either rotating the polarisation of the ionising source or by rotating the detector about the point of ionisation. For one photon ionisation, only two angles need to be measured (typically 0° and 90°) since only one β parameter is possible (equation 4.4). However, using REMPI as the ionisation technique may introduce higher order terms into the photoelectron angular distribution, thus requiring the measurement of photoelectron spectra at many different angles.

A major disadvantage of standard electron energy analysers used in photoelectron spectroscopy, including the time of flight method described above, is that they suffer from low electron transmission at low energies. Thus scaling corrections are required to obtain correct intensities. In fact, it becomes impossible to detect electrons ejected with near zero kinetic energy. For our experiments on benzene-argon van der Waals clusters (presented in the next chapter), it was desirable to have a knowledge of the complete electron energy distribution after ionisation. We note that previous work on benzene ionic distributions suffered from the above mentioned transmission problems at low electron energies [Long 1983]. This precluded the full determination of all possible vibrational levels populated after ionisation. As described in the previous chapter, we modified our existing ion imaging apparatus to measure photoelectron distributions,

which we will now show overcomes the problems associated with measuring the final ionic vibrational distributions after photoionisation.

In this chapter we present the very new technique of electron imaging (the electron equivalent to ion imaging) to record photoelectron spectra of benzene excited through various intermediate vibronic states. The term ‘electron imaging’ used here should not be confused with other uses in chemistry, such as images recorded using electron microscopy. Although the technique described here was initially used for the determination of populated vibrational levels after ionisation, an added bonus was the ability to simultaneously measure the angular distributions of photoejected electrons. A brief review comparing electron imaging with other photoelectron detection techniques is given by Wang *et al.* [Wang 1999].

Imaging of electrons was first performed by Helm *et al.*, when they studied the photoelectron angular distribution formed from the multiphoton ionisation of xenon [Helm 1993]. Parker and Eppink in mid-1997 demonstrated that the resolution obtained in these images could be substantially improved by using their newly developed technique of velocity mapping to image the photoelectrons formed from REMPI of molecular oxygen [Parker 1997; Eppink 1997]. Since then, a number of studies have utilised electron imaging on molecular systems such as CH₃I [Samartzis 1999], NO [Wang 1999], pyrazine [Suzuki 1999; Wang 1999] and W_n clusters [Pinaré 1998]. We note that photoelectron spectra measured using electron imaging have been obtained with relatively low resolution but they span a significant energy range (eg Eppink and Parker measure kinetic energies up to 40 000 cm⁻¹ with a nonoverlapped peak width of ~70 cm⁻¹ at 1 000 cm⁻¹ [Parker 1997; Chandler 1999]). A feature of the work we present here is that we are obtaining photoelectron spectra of low energy electrons (< 4 500 cm⁻¹) with high resolution. It is also interesting to note the recent appearance of imaging work that involves the coincident detection of an ion and the photoelectron formed from the same neutral species (see for example [Downie 1999; Davies 1999]). Although this

type of imaging can record angular distributions as a function of the initial orientation, it can take a week of continuous data collection to record the images [Downie 1999].

The energy gained by an electron, $E_{Kinetic}$, after a photoionising event will depend on the energy of the ionising light $E_{h\nu}$, the first ionisation potential of the molecule E_{IP} , the initial energy (electronic, vibrational and rotational) of the neutral $E_{Neutral}$, and finally, the resulting ion's internal energy E_{Ion} :

$$E_{Kinetic} = E_{h\nu} + E_{Neutral} - E_{IP} - E_{Ion} \quad 5.1$$

For the specific case of resonance enhanced multiphoton ionisation described in this chapter, the total input energy corresponds to two UV photons, the electron ejected originally came from the highest occupied molecular orbital, and the ionisation energy corresponds to the first ionisation potential. Thus equation 5.1 reduces to

$$E_{Kinetic} = 2h\nu + E_{Vib} - E_{IP} - E_{Vib}^+ \quad 5.2$$

where E_{Vib} is the vibrational energy in the neutral, and E_{Vib}^+ is the finally populated vibrational level in the ion. Thus, measuring electron energies while knowing the ionisation potential and initial molecule state, the vibrational energy levels of the ions can be determined.

When higher precision data are desired for investigating the structure of vibrational levels within the cation, there are two techniques which can give much superior resolution than photoelectron spectroscopy. Zero kinetic energy (ZEKE) or mass analysed threshold ionisation (MATI) spectroscopy allows rotationally resolved spectra of ionic vibrational levels [Müller-Dethlefs 1995]. The two techniques both rely on two colour resonant enhanced multiphoton ionisation. The first wavelength is fixed to a resonant transition while the second laser is scanned through the vibrational levels of

the ion. When the second wavelength coincides exactly with a vibration, then high lying Rydberg states are excited (ie molecules where the excited electron is in an orbit far from the core). These Rydberg molecules are extracted by pulsed field ionisation, and detected. ZEKE and MATI provide information on the ionic vibrational levels at the cost of the added complexity of two lasers. These techniques do not provide information on photoelectron angular distributions.

In this chapter we demonstrate the usefulness of electron imaging to gain direct information on the distribution of population into the vibrational states of large polyatomic ions produced by REMPI. In particular, we ionise benzene using four different resonant transitions, each resulting in different amounts of excess energy deposited into the ion. We show that electron imaging is a simple technique to determine both final vibrational distributions in the ion and photoelectron angular distributions. Our results are compared with those of earlier REMPI photoelectron spectra.

5.1.2 Benzene Ionic Spectroscopy

The ground electronic state of the benzene cation is degenerate, having $^2E_{1g}$ symmetry [Baltzer 1997]. Degenerate vibrations within a degenerate electronic state are subject to Jahn-Teller interactions due to the splitting of the potential function. This is discussed in detail by Herzberg [Herzberg 1966]. The implications of the Jahn-Teller effects for photoionisation using (1+1) REMPI have been discussed in detail by Long *et al.* [Long 1983]. Basically, each degenerate vibration in a degenerate electronic state will be split by Jahn-Teller effects. Since the $S_1 \leftarrow S_0$ transition of benzene is vibronically induced, with the degenerate e_{2g} mode ν_6 being the dominant inducing mode, REMPI via S_1 will lead to the involvement of ν_6 . As a degenerate mode, ν_6 is split in the cation ground state by the Jahn-Teller effect. When ionising from a degenerate intermediate

state, the change in vibrational angular momentum must be $\pm 1/2$. For example, ionising through 6^1 (having a vibrational angular momentum of ± 1) will populate the two split 6_1 vibrational levels, one of which has a vibrational angular momentum of $\pm 1/2$ and the other with a value of $\pm 3/2$. These vibrational levels are denoted in the ion as $6_1(1/2)$ and $6_1(3/2)$ respectively.

A number of studies have concentrated on characterising the vibrational levels of the ground electronic state of the benzene cation. A major study performed by Long *et al.* [Long 1983] recorded the photoelectron spectrum following the one colour (1+1) REMPI of benzene. Ten different intermediate S_1 states were probed, giving clear assignments to many of the ionic vibrational levels. For the first time in benzene, vibrational levels with vibronic angular momentum other than $1/2$ were seen, allowing the Jahn-Teller coupling parameters and unperturbed vibrational frequencies for a number of modes to be calculated.

Using mass resolved pulsed field ionisation spectroscopy, a much improved spectrum of the ionic vibrational states was observed [Krause 1992]. It was found that the $6_1(3/2)$ ionic state was further split into the $+3/2$ and $-3/2$ pairs. This effect was attributed to the quadratic dynamic Jahn-Teller effects.

Benzene has also been the subject of numerous studies on single photon photoionisation, of which the work by Baltzer *et al.* is a recent example [Baltzer 1997]. Baltzer *et al.* measured a series of low resolution photoelectron spectra using synchrotron radiation with photon energies ranging between 12 and 120 eV, and a higher resolution spectrum using He(I) radiation. The seven lowest electronic states of the benzene cation were observed and investigated in detail. The He(I) spectrum allowed observation of the vibronic structure in the cation, while the synchrotron data allowed the β anisotropy parameter to be measured for each electronic state over a large

energy range. Generally β was found to rise steadily with photon energy for each electronic state, and eventually reached a plateau at high photon energies.

The adiabatic ionisation potential is an important quantity in our work to determine the amount of excess energy that is available to the ion, and for calibration purposes. The first accurate determination of the ionisation potential was performed by Chewter *et al.* who, using ZEKE photoelectron spectroscopy, determined that first ionisation occurred at $74\ 555.0 \pm 0.4\ \text{cm}^{-1}$ [Chewter 1987a]. Later, Krause and Neusser used mass analysed pulsed field ionisation to determine the ionisation potential to be $74\ 555.5 \pm 0.5\ \text{cm}^{-1}$ [Krause 1992], which was in excellent agreement with the value obtained previously by Chewter *et al.* Recent high resolution spectroscopy of benzene by Neuhauser *et al.* have determined the ionisation potential between the rotationless ground state of the neutral to the rotationless ground state of the ion as $74\ 556.575 \pm 0.050\ \text{cm}^{-1}$ [Neuhauser 1997]. For the purpose of this study, we use the value of $74\ 556\ \text{cm}^{-1}$ and also note that such small differences in the ionisation potential will not affect our results or interpretations.

5.2 Experimental Details

The experimental apparatus used for this series of experiments was presented in chapter 4. All images reported are comprised of 30 000 sub-images of 500 ms duration which were ion counted. This corresponded to 150 000 laser shots with 1 to 20 electrons detected per laser shot. The actual number of electrons detected depended on the laser power which was adjusted so that no overlapping electron spots were present in the centre of the image. Photoelectron spectra and anisotropy values were determined as discussed in chapter 4. The images were calibrated by setting the outermost ring in the image to the excess energy, since this ring represents population of the vibrational ground state of the ion.

5.3 Results and Discussion

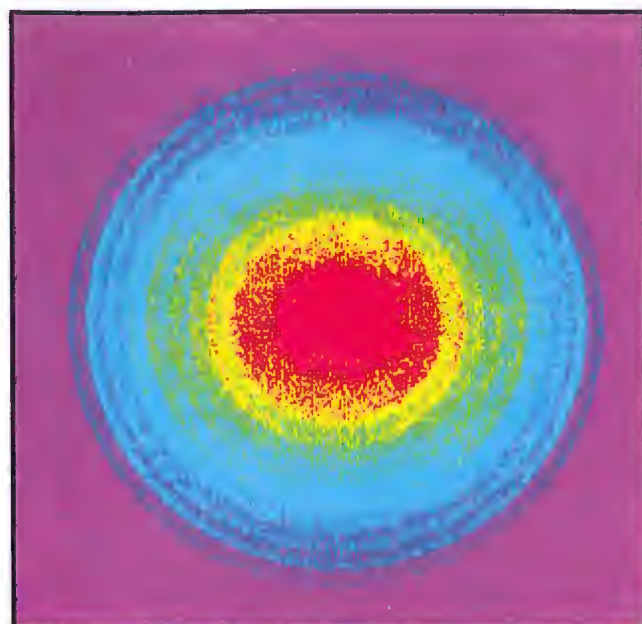
5.3.1 Photoelectron Spectra

Electron images produced by ionising benzene using four different resonant transitions, 6_0^1 , $6_0^1 1_0^1$, 6_1^0 , and $6_1^0 1_0^1$ were recorded. Since only one laser is used, the amount of energy above the 0_0 level in the ion is different for each level, and is given in table 5.1 along with the particular laser wavelengths used for each transition. Two dimensional images resulting from the four intermediate states are displayed in the top halves of figures 5.1 to 5.4. Underneath these images are the three dimensional electron distribution produce by the inverse Abel transform.

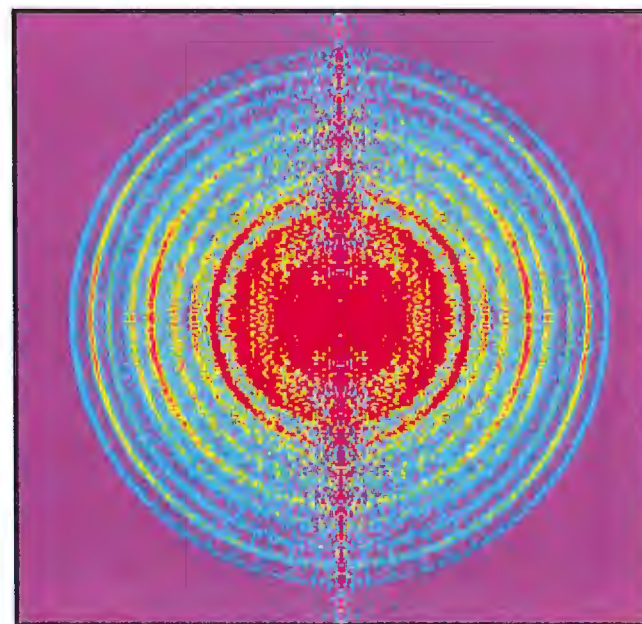
All the images show distinct rings as a result of ions populating different vibrational energy levels. As mentioned in the previous chapter, the central stripe in the transformed images is a result of performing the inverse Abel transform on real (noisy) data, and is ignored. The photoelectron spectra produced from the transformed images are shown in figure 5.5 for ionisation via the 6_0^1 and $6_0^1 1_0^1$ transitions, and in figure 5.6 for ionisation using 6_1^0 and $6_1^0 1_0^1$. Assignments on the spectra are taken from Long *et al.* [Long 1983]. To aid comparisons between the photoelectron spectra, the x -axis can be converted from the electron energy to the internal energy of the ion after ionisation. This requires knowledge of the ionisation potential and the laser wavelength (see table 5.1). Figure 5.7 shows the four photoelectron spectra displayed on a single graph with the x -axis modified to represent the internal ion energy.

When the photoelectron spectra produced by ionising via an intermediate state containing ν_6 are compared (ie figures 5.5a and 5.5b), the spectra are found to have the same form. In fact only one peak, the $1_2 6_1(3/2)$ peak, shows a major difference between

a)



b)

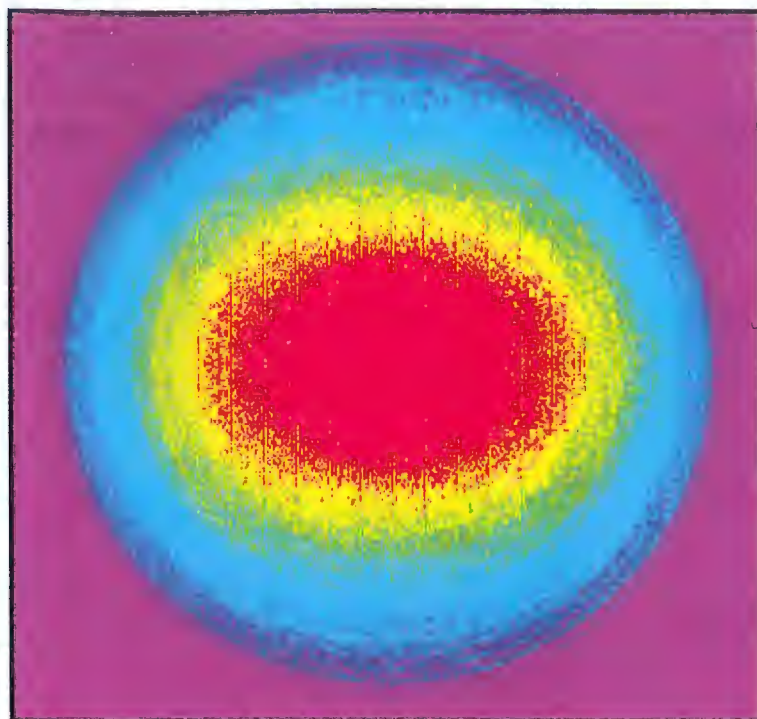


Minimum

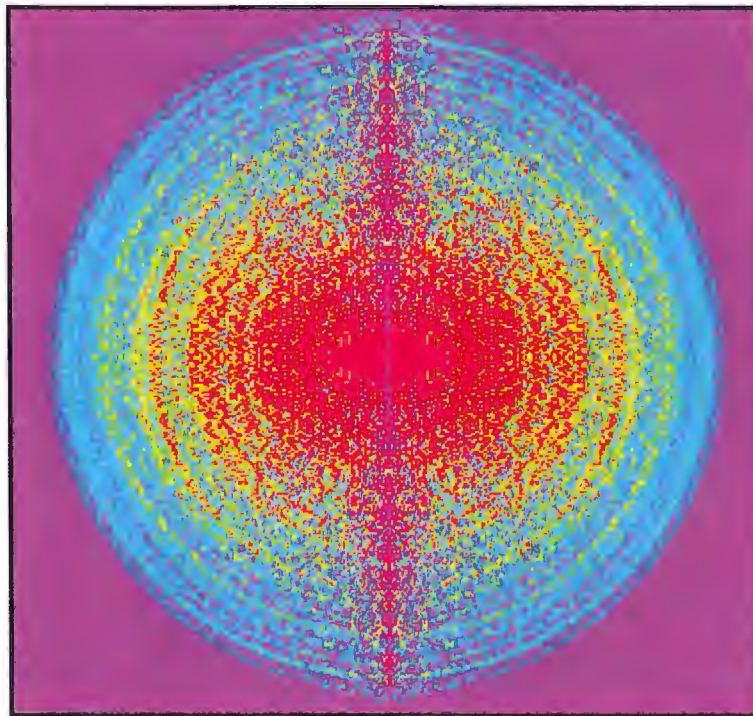
Maximum

Figure 5.1 6_0^1 photoelectron images: a) the two dimensional projection (experimental data) and b) the reconstructed three dimensional distribution. The excess energy is 2663 cm^{-1} . Laser polarisation is vertical in the images.

a)



b)

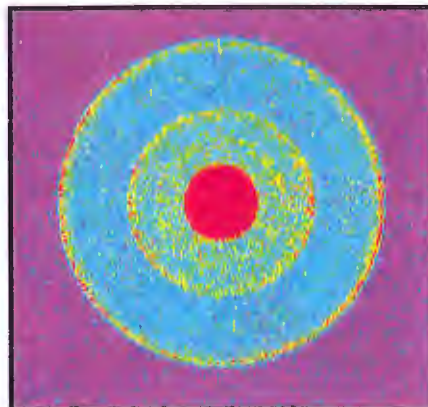


Minimum

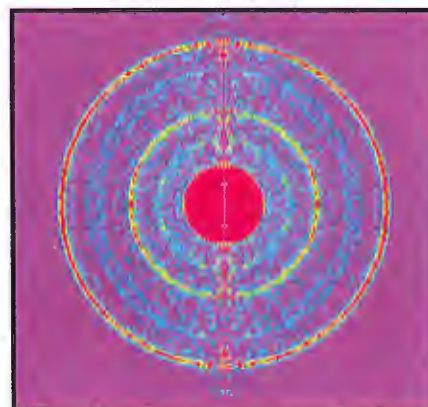
Maximum

Figure 5.2 $6_0^1 1_0^1$ photoelectron images: a) the two dimensional projection (experimental data) and b) the reconstructed three dimensional distribution. The excess energy is 4505 cm^{-1} . Laser polarisation is vertical in the images.

a)



b)

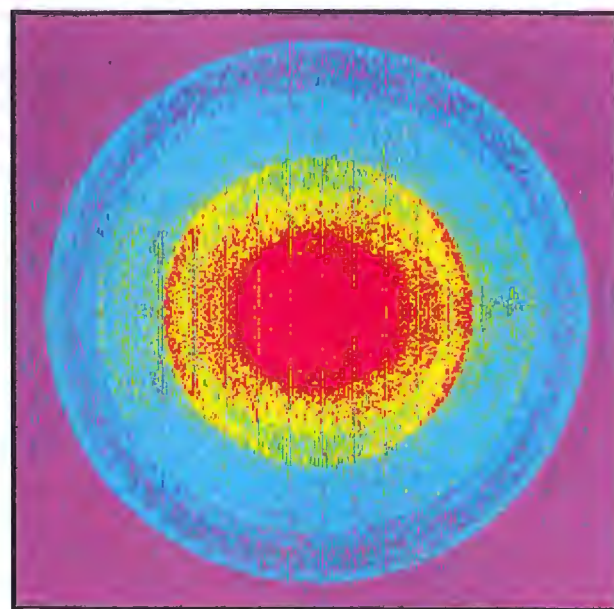


Minimum

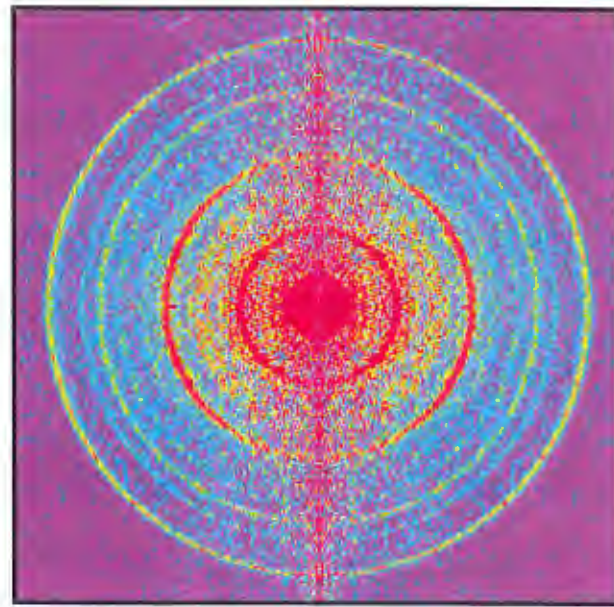
Maximum

Figure 5.3 6_1^0 photoelectron images: a) the two dimensional projection (experimental data) and b) the reconstructed three dimensional distribution. The excess energy is 1010 cm^{-1} . Laser polarisation is vertical in the images.

a)



b)

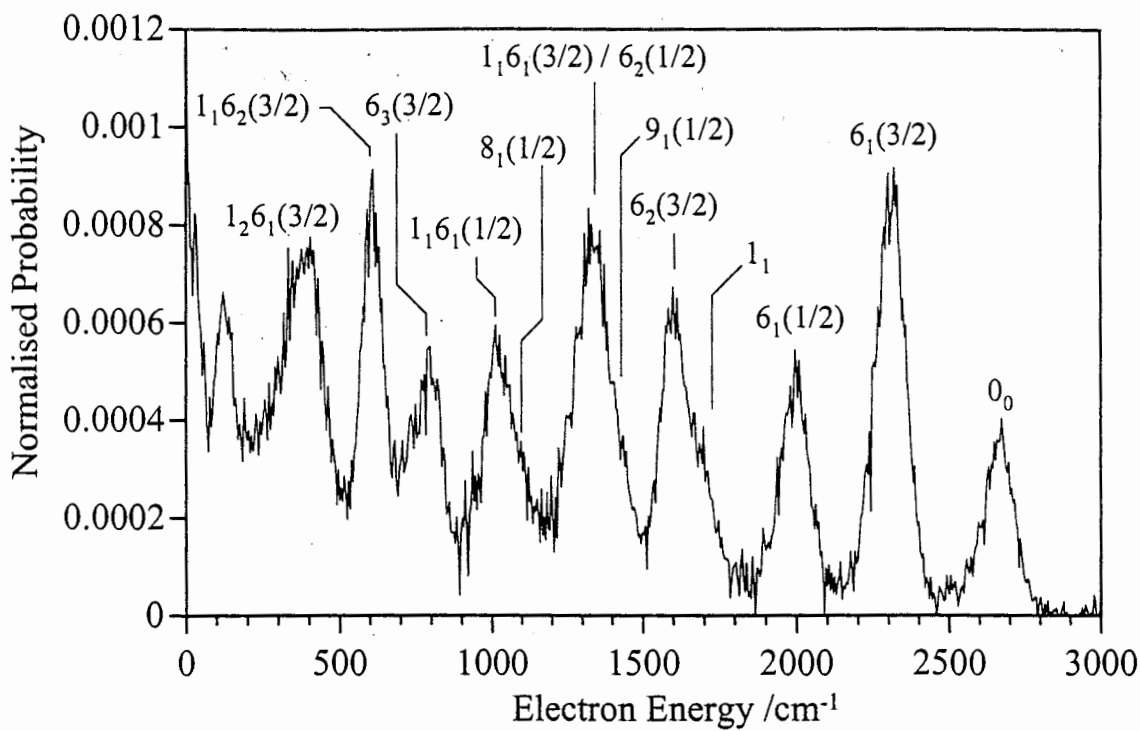


Minimum

Maximum

Figure 5.4 $6_1^{01}_0$ photoelectron images: a) the two dimensional projection (experimental data) and b) the reconstructed three dimensional distribution. The excess energy is 2857 cm^{-1} . Laser polarisation is vertical in the images.

a)



b)

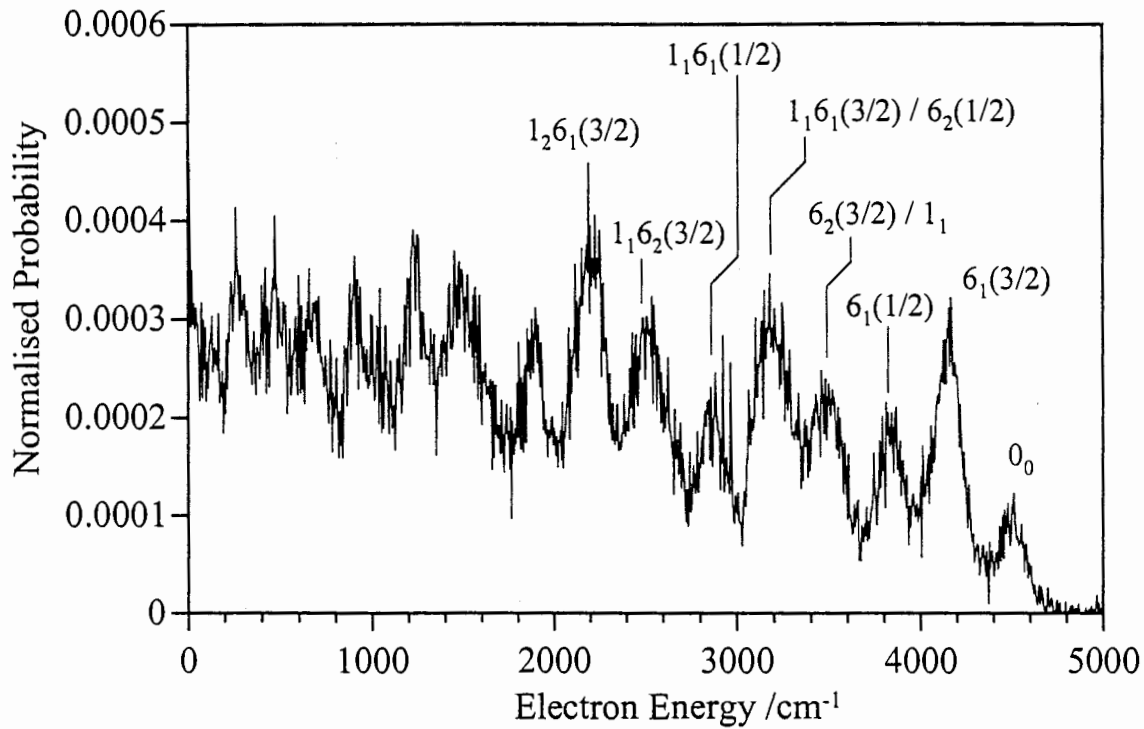
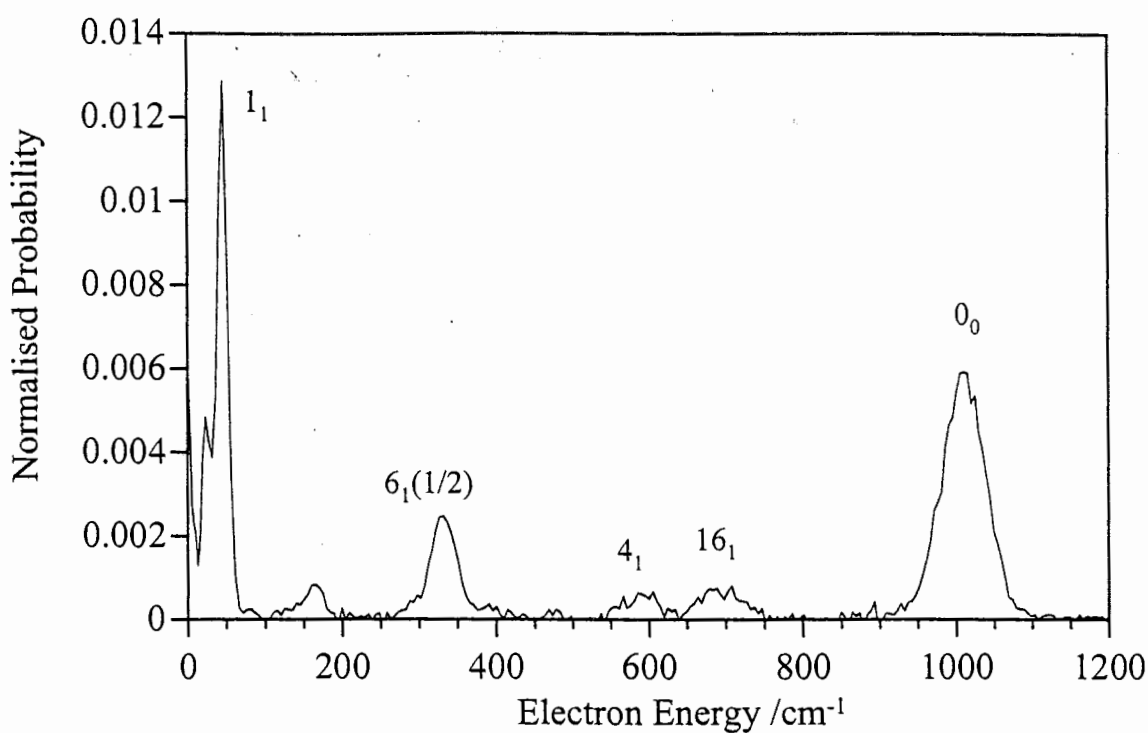


Figure 5.5 Photoelectron spectra of benzene ionised through a) 6_0^1 and b) $6_0^1 1_0^1$ resonant levels. The spectra are obtained from the images presented in figures 5.1 and 5.2.

a)



b)

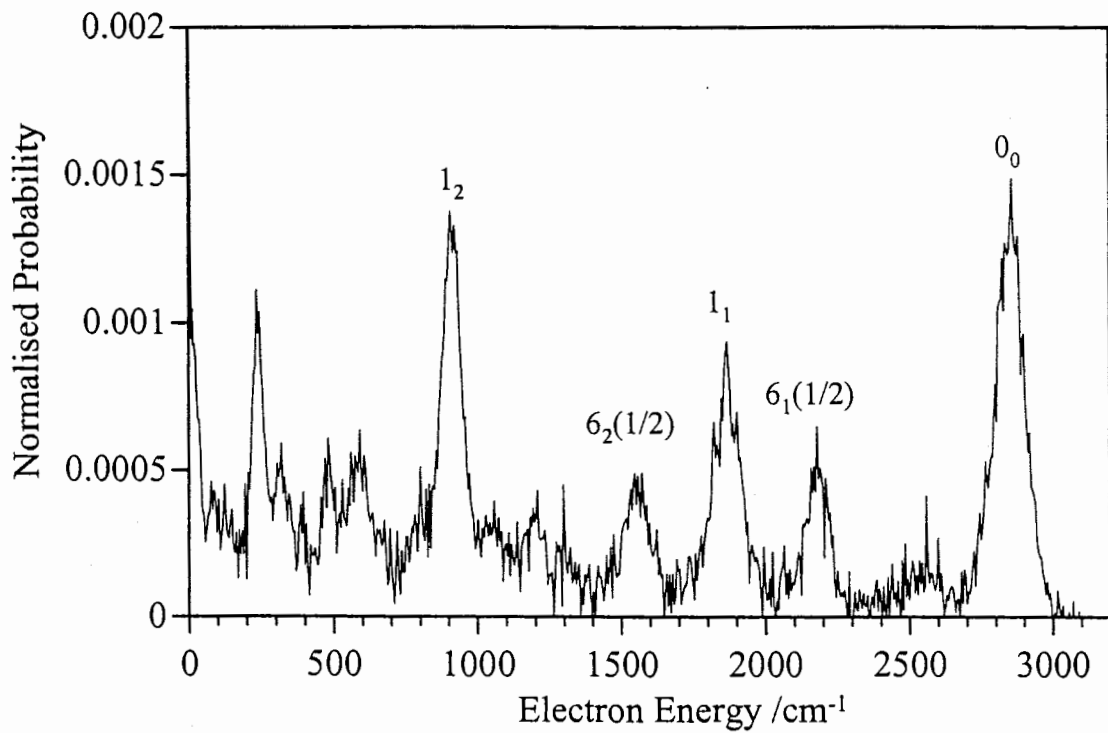


Figure 5.6 Photoelectron spectra of benzene ionised through a) 6_1^0 and b) $6_1^0 6_1^1 0_0$ resonant levels. The spectra are obtained from the images presented in figures 5.3 and 5.4.

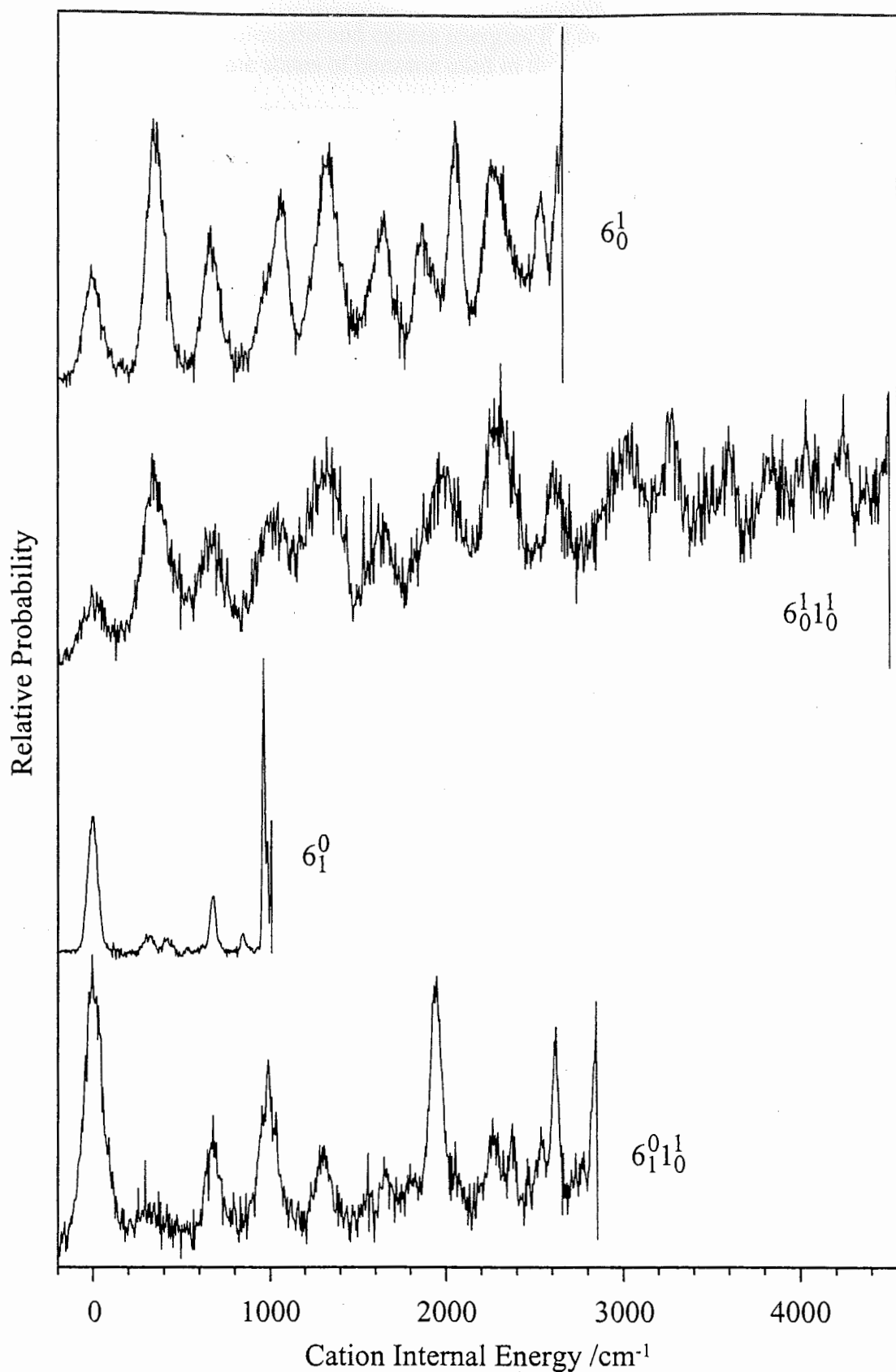


Figure 5.7 Photoelectron spectra of benzene ionised through the four resonant levels used in this study. The x -axis represents the energy remaining in the cation following ionisation.

Table 5.1 Laser wavelengths and excess energies for one colour excitation through the intermediate states of benzene used in this series of experiments.

| Resonant Transition | Laser Wavelength /cm ⁻¹ | Excess Energy ^a /cm ⁻¹ |
|---------------------|------------------------------------|----------------------------------------------|
| 6_0^1 | 38609.5 | 2663 |
| $6_0^1 6_0^1$ | 39530.6 | 4505 |
| 6_1^0 | 37479.0 | 1010 ^b |
| $6_1^0 6_0^1$ | 38402.3 | 2857 ^b |

^a Ionisation potential is 74 556cm⁻¹ [Krause 1992].

^b 6_1^0 is 608 cm⁻¹ [Page 1988].

the two spectra. The transition to the $1_2 6_1(3/2)$ level in the cation has a more favourable Frank-Condon overlap from $6^1 1^1$ than from 6^1 due to the different quanta of ν_1 in the intermediate state.

The spectra recorded using 0^0 and 1^1 as resonant states, also show large similarities between them (figures 5.6a and 5.6b). Again, due to different Frank-Condon factors, population of the 1_1 level is enhanced for ionisation via 1^1 . No evidence for vibrational levels containing the $6_1(3/2)$ vibrational mode is seen in either spectrum. This is consistent with the angular momentum constraints discussed above. However, it is interesting to note that in the one photon work by Baltzer *et al.*, they claim to see the $6_1(3/2)$ level with an intensity similar to that of the 4_1 and 16_1 levels [Baltzer 1997]. If present in figure 5.6, the $6_1(3/2)$ level would lie midway between the 4_1 and 16_1 levels. Clearly it is absent in our spectra. Baltzer *et al.* explained the appearance of the ‘forbidden’ $6_1(3/2)$ level by the possibility of continuum state vibronic interaction in the photoionisation process [Baltzer 1997]. It is interesting to note the appearance of the

16_1 level in the photoelectron spectra. From symmetry arguments, this can only be possible if the benzene ion is non-planar.

Figure 5.8 and 5.9 shows our photoelectron spectra compared with spectra obtained using REMPI with standard time of flight techniques. The time of flight spectra were recorded by Long *et al.* and have been taken directly from their publication [Long 1983]. The abscissa in our spectra have been changed to display the energy of the benzene ion after ionisation, facilitating comparison with Long *et al.*'s work.

The most obvious difference between time of flight spectra and electron imaging spectra revealed by figures 5.8 and 5.9 is that the full range of electron/ion energies are observed in our electron imaging spectra. Using standard time of flight techniques, the detection of low energy electrons becomes impossible due to the long flight times to the detector and the susceptibility they have to stray electric and magnetic fields. These problems, along with other sources of resolution degradation, have been discussed by Allendorf *et al.* [Allendorf 1989]. In the study by Long *et al.*, these problems prevent the observation of electrons having less than 500 cm^{-1} of energy. This turns out to be a substantial amount of energy, particularly for ionising through the 6_1^0 resonant transition since it corresponds to approximately half of the excess energy. The lack of transmission for low energy electrons is not an issue in our study since the technique of electron imaging ensures that all electrons will arrive at the detector.

The lack of transmission for low energy electrons is also responsible for a second difference. Peaks corresponding to low electron energies have very different intensities for the two different techniques. In Long *et al.*'s work, the peaks are attenuated as the kinetic energy of the photoelectron reduces. This is a direct consequence of the problems noted above. The electron imaging technique, however, actively accelerates all electrons towards the detector resulting in the same flight time for all electrons. This minimises the flight time of the electrons, so they are not exposed to stray fields for

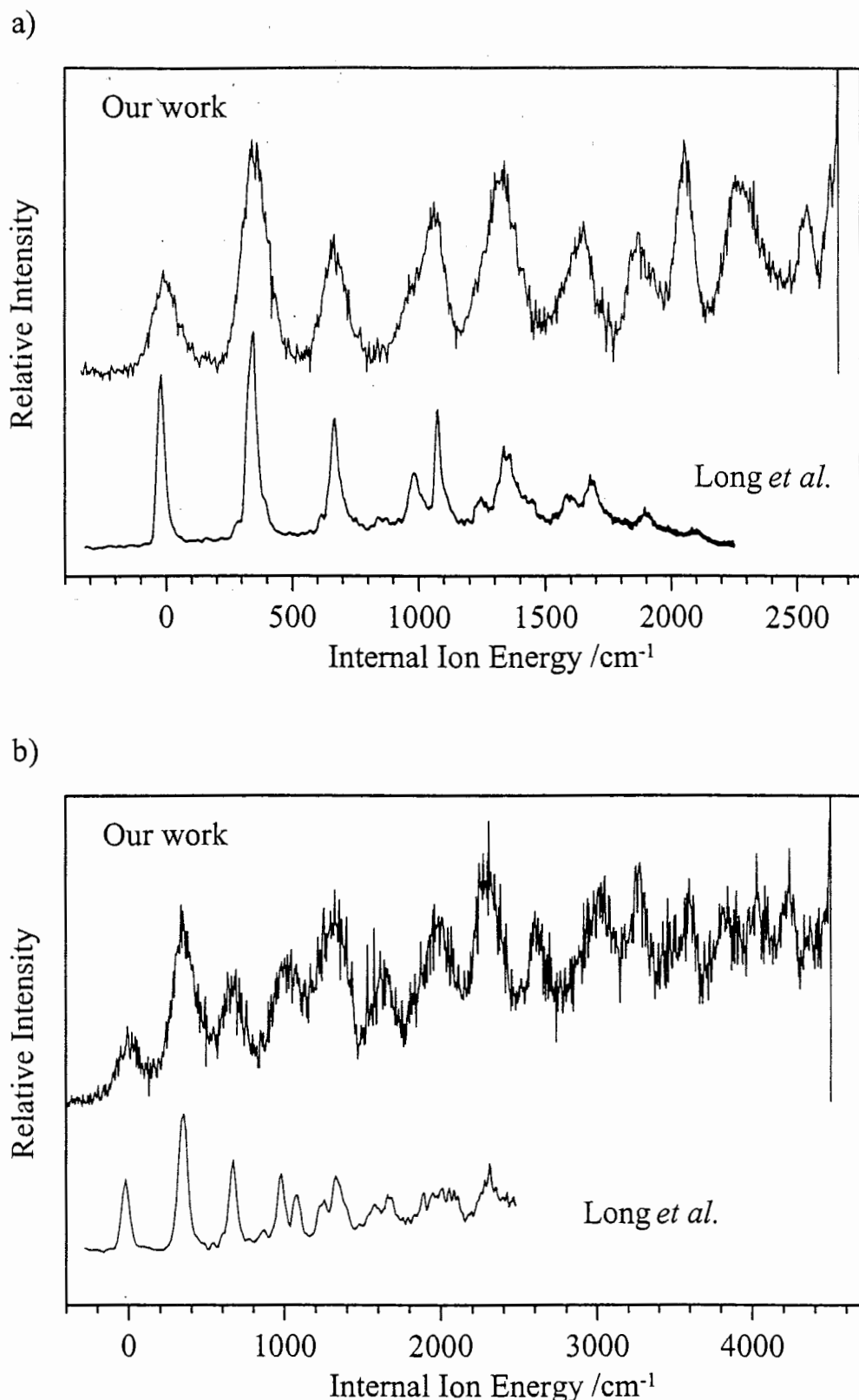


Figure 5.8 Comparison between our photoelectron spectra of benzene and those obtained by standard time of flight techniques recorded by Long *et al.* [Long 1983]. The spectra correspond to ionisation through the a) 6_0^1 and b) $6_0^1 1_0^1$ resonant levels. The x-axis represents the energy remaining in the ion.

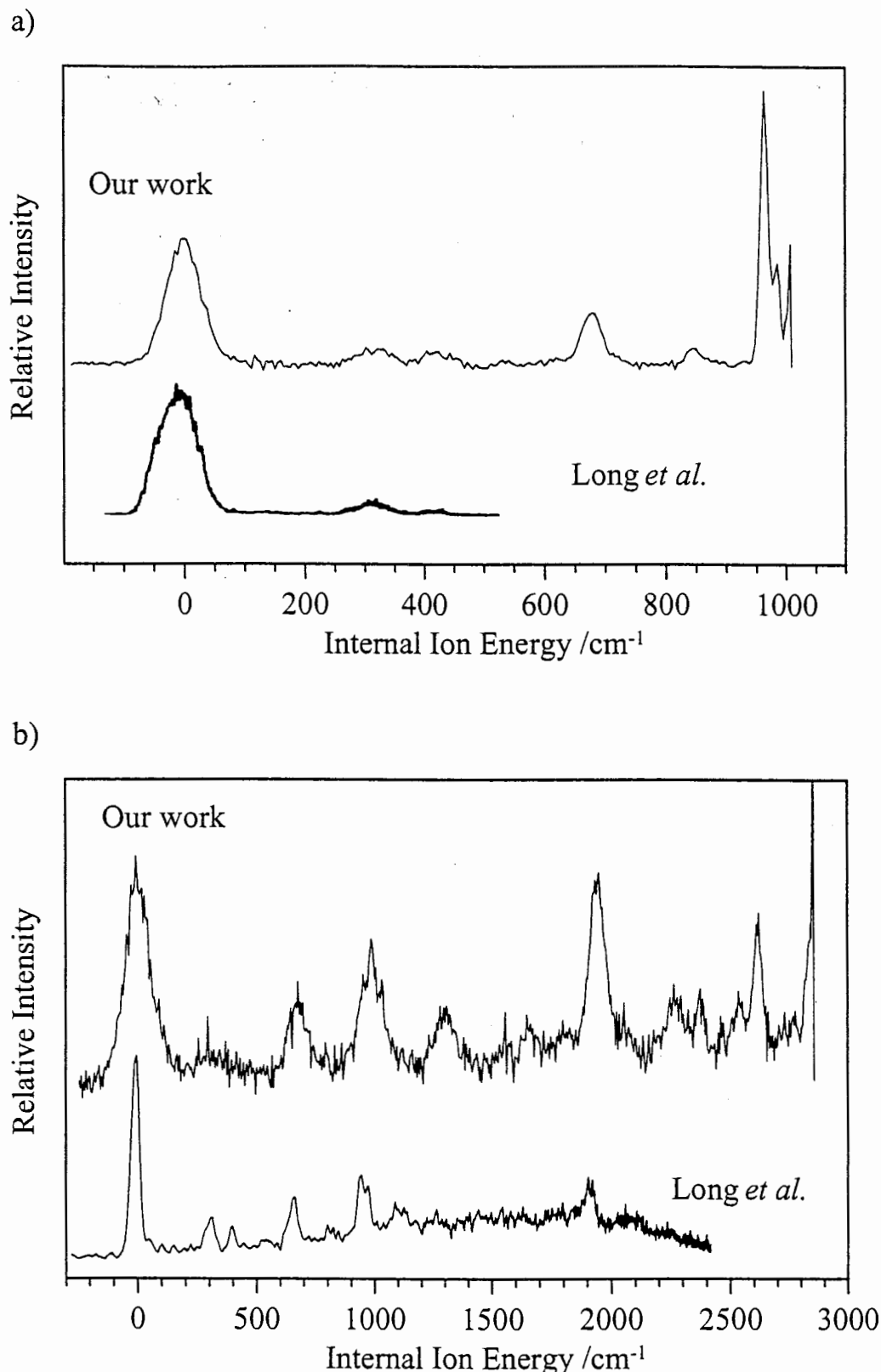


Figure 5.9 Comparison between our photoelectron spectra of benzene and those obtained by standard time of flight techniques recorded by Long *et al.* [Long 1983]. The spectra correspond to ionisation through the a) 6_1^0 and b) $6_1^0 1_0^1$ resonant levels. The x-axis represents the energy remaining in the ion.

excessive amounts of time. Thus photoelectron spectra recorded via electron imaging show more accurate peak intensities.

A knowledge of the entire photoelectron spectrum (with correct intensities) is necessary when using the information as a basis for further work. For instance, it is obvious that if one wishes to calculate Frank-Condon factors between a vibrational level in the neutral molecule to a level in an ionic state, then accurate photoelectron intensity data must be available for correct comparisons. In addition, experiments that utilise the ions produced by photoionisation often need a knowledge of the vibrational state population distribution produced. This requires correct, and energetically complete, photoelectron spectra. A specific example of this is work performed by Kiermeir *et al.* on benzene ions [Kiermeir 1988]. The only photoelectron spectra available to them were those of Long *et al.* [Long 1983], which are being discussed here. Kiermeir *et al.* produced benzene ions via (1+1) REMPI through the 6_1^0 resonant transition. From the work of Long *et al.* they assumed that more than 90% of ions were formed in the vibrational ground state of the benzene ion. As shown in figure 5.9, the results of our 6_1^0 photoionisation spectra and that of Long *et al.*'s are somewhat different, since our work does not suffer from transmission problems for low energy electrons. From our spectra, if we only consider the 4_1 , 16_1 , and 0_0 ionic vibrational levels (ie, the same levels observed in standard time of flight photoelectron spectra) then we see 84% of the population lies in the ground vibrational state. This figure is close to the value of 90% obtained using Long *et al.*'s data. The slight difference is attributed to the lower intensity of the 4_1 peak in the time of flight data as a result of the difficulties in detecting low energy electrons. However, the additional ion levels we observed ($6_1(1/2)$ and 1_1) contain significant population (48% of the total population). The time of flight method only observes half of the total number of electrons ejected. Using the complete photoelectron spectrum we find that only 43% of ions are formed in the ground vibrational level of the cation (far different from the 90% previously assumed). In other words, using standard techniques it was determined that only 10% of ions are populated

in vibrationally excited levels, but we find that this figure should be 57%. Thus, without full knowledge of the entire energy distribution, incorrect assumptions about the distributions have to be made, which may have implications on work using these distributions such as that by Kiermeir *et al.* [Kiermeir 1988]. The benefit of obtaining high resolution photoelectron spectra from the ion imaging technique is apparent.

The third noticeable difference between the spectra obtained from the two different techniques is the energy resolution. The peak widths that we have recorded are generally larger than those obtained in Long *et al.*'s work. An exception is the 6_1^0 data, for which the two techniques give spectra of comparable resolution. This is not due to any difference in experimental conditions between data sets, but is a direct consequence of the imaging technique. As discussed in the last chapter, the technique involves recording an image of the spatial distribution as the electrons hit the detector. The distance travelled from the centre axis is directly proportional to the speed (momentum) of the electrons, and since the image is recorded on a two dimensional array of constantly spaced pixels (CCD chip), it is the momentum resolution which remains constant in the image. The energy resolution obtainable in electron imaging will thus decrease with increasing energy proportional to the square root of the energy. For this reason, resolution for electron energies less than 1000 cm^{-1} are comparable with standard time of flight photoelectron spectra, but deteriorate at higher energies. As discussed in detail in chapter 4, the resolution we obtain here is reduced from the optimum because of the presence of stray magnetic fields which make the image blurred in some regions. After modification of the experimental design we expect to obtain peak widths of $\sim 20\text{ cm}^{-1}$ at electron energies of $1\ 000\text{ cm}^{-1}$.

5.3.2 Photoelectron Angular Distributions

It can easily be seen in the electron images (figures 5.1 - 5.4) that the distribution of electrons is not isotropic. Instead, electrons are preferentially ejected perpendicular to

the laser polarisation. We have used both fitting procedures as explained in the previous chapter to extract β values from the images. Firstly, a plot of the average intensity as a function of the angle was constructed and subsequently fitted to determine the anisotropy parameters. Secondly, the experimental two dimensional image was fitted using the radial plot generated from the three dimensional population distribution and variable anisotropy parameters. Although two photons are necessary to effect ionisation, and therefore the fourth order Legendre polynomial may become important, it was found by examining the residuals of each fit that only the $\cos^2\theta$ term (second order Legendre polynomial) was necessary.

In the first instance, the entire image was fitted to a single β value (i.e. fit to the equation $I(\theta) = A [1 + \beta P_2(\cos\theta)]$) using the two methods described above. The resulting values are listed in table 5.2. The β values reported represent values averaged over the rotational levels populated in the intermediate state, and all the vibrational states in the cation. Although it is known from femtosecond studies that anisotropy parameters depend on the time delay between the first excitation photon and the second ionising photon, our 5 ns laser pulse width ensures that the obtained β value represents a time averaged value. The errors represent three standard deviations as determined by the fitting the entire two dimensional raw image. This error assumes that the data is represented by a single β value [Press 1992].

As shown in the table 5.2 the β values calculated using the two different techniques are the same. This demonstrates the validity of the new fitting procedure. The fitting errors are six times smaller when fitting the experimental image than fitting the plot of intensity verses angle. This is attributed to 1) only one parameter being used for fitting to the experimental image as opposed to the two parameters required for the angular fit, 2) the increased number of points that are fitted when performing an image fit, and 3) the errors associated with determining the angular histogram (particularly at low values of R) because of the pixel make-up of the image.

Table 5.2 β values from different resonant transitions. Uncertainties indicate 3σ from the fits and do not include experimental uncertainties.

| Resonant Transition | Excess Energy /cm ⁻¹ | Fitted β value | |
|---------------------|---------------------------------|----------------------|--------------------|
| | | (a) | (b) |
| 6_0^1 | 2664 | -0.334 ± 0.022 | -0.325 ± 0.004 |
| $6_0^1 l_0^1$ | 4506 | -0.353 ± 0.023 | -0.355 ± 0.003 |
| 6_1^0 | 1011 | -0.220 ± 0.060 | -0.236 ± 0.010 |
| $6_1^0 l_0^1$ | 2858 | -0.335 ± 0.028 | -0.315 ± 0.005 |

(a) Fitted using a plot of the average intensity as a function of angle.

(b) Direct fitting of the experimental two dimensional image.

The measured β values range between -0.23 and -0.36. These values represent distributions in between an isotropic distribution ($\beta = 0$) and a $\sin^2\theta$ distribution ($\beta = -1$). Classically, this indicates that the electron experiences substantial torque as it is ejected from the molecule [Manson 1978], or quantum mechanically, the outgoing electron wave is scattered as it leaves the molecule. We have found that this is very different to the anisotropy of electrons photoejected from the (1+1) REMPI of *para*-difluorobenzene (*p*DFB). Using the same electron imaging instrument, we have found β values for REMPI of *p*DFB excited to similar excess energies as used here. It was found those values ranged between +1.0 and +1.4 [Bellm 1999]. An interesting trend in the anisotropy values determined for benzene is the dependence of the β value on the excess energy available to the ion. Figure 5.10 shows this dependence to be approximately linear over the energy range, decreasing as the excess energy increases.

An advantage of the fitting to the two dimensional experimental images to determine β is that one can visually compare the experimental and calculated images. From such a

comparison it appears that the outside rings generally have an anisotropy larger than that of the inner rings. For example, when ionising via the 6_0^1 transition it appears that the anisotropy becomes more negative as the electron kinetic energy increases. In order for us to examine this further, we have determined the variation in the β values with the final vibrational cation state using a number of different methods. The methodologies were developed using data for the 6_0^1 image and are discussed below.

In the first method the 6_0^1 three dimensional image was divided into nine separate annuli, each encompassing one of the main peaks seen in the photoelectron spectrum. For each annulus, a plot of the intensity versus the angle is constructed (see chapter 4). These angular distributions are subsequently fitted to the form $I(\theta) = A [1 + \beta P_2(\cos\theta)]$ where A and β are adjustable parameters, and $P_2(x)$ is the second order Legendre polynomial given by equation 4.5. An example fit is shown in figure 5.11 where data for populating $6_1(3/2)$ is shown. The β value of each peak is plotted against the electron energy corresponding to each peak and is shown in figure 5.12. It can be seen from analysing each peak individually that, over the entire energy range, the β value tends to get more anisotropic (more negative β value) as the electron energy increases, consistent with our observations from comparing the experimental and calculated two dimensional images.

The remaining methods of data analysis fit the experimentally derived radial data to the experimental two dimensional image while varying the beta value, as discussed in chapter 4 (section 4.3.5). For the second method we divide the three dimensional distribution radial plot (plot of average intensity versus the radius) into the nine regions corresponding to the major peaks seen in the photoelectron spectrum. Each peak was assigned an independent β value which was adjusted by the fitting procedure until a good match resulted between the raw image and the computed image. That is, a β value was determined for each peak by simultaneously fitting the nine β parameters to the raw image. The results of this fitting procedure are also shown in figure 5.12. Although we

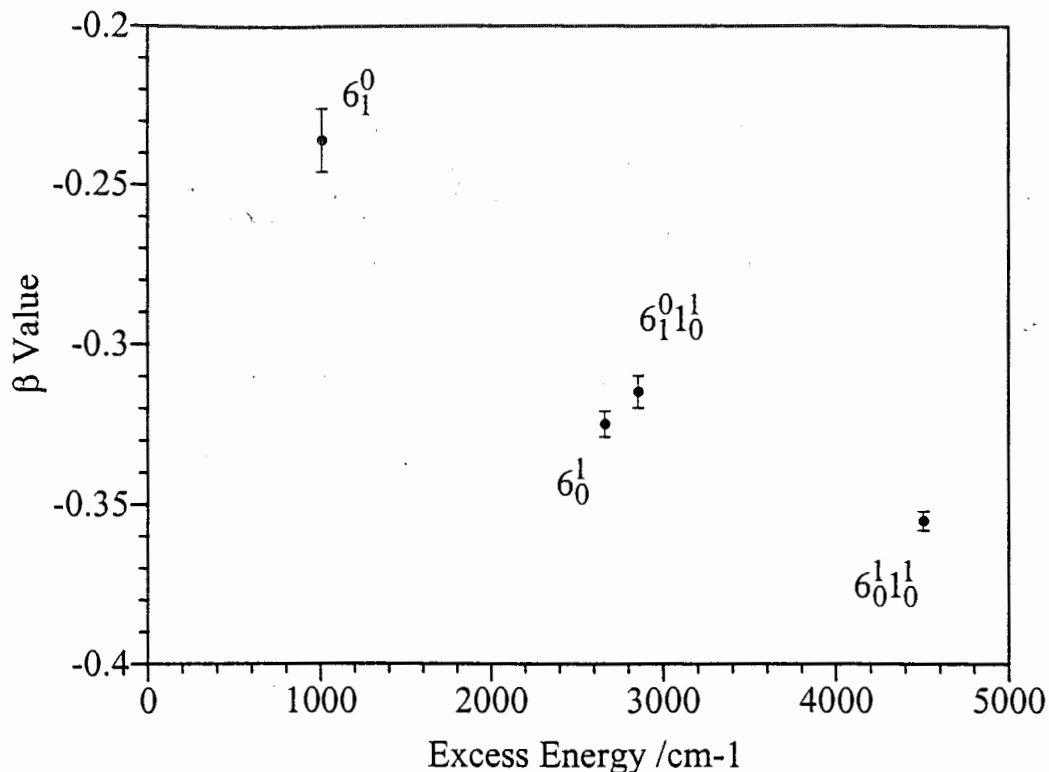


Figure 5.10 β parameters plotted against the excess energy for the (1+1) REMPI of benzene through the four resonant states studied.

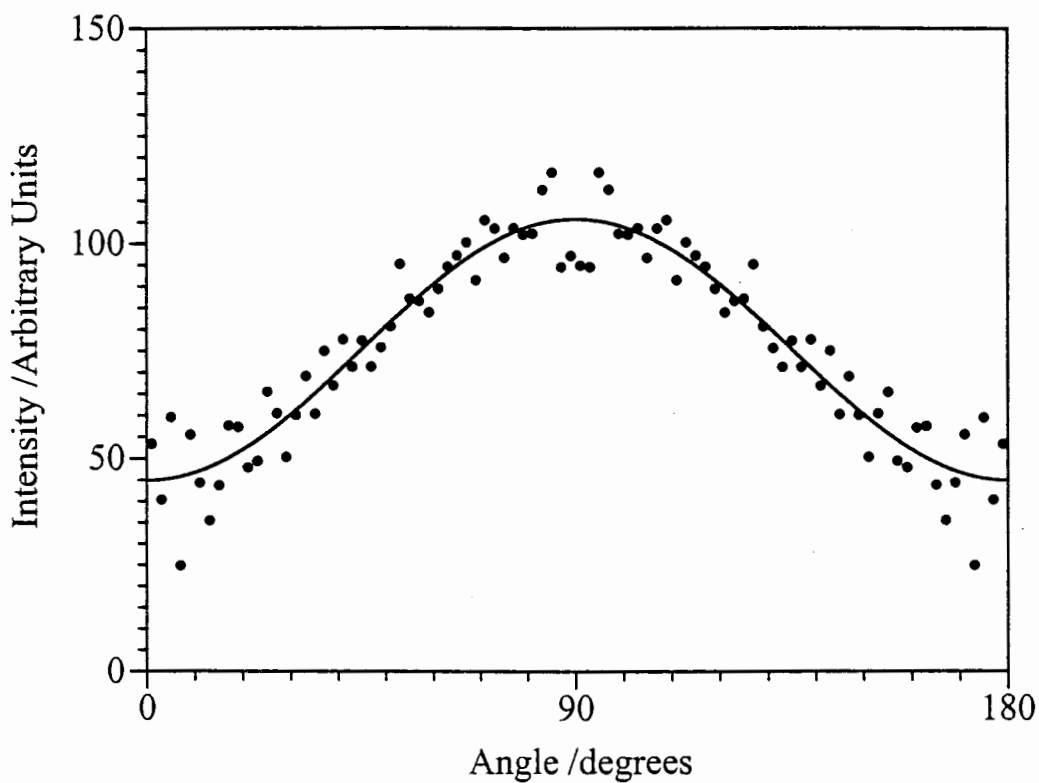


Figure 5.11 Photoelectron angular distribution for ionisation into the $6_1(3/2)$ vibrational level for the (1+1) REMPI of benzene via the 6_0^1 resonant transition. The smooth solid line represents the best fit β parameter.

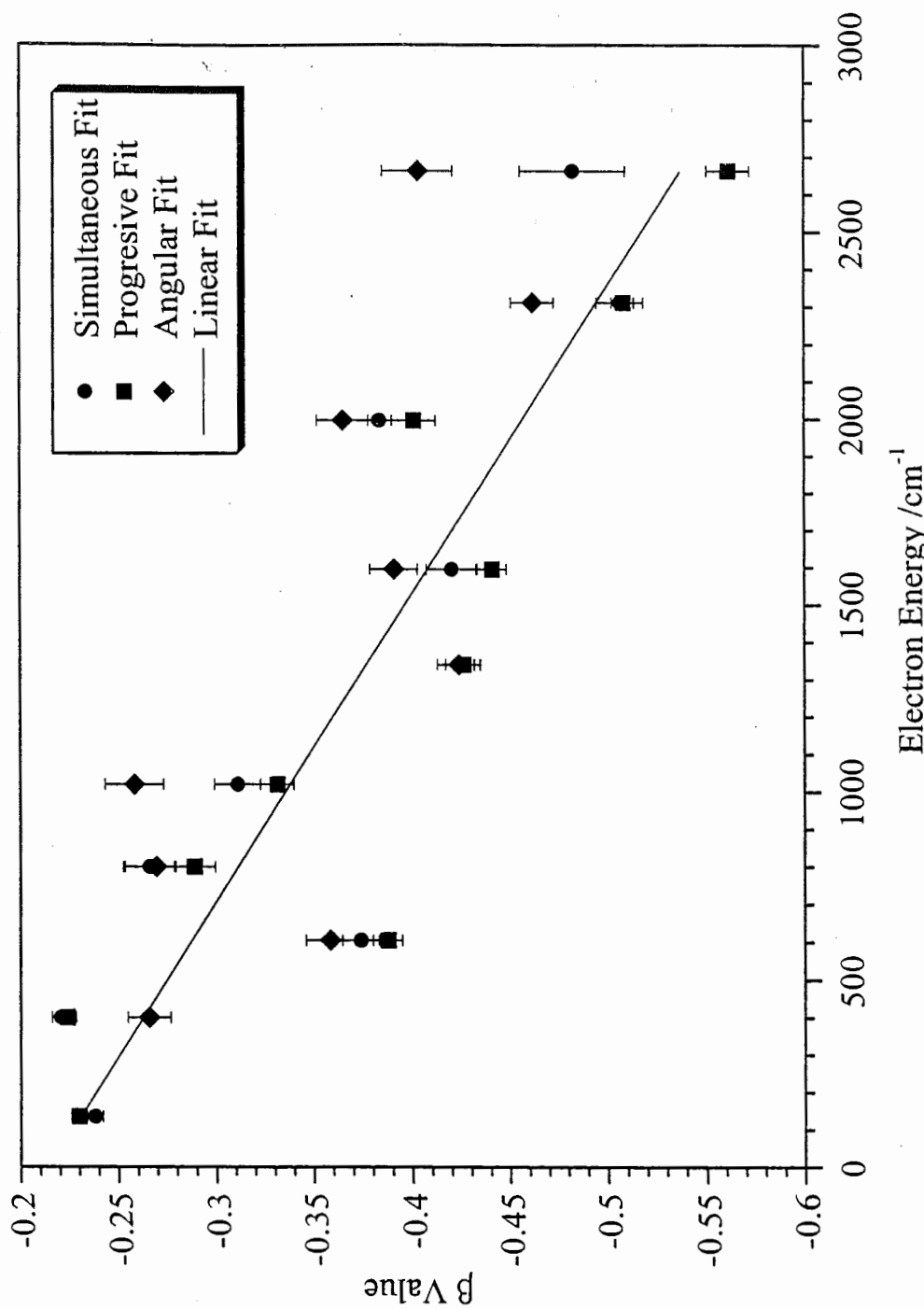


Figure 5.12 β parameters plotted against the electron energy for the nine major peaks seen in the 6_0^1 (1+1) REMPI photoelectron spectrum of benzene. Results using the three different methods used to determine anisotropy parameters are shown (see text for details). Errors representing 1σ and are determined by the fitting procedure. The solid line is obtained by fitting the image assuming β is linear with electron energy.

recognise the dangers in fitting data on a noisy nine dimensional surface, the calculated β values show a similar trend, where they decrease as the electron energy increases.

The third method of data analysis divides the three dimensional distribution radial plot into the nine regions as done in the previous method. A β value is determined for each peak one at a time. This is achieved by first fitting the outermost peak in the radial plot to the outermost ring in the raw image. This can be done since the forward Abel transform only requires data from infinity to the radius that is currently being calculated (see equation 4.1). In other words, none of the lower energy peaks are required in the fitting of the outermost ring. After a β value is determined for the outermost ring, the second to last peak is subsequently fitted to the raw image while keeping the beta value for the last peak fixed to the previously determined value. This allows the β value of the second to last peak to be determined. This process of sequentially determining β values continues for each of the nine peaks, allowing anisotropy parameters to be calculated for every peak. β values determined in this way are also shown on figure 5.12 and again show the general trend of increasing anisotropy as the electron energy is increased.

As evidenced in figure 5.12, each of the three fitting methods described above show that the β values tend to get more negative as the electron energy increases. The figure shows that the each of the different fitting methods return similar results. In fact, for all but the highest energy peak, there exists overlap within the 99% confidence level ($\pm 3\sigma$) for individual β values obtained using the three different methods. Furthermore, the trend appears to be linear with energy. This has prompted us to consider fitting the raw data assuming β to be linear with the electron energy. That is, using the radial plot data, we generate β values as a function of the radius, $\beta(r) = A + Br^2$, where A and B are adjustable parameters. The r term appears squared since the energy is proportional to the square of the radius. The A and B parameters are adjusted until a good fit is obtained with the raw image. We have chosen a linear function for simplicity, not

Table 5.3: Parameters obtained by fitting β to the data assuming a functional form of $\beta(E_{Kinetic}) = A + BE_{Kinetic} + C(E_{Kinetic})^2$. C was set to zero for the 6_0^1 , 6_1^0 , and $6_1^0 1_0^1$ images.

| Resonant Transition | Fitted Parameters | | |
|---------------------|-------------------|------------------------|-----------------------|
| | A | B /cm | C /cm ² |
| 6_0^1 | -0.214 | -1.21×10^{-4} | - |
| $6_0^1 1_0^1$ | -0.161 | -2.41×10^{-4} | 4.90×10^{-8} |
| 6_1^0 | -0.252 | 5.90×10^{-5} | - |
| $6_1^0 1_0^1$ | -0.285 | -2.85×10^{-5} | - |

because it has any physical significance in the ionisation process. The best linear fit using this method is shown as the solid line on figure 5.12, and appears to be a valid representation of the β values as determined by the other three methods.

The success of fitting β values to the 6_0^1 data set has allowed us to extend the fitting methods to the remaining data. We have used the simultaneous fitting procedure (fitting different β values to each peak at the same time) to determine β values for the major peaks seen in each of the photoelectron spectrum. We have chosen this procedure since it consistently gives values that are between those returned by the other two fitting methods, and is much easier to implement. Assumed forms for the manner in which β values varied with electron energy were also fitted. For 6_0^1 , 6_1^0 , and $6_1^0 1_0^1$ data sets, a linear function was assumed, but for $6_0^1 1_0^1$ a parabolic function was necessary. Figure 5.13 shows the β dependence on electron energy for each of the resonant transitions used for photoionisation. The parameters found by fitting the four images to assumed forms of the β dependence are tabulated in table 5.3.

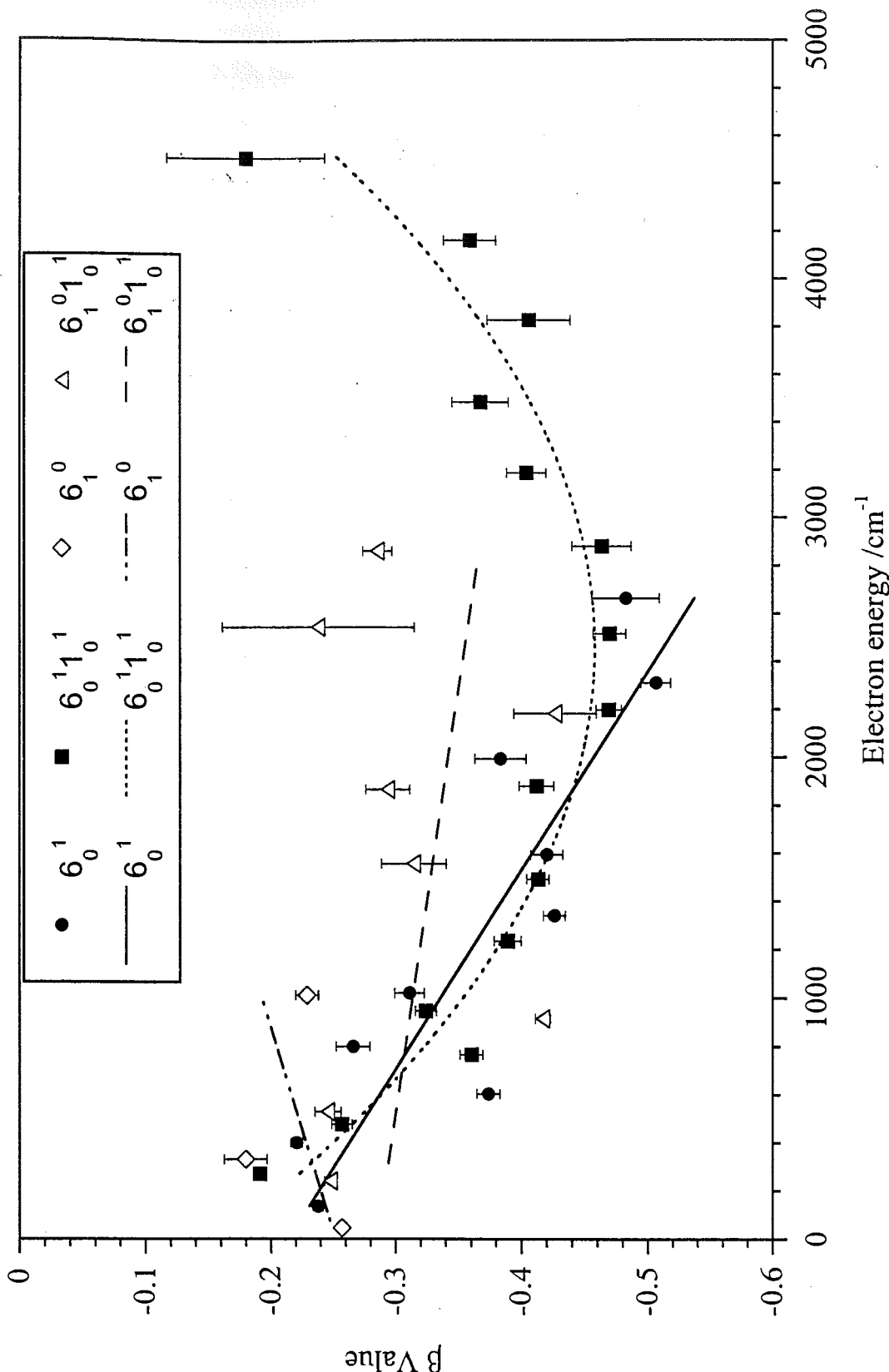


Figure 5.13 Fitted β values as a function of the electron energy for the four resonant transitions used for the (1+1) REMPI of benzene. The resonant transitions are labelled on the diagram. The points represent the β values determined by simultaneously fitting each vibrational peak in the image to a unique value of β . The lines are the result of fitting the image using an assumed form for the energy dependence of β .

As shown in figure 5.13, the anisotropy for each data set is approximately the same at low electron energies (β between -0.2 and -0.25). For the 6_0^1 and $6_0^1 1_0^1$ data sets, the β value data steadily decrease to approximately 2500 cm^{-1} . This is the maximum energy in the 6_0^1 data set. The $6_0^1 1_0^1$ data shows a minimum here, and the β values proceed to higher (less negative, i.e. the electron is less directional) values as the electron is ejected with more energy. Data for the 6_1^0 transition shows a tendency for β values to increase towards a more isotropic distribution with increasing energy. This, however, is tentative, since there are only a few data points covering a small energy range. The $6_1^0 1_0^1$ data set consists of a number of points that appear more scattered than any other data set. Fitting β to a linear function in energy, we find a slightly decreasing β value as the electron energy increases. It is difficult to say without further investigation whether the different behaviour between the $6_1^0 1_0^1$ data set and the 6_0^1 and $6_0^1 1_0^1$ data sets is due to ionisation through an intermediate state not containing a quanta of v_6 .

It would be interesting to see if there was any correlation between the final vibrational level populated and the anisotropy. Unfortunately this is currently unachievable because the limited resolution does not allow the complete separation of different vibrational peaks in the photoelectron spectrum.

We are unaware of any anisotropy parameters that have been measured for (1+1) REMPI of benzene with which comparisons can be made. One photon studies, however, show β to vary with electron energy [Baltzer 1997]. In this particular study, β was measured over all vibrational levels in the ground ionic state. Between the photon energies of 12.9 and 15 eV ($29\ 500 - 46\ 500\text{ cm}^{-1}$ excess energy), β rises from a near isotropic distribution to $\sim +0.3$ and then falls to near zero again. At photon energies above 15 eV, the β value rose steadily to ~ 30 eV where it subsequently leveled out to a value of $\sim +1.5$. In our experiments benzene is ionised from an excited electronic state, and ionised with much lower excess energies ($1000 - 5000\text{ cm}^{-1}$), making comparisons impractical. Further discussions of the anisotropy parameters require comprehensive

calculations to reveal the processes involved in the photoionisation through S_1 vibronic levels including the role, if any, of autoionisation (ionisation from a vibrationally excited Rydberg state). These calculations are beyond the scope of this thesis.

Our REMPI imaging experiments on the large polyatomic benzene have allowed us to measure anisotropy parameters resulting from the population of individual vibrational levels in the cation. We have shown that the anisotropy varies depending on the vibrational states populated in the cation. There appear to be very few data available that probe the variation of β with vibrational state, and hence it is not clear how general the behaviour observed here might be.

Photoelectron angular distributions have been measured for a number of large polyatomics using single photon ionisation, typically with a He(I) source. Such studies generally do not achieve vibrational resolution. The photoelectron angular distributions determined are values averaged over a wide range of electron energies, and therefore averaged over many vibrational levels. We have been able to find very few studies of photoelectron angular distributions using REMPI. Those that we could find pertain to small molecules, including the diatomics NO and H₂ and small polyatomics such as H₂O [Allendorf 1989, Öhrwall 1998, Lee 1992]. REMPI studies of small molecules have achieved measurements of photoelectron angular distributions with rotational resolution for highly excited rotational states.

The electron imaging experiments by Parker and Eppink show that ionisation of O₂ Rydberg states produces vibrationally excited O₂⁺ with the photoelectrons ejected in a $\sim \cos^2 \theta$ distribution for low vibrational quanta, and $\sim \sin^2 \theta$ distribution for high quanta (~20) [Parker 1987]. Molecular hydrogen also shows a variation in anisotropy with the populated vibrational level [Öhrwall 1998]. Öhrwall *et al.* measured the photoelectron spectra using He(I) radiation and a high resolution hemispherical analyser [Öhrwall 1998]. Since the rotational constants are very large for H₂, they were able to

record rotationally resolved photoelectron spectra. It was found that β values were constant (~ 1.85) for $\Delta N = 0$ rotational transitions in different vibrational levels, but β decreased for $\Delta N = \pm 2$ rotational transitions as the vibrational quanta increased. Allendorf *et al.* also find the anisotropy to be very sensitive to the rotational transition in their two colour REMPI studies of NO [Allendorf 1989].

5.4 Conclusion

We have shown the usefulness of the electron imaging technique for recording photoelectron spectra. Problems encountered in standard high resolution photoelectron spectroscopy vanish when using the electron imaging technique. This especially true for the detection of low energy electrons, which is traditionally difficult. The 100% collection efficiency allows a true representation of the vibrational distributions formed in the ion to be measured. This can be particularly important if one wishes to use the ion's vibrational distribution formed after ionisation as a starting point for further experiments. Photoelectron spectra with resolution equivalent to field free time of flight spectra can be routinely obtained. Modification of the present apparatus will allow even greater energy resolution.

In this work we have recorded photoelectron spectra with much lower electron energies than previously published. The maximum energy seen was ionisation from the $6_0^{1,1}$ (1+1) REMPI of benzene where population of the vibrational ground state produced electrons with $\sim 4\ 500\ \text{cm}^{-1}$ ($\sim 0.56\ \text{eV}$), with features clearly seen, and resolved at electron energies less than $200\ \text{cm}^{-1}$ ($\sim 0.025\ \text{eV}$). This is in stark contrast to most other electron imaging studies, where electron energies in excess of $40\ 000\ \text{cm}^{-1}$ (5 eV) are recorded, and very low energy electrons would be unresolved. The resolution we have obtained is similar to other electron imaging studies. For example Parker *et al.* give the

relationship $W \approx 20\sqrt{E}$ where W is the width of a nonoverlapped photoelectron peak (in meV) and E is the kinetic energy of the electron (in eV) [Chandler 1999]. From the 6_0^1 spectrum, we find our peak widths to be also given by this approximately formula and believe that resolution will substantially improve after modifications to the instrument (see chapter 4, section 4.5.4).

Electron imaging also allows the simultaneous measurement of the photoelectron angular distribution along with the energy distribution of the ejected photoelectron immediately following photoionisation. Information from these types of experiments will allow an increased understanding of the ionisation process in polyatomic molecules. Anisotropy parameters can be easily extracted from REMPI of molecules using the electron imaging technique, which has a clear advantage over more common techniques where the time consuming process of recording photoelectron spectra at many different orientations was required. Electron imaging opens up this field of research to routinely measure photoelectron angular distributions for molecules using various REMPI schemes.

Electron imaging of molecules has so far been limited to small polyatomics, with the notable exception of the work on pyrazine by Suzuki *et al.* [Suzuki 1999]. This work, however, concentrated mainly on the presence or absence of two well separated rings to infer information about the decay of the first excited singlet state. We have shown that the technique of electron imaging can be expanded to obtain reliable high resolution photoelectron spectra of large polyatomics, equal to the standard time of flight techniques currently used.

For benzene the average anisotropy parameter β was found to vary between -0.23 and -0.36 for the different intermediate states used in the REMPI process. On further investigation it was found that the anisotropy was dependent on the kinetic energy of the ejected electron. For ionisation via the $6_0^1 1_0^1$ resonant transition the data revealed a

decreased in β (increasing anisotropy) for energies up to $\sim 2500 \text{ cm}^{-1}$, after which the β value proceeded to increase towards an isotropic distribution. β values determined from the 6_0^1 data follows the same values as the $6_0^1 1_0^1$ data up to the maximum available electron energy. Ionisation through 6_1^0 , gives a slight increase in β with electron energy, while ionising through $6_1^0 1_0^1$ shows a slight decrease with energy.

Chapter 6

Photodissociation of benzene cation - argon_n (n=1,2) van der Waals clusters

6.1 Introduction

The study of Van der Waals clusters represents a very active area in physical chemistry research. The importance of this research is demonstrated by the number of journal issues devoted entirely to this topic [Chem. Rev. 1988, 1994; Faraday Disc. 1994]. There are several reasons for the continued interest in these types of systems. Van der Waals clusters allow the continuous study of physical properties between a bare molecule and one completely solvated [Felker 1994]. That is, by using mass selective techniques, a molecule surrounded by a known number of solute molecules can be investigated. In this way a particular physical property can be measured for a cluster where the number of solute molecules ranges from one up to the maximum permissible in the experimental apparatus used. Van der Waals clusters also allow the weak dispersion forces which bind these clusters to be studied from both an experimental and theoretical point of view. These interactions are important in many diverse areas of chemistry such as crystal packing, adsorption and molecular biology [Hobza 1994].

Van der Waals complexes are entities consisting of two or more molecules held together by weak intermolecular forces such as induced dipole - induced dipole

interactions. This weak bonding leads to the dissociation of van der Waals clusters with only small amounts of internal energy. At these low energies (low density of states), it is possible to observe the dissociation from different discrete cluster vibrational levels [Stephenson 1984; Jacobson 1988, Brumbaugh 1983]. These studies reveal how the dissociation rates depend on both the total energy in the cluster, and the type of vibration which was initially excited. An upper limit of the dissociation energy can be also be determined from these studies by noting the energy at which child products start to appear.

Dissociation of van der Waals clusters has been described as a ‘half collision’ [Rice 1986]. While a ‘full collision’ requires a collision partner to approach the target molecule, interact, and then finally leave, the ‘half collision’ of van der Waals molecule dissociation mimics the second half of this process. There was early optimism that studies of state-to-state energy transfer pathways in van der Waals molecule dissociation would reveal similarities with those seen in collision induced vibrational energy transfer for the same systems. Generally it has emerged that while the same subset of vibrational levels are populated in the two processes, often the state-to-state preferences are different [Rice 1986]. This may be due in part to the dependence of the state-to-state propensities for collision-induced vibrational energy transfer on the collision energy. Experiments on benzene-N₂ collisions, for example, reveal a shift towards the van der Waals molecule dissociation propensities with decreasing temperature [Waclawik 1993].

In addition to the difference in collision energies between van der Waals molecule dissociation and collision induced vibrational energy transfer, the former having zero collision energy, it has been pointed out by Bernshtein *et al.* that van der Waals molecule dissociation is also far more constrained [Bernshtein 1999]. This is because it always starts from the same geometry while a collision can take place anywhere around the surface of the molecule [Bernshtein 1999]. While the two types of ‘collisions’ have

the same interaction potential, in van der Waals molecule dissociations only a portion of the potential is sampled.

As we have noted in chapter 1, a longer term goal of our research group is to study collision-induced energy transfer using ion imaging detection. The study of van der Waals molecule dissociation using our single beam apparatus provides an opportunity to study systems of relevance to this longer term goal.

During a recent US/Australia workshop on “Large Molecule Energy Transfer”, diversifying studies of collision-induced energy transfer to more chemically relevant systems such as free radicals, ions, floppy molecules and those with internal rotors was identified as an essential future direction for research [King 1996]. Energy transfer in ion-neutral molecules is an area where data are required. Using our apparatus we can provide related data through the study of the dissociation of ionic aromatic van der Waals complexes. In this chapter we present data for the translational energy released during the dissociation of the ionic van der Waals complexes $(C_6H_6 \cdots Ar)^+$ and $(C_6H_6 \cdots Ar_2)^+$.

6.2 Previous Studies of van der Waals Molecule Dissociation

Many studies have investigated photodissociation of van der Waals clusters ranging from simple atom-diatom complexes [Smalley 1976] through to clusters consisting of multiple aromatic ring systems bound to polyatomic molecules (see, for example, Even *et al.*’s work on tetracene- X_n and fluorene- X_n clusters [Even 1983]). With such a diverse range, and given the focus of our experiment on aromatic ion systems, we limit ourselves to a discussion of van der Waals clusters containing a single aromatic molecule.

Photodissociation investigations involving aromatic van der Waals complexes have been performed on both homo- and hetero-molecular species. As we discuss below, the majority of studies have monitored the vibrational state of the aromatic after dissociation of the complex from a particular initial vibrational state. Due to the experimental difficulties involved, few studies have measured the translational energy released after dissociation. Early work was performed on the ground state benzene dimer ($C_6H_6)_2$. These experiments used an infrared laser to excite either the C-H stretching vibration ($\sim 3000\text{ cm}^{-1}$) [Vernon 1981] or the C-H in plane vibration ($\sim 1000\text{ cm}^{-1}$) [Johnson 1986; Nishiyama 1985] and inferred the recoiling translational energy distribution by either using time of flight methods [Nishiyama 1985] or by measurement of the angular distribution of the fragments [Vernon 1981].

The majority of studies of hetero-molecular systems, i.e. aromatic-X, have utilised the fortuitous properties of aromatic excited electronic states. The S_1 vibronic states of aromatics generally have strong absorption transitions that are within easy reach of commercial dye lasers, are relatively long lived, and have high fluorescence quantum yields, making them easy to study. In these studies, the aromatic-X complex was excited to a particular vibronic level in S_1 , and the dispersed fluorescence spectrum recorded. The fluorescence spectra were searched for peak positions corresponding to emission from the bare aromatic molecule. That is, after absorption and subsequent dissociation, the aromatic molecule was left in a number of different vibrational states. Emission from these final states allowed the observer to identify which vibrational levels were populated in the aromatic after dissociation, and the rate at which they were populated [Nimlos 1989; Jacobson 1988]. Conclusions from these works will be discussed below.

Two different approaches to analysing van der Waals dissociation data have been used [Nimlos 1989]. The first method considers intramolecular vibrational energy redistribution (IVR) and dissociation as distinct parallel processes. That is, the two

processes are totally independent of each other, and so a simple kinetic analysis can be applied. This was the original way to view such data. It has now been postulated (second method) that the dissociation process proceeds via a sequential process. That is, vibrational energy in the aromatic unit must first be transferred to the van der Waals modes through IVR. Once this energy is located in the van der Waals modes, IVR within these modes is assumed fast, so dissociation will occur as soon as enough energy is deposited into the reaction coordinate. This serial process relies on the vibrational modes within the aromatic being separated from the van der Waals modes. This is possible since the van der Waals modes are of much less energy than the aromatic modes, and it is seen that the vibrational frequencies of the aromatic molecule in aromatic-X clusters are virtually unchanged from the bare aromatic frequencies, indicating very little coupling. Using this approach, the theory of Rice-Ramsberger-Kassel-Marcus (RRKM theory) can be used to calculate dissociation rates if one limits the active phase space to only the van der Waals modes.

The first studies of dissociating aromatic van der Waals complexes were performed on *s*-tetrazine-Ar using laser induced fluorescence followed by dispersed fluorescence spectroscopy [Brumbaugh 1983; Ramaekers 1983]. Dissociation rates were found to be insensitive to the initial vibronic level that was populated. The vibrational levels populated in bare *s*-tetrazine after dissociation were, however, very dependent on the initially populated level and indicated that the out of plane modes ν_{16a} and ν_{16b} were important intermediates in the dissociation process [Ramaekers 1983]. Significant rotational excitation of *s*-tetrazine was also observed after dissociation.

The dissociation of benzene-Ar and benzene-He was also studied by laser induced fluorescence [Stephenson 1984]. Dissociation of these complexes populates only a small fraction of the possible states that are energetically available. In the case of benzene-Ar it is interesting that no dissociation was observed from the 6^1 level even

though recent work has determined that the binding energy is actually far less than the energy of the 6^1 vibrational level [Koch 1998].

Extensive *p*-difluorobenzene-Ar (*p*DFB-Ar) dissociation studies show very interesting results [Jacobson 1988]. The main conclusion reached is that the dissociation dynamics are highly dependent on the initial level populated. For example, initially exciting combination bands containing one quantum of the van der Waals stretch does not follow a rational pattern. The rate of dissociation from 5^1s^1 is approximately half that of 5^1 , but dissociation from 6^1s^1 is approximately twice that of 6^1 . v_8 (v_{16a} in Wilson's numbering scheme) in *p*DFB-Ar is unique since the frequency shift between the bare *p*DFB and *p*DFB-Ar is half that seen in all other modes. Thus there appears some sort of interaction between v_8 and the added argon atom, and one might expect to see an enhanced dissociation rate from this level. However, dissociation from 8^1 is either very slow or does not occur at all. Strangely, 6^2 dissociation is slower than 6^1 . *p*DFB-Ar van der Waals dissociation is clearly not just dependent on symmetry or the density of states.

Studies on aniline-Ar and aniline-CH₄ clusters from four vibronic levels show that dissociation of these clusters proceeds via a serial process [Nimlos 1989]. It was found that when aniline-Ar dissociated all vibrational levels that were energetically possible were populated. However, in aniline-CH₄ dissociation only the ground vibrational state in aniline was populated. It was concluded that the density of states of van der Waals modes is the most important parameter to account for the differences seen between the two clusters, and that the observation could only be explained by a serial process.

The strange behaviour seen in the above experiments is not without some theoretical backing. Molecular dynamics simulations of C₆H₆...Ar_n complexes were recently performed by Vacek *et al.* [Vacek 1998]. They studied the dynamics of IVR within the vibrational modes of benzene, and of IVR from the vibrationally excited benzene mode

to the van der Waals mode. They conclude that the rate of IVR between benzene vibrations and van der Waals vibrations is very slow and this is attributed to the energy mismatch between the vibrational modes of benzene and the van der Waals modes. More importantly, they say that the rate does not depend on the magnitude of the vibrational quantum, and low frequency benzene modes are not necessarily more efficient. This is similar to the behaviour seen in *p*DFB-Ar dissociation studies discussed above [Jacobson 1988].

A recent study by Yoder *et al.* has looked at the recoil velocities from the dissociation of triplet pyrazine-Ar using the ion imaging technique [Yoder 1999]. This is the only previous study of van der Waals molecule dissociation using the ion imaging technique. Yoder *et al.* observe that only a small fraction of the available vibrational energy is taken away as translational energy.

6.3 C₆H₆···Ar_n: Summary of Previous Work

Since our studies of benzene cation-argon clusters are produced via REMPI of benzene-argon neutral clusters, a knowledge of the behaviour of the neutral systems is essential for our work.

C₆H₆···Ar_n complexes are prototypical aromatic-atom van der Waals complexes used for experimental and theoretical studies because of their simplicity, high symmetry, and the vast amount of knowledge that exists for the benzene molecule. Much work has thus been performed on these systems. C₆H₆···Ar has been characterised by high resolution absorption spectra [Riedle 1996a, 1996b], microwave spectra [Brupbacher 1990], high resolution Raman spectra [Kim 1997] and numerous other experimental techniques. Extensive *ab-initio* calculations have been performed on C₆H₆···Ar to determine the

exact nature of the benzene-argon interaction potential [Koch 1998, 1999]. $C_6H_6 \cdots Ar_2$ has also been the focus of some experimental [Scherzer 1992; Weber 1991] and theoretical studies [Hobza 1996; Vacek 1994]. Experimental work on higher order clusters (up to $n = 70$) studied the differences between members of the $C_6H_6 \cdots Ar_n$ series [Knochenmuss 1994; Easter 1998]. The results of these theoretical and experimental studies are necessary for the interpretation of our data and are therefore reviewed below.

6.3.1 $S_1 \leftarrow S_0$ Spectroscopy of $C_6H_6 \cdots Ar$

Discussion of spectroscopic properties of van der Waals complexes requires some symbols to be defined. Figure 6.1 shows these definitions labelled on a potential energy curve. The figure and labels are an extension those used by Koch *et al.* [Koch 1998]. The symbols D_e^0 , D_e^1 and D_e^+ represent the depth of the interaction well in the ground, electronically excited and ionic states respectively. The energy required for the complex to dissociate from the ground vibrational state is denoted by D_0^0 , D_0^1 and D_0^+ for the ground, excited electronic and ionic states respectively. The distinction between these terms is important for comparing experimentally determined dissociation energies with those calculated, which ignore the zero point energy.

The $S_1 \leftarrow S_0$ transition of $C_6H_6 \cdots Ar$ has been studied extensively in the literature. Early laser induced fluorescence work by Stephenson and Rice [Stephenson 1984] and resonance enhanced multiphoton ionisation (REMPI) work by Menapace and Bernstein [Menapace 1987] determined that the strong 6_0^1 transition of the complex is 21 cm^{-1} lower in energy than the 6_0^1 transition in benzene. Thus the argon atom is bound tighter in the S_1 state than it is in the S_0 state. This is attributed to the increased polarisability of the electronically excited aromatic ring [Weber 1990]. Other vibronic levels of $S_1 C_6H_6 \cdots Ar$ were observed and found to be red shifted by a similar amount

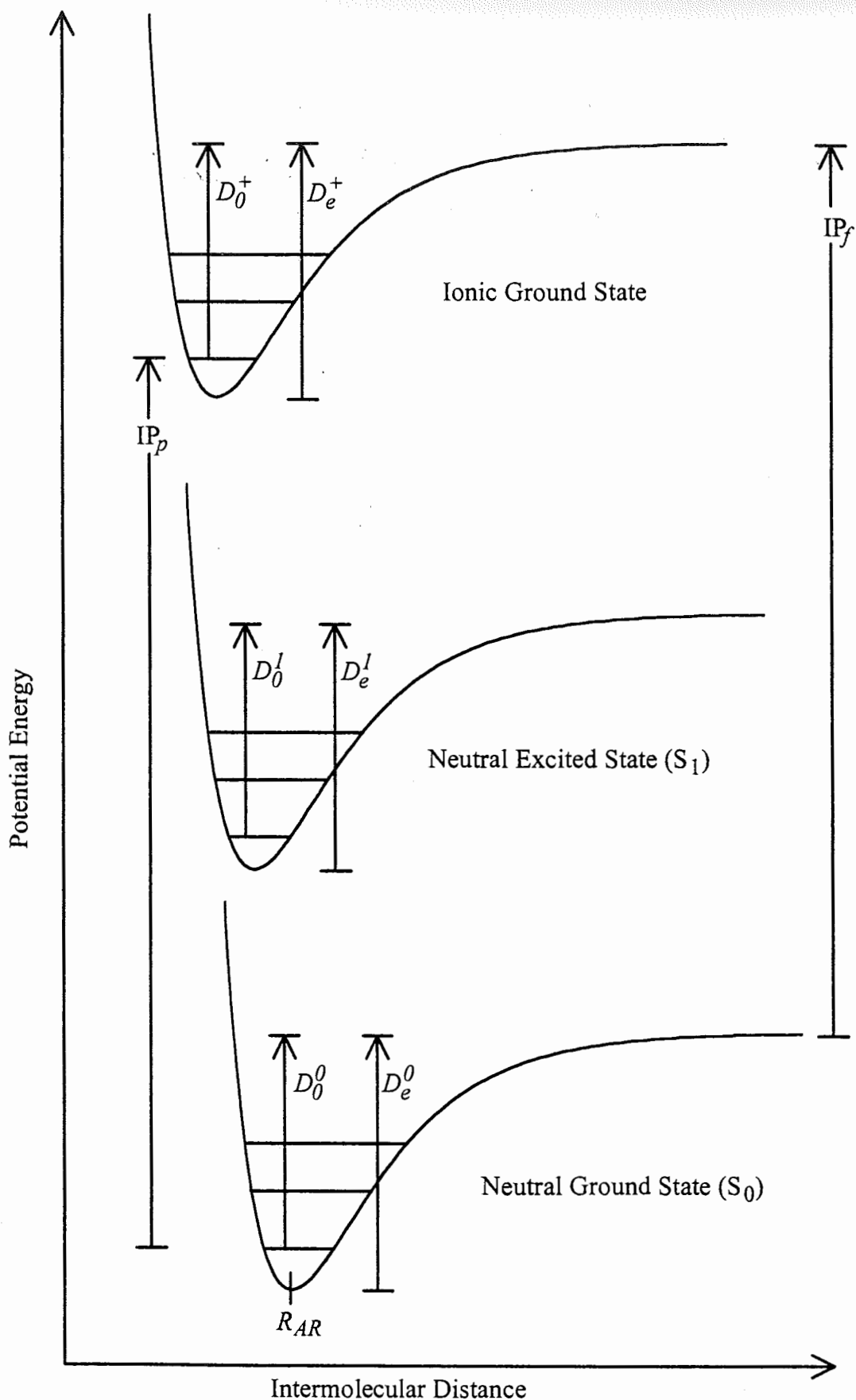


Figure 6.1 Potential energy diagram of a van der Waals molecule in the ground and excited neutral electronic states, and in the ground ionic state. The symbols used throughout this chapter are labelled on the diagram

[Stephenson 1984]. Later, rotationally resolved high resolution UV spectra of the 6_0^1 transition determined the rotationless origin to be red shifted by 21.018 cm^{-1} [Weber 1990].

6.3.2 Van der Waals vibrational modes of $C_6H_6\cdots Ar$

Although $C_6H_6\cdots Ar$ is one of the simplest aromatic-rare gas van der Waals molecules it has taken many years for the van der Waals vibrational modes to be accurately assigned and understood. Menapace *et al.* were the first to observe transitions involving these modes in the $S_1 \leftarrow S_0$ REMPI spectra around 6_0^1 [Menapace 1987]. Three transitions were observed, at displacements of $+30.9$, $+39.7$ and $+61.8\text{ cm}^{-1}$ from the 6_0^1 transition of the complex, and were assigned based on the results of simple atom-atom Lennard-Jones calculations. Later rotationally resolved high resolution work has determined the three frequencies to have energy shifts of $+31.164$, $+40.102$ and $+62.882\text{ cm}^{-1}$ relative to the 6_0^1 rotationless origin [Riedle 1996a, 1996b]. Following the original assignments by Menapace *et al.*, assignment of these observed van der Waals modes was a contentious issue for many years. All authors have agreed on the $+40.1\text{ cm}^{-1}$ peak as being due to the benzene-argon stretch, but the peaks at $+31.2$ and $+62.9\text{ cm}^{-1}$ have been assigned to a number of different combinations or overtones [Menapace 1987; Bludský 1992; van der Avoird 1993; Krause 1993a]. This was a result of the strange rotational contour of the low energy peak and anomalous peak intensities. The work of Riedle *et al.* [Riedle 1996b] has shown conclusively that the $+31.2\text{ cm}^{-1}$ transition is due to one quantum of the bend, and consequently the $+62.9\text{ cm}^{-1}$ transition is the first overtone of the bend.

In the ground electronic state of $C_6H_6\cdots Ar$, coherent ion dip spectroscopy has allowed the observation of seven van der Waals modes built on the 6_2 vibrational level [Sussmann 1995]. These modes were seen to be similar in value (within a few

wavenumbers) to their electronically excited counterparts. There is, however, a small difference in values, leading the authors to post a warning about comparing frequencies calculated using ground state potentials with the S_1 experimental frequencies (as was previously done). Later, Kim and Felker used high resolution non-linear Raman spectroscopy to measure the true (no benzene vibrational modes excited) van der Waals vibrations in the electronic ground state [Kim 1997]. They found no significant differences between the van der Waals frequencies built on either the 0_0 or 6_2 vibrational modes, thus indicating little coupling between 6_2 and the van der Waals modes. Subsequent work by Neuhauser *et al.* applied coherent ion dip spectroscopy to extend the number of known van der Waals levels [Neuhauser 1998].

6.3.3 Structure of $C_6H_6\cdots Ar$

The high resolution 6_0^1 spectrum of the complex shows that it retains the symmetric top configuration of benzene and lacks any asymmetry splitting of rotational lines [Weber 1990]. The complex must therefore have C_6 symmetry where the argon atom is located centrally above the benzene ring. The argon atom was determined to be located 3.583 Å away from the ring in the ground state and 3.523 Å in the excited state. That is, upon electronic excitation, the argon-benzene distance decreases by about 60 mÅ. The first microwave studies, performed by Brupbacher and Bauder, estimate the benzene-argon distance, R_{AR} , as 3.53 Å in the ground state [Brupbacher 1990]. All theoretical calculations pertaining to the structure of $C_6H_6\cdots Ar$ demonstrate that although there are several minima sites surrounding the benzene molecule, the least energetic configuration occurs when the argon atom is situated above the benzene ring on the C_6 axis [Hobza 1992].

6.3.4 Dissociation Energy of $C_6H_6\cdots Ar$

Experimental measurements of van der Waals molecule well depths are difficult. Determinations of the S_1 well depth are based on the disappearance of the complex signal and/or the appearance of child fragments with increasing energy. For the $C_6H_6\cdots Ar$ complex, the vibrational energy levels near the dissociation energy are very sparse so only lower and upper bounds can be obtained. The binding energy was first determined by Stephenson and Rice to be greater than 608 cm^{-1} in the ground state and 629 cm^{-1} in the excited state based on the apparent stability of ${}^1C_6H_6\cdots Ar$ [Stephenson 1984]. It is now believed from pulsed field ionisation experiments that the dissociation energy has an upper limit of $D_0^1 = 361\text{ cm}^{-1}$ and therefore $D_0^0 = 340\text{ cm}^{-1}$ [Krause 1993b].

The lack of precision in the experimental determination of the dissociation energy for $C_6H_6\cdots Ar$ means we have to rely on the ability of computational chemists to accurately reproduce the benzene-argon interaction potential. Fortunately, much effort has been directed towards calculating and describing this potential. Generally, the results of calculated potentials are used to compute the van der Waals vibrational modes and compare with known experimental values. This way the interaction potentials can be fine tuned and guided towards agreement with experiment values, thus giving more accurate potentials [Riedle 1996a]. The calculated vibrational energies have also aided assignment of van der Waals transitions in observed spectra.

The first *ab-initio* calculations for $C_6H_6\cdots Ar$ were performed by Hobza *et al.* using the MP2 level of theory [Hobza 1991]. Since van der Waals complexes are completely due to electron correlation effects, simpler theories (which exclude electron correlation) will never lead to a stable complex. From these calculations it was found that the argon *f* orbital had a large influence on the potential energy surface, causing more than a 20%

reduction in the value of the dissociation energy. D_e^0 was determined to be 429 cm^{-1} . The benzene-argon distance, R_{AR} , was calculated to be and as 3.526 \AA .

Later work, still using MP2 theory but with improved basis sets, arrive at a D_e^0 value of 553 cm^{-1} and R_{AR} of 3.41 \AA [Klopper 1994]. These authors pointed out the likely overestimation of the dissociation energy using MP2 theory, hence a higher level of theory is required to accurately determine the binding energy. Work by Hobza *et al* [Hobza 1996] used the CASPT2 method to determine the dissociation energy in the ground state $D_e^0 = 715 \text{ cm}^{-1}$ and in the excited state $D_e^1 = 787 \text{ cm}^{-1}$. These values would lead to a $S_1 \leftarrow S_0$ red shift of 72 cm^{-1} , which is more than three times that experimentally observed.

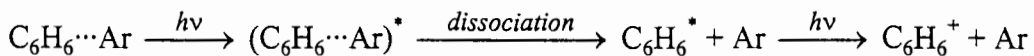
In recent work, Koch *et al.* [Koch 1998] calculated the ground state interaction using increasing levels of theory, up to couple cluster singles and doubles including connected triples corrections, and the excited state surface using couple cluster singles and doubles. After appropriate corrections, the ground state binding energy was estimated to be $D_e^0 = 389 \pm 2 \text{ cm}^{-1}$ and in the excited state $D_e^1 = 405 \pm 2 \text{ cm}^{-1}$. The calculated difference in binding energies was 16 cm^{-1} , which is reasonably close to the experimental value of 21 cm^{-1} . Koch *et al.*'s work was subsequently expanded by calculating the interaction at many different geometries resulting in a highly accurate potential energy surface for the benzene-Ar complex [Koch 1999].

Throughout this chapter the binding energies calculated by Koch *et al.* will be used. These authors give a zero point energy of 50 cm^{-1} , resulting in the dissociation energies from the first vibrational level to be $D_0^0 = 339 \pm 2 \text{ cm}^{-1}$ in the ground state, and $D_0^1 = 355 \pm 2 \text{ cm}^{-1}$ in the excited state [Koch 1999]. This value agrees well with the experimental upper limits of $D_0^0 = 340 \text{ cm}^{-1}$ and $D_0^1 = 361 \text{ cm}^{-1}$ [Krause 1993b].

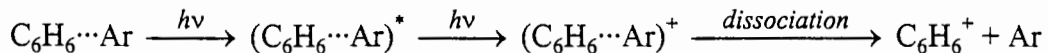
6.3.5 Dissociation Dynamics of $C_6H_6\cdots Ar$ in 1+1 REMPI

Our experiments on the dissociation of $(C_6H_6\cdots Ar)^+$ monitor the $C_6H_6^+$ product after dissociation. It is thus necessary to examine the possible pathways by which this ion may be formed in the experiment. There are two processes which will yield benzene ions from neutral van der Waals complexes. The first pathway is for the complex to dissociate on the S_1 surface after the absorption of one photon. Absorption of another photon by the benzene fragment will place it in the ionisation region. The second mechanism requires the complex to sequentially absorb two photons causing it to ionise and subsequently dissociate. The two processes can be summarised as follows:

Mechanism 1



Mechanism 2



Early laser induced fluorescence studies of $C_6H_6\cdots Ar$ showed the complex to be a stable molecule in both the 6_1 and 6^1 states [Stephenson 1984]. The evidence came from the observation of vibrationally hot 6_1 $C_6H_6\cdots Ar$ in the molecular beam, and the lack of dissociation or vibrational relaxation from the 6^1 level. Further experimental evidence comes from the two colour soft REMPI of $C_6H_6\cdots Ar$ by Schmidt *et al.* [Schmidt 1991a]. They did not observe any fragmentation when ionising through the 6^1 level.

Recent high resolution work by Riedle *et al.* have discussed the dissociation of $C_6H_6\cdots Ar$ from the 6^1 vibrational level in detail [Riedle 1996a]. They noticed no

broadening of the rotational lines in the 6_0^1 spectrum and concluded that dissociation of 6^1 must have a lifetime greater than 5 ns. Using simple calculations, they suggest the lifetime is around $70\text{ }\mu\text{s}$. Molecular dynamics simulations performed by Vacek et al. also show that dissociation from 6_0^1 is slow on a 10 ns time scale [Vacek 1998]. Thus, both the experimental and theoretical evidence is that with the 5 ns pulse width lasers used in our experiments dissociation within S_1 is negligible and the observed dissociation occurs wholly on the ionic surface, ie via mechanism 2.

6.3.6 $S_1 \leftarrow S_0$ Spectroscopy and Structure of $C_6H_6 \cdots Ar_2$

Although most attention has been paid to the simplest benzene-argon cluster, some spectroscopic work has also been performed with clusters containing two or more argon atoms. In an elegant study by Schmidt *et al.*, $S_1 \leftarrow S_0$ 6_0^1 two colour soft ionisation REMPI spectra for $C_6H_6 \cdots Ar_n$ clusters were presented for $n \leq 9$ [Schmidt 1991a]. In the 6_0^1 region of $C_6H_6 \cdots Ar_2$, three peaks were observed which were red shifted with respect to the 6_0^1 absorption peak of bare benzene. These peaks were seen at -41, -17, and -7 cm^{-1} . The -41 cm^{-1} band was assigned as the 6_0^1 transition of the $C_6H_6 \cdots Ar_2$ complex on the basis of the addition rule first discussed by Kenny *et al.* [Kenny 1980]. This states that if there is an effect produced by placing one molecule on a host molecule, then this effect is increased by the same amount for each additional molecule added in geometrically equivalent positions. The $C_6H_6 \cdots Ar$ complex is 21 cm^{-1} more strongly bound in the excited state, so one would expect the complex having two argon atoms on opposing sides of the benzene ring (denoted here as the (1|1) structure) to be 42 cm^{-1} more tightly bound. Thus, the 41 cm^{-1} red shifted peak was assigned to the 6_0^1 transition of the (1|1) structure. The successful application of the addition rule for this case demonstrates the benzene argon interaction on one side of the benzene ring is not influenced by the argon atom on the opposite side of the ring.

The 6_0^1 transition of the other isomer, where both argon atoms lie on the same side of the benzene ring (termed the (2|0) structure), was assigned to the -17 cm^{-1} band on the evidence of ionisation efficiency spectra [Schmidt 1991a]. These authors calculate the barrier for conversion between the two isomers to be approximately 200 cm^{-1} . Finally, the -7 cm^{-1} transition was tentatively assigned to the van der Waals symmetric stretch mode of the (1|1) structure.

At the same time as Schmidt *et al.*'s work, the $S_1 \leftarrow S_0$ 6_0^1 transition of $\text{C}_6\text{H}_6 \cdots \text{Ar}_2(1|1)$ was studied in more considerably more detail by Weber and Neusser [Weber 1991]. Using one colour (1+1) REMPI they observed bands which appeared at identical positions in both the $(\text{C}_6\text{H}_6 \cdots \text{Ar}_2)^+$ and $(\text{C}_6\text{H}_6 \cdots \text{Ar})^+$ mass resolved spectra. Rotationally resolved spectra of the -41 cm^{-1} 6_0^1 transition while monitoring both masses showed identical rotational structure, confirming that the $(\text{C}_6\text{H}_6 \cdots \text{Ar})^+$ ion resulted from the dissociation of $\text{C}_6\text{H}_6 \cdots \text{Ar}_2$ (either as $\text{C}_6\text{H}_6 \cdots \text{Ar}_2$ or $(\text{C}_6\text{H}_6 \cdots \text{Ar}_2)^+$). Analysis of the rotationally resolved spectrum proved that the species being investigated was indeed the (1|1) structure, with the argon atoms located on the C_6 axis. The benzene argon distance in the ground electronic state was determined as 3.577 \AA , which is the same bond length seen in $\text{C}_6\text{H}_6 \cdots \text{Ar}$ (3.583 \AA) within the 5 m\AA experimental error. Similarly, the excited state values are the same within experimental error (3.517 \AA in $\text{C}_6\text{H}_6 \cdots \text{Ar}_2$, compared with 3.523 \AA in $\text{C}_6\text{H}_6 \cdots \text{Ar}$). The aromatic ring appears to effectively shield any interaction between the two argon atoms residing on opposite faces of the benzene molecule.

Following their initial work, Schmidt *et al.* measured the rotational contour of the -41 and -17 cm^{-1} 6_0^1 transitions with higher resolution [Schmidt 1991b]. The two contours were found to be very different. Using a semi-empirical atom-atom interaction sum model, they determined a likely geometry for the (2|0) structure which was then used to generate a calculated rotational contour. The predicted spectrum gave a general shape

similar to that measured experimentally, suggesting that the -17 cm^{-1} band was from at (2|0) structure.

Confirmation for two different types of isomers in the molecular beam was provided by Scherzer *et al.* using mass selective hole-burning techniques [Scherzer 1992]. It was conclusively shown that the -41 , and -7 cm^{-1} bands originate from the same ground state species, while the -17 cm^{-1} band is due to another species having identical mass. This adds considerable weight to the earlier assignments of Schmidt *et al.* [Schmidt 1991a; 1991b].

6.3.7 Dissociation Dynamics of $C_6H_6\cdots Ar_2$ in 1+1 REMPI

Another important result to arise from Schmidt *et al.*'s work is information regarding the dissociation and relaxation dynamics of $C_6H_6\cdots Ar_n$ van der Waals clusters [Schmidt 1991a]. The use of two colour REMPI allows the ionisation to take place just above the ionisation threshold and therefore minimise any ionic fragmentation. If there was any dissociation on the S_1 surface, then peaks will be seen in the child's spectrum at the wavelength of the parent's absorption band. Since they observed no evidence for this on the time scale of their experiments we are able to assume that the $C_6H_6\cdots Ar_n$ complexes of interest in our experiments ($n = 1, 2$) do not dissociate before ionisation. We have noted in section 6.3.5 that there is extensive evidence that $C_6H_6\cdots Ar$ does not dissociate from 6^1 , the intermediate level in our REMPI studies. The evidence from Schmidt *et al.*'s work is that this is also the case for the benzene- Ar_2 complex.

In this context we note that while the appearance of $(C_6H_6\cdots Ar)^+$ in the one colour REMPI mass spectrum of $6^1 C_6H_6\cdots Ar_2$ was attributed to the photodissociation of $C_6H_6\cdots Ar_2$, it could not be determined whether the dissociation occurred in the S_1 or ionic state [Weber 1991]. The linewidths of the 6_0^1 rotational lines were larger than the

experimental resolution indicating some sort of relaxation process in the S₁ state. This processes could either be IVR followed by rapid dissociation, or IVR within the benzene molecule without the subsequent dissociation. Given the observations by Schmidt *et al.* it is apparent that the latter process is responsible. Nesbitt has discussed the distinction between these two processes, and their relationship to rotational linewidths in van der Waals clusters [Nesbitt 1988].

6.3.8 Knowledge of the (C₆H₆···Ar_n)⁺ van der Waals ions.

In the previous chapter aspects of the benzene cation spectroscopy were presented. For the present dissociation work, the spectroscopic and dynamic details of both the (C₆H₆···Ar)⁺ and (C₆H₆···Ar₂)⁺ ions require further discussion.

The ionisation potential of C₆H₆···Ar was first determined by Chewter *et al.* using zero electron kinetic energy (ZEKE) spectra [Chewter 1987b]. They determined the ionisation potential of the complex to be red shifted by 172 cm⁻¹ compared with that of the bare benzene molecule, resulting in an ionisation potential of 74 383 ± 2 cm⁻¹. This implies that the complex ion is 151 cm⁻¹ more stable than the S₁ neutral complex, due to a stronger ion--induced-dipole interaction.

Schmidt *et al.* also measured the ionisation potentials of C₆H₆···Ar and both structural isomers of C₆H₆···Ar₂ [Schmidt 1991a]. The ionisation potential of C₆H₆···Ar, C₆H₆···Ar₂(1|1) and C₆H₆···Ar₂(2|0) were found to have shifts relative to the C₆H₆ ionisation value of -170, -334, and +137 cm⁻¹ respectively. Thus the reduction of the ionisation potential due to the addition of an argon atom to benzene is approximately the same as the addition of an extra argon atom to C₆H₆···Ar. Again this demonstrates the applicability of the addition rule.

Krause and Neusser extended their mass resolved pulsed field ionisation studies of benzene to include the $C_6H_6\cdots Ar$ complex [Krause 1993b] and $C_6H_6\cdots Ar_2(1|1)$ complex [Neusser 1994]. They confirmed the 172 cm^{-1} red shift of the ionisation potential in $C_6H_6\cdots Ar$ as seen in the previous ZEKE experiment, and the 334 cm^{-1} red shift for $C_6H_6\cdots Ar_2(1|1)$ as observed by Schmidt *et al.* The ionisation potential for $C_6H_6\cdots Ar_2(1|1)$ is thus $74\ 221 \pm 2\text{ cm}^{-1}$.

6.3.9 Dissociation energy of the $(C_6H_6\cdots Ar)^+$ and $(C_6H_6\cdots Ar_2)^+$ van der Waals ions

The dissociation energy of van der Waals ionic clusters, D_0^+ , is easily calculated from a knowledge of the ground state dissociation energy, D_0^0 , and the ionisation potentials of the parent van der Waals molecule, IP_P , and the ionisation of the fragment, IP_f .

$$D_0^+ = D_0^0 + IP_f - IP_P \quad 6.1$$

Thus for $(C_6H_6\cdots Ar)^+$, where the ground state dissociation energy is $339 \pm 2\text{ cm}^{-1}$, the ionisation potential is $74\ 383 \pm 2\text{ cm}^{-1}$ and the ionisation potential of benzene (the fragment) is $74\ 556\text{ cm}^{-1}$, D_0^+ is determined to be $512 \pm 3\text{ cm}^{-1}$.

The dissociation energy for the removal of one Ar atom in $(C_6H_6\cdots Ar_2(1|1))^+$ is also expected to be similar in value since, as discussed above, the argon atoms on opposite sides of the ring do not interfere with each other. Although there are no experimental values of dissociation energies for $C_6H_6\cdots Ar_2(1|1)$, there are values calculated using *ab initio* methods. Hobza *et al.* calculated the ground and first excited electronic state binding energies for both $C_6H_6\cdots Ar$ and $C_6H_6\cdots Ar_2(1|1)$ [Hobza 1996]. For $C_6H_6\cdots Ar$ the energies were 649.2 and 734.2 cm^{-1} for the ground and excited states respectively. For $C_6H_6\cdots Ar_2(1|1)$ values of 1324.7 and 1498.9 cm^{-1} were found for the ground and excited states respectively. The values for $C_6H_6\cdots Ar_2$ represent the binding energy of

two argon atoms attaching onto a benzene ring. In our experiments we are interested in the binding energy of one argon atom attaching to $C_6H_6\cdots Ar$, so we can subtract the binding energies for the $C_6H_6\cdots Ar$ complex from the $C_6H_6\cdots Ar_2(1|1)$ complex to determine the binding energies relevant to our study. Thus $C_6H_6\cdots Ar_2(1|1)$ is calculated to have a binding energy of 675.5 cm^{-1} in the ground state, and 764.7 cm^{-1} in the excited state. These values are respectively 4.05% and 4.15% larger than for $C_6H_6\cdots Ar$. Although the magnitude of the calculated values are in error, we can use the relative differences to determine a value of D_0^0 for $C_6H_6\cdots Ar_2(1|1)$. Assuming an increase of 4.1%, we find the dissociation energy of $C_6H_6\cdots Ar_2(1|1)$ to be $D_0^0 = 353 \pm 2\text{ cm}^{-1}$. Since the ionisation potential of $C_6H_6\cdots Ar_2(1|1)$ is $74\ 221 \pm 2\text{ cm}^{-1}$, and that of $C_6H_6\cdots Ar$ is $74\ 383\text{ cm}^{-1} \pm 2\text{ cm}^{-1}$ then the dissociation energy of $(C_6H_6\cdots Ar_2(1|1))^+$ is estimated to be $515 \pm 4\text{ cm}^{-1}$, of similar value to that for $(C_6H_6\cdots Ar)^+$. Thus, for our purposes we assume that the dissociation energy of both van der Waals cations are the same.

Experimental evidence for the dissociation of the $(C_6H_6\cdots Ar)^+$ complex comes from Krause and Neusser [Krause 1993b]. Using the $S_1\ 6^1$ vibronic level as an intermediate state, the pulsed field ionisation spectrum showed no signal at the $C_6H_6\cdots Ar$ mass above the ionic 4^1 level. There was, however, signal seen at the benzene mass originating from the complex ion excited to higher energies. Thus at these higher internal energies ($>629\text{ cm}^{-1}$), the ion dissociates within the $10\mu s$ time scale of their experiment. Weak signal appearing at the benzene mass at the wavelength corresponding to the complex's $6^1(3/2)$ level was attributed to dissociation following the absorption of a third photon. This signal subsequently disappeared at low laser powers ($200\ \mu J$). Thus, to study the dissociation of $(C_6H_6\cdots Ar)^+$ in our experiments low laser powers must be employed.

6.4 Experimental Details

In this chapter we present the results of experiments that measure the kinetic energy released in the van der Waals dissociation of both $(C_6H_6\cdots Ar)^+$ and $(C_6H_6\cdots Ar_2(1|1))^+$. The ions were formed after (1+1) REMPI through the 6_0^1 transition. The ion imaging apparatus discussed in chapter 4 was used to measure the translational energy released in these dissociations.

The laser is tuned to the 6_0^1 transition of the species under investigation. Absorption of second photon at this wavelength will take the complex over the ionisation potential causing it to ionise. The resulting vibrational distributions will depend on the Frank Condon factors for the transition from the S_1 state to the ionised species. Ions produced with vibrational energies in excess of the dissociation energy have the possibility to eject the argon atom. This ejection will of course cause the child ion to recoil and it is this velocity that can be measured using the ion imaging apparatus.

The wavelengths chosen for this study were $38\ 585\ cm^{-1}$ for $C_6H_6\cdots Ar$ and $38\ 565\ cm^{-1}$ for $C_6H_6\cdots Ar_2$. The $C_6H_6\cdots Ar$ wavelength represents the maximum of the 6_0^1 transition for this species while the $C_6H_6\cdots Ar_2$ wavelength was deliberately red shifted from the maximum of the complex's 6_0^1 transition. This was done so no absorption by higher clusters would occur. If such dissociation was present there is the possibility of dissociation products having the same mass as that being detected. For the $C_6H_6\cdots Ar$ case, the wavelength is sufficiently far enough away from the $C_6H_6\cdots Ar_2\ (2|0)\ 6_0^1$ transition to prevent absorption and therefore the possible dissociation and removal of both argon atoms to form bare benzene, the species detected in the experiment. Similarly, for the $C_6H_6\cdots Ar_2$ case, the wavelength was slightly red shifted to prevent the absorption of $C_6H_6\cdots Ar_3$, which has its 6_0^1 transition blue shifted from that of $C_6H_6\cdots Ar_2$ [Schmidt 1991a]. This removes the possibility of the detected $C_6H_6\cdots Ar$ being formed by the removal of two argon atoms from $C_6H_6\cdots Ar_3$. Finally, the 6_0^1

absorption transition of $C_6H_6\cdots Ar_2$ lies close to the corresponding transition in $(C_6H_6)_2$ (the 6_0^1 transition in $(C_6H_6)_2$ is split into two peaks centred at $38\ 567\ cm^{-1}$ with a $4\ cm^{-1}$ separation [Hopkins 1981]), however the dissociation products (bare benzene) would not be detected at the $C_6H_6\cdots Ar$ mass probed in the experiment.

Although great care has been taken to remove all interference from dissociating products, there is still a constant background that is observed. A problem with monitoring the benzene mass for the dissociation of $C_6H_6\cdots Ar$ is that the excitation wavelength is within the tail of the benzene 6_0^1 room temperature rotational contour. Residual benzene present within the chamber (from the previous expansion pulse) is observed as a very broad background. There is also a sharp peak in the centre of the images having the same shape as that of the molecular beam. We attribute this to off resonance ionisation or the electron impact ionisation of species in the molecular beam (when species are ionised, the photoelectron is accelerated parallel to the beam direction because of the electric field and can cause electron impact ionisation). Fortunately, the shape of these interferences are somewhat wavelength independent since the room temperature benzene spectrum is quite broad and featureless in this region. Background data can thus be collected at wavelengths off resonance with the complex absorption peaks.

The timescale of dissociation to which our experiments are sensitive needs some consideration. This is something not often mentioned in ion imaging work, since it has largely been used to study process in which there is rapid photodissociation. For slow dissociations, where the ion travels some distance in the acceleration region before dissociating, the ion will arrive at later times due to the heavier mass in the initial accelerating region. Since the mass gate used for detection is 400 ns wide centred about the cold fragment's arrival time, our apparatus measures dissociations occurring within 200 ns. Experimentally we found that by scanning the mass gate, the dissociation occurred rapidly since the child ions arrived in a narrow time window.

The time of flight apparatus used here was discussed in detail in the previous chapter, so only those experimental conditions pertaining to the dissociation work will be discussed.

The sample vessel was pressurised with a mixture of one percent benzene vapour (BDH 99.7%, freeze-pumped-thawed) in argon (BOC 99.997%). The backing pressure behind the nozzle was held constant at 500 kPa. Laser powers were kept deliberately low ($\sim 0.5 \mu\text{J}$) to (1) prevent three photon absorption by the complex [Krause 1993b], (2) minimise Coulombic repulsion between ions, and (3) ensure that not too many ions appear in the centre of the image, making ion counting impossible. Each image was integrated over five laser shots to yield approximately four to six ions per image. Thus typically one ion is detected per laser shot.

It was shown in chapter 5 that the photoionisation process produces ions with a range of internal energies, some of which are insufficient for dissociation. The beam thus retains a population of parent cations of the species being studied. This allowed experimental conditions to be optimised by setting the mass gate to observe the parent mass signal and optimising both the position of the laser intersection and the time delay between the nozzle and laser. The timing of the mass gate was then changed to view the child's mass. Optimisation of the pulse delay for the detector was performed by changing the laser wavelength to directly excite the child product.

Elimination of background interference was achieved by recording images with the wavelength on and off resonance. To ensure reliable use of these backgrounds over the long time of data collection, the data were collected in two segments of 100 000 laser shots. Between the data runs, and at the end, an off resonant background was recorded. The wavelength for the background was alternated between the high energy side and low energy side of the absorption peak (each was equidistant from the resonant

wavelength). Ideally the background would be linear with wavelength so it can simply be subtracted from the signal image. However, in our case the absorption profile of residual room temperature deviates slightly from linearity, so the background required a small amount of scaling.

Calibration of the energy scale was achieved by measuring the photoelectron image of benzene using the 6_1^0 transition as the resonant step. This was done by only moving the laser wavelength, reversing the polarity of the accelerating plates and changing the detector pulsing to electron mode (see chapter 4 for more details). Therefore the calibration image is collected under the same experimental conditions as the dissociation images.

6.5 Data Analysis

The data were analysed by plotting the average intensity as a function of the distance from the centre of the image, r , to create a radial plot of the image (see chapter 4). This of course assumes a circularly symmetric image, which requires the van der Waals molecule dissociation to occur on a timescale greater than the complex's rotational period. Comparing the intensity profile of horizontal and vertical slices through the image showed it to be symmetric. Circular symmetry (ie $\beta = 0$) was also observed by Yoder *et al.* in their pyrazine-argon work [Yoder 1999]. Radial plots of the images collected on resonance and off resonance were subtracted to obtain the resulting dissociation radial plot.

From this point, the inverse Abel transform was calculated in two complementary ways. The first method was similar to that given by Yoder *et al.*, where the radial data were first fitted to a sum of Gaussians [Yoder 1999]. In the current work, the sum of two

Gaussians were fitted using the Levenberg-Marquardt non-linear least squares fitting method [Press 1992]. The statistical nature of ion counting allows errors to be easily determined, and thus these statistical errors were used as weights in the least squares fit. Since the inverse Abel function of a Gaussian is itself a Gaussian [Bracewell 1977], the three dimensional radial distribution of the dissociating products can be calculated. For a sum of Gaussians given by

$$G(r) = \sum_i A_i e^{-k_i r^2} \quad 6.2$$

the inverse Abel transform is given by

$$F(R) = \sum_i B_i e^{-k_i R^2} \text{ where } B_i = A_i \sqrt{\frac{k_i}{\pi}} \quad 6.3$$

The second method of data analysis is to perform the inverse Abel transform directly on the radial data. The method to perform these calculations was presented in chapter 4. It was necessary to apply a three point moving average to the data to get sufficiently smooth distribution curves since the inverse Abel transform is a differentiation process and thus amplifies any noise.

After using either method to calculate the inverse Abel transform, it is then a simple matter of multiplying the radial intensity, $F(R)$, by R^2 to obtain the velocity population distribution. The distribution is then converted to an energy distribution by squaring the x -coordinate and dividing the intensities by \sqrt{E} to correct the probabilities in the transformation from velocity space to energy space [Bomse 1983]. This distribution describes the kinetic energy obtained by the benzene containing fragment after dissociation. Since the function $F(R)$ is multiplied by R^2 then one must be careful about quality of the data at large values of R . The multiplication process reduces the signal-

to-noise ratio as R is increased. This also needs to be considered if a fitted function to the radial plot is used to perform the inverse Abel transform.

It is of more interest to determine the total kinetic energy released during the dissociation, which is easily calculated using the law of conservation of momentum. The total kinetic energy released, E_{total} , is given by

$$E_{total} = E_A \left(1 + \frac{m_A}{m_B} \right) \quad 6.4$$

where E_A is the energy of fragment A and the masses of fragment A and fragment B are denoted m_A and m_B . Finally, the resultant distribution is normalised so that the integral of the distribution is unity.

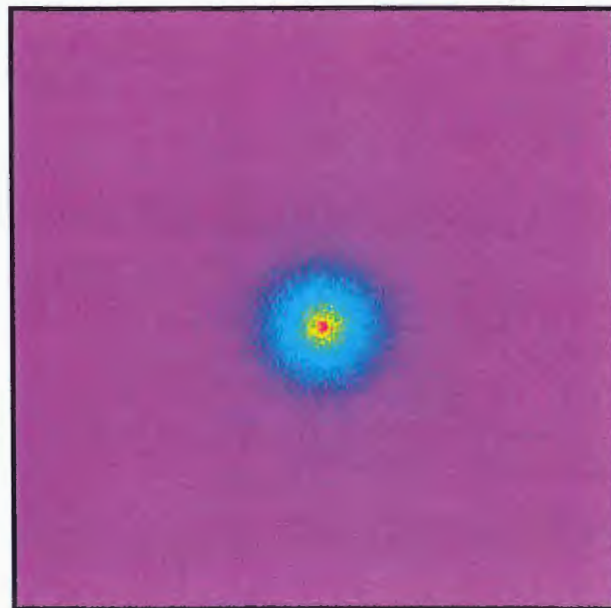
6.6 Results

Raw data images of the dissociation and background data are shown for the dissociation of $(C_6H_6\cdots Ar)^+$ and $(C_6H_6\cdots Ar_2)^+$ in figures 6.2 and 6.3 respectively. In the $C_6H_6\cdots Ar$ case the benzene mass is being monitored, and for the $C_6H_6\cdots Ar_2$ case the mass of the $C_6H_6\cdots Ar$ fragment is monitored. The figures clearly show that when the laser is off resonance there is a weak broad background and a narrow spot in the centre of the image. This narrow spot represents the narrow range of velocities present in the molecular beam. The size of this spot agrees well with the calculated temperature of the beam. When the laser is tuned to the 6_0^1 transition of the complex, a large intense spot dominates the image. This spot is attributed to the recoiling velocities of the benzene containing dissociation product. It is immediately apparent that the spread of dissociating molecules is radially much larger than the molecular beam, so deconvolution is not necessary in our case. This is in contrast to Yoder *et al.*'s work

a)



b)



Minimum

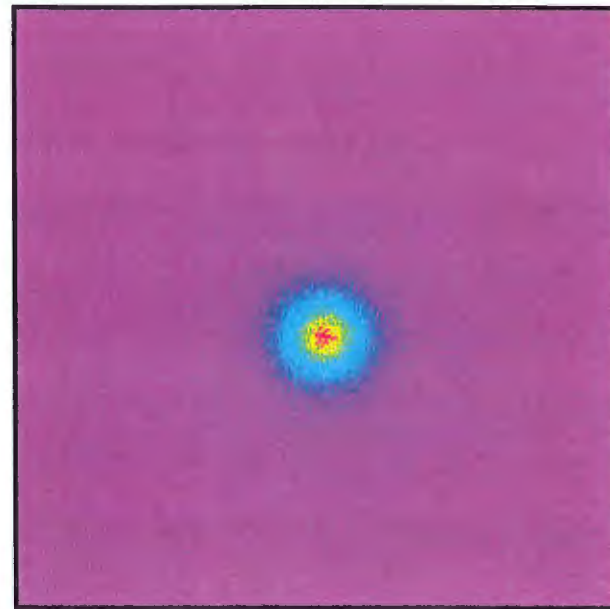
Maximum

Figure 6.2 Ion images recorded at the $C_6H_6^+$ mass with a) the laser off resonance and b) the laser tuned to the 6_0^1 absorption transition of the $C_6H_6\cdots Ar$ van der Waals molecule.

a)



b)



Minimum

Maximum

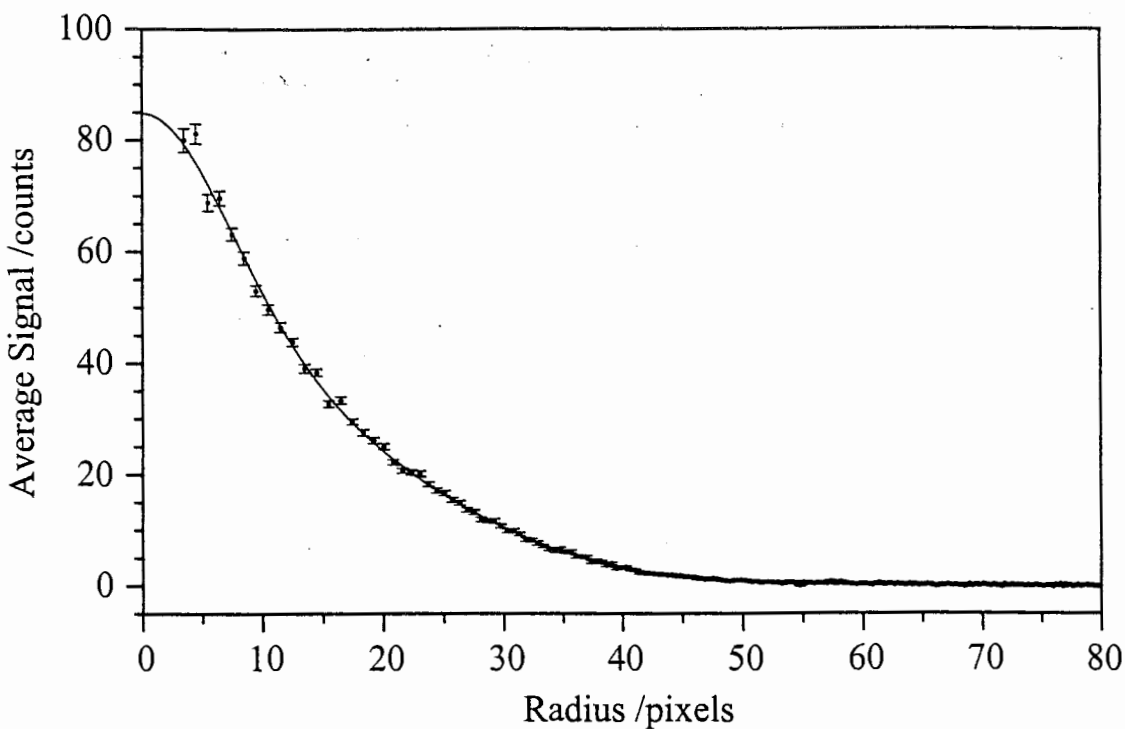
Figure 6.3 Ion images recorded at the $(C_6H_6\cdots Ar)^+$ mass with a) the laser off resonance and b) the laser tuned to the 6_0^1 absorption transition of the $C_6H_6\cdots Ar_2$ van der Waals molecule.

where the measured signal and beam size's were of comparable size, requiring deconvolution to determine the true recoiling energy distribution [Yoder 1999]. We attribute our increased resolution to the method of ion counting in preference to direct integration on the CCD chip. As discussed in chapter 4, ion counting effectively eliminates the finite size of the ion spot formed on the phosphor screen, thus giving more realistic beam widths.

Both the signal and background images were converted to plots of the average radial intensity versus the radial distance, termed a radial plot. The background radial plot was subtracted from the signal plot to determine the resultant radial plot which was subsequently fitted a sum of Gaussians. These plots are shown in figure 6.4 for both the dissociation of $(C_6H_6\cdots Ar)^+$ and $(C_6H_6\cdots Ar_2)^+$. It was found that the sum of two Gaussian functions were adequate to describe the radial plot. The two data sets were recorded under identical experimental conditions (extraction voltages and camera magnification) so a direct comparison based on CCD pixel distance can be made. Although the radial plots show a similar trend, it can be seen that the fragment velocities from the dissociation from $(C_6H_6\cdots Ar)^+$ decay slower with increasing velocity than does dissociation from $(C_6H_6\cdots Ar_2)^+$. This is most evident if one compares the signal intensity in the region between 20 and 40 pixels.

As discussed above, the radial plots were transformed using the inverse Abel transform and converted to the three dimension energy population distribution. The transform was applied to both the smoothed raw data using the inverse Abel transform algorithm discussed in chapter 4, and also the fitted data using the analytical expression given in equation 6.3. The resulting distributions were converted to a wavenumber scale using the 6_1^0 electron image of benzene as a calibrant. Plots of the final energy population distributions representing the fragment kinetic energies are given in figure 6.5. The smooth solid line represents the inverse Abel transform of the Gaussian functions fitted to the radial plot. For the purpose of normalisation the raw data has been scaled by the

a)



b)

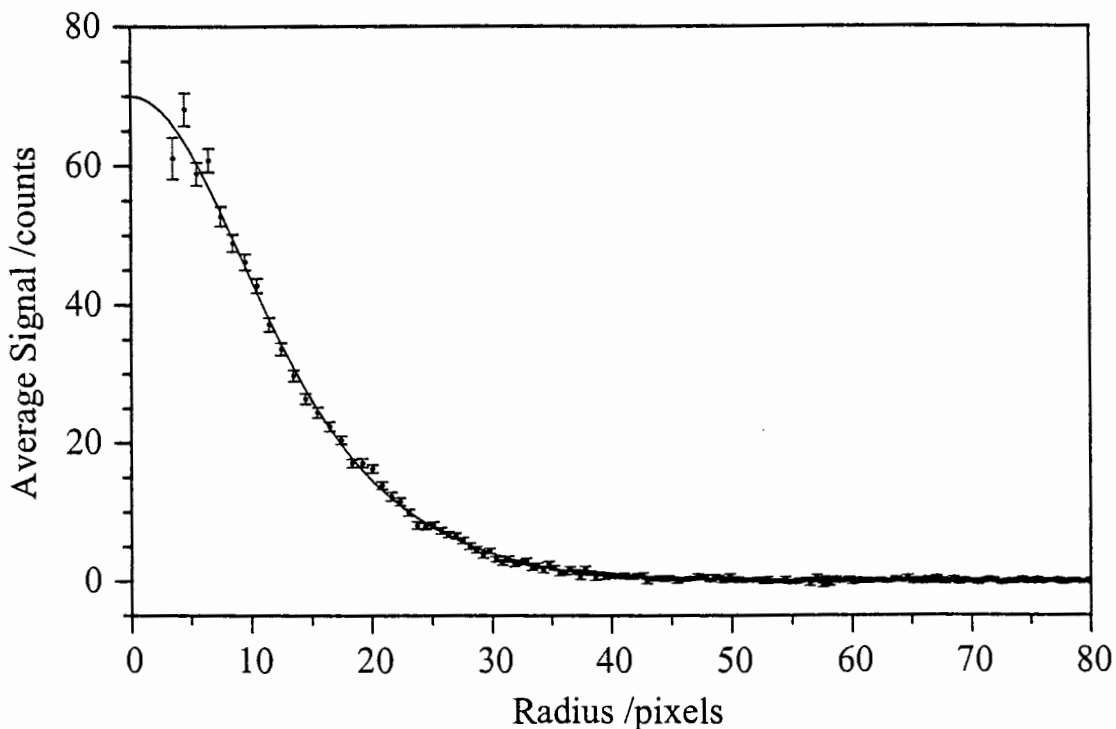


Figure 6.4 Plots of the average radial intensity versus the distance from the centre of the ion image for a) C_6H_6^+ fragments from the dissociation of $(\text{C}_6\text{H}_6 \cdots \text{Ar})^+$ and b) $(\text{C}_6\text{H}_6 \cdots \text{Ar})^+$ fragments from the dissociation of $(\text{C}_6\text{H}_6 \cdots \text{Ar}_2)^+$. The smooth lines are the best fit to the data using a sum of two Gaussians.

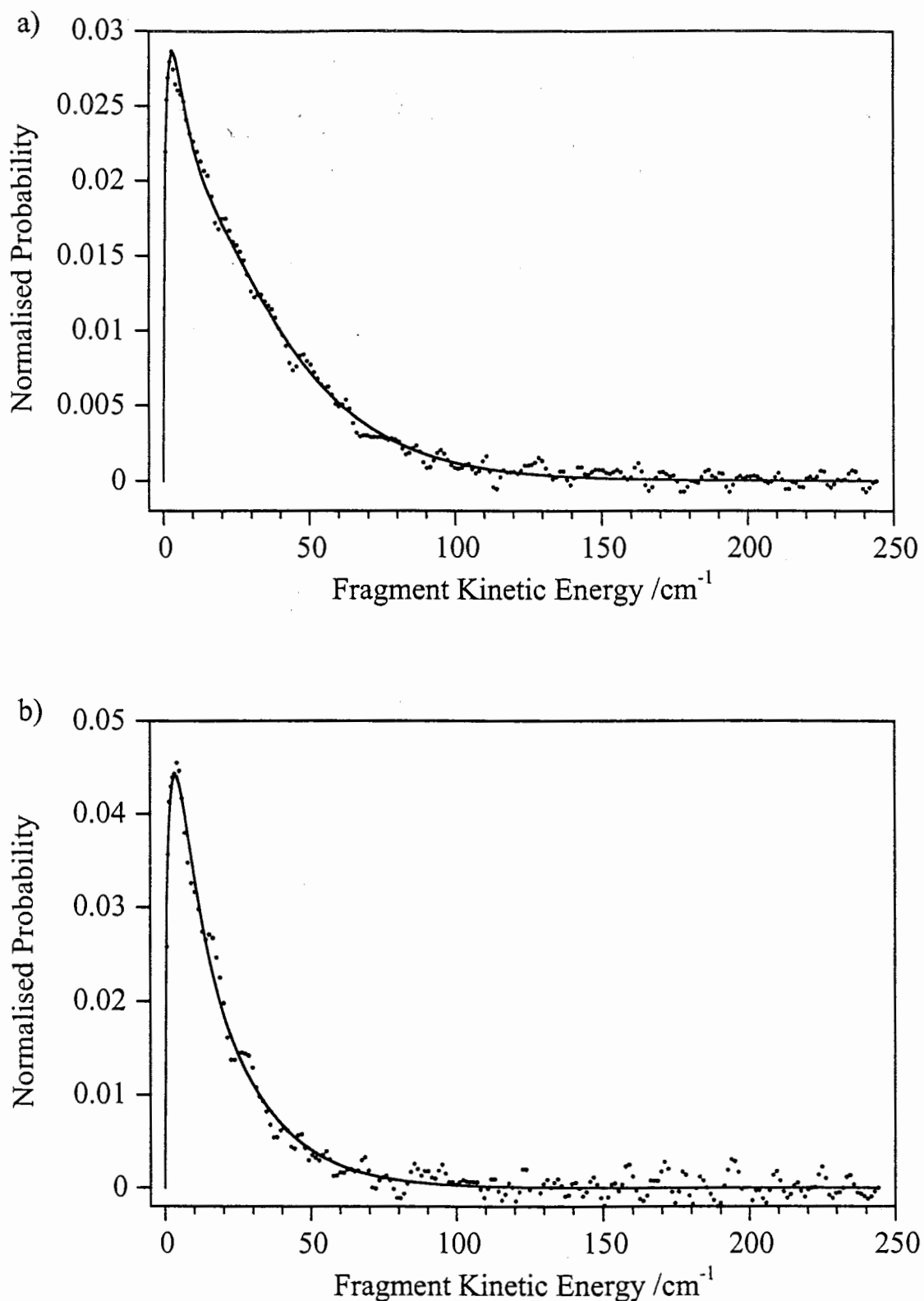


Figure 6.5 Normalised plots of the kinetic energy population distribution for a) C_6H_6^+ fragments from the dissociation of $(\text{C}_6\text{H}_6 \cdots \text{Ar})^+$ and b) $(\text{C}_6\text{H}_6 \cdots \text{Ar})^+$ fragments from the dissociation of $(\text{C}_6\text{H}_6 \cdots \text{Ar}_2)^+$. The solid lines represent the distribution calculated using the best fit sum of two Gaussians to the radial plot. The points give the distributions obtained from the direct (numerical) inverse Abel transformation of the radial plots.

same factor that was necessary for the normalisation of the fitted curve. Since the fit is analytic, the required normalisation factor can be easily computed analytically. As seen in figure 6.5, the slight differences in the radial plots become amplified by the conversion of the x -axis to an energy scale. Dissociation of both $(C_6H_6\cdots Ar)^+$ and $(C_6H_6\cdots Ar_2)^+$ show a sharp rise in the kinetic energy distribution followed by a exponential-like decay. The distribution decays much more rapidly for the dissociation of $(C_6H_6\cdots Ar_2)^+$ than for $(C_6H_6\cdots Ar)^+$.

Finally the kinetic energy distribution of the fragment is converted to distributions describing the total energy released in the dissociation process (equation 6.4). Plots of the distribution of total energy released are shown in figure 6.6. Again, each plot has been normalised using the parameters from the fitted curve. As shown in figure 6.6 the distributions of total energy for the dissociation of $(C_6H_6\cdots Ar)^+$ and $(C_6H_6\cdots Ar_2)^+$ are now similar. The different distributions obtained in the radial plots and fragment energy distributions are due primarily to the different fragment masses and the momentum conservation law.

Although the two total kinetic energy released distributions look similar, there are subtle differences. The distributions obtained by the two methods of analysis are essentially identical and show a slightly faster rise and a faster decay for the dissociation of $C_6H_6\cdots Ar_2$ in comparison to $C_6H_6\cdots Ar$.

The transformation converting radial plots of pixel intensity into the energy distribution, $P(E)$, transforms the original best fit sum of Gaussians of the radial plots (equation 6.2) into

$$P(E) = \sqrt{E} \sum_i C_i e^{-k_i E} \quad 6.5$$

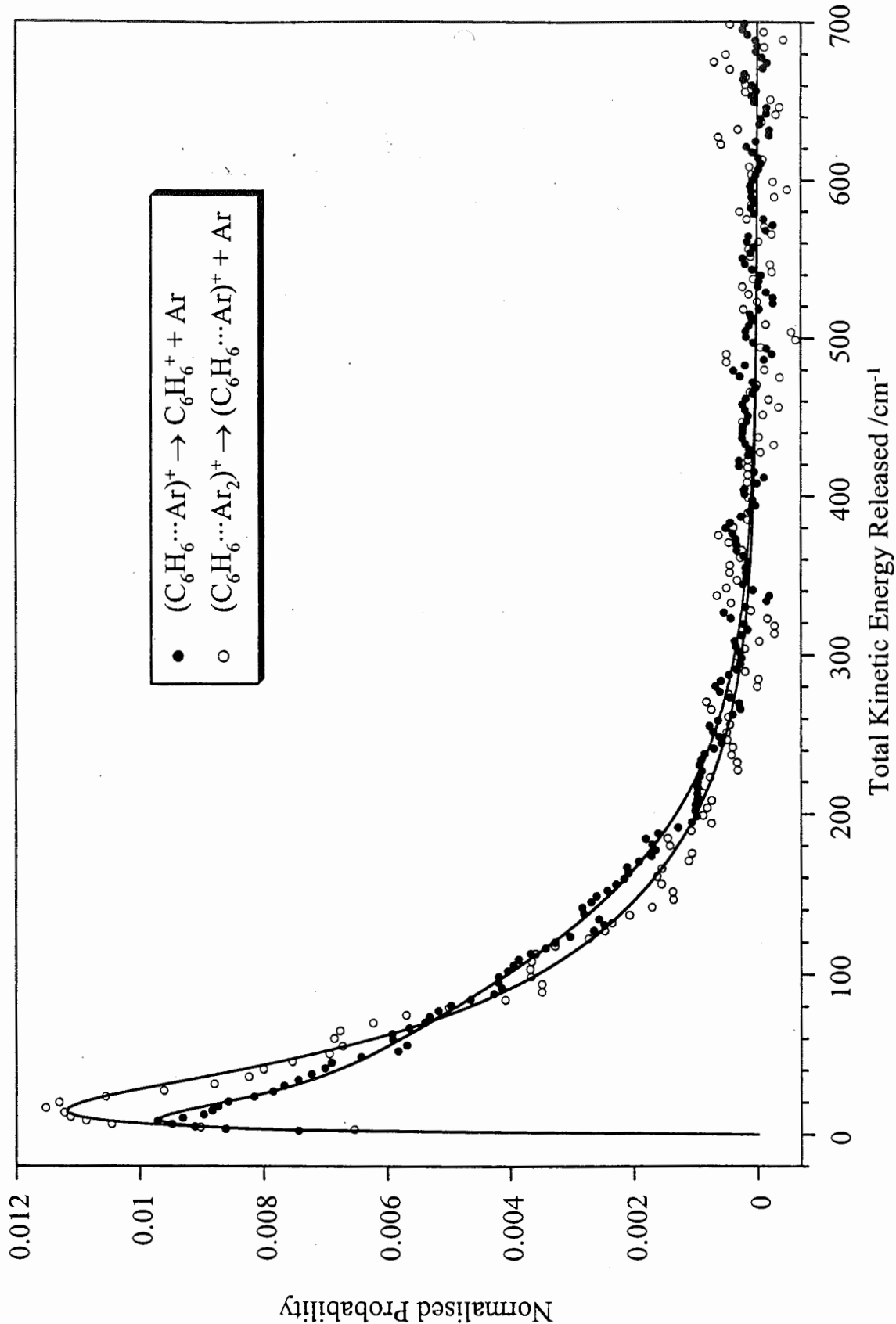


Figure 6.6 Normalised plots of the total energy released in the dissociation of $(C_6H_6 \cdots Ar)^+$ and $(C_6H_6 \cdots Ar_2)^+$. The smooth lines represent the distribution calculated using the best fit sum of two Gaussians to the radial plot. The points give the distributions obtained from the direct (numerical) inverse Abel transformation of the radial plots.

Table 6.1 Best fit parameters for the total kinetic energy released from the dissociation of $(C_6H_6\cdots Ar)^+$ and $(C_6H_6\cdots Ar_2)^+$. Also included is the average kinetic energy released.

| van der Waals Complex | Fitted Parameters ^a | | | | $\langle\langle\Delta E\rangle\rangle$ $/cm^{-1}$ |
|-----------------------------|--------------------------------|----------|---------|----------|------------------------------------------------------|
| | C_1 | k_1/cm | C_2 | k_2/cm | |
| $C_6H_6\cdots Ar$ | 0.00384 | 0.0914 | 0.00176 | 0.0147 | 92 ± 4 |
| $C_6H_6\cdots Ar_2$ | 0.00343 | 0.0482 | 0.00154 | 0.0154 | 78 ± 5 |

^a Parameters correspond to the form of equation 6.5 and have been determined from the best fit to the radial plot using equation 6.2.

Where C_i is the equivalent of B_i in equation 6.3, but divided by a normalisation constant to ensure the full integrated probability of the total energy distribution is unity. The final parameters, for C_i and k_i determined from the initial Gaussian fit of the radial plots, are presented in table 6.1.

6.7 Discussion

6.7.1 Population distribution following ionisation.

It is desirable to know the distribution of ion energies formed in the photoionisation of the benzene-argon clusters so that the translational energy distributions of the fragments can be related to the initial internal energies. The distribution of ion internal energies is mirrored in the photoelectron energy distribution, i.e. the photoelectron spectrum. Unfortunately, photoelectron spectra of these clusters are presently not available in the

literature. We have attempted to measure the photoelectron spectrum of $C_6H_6\cdots Ar$ using REMPI via the 6_0^1 transition. However, the wavelength corresponding to the 6_0^1 transition in the cluster also coincides with a section of the broad 6_0^1 rotational contour of room temperature (background) benzene. Although we have been able to remove this interference by background subtraction in the case of ion imaging, the signal to noise ratio in electron mode was inadequate to obtain acceptable images. Nevertheless, we can make some assumptions on the initial distribution of the cluster cations based on our measurement of the photoelectron spectrum of the benzene monomer and the known spectroscopic properties of the benzene-argon cations.

Neusser and Krause have recorded the mass analysed pulsed field threshold ionisation spectrum of C_6H_6 , $C_6H_6\cdots Ar$ and $C_6H_6\cdots Ar_2$ between the vibrational ground state of the ion up to the $6_1(3/2)$ level [Neusser 1994]. They observed that the vibrational frequency of the $6_1(+3/2)$ and $6_1(-3/2)$ doublet had the same frequency in each of the species. This is not at all surprising since it has been found that in the S_1 state of benzene rare-gas van der Waals clusters the observed frequencies remain unchanged from those in benzene [Stephenson 1984]. The notable exception is ν_{16} , which is seen to have a small shift [Stephenson 1984; Riedle 1996a] upon complexation. This behaviour has also been seen in other aromatic-argon clusters such as *s*-tetrazine [Brumbaugh 1983] and p-difluorobenzene [Jacobson 1988], where the frequency of ν_{16a} (one of the degenerate components of ν_{16} in benzene) undergoes the greatest change. Vibrations containing ν_{16} , however, do not play a large role in our recorded photoelectron spectra (see chapter 5). It thus appears that the addition of an argon atom to one side of the benzene ring does not have much influence on the vibrational motion of the atoms within the benzene molecule. As discussed in section 6.3, the addition of another argon atom to the other side of the benzene ring repeats the effect of adding the first atom to the ring (i.e. there is no interaction between the two argon atoms). We therefore suggest that the benzene cation vibrational frequencies in $(C_6H_6\cdots Ar_2)^+$ and $(C_6H_6\cdots Ar)^+$ will be the same as those in C_6H_6 . We can then assume that the position of vibrational bands seen in the

Table 6.2 Energy values relevant to the study of the dissociation of $(C_6H_6\cdots Ar)^+$ and $(C_6H_6\cdots Ar_2)^+$ van der Waals cations via the 6_0^1 transition.

| van der Waals Complex | Ionisation Potential /cm ⁻¹ | Wavelength /cm ⁻¹ | Excess Energy /cm ⁻¹ | Energy above D_0^+ /cm^{-1} |
|-----------------------------|-------------------------------------------|---------------------------------|------------------------------------|----------------------------------|
| C_6H_6 | 74556 ^a | 38610 | 2663 | — |
| $C_6H_6\cdots Ar$ | 74383 ^b | 38585 | 2787 | 2275 |
| $C_6H_6\cdots Ar_2$ | 74221 ^c | 38565 | 2909 | 2397 |

^a See chapter 5, section 5.1.2

^b [Chewter 1987b; Krause 1993b]

^c [Neusser 1994]

photoelectron spectra of benzene can be extended to the photoelectron spectra of both $C_6H_6\cdots Ar$ and $C_6H_6\cdots Ar_2$. Moreover, since the photoelectron intensities depend on the Frank-Condon overlap, we believe they will also be similar for each the three species. Therefore we can assume the benzene photoelectron spectra provides a good basis for determining the vibrational states populated after ionisation of the $C_6H_6\cdots Ar$ and $C_6H_6\cdots Ar_2$ van der Waals molecules.

Table 6.2 shows the amount of excess energy after ionisation of benzene and the two van der Waals complexes under investigation. As shown in this table, the maximum energy available to the $C_6H_6\cdots Ar$ and $C_6H_6\cdots Ar_2$ cations after ionisation via the 6_0^1 transition is greater than that of bare benzene by 124 and 246 cm⁻¹ respectively. Consequently, the photoelectron spectrum recorded for benzene does not extend to high

enough energies to completely determine the high energy end of the population distribution. However, from the REMPI photoelectron spectra presented in the previous chapter, we know that ionisation via the 6_0^1 and $6_0^1 1_0^1$ transitions leads to very similar structure. Since the excess energy after ionisation via $6_0^1 1_0^1$ is significantly higher, we can fill in the missing gap between the maximum ion energies for C_6H_6 and $C_6H_6\cdots Ar_2$. The next peak in the $6_0^1 1_0^1$ photoelectron spectrum after 2663 cm^{-1} (maximum excess energy in the 6_0^1 REMPI of benzene) is at $\sim 3010\text{ cm}^{-1}$ (see figure 5.7 in the previous chapter). This is larger than the 246 cm^{-1} gap outlined above, so no new peaks are expected to be seen in the $C_6H_6\cdots Ar$ and $C_6H_6\cdots Ar_2$ photoelectron spectra. There is, however, a broad background observed in the photoelectron spectra at high internal energies of the cation. This presumably arises through small population in the large number of vibrational levels that occur at these energies. In the region between 2663 cm^{-1} and the maximum excess energy for $C_6H_6\cdots Ar$ and $C_6H_6\cdots Ar_2$, population of these background states is possible. Thus we can assume that the distribution of vibrational states that are formed after ionising via the 6_0^1 resonant transition are similar for both $C_6H_6\cdots Ar$ and $C_6H_6\cdots Ar_2$ photoionisation bearing in mind that higher background states may also be populated. The cation energy distribution (determined from the 6_0^1 photoelectron spectrum of benzene) is given in figure 6.7. Also marked on the figure is the maximum internal energy available for the $(C_6H_6\cdots Ar)^+$ and $(C_6H_6\cdots Ar_2)^+$ cations.

Since dissociation can occur from different energy levels within the van der Waals cation, we calculate the average energy prior to dissociation, $\langle E \rangle$, so our results can be compared with other studies. Using the 6_0^1 photoelectron spectrum of benzene, which we presented in the previous chapter, the average energy is $\langle E \rangle = 1750\text{ cm}^{-1}$ for both $(C_6H_6\cdots Ar)^+$ and $(C_6H_6\cdots Ar_2)^+$ if one ignores the possible contribution from the background states between where the benzene spectrum cuts out and the maximum energy available. In determining this value all the population below the dissociation energy of 512 cm^{-1} has been ignored since energies less than this will not lead to

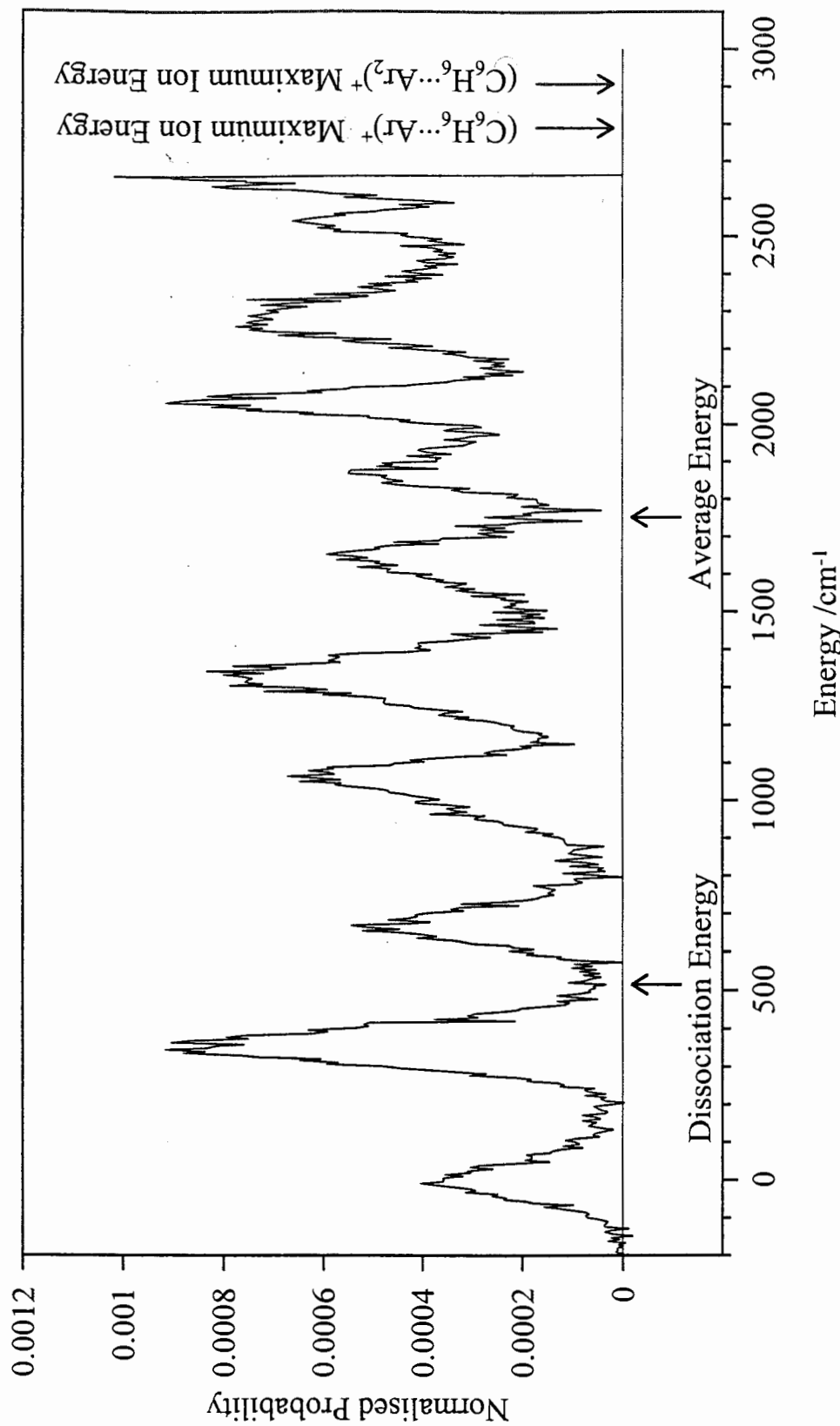


Figure 6.7 Internal energy distribution after photoionisation of benzene. Marked on the diagram are the maximum energies for $(C_6H_6\cdots Ar)^+$ and $(C_6H_6\cdots Ar_2)^+$. van der Waals molecules prior to dissociation. Also marked on the plot is the dissociation energy for the removal of one argon atom from both the $(C_6H_6\cdots Ar)^+$ and $(C_6H_6\cdots Ar_2)^+$ van der Waals complexes.

dissociation. However, as outlined in previous paragraph, it is likely that higher energy background states will be populated. By assuming that the background continues to increase linearly from 2663 cm^{-1} up to the maximum internal energy then we can estimate values for the $(\text{C}_6\text{H}_6\cdots\text{Ar})^+$ and $(\text{C}_6\text{H}_6\cdots\text{Ar}_2)^+$ cations. After applying such a procedure we find that $\langle E \rangle \sim 1820\text{ cm}^{-1}$ for $(\text{C}_6\text{H}_6\cdots\text{Ar})^+$ and $\langle E \rangle \sim 1880\text{ cm}^{-1}$ for $(\text{C}_6\text{H}_6\cdots\text{Ar}_2)^+$. We regard these later values as providing the better estimates.

6.7.2 Distribution of total energy released

The final distributions for the dissociation of $(\text{C}_6\text{H}_6\cdots\text{Ar})^+$ and $(\text{C}_6\text{H}_6\cdots\text{Ar}_2)^+$ shown in figure 6.6 both show a sharp rise to a maximum at $10\text{-}15\text{ cm}^{-1}$ followed by exponential-like decay. The energy distribution for dissociation of $(\text{C}_6\text{H}_6\cdots\text{Ar}_2)^+$ shows a faster decay than that of $(\text{C}_6\text{H}_6\cdots\text{Ar})^+$. The sharp rise seen in our study has not always been observable in previous studies of van der Waals molecule dissociation because of limitations inherent to their experimental methodology. Previous experiments have usually measured the recoil velocities by placing a movable detector at an angle to the molecular beam. The detectors used in such experiments have angular resolutions which prevent the separation of low energy recoil velocities from the molecular beam [Bromse 1983]. However, in studies where the experimental equipment has allowed observation of the low kinetic energy releases, an initial sharp rise has been observed [Hoffbauer 1983].

Various functional forms to describe the energy distributions $P(E)$ for dissociation of van der Waals molecules have been investigated [Bromse 1983], although the most commonly used expression is

$$P(E) \propto \sqrt{E} e^{-kE} \quad 6.6$$

which has the same form as a Maxwell-Boltzmann (i.e. thermal) distribution. We find that when our data are fitted to such a distribution, poor fits are obtained. The best fit curves cannot reproduce the sharp rising edge of the distribution, resulting in a displaced maximum to higher energies, and the fits decay far too quickly. This is not at all surprising since equation 6.6 transforms into a single Gaussian for the radial plots of pixel intensity, and we had found that a single Gaussian was insufficient to describe the data. Fitting the raw energy distribution data directly to a sum of two functions of the form of equation 6.6 (i.e. equation 6.5 above) results in a much better fit and, importantly, the fit was found to be within the fitting error of that obtained by fitting the original radial plot to two Gaussians. The fit to the raw energy distribution data thus provides an internal consistency check for the suitability of applying our inverse Abel transform algorithm on real (noisy) data, and confirms that the three point smoothing average used in the analysis did not significantly perturb the resultant energy distribution.

A parameter of interest in energy transfer studies is the average energy transferred per collision $\langle\Delta E\rangle$ (see chapter 3). For the dissociation of van der Waals molecules studied here, the energies of the ions prior to dissociation is only known as a distribution of energies, not at just one single energy. Thus we report a value for $\langle\langle\Delta E\rangle\rangle$, the average energy released, averaged over all initial internal energies of the undissociated ion. The value of $\langle\langle\Delta E\rangle\rangle$ can easily be determined analytically from the parameters presented in table 6.1 and is also presented in that table. For the dissociation of $(C_6H_6 \cdots Ar)^+$, a value of $92 \pm 4 \text{ cm}^{-1}$ was found for $\langle\langle\Delta E\rangle\rangle$, while a value of $79 \pm 5 \text{ cm}^{-1}$ was found for $(C_6H_6 \cdots Ar_2)^+$.

6.7.3 Dissociation of $(C_6H_6\cdots Ar)^+$

Both energy distributions show that the probability peaks at very low energy ($10\text{-}15\text{ cm}^{-1}$) and decays such that the probability of releasing kinetic energies above 400 cm^{-1} is very small. 400 cm^{-1} represents approximately one sixth of the total energy that is available for release (see table 6.2) and approximately one third of the average excess energy in the case of $(C_6H_6\cdots Ar)^+$. Thus the $C_6H_6^+$ cation fragment must contain significant residual internal energy, i.e. in rotation and vibration. This type of behaviour in van der Waals dissociations appears to be a common feature of the systems studied to date. Recent work by Yoder *et al.* using ion imaging studied the dissociation of triplet state pyrazine-Ar van der Waals clusters excited to $\sim 4000\text{ cm}^{-1}$ [Yoder 1999]. They also found that most of the energy distribution occurs at energies less than 600 cm^{-1} . Again this indicates that the fragment molecule was left vibrationally (and rotationally) excited. Yoder *et al.* determine the average energy released $\langle\langle\Delta E\rangle\rangle = 95\text{ cm}^{-1}$, which is similar to our value for the dissociation of $(C_6H_6\cdots Ar)^+$, although our values involve a lower initial average energy. In figure 6.8 both the distributions that we obtain here and that obtained by Yoder *et al.* for the pyrazine dissociations are shown on the same plot. The data from Yoder *et al.* has been taken directly from figure 4 in their publication [Yoder 1999]. The intensity is now displayed on a log scale. It is interesting to note a qualitative difference in the shape of the distributions. Yoder *et al.* observe a longer tail in their distributions due to a small number of van der Waals molecules dissociating with larger kinetic energy releases. Although the distributions are different, the $\langle\langle\Delta E\rangle\rangle$ values that we obtain are only slightly different to those measured by Yoder *et al.* This is simply due to the long tail containing only a very small proportion of the total population. The different shapes for these distributions are discussed in section 6.7.4.

There have been a couple of studies of aromatic-rare gas van der Waals molecules that show the production of highly rotationally excited products following dissociation. A study by Brumbaugh *et al.* observed the final vibrational levels populated after excitation of different vibrational levels in electronically excited *s*-tetrazine-argon van der Waals clusters [Brumbaugh 1983]. For the cases where the rotational energy distribution was obtained, they found that considerable amounts of energy were partitioned into rotation of the *s*-tetrazine. Rotational excitation was also found in a study on dissociation of S₁ pyrimidine clusters [Saigusa 1983]. It was found that the dissociation primarily populated the ground vibrational level with large amounts of rotational energy. A recent study of the *para*-difluorobenzene - argon cluster found broad lines in transitions from the *p*DFB fragment indicating significant rotational excitation in this fragment [Lembach 1998].

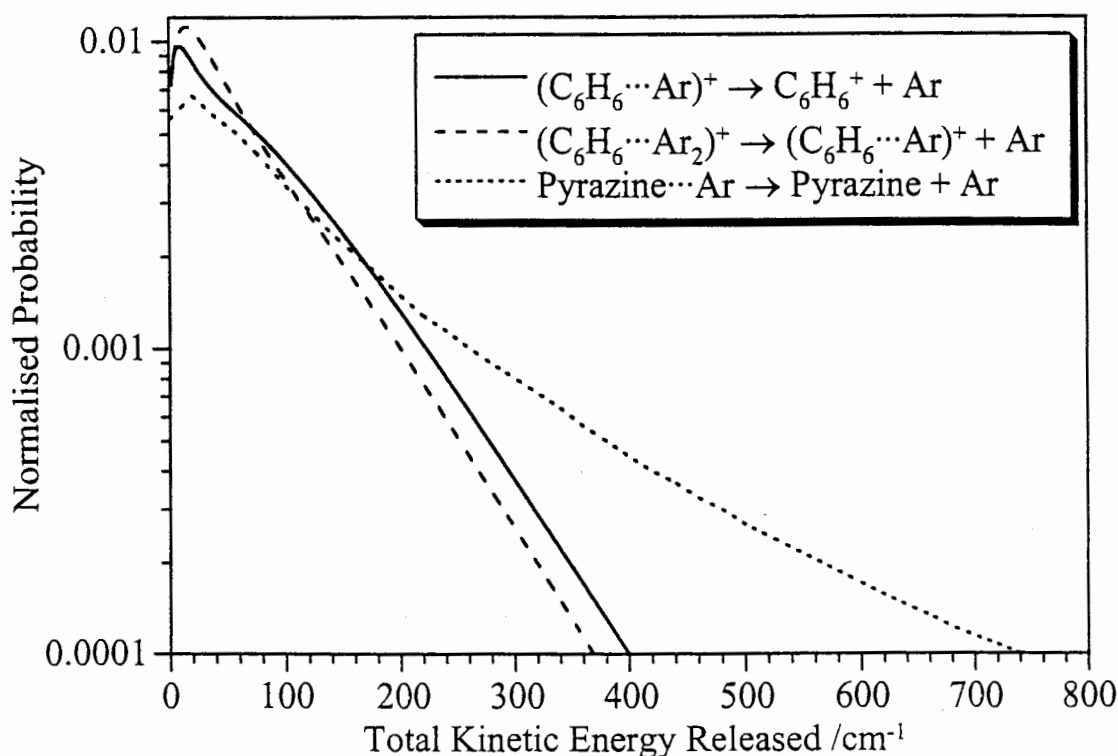


Figure 6.8 Normalised plots of the total energy released in the dissociation of $(C_6H_6 \cdots Ar)^+$, $(C_6H_6 \cdots Ar_2)^+$, and pyrazine...Ar. The data for the benzene-argon clusters are those reported here, while the pyrazine-argon cluster data is taken directly from Yoder *et al.* [Yoder 1999].

Dissociation of ethylene dimers also shows a similar trend. Studies of the kinetic energy released in ethylene and deuterated ethylene dimer dissociation were performed by Hoffbauer *et al.* [Hoffbauer 1983]. They found for both $(C_2H_4)_2$ and $(C_2D_4)_2$ van der Waals clusters that excitation to $\sim 800\text{ cm}^{-1}$ above the dissociation energy results in only a small fraction of the available energy ($\langle \Delta E \rangle = 71\text{ cm}^{-1}$) being transferred into translational energy. For dissociation of $(C_2H_4)_2$, the loss of 71 cm^{-1} into translation means that there are no vibrational levels, except for the ground state, that can be populated (for $(C_2D_4)_2$ a number of vibrational states are possible). Thus, for $(C_2H_4)_2$ all the remaining energy (most of the total energy) had to be taken up as rotational energy of the fragments.

It appears, however, that when complexes are excited close to threshold, the fraction of the energy that is partitioned into rotation is decreased. This has been revealed in studies measuring the kinetic energy released during benzene-benzene van der Waals dissociation. At an excitation energy of $\sim 1000\text{ cm}^{-1}$, which is only $140\text{-}240\text{ cm}^{-1}$ above the dissociation energy, average kinetic energy releases were measured to be 50 cm^{-1} by Nishiyama and Hanazaki [Nishiyama 1985] and 78 cm^{-1} by Johnson *et al.* [Johnson 1986]. These average translational energy values are similar to those seen when much larger amounts of energy are available. Thus a much larger fraction of the total energy is found in translational energy and, conversely, a much smaller fraction in rotational energy, than was seen in the studies described in the preceding paragraphs. In contrast to this benzene dimer work at 1000 cm^{-1} , earlier work on the benzene dimer by Vernon *et al.* used excitation at $\sim 3000\text{ cm}^{-1}$ and observed that a only small fraction of the available energy was absorbed as kinetic energy [Vernon 1981]. Unfortunately these authors did not publish a value for the average kinetic energy released.

The results of our experiment and those mentioned above can be explained qualitatively by the momentum gap law introduced by Ewing [Ewing 1979]. This theory predicts that van der Waals dissociation will populate states that consist of low changes in

momentum (ie consist of low kinetic energy releases). The basis of this law comes from the poor overlap of the wavefunctions between the molecules forming the van der Waals molecule prior to dissociation and the translational wave function of the separating species.

A final point to note is the theoretical work by Bernshtein and Oref who ran quasiclassical trajectory calculations on the benzene-argon system at an initial internal energy of 51 900 cm⁻¹ [Bernshtein 1999]. These workers used both a Lennard-Jones and an *ab initio* potential in their simulations. They found the average kinetic energy released from the dissociation process to be 150 and 43 cm⁻¹ for the Lennard-Jones and *ab initio* potentials respectively. Based on our results and those for pyrazine-Ar by Yoder *et al.*, the latter figure appears to be lower than expected by a factor of two or more. As we discuss in the following section, the distributions appear to shift towards higher energy and include a higher energy tail with increasing internal energy.

6.7.4 Dissociation of $(C_6H_6\cdots Ar_2)^+$

In the present study we observe the $(C_6H_6\cdots Ar)^+$ fragment after removal of an argon atom from the $(C_6H_6\cdots Ar_2)^+$ parent. There are, however, parent ions that are created with sufficient energy to allow removal of both argon atoms. This would produce the benzene monomer, which is not observed in our experiment. A number of experimental observations give us an insight into the energy levels that give rise to the removal of only one argon atom. Firstly, Krause and Neusser observe in the pulsed field threshold ionisation spectrum of $C_6H_6\cdots Ar$ that no signal is seen for the parent mass at energies above the dissociation energy, but signal is seen at the benzene (child product) mass [Krause 1993b]. This indicates that the $(C_6H_6\cdots Ar)^+$ van der Waals complex is not stable at energies above the dissociation energy. Moreover, it suggests that after removal of an argon atom from $(C_6H_6\cdots Ar_2)^+$ further fragmentation will occur if the

$(C_6H_6\cdots Ar)^+$ fragment is formed in a vibrational level with an energy above the $(C_6H_6\cdots Ar)^+$ dissociation energy.

Secondly, after REMPI of the 6_0^1 transition of $C_6H_6\cdots Ar_2$ we find the intensity of the $(C_6H_6\cdots Ar)^+$ signal is less than that of $(C_6H_6\cdots Ar_2)^+$ by a factor of 0.66. This is the same as the value of 0.7 seen by Weber and Neusser [Weber 1991]. We know from our photoelectron spectrum that only a small proportion ($\sim 15\%$) of the total number of $(C_6H_6\cdots Ar_2)^+$ ions are formed with energies less than the dissociation energy. Thus, we suggest that $\sim 10\%$ of the total number of $(C_6H_6\cdots Ar_2)^+$ cations that are formed dissociate into energy levels that produce a stable $(C_6H_6\cdots Ar)^+$ cation, thereby giving the observed $\sim 2:3$ $(C_6H_6\cdots Ar_2)^+:(C_6H_6\cdots Ar)^+$ ratio. The majority of the $(C_6H_6\cdots Ar_2)^+$ ions therefore completely fragment into the three moieties.

The $(C_6H_6\cdots Ar_2)^+$ ions whose dissociation we observe must have a minimum internal energy corresponding to the dissociation energy for loss of an Ar atom (512 cm^{-1}). The maximum energy these ions can possess can in principle be large, provided sufficient energy is removed as translation to leave the $(C_6H_6\cdots Ar)^+$ fragment with less than its dissociation energy (512 cm^{-1}). We know, however, that the average translational energy released is only 79 cm^{-1} . The maximum internal energy that a $(C_6H_6\cdots Ar_2)^+$ ion can have so that it releases 79 cm^{-1} into translation and is left with just insufficient energy to further fragment is $\sim(512\text{ cm}^{-1} \times 2 + 79\text{ cm}^{-1})$. Using this as an upper bound and using the distribution seen in the benzene REMPI 6_0^1 photoelectron spectrum, we estimate that the average energy of the $(C_6H_6\cdots Ar_2)^+$ clusters whose fragmentation we are observing is $\langle E \rangle \sim 860\text{ cm}^{-1}$. This estimation is clearly indicative only, being based on a number of assumptions. Nevertheless, it indicates the substantial reduction in the initial average energy in the $(C_6H_6\cdots Ar_2)^+$ experiments compared with that in the $(C_6H_6\cdots Ar)^+$ dissociation experiments, where the average initial energy is $\sim 1820\text{ cm}^{-1}$. We suggest the lower $\langle\langle \Delta E \rangle\rangle$ value obtained for the dissociation of $(C_6H_6\cdots Ar_2)^+$

compared to $(C_6H_6\cdots Ar)^+$ is a direct consequence of the lower average energy in the $(C_6H_6\cdots Ar_2)^+$ cation before dissociation.

The shapes of the distributions shown in figure 6.8 can now be discussed. There appears to be a relationship between the shape of the distribution and the average internal energy prior to dissociation. Dissociation of pyrazine-Ar, $(C_6H_6\cdots Ar)^+$, and $(C_6H_6\cdots Ar_2)^+$ originate from average energies of ~ 4000 , ~ 1820 and $\sim 860\text{ cm}^{-1}$ respectively. $(C_6H_6\cdots Ar_2)^+$ has the lowest $\langle E \rangle$ value and has the fastest decay, showing very little high energy tail. The $(C_6H_6\cdots Ar)^+$ distribution has a higher $\langle E \rangle$ and also displays a slightly slower decay than does the $(C_6H_6\cdots Ar_2)^+$ distribution, with a slight tail to higher energies. The system with the highest internal energy, pyrazine-Ar, shows the slowest decay in the distribution, and also displays the largest tail. From just these three data sets it is difficult to determine whether this is a general trend, and more work on different systems is required to complete the picture. One may intuitively expect the observed trends since it seems reasonable that if the van der Waals cluster has more energy to expend, then more energy will be transferred into the kinetic energy of the separating fragments. It is also interesting to note that in the quasiclassical trajectory calculations on the benzene-argon system performed at an initial internal energy of $51\,900\text{ cm}^{-1}$, Bernshtein and Oref also observe a high energy tail in the distribution [Bernshtein 1999]. The tail was bigger for their Lennard-Jones potential than for the *ab initio* potential.

6.7.5 Comparison with energy transfer experiments

In their work on the dissociation of pyrazine-argon clusters, Yoder *et al.* were able to compare their average recoil energy with the average energy transferred per collision for pyrazine argon collisions excited to a similar energy [Yoder 1999]. In our case no such experimental data exist for comparison. However, energy transfer experiments

have been performed on highly excited ground state benzene using a variety of collision partners [Yerram 1990; Barker 1993, 1995]. For the case of argon as a collision partner, the maximum energy transferred per collision was $\sim 40 \text{ cm}^{-1}$ at an internal energy of $\sim 40\,000 \text{ cm}^{-1}$. Extrapolation of their data shows that at an average internal energy of 2000 cm^{-1} (a similar amount of energy to that used in our current work), the average energy transferred per collision is only a few wavenumbers, much lower than what we observe. In fact, only medium sized polyatomics such as SF_6 , $n\text{-C}_4\text{H}_{10}$, $c\text{-C}_3\text{H}_6$, and C_3H_6 show energy transfers similar to the values we observe in our experiment [Yerram 1990; Barker 1993, 1995].

A major difference is that the energy transfer experiments were performed at room temperature where there are both ‘up’ and ‘down’ collisions. The presence of ‘up’ collisions means that the average energy transferred is automatically reduced compared with our van der Waals complex dissociation experiments which measure only ‘down’ transfer. Using the translational energy distribution from the $(\text{C}_6\text{H}_6\cdots\text{Ar})^+$ van der Waals cation dissociation as the downward energy transfer probability function for benzene-Ar collisions, we can construct the upward distribution at a particular vibrational energy and temperature from microscopic reversibility [Gilbert 1990]. Hence we can calculate a value for the average energy transferred per collision at that energy and temperature. Using this approach we estimate that at a vibrational energy of 1820 cm^{-1} in S_0 benzene the average energy transferred per collision is $\sim 10 \text{ cm}^{-1}$. This compares reasonably with the value of $\sim 2\text{-}3 \text{ cm}^{-1}$ extracted from the infrared fluorescence experiments [Barker 1993, 1995], given that such data have to be extrapolated over a significant energy range to obtain this value.

For our case of van der Waals molecule dissociation of benzene-argon cations, the dissociation occurs on a different potential energy surface to that of the collisional energy transfer studies. As discussed in section 6.3.9, both van der Waals complexes studied here show the cationic-argon complex to have a deeper well in the

intermolecular potential than does the corresponding neutral-argon species. This, however, is unlikely to lead to large differences since the energy transfer experiments of Barker *et al.* show similarly small values of $\langle\langle\Delta E\rangle\rangle$ at $\sim 2000 \text{ cm}^{-1}$ for a variety of gasses having a variety of different Lennard-Jones parameters and different masses.

Other differences besides the presence of both up and down transfer in the collision process are, of course, present and will contribute to differences between the van der Waals molecule dissociation and collisional transfer results. Yoder *et al.*, among others, note that comparing results of van der Waals dissociation studies with energy transfer experiments is not straightforward [Yoder 1999]. As pointed out previously, collisions can sample the entire potential energy surface around the molecule. That is, they can approach the target molecule from any direction, whereas van der Waals molecule dissociation always starts from the same geometry. The $\langle\langle\Delta E\rangle\rangle$ values from energy transfer experiments are extracted using an assumed form of the collision frequency (generally the Lennard-Jones collision frequency) with the assumption that all collisions participate in the transfer of energy. Inaccuracies in this assumption will lead to errors in the energy transfer values extracted. Subtle effects can also arise from differences in the collision energy. The energy transfer experiments detailed above were performed at room temperature where there is a broad range of collision energies, governed by the Maxwell-Boltzmann distribution of speeds. We have already noted the significant effect of these experiments averaging over ‘up’ and ‘down’ collisions on the average energy transferred. In the dissociation of van der Waals molecules the ‘collision partner’ is initially at rest (zero collision energy). Varying the collision energy is known to have an effect on the pathways for energy transfer. For example, from experiments on state-to-state energy transfer in benzene-N₂ collisions there is a shift towards the van der Waals molecule dissociation propensities as the temperature is decreased [Waclawik 1993]. Thus in collisional studies one can expect to see differences in the downward energy transfer function as the temperature is varied.

6.8 Conclusion

We have successfully measured the recoil velocities of the fragments following van der Waals dissociation of $(C_6H_6\cdots Ar_2)^+$ and $(C_6H_6\cdots Ar)^+$ by ejection of an argon atom. The experiment was performed using the ion imaging apparatus described in chapter 4, that was specifically built to measure van der Waals recoil velocities. Using ion counting we were able to achieve much better spatial resolution on the detector than that obtained in the only other ion imaging experiment pertaining to van der Waals dissociations [Yoder 1999].

The ions were produced by photoionisation of the van der Waals clusters via the 6^1_0 intermediate state. This produced a range of initial vibrational energies in the cation prior to dissociation. Since no photoelectron spectra exist for the benzene-argon van der Waals clusters, and only an incomplete photoelectron spectrum was available in the literature for benzene [Long 1983], it was necessary to use the photoelectron spectrum of benzene recorded in the previous chapter to determine the initial vibrational distribution. Based on observed spectroscopic properties of the benzene-argon van der Waals clusters we assume the initial distribution for the clusters will be similar to that of the benzene monomer. In the case of $(C_6H_6\cdots Ar_2)^+$ we observe only the small fraction of the clusters that dissociate to form $(C_6H_6\cdots Ar)^+$ below its dissociation energy. The average excitation energies prior to dissociation were determined to be $\sim 1820 \text{ cm}^{-1}$ for $(C_6H_6\cdots Ar)^+$ and $\sim 860 \text{ cm}^{-1}$ for $(C_6H_6\cdots Ar_2)^+$.

The average energies released in the dissociation of $(C_6H_6\cdots Ar)^+$ and $(C_6H_6\cdots Ar_2)^+$ were 92 ± 4 and $79 \pm 5 \text{ cm}^{-1}$ respectively. This indicates that a majority of the energy remains as internal energy (i.e. in vibrational and/or rotational energy) of the fragment containing the benzene cation. This effect has been seen previously in a number of other studies of van der Waals molecule dissociation. The values for the average

energy released are similar to those obtained in other studies involving aromatic van der Waals molecules.

Although the energy distributions are qualitatively similar, they have discernible differences which we attribute to the differences in the average initial energies of the dissociating complexes.

Chapter 7

Thesis Summary and Concluding Remarks

This thesis describes a number of different areas related to the field of collision induced energy transfer. In chapter one we discussed the S_1-S_0 ($^1B_2 - ^1A_1$) absorption spectrum of toluene. Although interesting from a purely spectroscopic viewpoint, such an investigation is also necessary for the interpretation of future work in collisional relaxation experiments of S_1 toluene. Without this knowledge, an incomplete understanding of the final vibrational levels populated after deactivation would have resulted. While researching the history of the spectroscopy of toluene it became apparent that the current numbering system to describe the vibrational modes was inadequate. Vibrational frequencies were assigned to particular modes based on their similarity with those of benzene. Since the vibrational modes are significantly altered with the addition of a methyl group, the vibrational frequencies were consistently given different assignments by different authors. To alleviate this confusion we have suggested a numbering system based on that given by Mulliken [Mulliken 1955]. Redefinitions based on this convention have previously alleviated the assignment problems for the difluorobenzenes, and similarly we believe this will remove the problems associated with the labelling in toluene vibrational modes. The new numbering system proposed here has already been adopted by other authors investigating spectroscopic of toluene [Shaw 1998].



the spectroscopy

Using dispersed fluorescence spectroscopy, we have assigned most of the features seen in the excitation spectrum of jet-cooled toluene up to 2000 cm⁻¹ above the origin band. This has resulted in the determination of the S₁ vibrational frequencies of all modes with S₀ frequencies up to ~730 cm⁻¹. The assignments of inactive fundamentals were aided by the presence of Fermi resonances and vibrational energy transfer experiments.

Intramolecular vibrational redistribution (IVR), an important process for modelling dissociation reactions (including van der Waals dissociations), was found to start occurring at a relative low energy. This is attributed to the methyl rotor accelerating the vibrational mode mixings. The rates of IVR are also dependent on the particular vibrational mode that is excited. Fluorescence lifetimes were also measured for the majority of bands observed in the excitation spectrum. These are necessary for the analysis of energy transfer studies. The lifetimes display a steady decrease as the level of vibrational excitation increases.

In chapter three the results of an investigation into the vibrational relaxation of highly excited hexafluorobenzene (HFB) were presented. An important part of this work was the comparison between two different preparation methods. Many different methods have previously been used to prepare polyatomic molecules in highly vibrationally excited states. However, no direct comparison between the different techniques has been performed. We have presented results for the collisional deactivation of highly excited HFB prepared using both infrared multiphoton absorption (IRMPA) and ultraviolet absorption followed by rapid internal conversion (UV-IC). These two methods produce an ensemble of molecules having distinctly different initial energy distributions. UV-IC produces molecules with a narrow distribution centred around the wavelength used for excitation, while IRMPA produces a broad distribution because of the random and stepwise nature of the multiphoton absorption process. The broad distribution resulting from IRMPA has prevented the technique from reaching its full potential.

Under the experimental conditions employed in our experiments, the IRMPA excitation technique produces a distribution with an average internal energy of $\sim 16\ 000\ \text{cm}^{-1}$ while the UV-IC technique results in an average internal energy of $\sim 40\ 000\ \text{cm}^{-1}$. After the formation of highly vibrationally excited HFB, the internal energy was monitored by recording the infrared fluorescence (IRF) intensity as a function of the number of collisions with the argon bath gas. It was found that the average energy transferred per collision $\langle\langle\Delta E\rangle\rangle$ was, within experimental error, the same for the two different methods of initial state preparation. This is a significant result since it demonstrates the validity of using the IRMPA technique in energy transfer studies.

There is continued debate as to the functional form of $\langle\langle\Delta E\rangle\rangle$ with internal energy. Previously it has been observed that in some molecular systems (including HFB) the values of $\langle\langle\Delta E\rangle\rangle$ increase approximately linearly with energy and roll off at high internal energies. Although our experimental results have been modelled assuming a function which allow for this roll off, it was found that within experimental error $\langle\langle\Delta E\rangle\rangle$ increases linearly with energy. That is, over the $0 - 40\ 000\ \text{cm}^{-1}$ energy range no roll off was observed.

The success of the IRMPA experiment with argon led us to use this technique to measure $\langle\langle\Delta E\rangle\rangle$ values using the monatomics as collision partners. Again, the $\langle\langle\Delta E\rangle\rangle$ function was deliberately modelled using a function with a non-linear component, but it was found that for all monatomic collision partners $\langle\langle\Delta E\rangle\rangle$ varied linearly over the energy range sampled in the experiment. $\langle\langle\Delta E\rangle\rangle$ was found to increase going from helium to neon to argon but subsequently reduced going to krypton and xenon. Quasiclassical trajectory simulations performed by Lenzer *et al.* do not reproduce the trend observed here [Lenzer 1995].

In comparison with the values for other aromatic molecules, the values for the average energy transferred per collision are much larger for hexafluorobenzene. This is also

concluded from quasiclassical trajectory simulations and is attributed to the increased number of low frequency vibrational modes in HFB.

It is apparent that theoretical advancements in the prediction of $\langle\langle\Delta E\rangle\rangle$ values for highly excited polyatomic molecules are required to further interpret our results. The results reported here represent an ideal test-bed for future theoretical calculations on the collisional deactivation of highly excited molecules by monatomic colliders. Not until these results are explained can one start to predict $\langle\langle\Delta E\rangle\rangle$ values using diatomic and polyatomic collision partners.

Chapter four presented the design and testing of an ion imaging spectrometer for use in energy transfer experiments. It was also found that the addition of some layers of magnetic shielding material sufficiently reduced the stray magnetic fields to allow the imaging of photoelectrons. This allows the simultaneous measurement of both photoelectron angular distributions and photoelectron spectra. By photoionising benzene via a one colour (1+1) REMPI process and imaging the photoelectrons, the imaging properties of the spectrometer could be investigated. It was found that slight deformations in the resulting images were present and attributable to stray magnetic fields altering the electron's trajectory. One type of deformation resulted in having a slight oval appearance to the image. We have developed a method which effectively reshapes the deformed image back into a circular image, resulting in increased energy resolution in the derived photoelectron spectra.

The instrument can easily detect and measure low energy ions and electrons. In fact, we observe detailed structure at electron energies far less than those reported previously in the literature. We have found that our energy resolution in the photoelectron spectra are identical to that of the best published spectra, and furthermore, under optimum conditions (where deformations are insignificant) we have found that the energy resolution is about three times better than this.

Photoelectron spectra and the photoelectron angular distributions from the (1+1) REMPI of benzene through four S_1 intermediate states were presented in detail in chapter five. Previously, high resolution photoelectron spectroscopy has relied on the use of field free time of flight methods. This technique, however, can not detect low energy electrons, and so the entire time of flight spectrum can not be recorded. Intensities in the photoelectron spectra obtained by time of flight techniques are also attenuated towards the low energy end of the spectrum. Electron imaging, on the other hand, provides information on the entire electron energy range with constant detection efficiency at all electron energies. While the time of flight method provides higher resolution at high electron energies, the imaging technique has higher resolution at lower electron energies ($<1000\text{ cm}^{-1}$).

The angular distribution by which the electrons are ejected is easily obtained from the electron images. This is unlike the previously used field free time of flight techniques which required the measurement of photoelectron spectra at many different angles between the detector and the light polarisation. Measurements of angular distributions provide information on the dynamics of the photoionisation process. We have determined anisotropy parameters for each of the four recorded images of the (1+1) REMPI of benzene. It was found that only the $\cos^2\theta$ term was necessary to describe the angular distribution and thus it can be described by the familiar β value. β was found to vary between -0.21 and -0.35, indicating that the electrons are preferentially ejected perpendicular to the laser polarisation. On closer inspection of the images, it was found that the anisotropy varied depending on which vibrational level the cation was formed in. The images were fitted by assigning each peak a different β value. For example, REMPI via the $6_0^1 1_0^1$ transition shows that β becomes more negative (tending towards a $\sin^2\theta$ distribution) as the electron energy increases, but at $\sim 2500\text{ cm}^{-1}$ the trend reverses back towards a more isotropic distribution. We are currently engaging in discussions with workers who calculate such β values. The results of these calculations will

provide much needed insight into reasons for the anisotropy trends observed in our experiments.

In chapter six we describe experiments in which we monitor the van der Waals molecule dissociation of benzene-argon cation clusters, in particular the removal of an argon atom from the $(C_6H_6\cdots Ar)^+$ and $(C_6H_6\cdots Ar_2)^+(1|1)$ clusters. These ions were created using (1+1) REMPI via the 6_0^1 transition. The photoelectron spectrum of benzene presented in chapter five for ionisation through the 6_0^1 transition was required to determine the initial population prior to dissociation. Prior to the recording of that spectrum, only incomplete photoelectron spectra were available in the literature. It was determined that the average energy of the dissociating van der Waals cations before dissociation was $\sim 1800 \text{ cm}^{-1}$.

The average energy released as kinetic energy during removal of an argon atom from $(C_6H_6\cdots Ar)^+$ and $(C_6H_6\cdots Ar_2)^+$ clusters was found to be 92 ± 4 and $78 \pm 5 \text{ cm}^{-1}$ respectively. For the dissociation of $(C_6H_6\cdots Ar)^+$ the kinetic energy released represents only a small fraction of the total energy that requires redistributing. A large proportion of the total energy is therefore taken up as internal (i.e. rotational and vibrational) energy of the benzene cation fragment. Given the trends seen by previous workers, we suggest that there will most likely be significant rotational excitation of the benzene cation. The situation for $(C_6H_6\cdots Ar_2)^+$ is more complicated, since it is possible that enough energy remains in the $(C_6H_6\cdots Ar)^+$ fragment to eject the remaining argon atom. We suggest that the $(C_6H_6\cdots Ar)^+$ signal that we observe originates from those $(C_6H_6\cdots Ar_2)^+$ cations that are formed with little energy above the dissociation energy so that after the dissociation the $(C_6H_6\cdots Ar)^+$ fragment has insufficient energy to remove the remaining argon atom. This means that, as a result of the experiment viewing fragmentation of only a subset of the $(C_6H_6\cdots Ar_2)^+$ cations, the initial internal ion energy is different for the $(C_6H_6\cdots Ar)^+$ and $(C_6H_6\cdots Ar_2)^+$ van der Waals cations. We attribute the differences seen in the kinetic energy released distributions for the

$(C_6H_6\cdots Ar)^+$ and $(C_6H_6\cdots Ar_2)^+$ cations to the different initial energy distributions for these species.

The ion imaging spectrometer that we have designed and built has proven to be a successful instrument in the recording of photoelectron spectra and angular distributions as well recording images of the recoil velocities from the dissociation of van der Waals molecules. The number of applications that this instrument can be used for is almost endless. Already this instrument has been used to measure photoelectron spectra and angular distributions in the (1+1) REMPI of *para*-difluorobenzene. An exciting achievement was the recording of the photoelectron image from the *para*-difluorobenzene-argon (*p*DFB \cdots Ar) cluster [Bellm 1999]. Although we found it impossible to record photoelectron images of benzene-argon van der Waals clusters, the transitions of *p*DFB \cdots Ar are sufficiently far enough away from background *p*DFB interferences that such spectra are obtainable.

Another exciting use of our imaging spectrometer is the determination of the binding energies of van der Waals complexes. As noted in chapter six, binding energies are difficult to determine experimentally. Only upper and lower bounds for the dissociation energy could be found based on the appearance of emission from fragment molecules observed in the dispersed fluorescence spectra. Using the instrument described in this thesis dissociation energies can be determined directly. The *p*DFB recoil velocities from the dissociation of *p*DFB \cdots Ar and *p*DFB \cdots N₂ have been measured using a number of different intermediate states in the REMPI process [Bellm 1999]. In these systems the energy above the dissociation energy after ionising through the 6_0^1 transition is only $\sim 50\text{ cm}^{-1}$. An abrupt cut off is seen in the kinetic energy probability distribution plots due the maximum permissible energy release. This provides an experimental value for the van der Waals binding energy. This type of experiment is only possible since the instrument can easily measure such small kinetic energy releases.

The instrument can be used for the routine measurement of van der Waals binding energies. A general scheme for such a measurement is to use two colour REMPI, designed so that the van der Waals cation is produced just above its dissociation energy. By measuring the kinetic energy released, and knowing the ionisation energy of the van der Waals molecule, one determines the binding energy in the cation ground state. Provided that the ionisation energy of the parent molecule and the spectral shift for the electronic van der Waals transition is known, the binding energy in the intermediate and ground electronic states can be determined.

We have noted in chapter 4 that the instrument should be modified for future electron imaging experiments. In particular, every effort should be made to reduce the impact of stray magnetic fields. We anticipate that following such modifications, high resolution photoelectron spectra should be obtainable over the full image rather than the small section that exists currently.

Appendix 1

Forward and Inverse Abel Transform Algorithm

The algorithm used in this work for the calculation of the forward and inverse Abel transforms is based on that derived by Hansen and Law [Hansen 1985]. In their derivation they make two assumptions which are not valid in our situation. Firstly, our data do not always have a constant spacing along the x -axis. Although the spacing is constant for transforming an experimental image, when we transform a radial plot the spacing between data points gets smaller as the radius is increased (see chapter 4 for full details). Secondly, Hansen and Law assume that the value of the function is constant between data points. We have used their approach to derive formulae which can be used on data where the x -axis has non-constant step sizes and assumes that the function varies linearly between data points.

We label the function to be projected as $f(R')$ and the projection as $g(r')$. The primes attached to the variables R' and r' are present to be consistent with the definitions made in chapter 4. Since the data is made up of a series of data points, we denote the n th data point as R'_n and r'_n for the $f(R')$ and $g(r')$ functions respectively. The forward Abel transform is given by [Hansen 1985]:

$$g(r'_n) = [1 \ 1 \ \dots \ 1] \ \mathbf{x}(r'_n) \quad A1.1$$

where $\mathbf{x}(r'_n)$ is a column matrix with K entries (termed the ‘system state vector’):

$$\mathbf{x}(r'_n) = \Phi(r'_n, r'_{n+1})\mathbf{x}(r'_{n+1}) + 2 \int_{r'_{n+1}}^{r'_n} \Phi(r'_n, R)\mathbf{B}f(R')dR' \quad A1.2$$

where

$$\Phi(r'_n, r'_{n+1}) = \begin{pmatrix} \left(\frac{r'_{n+1}}{r'_n}\right)^{\lambda_1} & 0 & \dots & 0 \\ 0 & \left(\frac{r'_{n+1}}{r'_n}\right)^{\lambda_2} & \dots & 0 \\ \vdots & \vdots & & \vdots \\ 0 & 0 & \dots & \left(\frac{r'_{n+1}}{r'_n}\right)^{\lambda_K} \end{pmatrix} \quad A1.3$$

and

$$\mathbf{B} = [b_1 \ b_2 \ \dots \ b_K]^T \quad A1.4$$

The parameters b_k and λ_k are constants specific to the forward/inverse Abel transform and are determined by fitting a series of exponential functions to an 'impulse response function', $[1 - \exp(-2t)]^{-1/2}$, for the transformation. Specifically, the equation

$$\sum_{k=1}^K b_k \exp(\lambda_k t) = [1 - \exp(-2t)]^{-1/2} \quad A1.5$$

is fitted to determine the best parameters for b_k and λ_k . The values for the b_k and λ_k coefficients used here are the same as those published by Hansen and Law and are given in table A1.1. These coefficients are used for both the forward and inverse algorithms.

As seen in equation A1.2, computation of the n th point relies on the knowledge of the $(n+1)$ th point. The transformation is thus computed starting at the largest r value and working inward towards the origin. For the furthest point (initial point of the calculation) we assume that $\mathbf{x}(r'_{n+1}) = \mathbf{0}$. This is a necessary boundary condition for the computation of both the forward and inverse transforms.

Table A1.1 Coefficients used in the computation of the forward and inverse Abel transform. The values have been taken directly from Hansen and Law [Hansen 1985].

| k | b_k/π | λ_k |
|-----|-----------|-------------|
| 1 | 0.318 | 0 |
| 2 | 0.19 | -2.1 |
| 3 | 0.35 | -6.2 |
| 4 | 0.82 | -22.4 |
| 5 | 1.8 | -92.5 |
| 6 | 3.9 | -414.5 |
| 7 | 8.3 | -1889.4 |
| 8 | 19.6 | -8990.9 |
| 9 | 48.3 | -47391.1 |

The inverse Abel transform has a similar form to that of its forward counterpart, viz.,

$$f(R'_n) = [1 \quad 1 \quad \dots \quad 1] \quad \mathbf{x}(R'_n) \quad \text{A1.6}$$

where

$$\mathbf{x}(R'_n) = \Phi(R'_n, R'_{n+1}) \mathbf{x}(R'_{n+1}) - \frac{1}{\pi} \int_{R'_{n+1}}^{R'_n} \frac{\Phi(R'_n, r') \mathbf{B} g'(r') dr'}{r'} \quad \text{A1.7}$$

and

$$\Phi(R'_n, R'_{n+1}) = \begin{pmatrix} \left(\frac{R'_{n+1}}{R'_n}\right)^{\lambda_1} & 0 & \dots & 0 \\ 0 & \left(\frac{R'_{n+1}}{R'_n}\right)^{\lambda_2} & \dots & 0 \\ \vdots & \vdots & & \vdots \\ 0 & 0 & \dots & \left(\frac{R'_{n+1}}{R'_n}\right)^{\lambda_K} \end{pmatrix} \quad \text{A1.8}$$

Since the b_k parameters are the same for the forward and the inverse transform, the **B** matrix is the same as for the forward transform (equation A1.4). The derivative of $g(r')$ appearing in the integrand of equation A1.7 is responsible for the large amount of noise observed in the computation of the inverse Abel transform.

Evaluation of the integral in equations A1.2 and A1.7 is relatively straight forward if one assumes that the function to be transformed is a staircase function with constant x -spacing. This was the approach taken by Hansen and Law, but we present a different approach here. For an abscissa with varying spacing and assuming the function varies linearly between each data point, the forward Abel transform (equation A1.2) reduces to

$$\mathbf{x}(r'_{n+1}) = \Phi(r'_{n+1})\mathbf{x}(r'_n) + \Gamma(r'_{n+1}) \quad \text{A1.9}$$

where

$$\Gamma(r'_{n+1}) = \begin{pmatrix} 2b_1\gamma(r'_{n+1}, \lambda_1) \\ 2b_2\gamma(r'_{n+1}, \lambda_2) \\ \vdots \\ 2b_K\gamma(r'_{n+1}, \lambda_K) \end{pmatrix} \quad \text{A1.10}$$

and

$$\begin{aligned} \gamma(r'_{n+1}, \lambda) &= \frac{mr'^2}{\lambda+2} \left(1 - \left(\frac{r'_{n+1}}{r'_n} \right)^{\lambda+2} \right) \\ &\quad + \frac{(f(r'_n) - mr'_n)r'_n}{\lambda+1} \left(1 - \left(\frac{r'_{n+1}}{r'_n} \right)^{\lambda+1} \right) \quad \lambda \neq -1, -2 \end{aligned}$$

$$m = \frac{f(r'_{n+1}) - f(r'_n)}{r'_{n+1} - r'_n} \quad \text{A1.11}$$

For the case of the inverse Abel transform a similar expression is found

$$\mathbf{x}(R'_n) = \Phi(R'_n, R'_{n+1})\mathbf{x}(R'_{n+1}) + \Gamma(R'_{n+1}) \quad \text{A1.12}$$

where

$$\Gamma(R'_{n+1}) = \begin{pmatrix} -\frac{b_1}{\pi} \gamma(R'_{n+1}, \lambda_1) \\ -\frac{b_2}{\pi} \gamma(R'_{n+1}, \lambda_2) \\ \vdots \\ -\frac{b_K}{\pi} \gamma(R'_{n+1}, \lambda_K) \end{pmatrix} \quad \text{A1.13}$$

and

$$\gamma(R'_{n+1}, \lambda) = \begin{cases} \frac{mR'_n}{\lambda+1} \left(1 - \left(\frac{R'_{n+1}}{R'_n} \right)^{\lambda+1} \right) \\ \quad + \frac{(g'(R'_n) - mR'_n)}{\lambda} \left(1 - \left(\frac{R'_{n+1}}{R'_n} \right)^\lambda \right) & \lambda \neq -1, 0 \\ m(R'_n - R'_{n+1}) - (g'(R'_n) - mR'_n) \ln \left(\frac{R'_{n+1}}{R'_n} \right) & \lambda = 0 \end{cases}$$

$$m = \frac{g'(R'_{n+1}) - g'(R'_n)}{R'_{n+1} - R'_n} \quad \text{A1.14}$$

Although the above equations look formidable at first glance, they are in fact relatively simple to implement on a computer, requiring only ~20 lines of code.

References

- Abel 1992a B. Abel, H. Hippeler, and J. Troe, "Infrared multiphoton excitation dynamics of CF₃I. I. Populations and dissociation rates of highly excited rovibrational states," *J. Chem. Phys.* **96**, 8863, (1992).
- Abel 1992b B. Abel, H. Hippeler, and J. Troe, "Infrared multiphoton excitation dynamics of CF₃I. II. Collisional effects on vibrational and rotational state populations," *J. Chem. Phys.* **96**, 8872, (1992).
- Allendorf 1989 S. W Allendorf, D. J. Leahy, D. C. Jacobs, and R. N. Zare, "High-resolution angle- and energy-resolved photoelectron spectroscopy of NO: Partial wave decomposition of the ionization continuum," *J. Chem. Phys.* **91**, 2216, (1989)
- Atkins 1997 P. W. Atkins, *Physical Chemistry*, 6th edition, (W H Freeman & Co, New York, 1997).
- Bagratashvili 1980 V. N. Bagratashvili, Y. G. Vainer, V. S. Doljikov, S. F. Koliakov, A. A. Makarov, L. P. Malyavkin, E. A. Ryabov, E. G. Silkis, and V. D. Titov, "Raman spectroscopy of infrared multiple-photon excited molecules," *Appl. Phys.* **22**, 101, (1980).
- Bagratashvili 1981 V. N. Bagratashvili, Y. G. Vainer, V. S. Doljikov, V. S. Letokhov, A. A. Makarov, L. P. Malyavkin, E. A. Ryabov, and E. G. Silkis, "Observation of nonequilibrium vibrational distribution in infrared multiphoton excitation of molecules by Raman spectroscopy," *Opt. Lett.* **6**, 148, (1981).
- Bagratashvili 1985 V. N. Bagratashvili, V. S. Letokhov, A. A. Makarov, and E. A. Ryabov, *Multiple Photon Infrared Laser Photophysics and Photochemistry* (Harwood, London, 1985).
- Baker 1977 A. D. Baker and C. R. Brundle, "An introduction to electron spectroscopy," in *Electron spectroscopy: theory, techniques and applications Vol. 1*, p 1, (Eds C. R. Brundle and A. D. Baker, Academic Press, London, 1977)

- Balfour 1994a W. J. Balfour and Y. Fried, "Spectroscopic studies on toluene and some deuterated derivatives. I. Vibrational spectra," *Can. J. Phys.* **72**, 1218, (1994).
- Balfour 1994b W. J. Balfour and R. S. Ram, "Spectroscopic studies on toluene and some deuterated derivatives. II. Electronic spectra," *Can. J. Phys.* **72**, 1225, (1994).
- Baltzer 1997 P. Baltzer, L. Karlsson, B. Wannberg, G. Öhrwall, D. M. P. Holland, M. A. MacDonald, M. A. Hayes, and W. von Niessen, "An experimental and theoretical study of the valence shell photoelectron spectrum of the benzene molecule," *Chem. Phys.* **224**, 95, (1997).
- Barker 1988 J. R. Barker and M. L. Yerram, in *Multiphoton Processes*, edited by S. J. Smith and P. L. Knight (Cambridge University Press, Cambridge, 1988), pp. 201.
- Barker 1993 J. R. Barker and B. M. Toselli, "Infrared-emission studies of the vibrational deactivation of benzene-derivatives," *Int. Rev. Phys. Chem.* **12**, 305, (1993).
- Barker 1995 J. R. Barker, J. D. Brenner, B. M. Toselli "The vibrational deactivation of large molecules by collisions and by spontaneous infrared emission," in *Vibrational Energy Transfer Involving Large and Small Molecules, Advances in Chemical Kinetics and Dynamics*, vol 2; ed J. R. Barker, (JAI Press, Greenwich, CT, 1995), pp. 393.
- Bellm 1999 S. M. Bellm, Private Communication, (1999)
- Benson 1982 S. W. Benson, *The Foundations of Chemical Kinetics*, (Krieger Publishing: Florida, 1982).
- Bernshtein 1999 V. Bernshtein and I. Oref, "Energy release in benzene-argon cluster dissociation - quasiclassical trajectory calculations," *Chem. Phys. Lett.* **300**, 104, (1999).
- Beyer 1973 T. Beyer and D. F. Swinehart, "Number of multiply-restricted partitions," *Comm. Assoc. Comput. Machines* **16**, 379, (1973).
- Bieske 1990 E. J. Bieske, R. I. McKay, F. R. Bennett and A. E. W. Knight, "Photodissociation spectroscopy of aromatic-rare gas cluster ions: Low frequency vibrations in p-difluorobenzene + argon," *J. Chem. Phys.* **92**, 4620, (1990).
- Bieske 1991a E. J. Bieske, M. W. Rainbird and A. E. W. Knight, "The van der Waals vibrations of aniline-(argon)₂ in the S₁ electronic state," *J. Chem. Phys.* **94**, 7019, (1991).

- Bieske 1991b E. J. Bieske, A. S. Uichanco, M. W. Rainbird and A. E. W. Knight, "Mass selected resonance enhanced multiphoton ionization spectroscopy of aniline-Ar_n (n=3,4,5, ...) van der Waals complexes," *J. Chem. Phys.* **94**, 7029, (1991).
- Blondeau 1971 J. M. Blondeau and M. Stockburger, "Resonance fluorescence of aromatic molecules in the vapour phase," *Ber. Bunsenges. Phys. Chem.* **75**, 450, (1971).
- Bludský 1992 O. Bludský, V. Spirko, V. Hrouda, and P. Hobza, "Vibrational dynamics of the benzene...argon complex," *Chem. Phys. Lett.* **196**, 410, (1992).
- Boesl 1992 U. Boesl, R. Weinkauf and E. W. Schlag, "Reflectron time-of-flight mass spectrometry and laser excitation for the analysis of neutrals, ionized molecules and secondary fragments," *Int. J. Mass Spectrom. Ion Processes* **112**, 121, (1992).
- Bogomolov 1960 A. M. Bogomolov, "Vibrational spectra of aromatic compounds VII. Characteristic vibrations of monosubstituted benzenes," *Opt. Spectry* **9**, 162, (1960).
- Bontyan 1993 L. S. Bontyan, A. G. Suits, P. L. Houston, and B. J. Whitaker, "State-resolved differential cross sections for crossed-beam Ar-NO inelastic scattering by direct ion imaging", *J. Phys. Chem.* **97**, 6342, (1993).
- Borg 1994 R. A. J. Borg, E. R. Waclawik, Mudjijono, and W. D. Lawrance, "A strong collision partner dependence for vibrational energy transfer in benzene and benzene-*d*₆. He versus D2," *Chem. Phys. Lett.* **218**, 320, (1995).
- Bracewell 1977 R. N. Bracewell, *The Fourier Transform and Its Applications*, 2nd ed. (McGraw-Hill, New York, 1977).
- Breen 1987 P. J. Breen, J. A. Warren, E. R. Bernstein and J. I. Seeman, "A study of nonrigid aromatic molecules by supersonic molecular jet spectroscopy. I. Toluene and the xylenes," *J. Chem. Phys.* **87**, 1917, (1987).
- Brenner 1993 J. D. Brenner, J. P. Ernjeri, and J. R. Barker, "Population distributions in the vibrational deactivation of benzene and benzene-*d*₆. First and second moments derived from two-color infrared fluorescence measurements," *Chem. Phys.* **175**, 99, (1993).
- Bromse 1983 D. S. Bromse, J. B. Cross, and J. J. Valentini, "The dynamics of infrared photodissociation of van der Waals molecules containing ethylene: An experimental study," *J. Chem. Phys.* **78**, 7175, (1983).

- Brown 1985 T. C. Brown, K. D. King, J.-M. Zellweger, and J. R. Barker, "Experimental studies of population-distributions produced by infrared multiphoton absorption," *Ber. Bunsen-Ges. Phys. Chem.* **89**, 301, (1985).
- Brumbaugh 1983 D. V. Brumbaugh, J. E. Kenny, and D. H. Levy, "Vibrational predissociation and intramolecular vibrational relaxation in electronically excited *s*-tetrazine-argon van der Waals complex," *J. Chem. Phys.* **78**, 3415 (1983).
- Brundle 1977 C. R. Brundle and A. D. Baker, "Electron spectroscopy: theory, techniques and applications," Vol. 1, Academic Press, London, (1977).
- Brupbacher 1990 Th. Brupbacher and A. Bauder, "Rotational spectrum and dipole moment of the benzene-argon van der Waals complex," *Chem. Phys. Lett.* **173**, 435, (1990).
- Bullock 1995 W. J. Bullock, "Theoretical and experimental investigations of IVR in aromatic molecules," Ph.D. Thesis, Flinders University, Adelaide, Australia (1995).
- Chandler 1987 D. W. Chandler and P. L. Houston, "Two-dimensional imaging of state-selected photodissociation products detected by multiphoton ionization," *J. Chem. Phys.* **87**, 1445, (1987).
- Chandler 1989 D. W. Chandler, J. W. Thoman Jr, M. H. M. Janssen, and D. H. Parker, "Photofragment imaging: The 266 nm photodissociation of CH₃I," *Chem. Phys. Lett.* **156**, 151, (1989).
- Chandler 1999 D. W. Chandler and D. H. Parker, "Velocity mapping of multiphoton excited molecules," in *Advances in photochemistry* Vol. 25, p 59, (Eds D. C. Neckers, D. H. Volman, and G. von Bünau, Wiley-Interscience, New York, 1999).
- Chang 1998 B.-Y. Chang, R. C. Hoetzlein, J. A. Mueller, J. D. Geiser, and P. L. Houston, "Improved two dimensional product imaging: The real-time ion-counting method," *Rev. Sci. Instrum.* **69**, 1665, (1998).
- Chem. Rev. 1988 "Van der Waals interactions," *Chemical Reviews*, vol. 88, no. 6, (1988).
- Chem. Rev. 1994 "Van der Waals molecules" *Chemical Reviews*, vol. 94, no. 7, (1994).
- Chen 1984 X. Chen, L. Li, F. Sun, and C. Zhang, "IR-UV double resonance studies of vibrational relaxation of hexafluorobenzene," *Acta Optica Sinica* **4**, 781, (1984).

- Chewter 1987a L. A. Chewter, M. Sander, K. Müller-Dethlefs, and E. W. Schlag, "High resolution zero kinetic energy photoelectron spectroscopy of benzene and determination of the ionization potential," *J. Chem. Phys.* **86**, 4737, (1987).
- Chewter 1987b L. Chewter, K. Müller-Dethlefs and E. W. Schlag, "Determination of the ionization energy of the benzene-argon complex by zero kinetic energy photoelectron spectroscopy," *Chem. Phys. Lett.* **135**, 219, (1987).
- Coronado 1994 E. A. Coronado, C. A. Rinaldi, G. F. Velardez, and J. C. Ferrero, "Dependence of the collisional relaxation of highly vibrationally excited polyatomic molecules on the population distribution function," *Chem. Phys. Lett.* **227**, 164, (1994).
- Coronado 1996 E. A. Coronado and J. C. Ferrero, "Evolution of the moments and transition probability models in energy transfer processes," *Chem. Phys. Lett.* **257**, 674, (1996).
- Coronado 1997 E. A. Coronado and J. C. Ferrero, "Collisional relaxation of highly vibrationally excited *cis*-ClFC=FCCl prepared by multiphoton excitation," *J. Phys. Chem. A* **101**, 9603, (1997).
- Dahl 1995 D. A. Dahl, "SIMION V6," (Idaho National Engineering Laboratory, 1995)
- Damm 1990 M. Damm, H. Hippler, H. A. Olschewski, J. Troe, and J. Willner, "Efficient collisional energy transfer of vibrationally highly excited C₆F₆ molecules in the ground electronic state," *Z. Phys. Chem. N. F.* **166**, 129, (1990).
- Davies 1999 J. A. Davies, J. E. LeClaire, R. E. Continetti, and C. C. Hayden, "Femtosecond time-resolved photoelectron-photoion coincidence imaging studies of dissociation dynamics," *J. Chem. Phys.* **111**, 1, (1999).
- Downie 1999 P. Downie and I. Powis, "The 5 a_1^{-1} photoionization of oriented CF₃I molecules: Angular distributions of the ka_1 and ke photoelectron continua," *J. Chem. Phys.* **111**, 4535, (1999).
- Draeger 1985 J. A. Draeger, "The methylbenzenes I. Vapour-phase vibrational fundamentals, internal rotations and a modified valence force field," *Spectrochim. Acta* **41A**, 607, (1985).
- Droz-Georget 1997 T. Droz-Georet, M. Zyrianov, H. Reisler, and D. W. Chandler, "Correlated distributions in the photodissociation of HNCO to NH(X³ Σ^+ , a¹ Δ) + CO(X¹ Σ^+) near the barrier on S₁," *Chem. Phys. Lett.* **276**, 316, (1997).

- Durana 1977 J. F. Durana and J. D. McDonald, "Infrared chemiluminescence studies of chlorine substitution reactions with brominated unsaturated hydrocarbons," *J. Chem. Phys.* **64**, 2518, (1977).
- Easter 1998 D. C. Easter, L. Bailey, J. Mellot, M. Tirres, and T. Weiss, "Structure and dynamics of intermediate benzene-argon clusters: $(C_6H_6)Ar_n$, $n=13-40$," *J. Chem. Phys.* **108**, 6135, (1998).
- Eaton 1973 V. J. Eaton and D. Steele, "The vibrational force field of halogenated aromatic molecules: In-plane vibrations of benzene and fluorobenzenes," *J. Mol. Spectrosc.* **48**, 446, (1973).
- Eppink 1997 A. T. J. B. Eppink and D. H. Parker, "Velocity map imaging of ions and electrons using electrostatic lenses: Application in photoelectron and photofragment ion imaging of molecular oxygen," *Rev. Sci. Instrum.* **68**, 3477, (1997).
- Even 1983 U. Even and J. Jortner, "Spectroscopy of large molecular complexes in supersonic jets," *J. Chem. Phys.* **78**, 3445, (1983).
- Ewing 1979 G. E. Ewing, "A guide to the lifetimes of vibrationally excited van der Waals molecules: The momentum gap," *J. Chem. Phys.* **71**, 3143 (1979).
- Faidas 1988 H. Faidas and K. Siomos, "Two-photon excitation spectroscopy of benzene and toluene in nonpolar liquids," *J. Mol. Spectrosc.* **130**, 228, (1988).
- Faraday Disc. 1994 "Structure and dynamics of van der Waals Complexes," *Faraday Discussions*, no. 97, (1994).
- Felker 1994 P. M. Felker, P. M. Maxton, and M. W. Schaeffer, "Nonlinear Raman studies of weakly bound complexes and clusters in molecular beams," *Chem. Rev.* **94**, 1787, (1994).
- Fischer 1981 G. Fischer, J. R. Reimer and I. G. Ross, "CNDO calculation of second order vibronic coupling in the $^1B_{2u}-^1A_{1g}$ transition of benzene," *Chem. Phys.* **62**, 187, (1981).
- Fuson 1960 N. Fuson, C. Garrigou-Lagrange and M. L. Josien, "Spectre infrarouge et attribution des vibrations des toluènes $C_6H_5CH_3$, $C_6H_5CD_3$ et $C_6D_5CD_3$," *Spectrochim. Acta* **16**, 106, (1960).
- Garrett 1992 A. W. Garrett, D. L. Severance and T. S. Zwier, "Multiphoton ionization studies of $C_6H_6-(CH_3OH)_n$ clusters. I. Comparisons with $C_6H_6-(H_2O)_n$ clusters," *J. Chem. Phys.* **96**, 7245, (1992).

- Gascooke 1998a J. R. Gascooke, Z. T. Alwahabi, K. D. King, and W. D. Lawrence, "A direct comparison of vibrational deactivation of hexafluorobenzene excited by infrared multiple photon absorption and internal conversion," *J. Chem. Phys.* **109**, 3868, (1998).
- Gascooke 1998b J. R. Gascooke, Z. T. Alwahabi, K. D. King, and W. D. Lawrence, "Vibrational deactivation of highly excited hexafluorobenzene," *J. Phys. Chem.* **102**, 8505, (1998).
- Ghosh 1988 P. N. Ghosh, P. K. Panja, C. M. Pal, "Local mode mixing of the vibrational overtone manifold of the carbon-hydrogen stretching modes in toluene," *Chem. Phys. Lett.* **148**, 337, (1988).
- Gilbert 1990 R. G. Gilbert and S. Smith, "Theory of Unimolecular and recombination reactions" Blackwell Scientific Publications, 1990.
- Ginsburg 1946 N. Ginsburg, W. W. Robertson and F. A. Matsen, "The near-ultraviolet absorption spectrum of toluene vapour," *J. Chem. Phys.* **14**, 511, (1946).
- Goode 1997 J. G. Goode, J. D. Hofstein, and P. M. Johnson, "The observation of strong pseudo-Jahn-Teller activity in the benzene cation \tilde{B}^2E_{2g} state," *J. Chem. Phys.* **107**, 1703, (1997).
- Goodman 1981 L. Goodman and R. P. Rava, "Two-photon spectra of substituted benzenes" *J. Chem. Phys.* **74**, 4826, (1981).
- Gotch 1990 A. J. Gotch and T. S. Zwier, "The spectroscopy and dynamics of π hydrogen-bonded complexes: Benzene-HCl/DCl and toluene-HCl/DCl," *J. Chem. Phys.* **93**, 6977, (1990).
- Hansen 1985 E. W. Hansen and P.-L. Law, "Recursive methods for computing the Abel transform and its inverse," *J. Opt. Soc. Am. A* **2**, 510, (1985).
- Hartland 1997 G. V. Hartland, D. Qin, H.-L. Dai, and C. J. Chen, "Collisional energy transfer of highly vibrationally excited NO₂: The role of intramolecular vibronic coupling and the transition dipole coupling mechanism," *Chem. Phys.* **107**, 2890, (1997).
- Heck 1995 A. J. R. Heck and D. W. Chandler, "Imaging techniques for the study of chemical reaction dynamics," *Annu. Rev. Phys. Chem.* **46**, 335, (1995).
- Helm 1993 H. Helm, N. Bjerre, M. J. Dyer, D. L. Huestis, and M. Saeed, "Images of photoelectrons formed in intense laser fields," *Phys. Rev. Lett.* **70**, 3221, (1993).

- Herzberg 1966 G. Herzberg, "Molecular spectra and molecular structure: III Electronic Spectra and electronic structure of polyatomic molecules," (van Nostrand Reinhold Company, New York, 1966).
- Hickman 1996 C. G. Hickman, J. R. Gascooke, and W. D. Lawrence, "The S₁-S₀ (B₂-A₁) transition of jet-cooled toluene. Excitation and dispersed fluorescence spectra, fluorescence lifetimes, and IVR," *J. Chem. Phys.* **104**, 4887, (1996).
- Hobza 1991 P. Hobza, H. L. Selzle, and E. W. Schlag, "Ab initio calculations on the structure, stabilization, and dipole moment of benzene...Ar complex," *J. Chem. Phys.* **95**, 391, (1991).
- Hobza 1992 P. Hobza, O. Bludský, H. L. Selzle, and E. W. Schlag, "Ab initio second- and fourth-order Møller-Plesset study on structure, stabilization energy, and stretching vibration of benzene...X (X=He,Ne,Ar,Kr,Xe) van der Waals molecules", *J. Chem. Phys.* **97**, 335, (1992).
- Hobza 1994 P. Hobza, H. L. Selzle, and E. W. Schlag, "Structure and properties of benzene-containing molecular clusters: Nonempirical ab initio calculations and experiments," *Chem. Rev.* **94**, 1767, (1994).
- Hobza 1996 P. Hobza, O. Bludský, H. L. Selzle, and E. W. Schlag, "Ab initio calculations on the structure, vibrational frequencies, and valence excitation energies of the benzene...Ar and benzene...Ar₂ cluster," *Chem. Phys. Lett.* **250**, 402, (1996).
- Hoffbauer 1983 M. A. Hoffbauer, K. Liu, C. F. Giese, and W. R. Gentry, "The dynamics of ethylene dimer infrared photodissociation in pulsed molecular beams," *J. Chem. Phys.* **78**, 5567, (1983).
- Hopkins 1980a J. B. Hopkins, D. E. Powers and R. E. Smalley, "Vibrational relaxation in jet-cooled alkylbenzenes. I. Absorption spectra," *J. Chem. Phys.* **72**, 5039, (1980).
- Hopkins 1980b J. B. Hopkins, D. E. Powers, S. Mukamel and R. E. Smalley, "Vibrational relaxation in jet-cooled alkylbenzenes. II. Fluorescence spectra," *J. Chem. Phys.* **72**, 5049, (1980).
- Hopkins 1981 J. B. Hopkins, D. E. Powers and R. E. Smalley, "Mass-selective two-color photoionization of benzene clusters," *J. Phys. Chem.* **85**, 3739, (1981).
- Ichimura 1984 T. Ichimura, Y. Mori, N. Nakashima, and K. Yoshihara, "Formation of hot hexafluorobenzene in the 193 nm photolysis," *Chem. Phys. Lett.* **104**, 553, (1984).

- Ichimura 1985 T. Ichimura, Y. Mori, N. Nakashima, and K. Yoshihara, "ArF laser flash photolysis of hexafluorobenzene vapour: Formation of hot molecules and their collisional relaxation," *J. Chem. Phys.* **83**, 117, (1985).
- Ichimura 1987 T. Ichimura, M. Takahashi, and Y. Mori, "Collisional deactivation of highly vibrationally excited hexafluorobenzene molecules" *Chem. Phys.* **114**, 111, (1987).
- Jacobson 1988 B. A. Jacobson, S. Humphrey, and S. A. Rice, "Direct measurements of vibrational predissociation of *p*-difluorobenzene-argon," *J. Chem. Phys.* **89**, 5624, (1988).
- Jacon 1977 M. Jacon, C. Lardeux, R. Lopez-Delgado, and A. Tramer, "On the 'third decay channel' and vibrational redistribution problems in benzene derivatives," *Chem. Phys.* **24**, 145, (1977).
- Johnson 1986 R. D. Johnson, S. Burdenski, M. A. Hoffbauer, C. F. Giese, and W. R. Gentry, "Infrared photodissociation of benzene dimers in the 1000 cm⁻¹ frequency region," *J. Chem. Phys.* **84**, 2624, (1986).
- Jung 1997 Y.-J. Jung, Y. S. Kim, W. K. Kang, and K.-H. Jung, "Photoelectron imaging spectroscopy for (2+1) resonance-enhanced multiphoton ionization of atomic iodine produced from *A*-band photolysis of CH₃I," *J. Chem. Phys.* **107**, 7187, (1997).
- Kahane-Paillous 1958 J. Kahane-Paillous and S. Leach, "Les spectres électroniques des dérivés monosubstitués du benzène I. Le spectra d'émission du toluène," *J. Chim. Phys. Physicochim. biol.* **55**, 439, (1958).
- Kenny 1980 J. E. Kenny, K. E. Johnson, W. Sharfin, and D. H. Levy "The photodissociation of van der Waals molecules: Complexes of iodine, neon and helium," *J. Chem. Phys.* **88**, 6182, (1988).
- Kiermeir 1988 A. Kiermeir, H. Kühlewind, N. J. Neusser, and E. W. Schlag, "Production and unimolecular decay rate of rotationally selected polyatomic molecular ions," *J. Chem. Phys.* **88**, 6182, (1988).
- Kim 1997 W. Kim and P. M. Felker, "Ground-state intermolecular spectroscopy and pendular state in benzene-argon," *J. Chem. Phys.* **107**, 2193, (1997).
- Kincaid 1991 E. H. Kincaid, V. Worah and M. D. Schuh, "Collision-induced state-to-state flow of vibrational energy in S₁ toluene," *J. Chem. Phys.* **94**, 4842, (1991).

- Kitsopoulos 1993 T. N. Kitsopoulos, M. A. Buntine, D. P. Baldwin, R. N. Zare, and D. W. Chandler, "Reaction product imaging: The H + D₂ reaction," *Science* **260**, 1605, (1993).
- King 1996 K. D. King and J. R. Barker, "US/Australia Workshop on Energy Transfer," held on July 7-12, 1996, McLaren Vale, South Australia.
- Klopper 1994 W. Klopper and H. P. Lüthi, Th. Brupbacher and A. Bauder, "Ab initio computations close to the one-particle basis set limit on the weakly bound van der Waals complexes benzene-neon and benzene-argon," *J. Chem. Phys.* **101**, 9747, (1994).
- Knight 1975 A. E. W. Knight, C. S. Parmenter and M. W. Schuyler, "An extended view of the benzene 260 nm transition via single vibronic level fluorescence. I. General aspects of benzene single vibronic level fluorescence," *J. Am. Chem. Soc.* **97**, 1993, (1975).
- Knight 1988a A. E. W. Knight, "IVR viewed through state-selected dispersed fluorescence spectroscopy of jet-cooled polyatomics," *Ber. Bunsenges. Phys. Chem.* **92**, 337, (1988).
- Knight 1988b A. E. W. Knight and S. H. Kable, "The S₁-S₀(¹B_{2u}-¹A_g) transition of p-difluorobenzene cooled in a supersonic free jet expansion. Excitation and dispersed fluorescence spectra, vibrational assignments, Fermi resonances, and forbidden transitions," *J. Chem. Phys.* **89**, 7139, (1988).
- Knochenmuss 1994 R. Knochenmuss, D. Ray, and W. P. Hess, "Electronic absorption spectra of large benzene·Ar_n clusters," *J. Chem. Phys.* **100**, 44, (1994).
- Koch 1998 H. Koch, B. Fernández and O. Christiansen, "The benzene-argon complex: A ground and excited state ab-initio study," *J. Chem. Phys.* **108**, 2784, (1998).
- Koch 1999 H. Koch, B. Fernández and J. Makarewicz, "Ground state benzene-argon intermolecular potential energy surface," *J. Chem. Phys.* **111**, 198, (1999).
- Krajnovich 1987 D. J. Krajnovich, C. S. Parmenter and D. L. Catlett Jr, "State-to-state vibrational transfer in atom-molecule collisions. Beams vs. bulbs," *Chem. Rev.* **87**, 237, (1987).
- Krause 1992 H. Krause and H. J. Neusser, "Dissociation of state-selected complex ions studied by mass-selective pulsed field threshold ionization spectroscopy," *J. Chem. Phys.* **97**, 5923, (1992).
- Krause 1993a H. Krause and H. J. Neusser, "The van der Waals modes of the (benzene-Ar)⁺ complex studied by mass selective pulsed field threshold ionization," *Chem. Phys. Lett.* **213**, 603, (1993).

- Krause 1993b H. Krause and H. J. Neusser, "Dissociation energy of neutral and ionic benzene-noble gas dimers by pulsed field threshold ionization spectroscopy," *J. Chem. Phys.* **99**, 6278, (1993).
- Krogh-Jespersen 1979 K. Krogh-Jespersen, R. P. Rava and L. Goodman, "Two-photon ionization spectrum of the $^1L_b \leftarrow S_0$ transition in toluene," *Chem. Phys.* **44**, 295, (1979).
- La Lau 1971 C. La Lau and R. G. Snyder, "A valence force field for alkyl benzenes toluene, *p*-xylene, *m*-xylene, mesitylene, and some of their deuterated analogues," *Spectrochim. Acta* **27A**, 2073, (1971).
- Lawrance 1988 W. D. Lawrance and A. E. W. Knight, "Rotational mechanisms in intramolecular vibrational energy redistribution: An examination of centrifugal and Coriolis coupling and the states contributing to time dynamical measurements," *J. Phys. Chem.* **92**, 5900, (1988).
- Lee 1992 M.-T. Lee, K. Wang, V. McKoy, and L. E. Machado, "Rotationally resolved photoelectron spectra in resonance enhanced ionization of H_2O via the C^1B_1 Rydberg state," *J. Chem. Phys.* **97**, 3905, (1992).
- Lembach 1998 G. Lembach and B. Brutschy, "Vibrational predissociation of *p*-difluorobenzene·Ar studied by mass-analysed threshold ionization spectroscopy," *J. Phys. Chem. A* **102**, 6068, (1998).
- Lenzer 1995 T. Lenzer, K. Luther, J. Troe, R. G. Gilbert, and K. F. Lim, "Trajectory simulations of collisional energy transfer in highly excited benzene and hexafluorobenzene," *J. Chem. Phys.* **103**, 626, (1995).
- Lenzer 1997 T. Lenzer and K. Luther, "Trajectory studies on the collisional relaxation of highly excited benzenes by mono- and polyatomic colliders," *Ber. Bunsen-Ges. Phys. Chem.* **101**, 581, (1997).
- Leugers 1982a M. A. Leugers and C. J. Seliskar, "The rotation-torsion contour of the 2668 Å origin band of toluene. High-resolution 295 K absorption spectrum," *J. Mol. Spectrosc.* **91**, 150, (1982).
- Leugers 1982b M. A. Leugers and C. J. Seliskar, "The rotation-torsion contour of the 2668 Å origin band of toluene. Calculation of the molecular beam fluorescence excitation spectrum," *J. Mol. Spectrosc.* **91**, 209, (1982).
- Leugers 1983 C. J. Seliskar, M. Heaven, and M. A. Leugers, "The free jet spectrum of the toluene 2668 Å origin band," *J. Mol. Spectrosc.* **97**, 186, (1983).
- Levine 1987 R. D. Levine, R. B. Bernstein, "Molecular Reaction Dynamics and Chemical Reactivity," Oxford University Press, 1987.

- Long 1983 S. R. Long, J. T. Meek, and J. P. Reilly, "The laser photoelectron spectrum of gas phase benzene," *J. Chem. Phys.* **79**, 3206, (1983).
- Manson 1978 S. T. Manson and D. Dill, "The photoionization of atoms: Cross-sections and photoelectron angular distributions," in *Electron spectroscopy: theory, techniques and applications Vol. 2*, p 157, (Eds C. R. Brundle and A. D. Baker, Academic Press, London, 1977).
- Masaki 1936 K. Masaki, "Normal frequencies of vibration of benzene compounds in the ultraviolet absorption," *Bull. Chem. Soc. Japan.* **11**, 346, (1936).
- Menapace 1987 J. A. Menapace and E. R. Bernstein, "Calculation of the vibronic structure of solute/solvent van der Waals clusters," *J. Phys. Chem.* **91**, 2533, (1987).
- Michaels 1995 C. A. Michaels, A. S. Mullin, and G. W. Flynn, "Long- and short-range interactions in the temperature dependent collisional excitation of the antisymmetric stretching $\text{CO}_2(00^01)$ level by highly vibrationally excited pyrazine," *J. Chem. Phys.* **102**, 6682, (1995).
- Michaels 1997a C. A. Michaels and G. W. Flynn, "Connecting quantum state resolved scattering data directly to chemical kinetics: Energy transfer distribution functions for the collisional relaxation of highly excited molecules from state resolved probes of the bath," *J. Chem. Phys.* **106**, 3558, (1997).
- Michaels 1997b C. A. Michaels, Z. Lin, A. S. Mullin, H. C. Tapalian, and G. W. Flynn, "Translational and rotational excitation of the $\text{CO}_2(00^00)$ vibrationless state in the collisional quenching of highly vibrationally excited perfluorobenzene: Evidence for impulsive collisions accompanied by large energy transfers," *J. Chem. Phys.* **106**, 7055, (1997).
- Michaels 1998 C. A. Michaels, A. S. Mullin, J. Park, J. Z. Chou and G. W. Flynn, "The collisional deactivation of highly vibrationally excited pyrazine by a bath of carbon dioxide: Excitation of the infrared inactive (10^00) , (02^00) , and (02^20) bath vibrational modes," *J. Chem. Phys.* **108**, 2744, (1998).
- Miller 1996a L. A. Miller and J. R. Barker, "Collisional deactivation of highly vibrationally excited pyrazine," *J. Chem. Phys.* **105**, 1383, (1996).
- Miller 1996b L. A. Miller, C. D. Cook, and J. R. Barker, "Temperature effects in the collisional deactivation of highly vibrationally excited pyrazine by unexcited pyrazine," *J. Chem. Phys.* **105**, 3012, (1996).

- Moss 1983 D. B. Moss, S. H. Kable and A. E. W. Knight, "Translational temperature dependence of mode-to-mode vibrational energy flow in ${}^1\text{B}_{3u}$ naphthalene induced by low energy collisions with Ar," *J. Chem. Phys.* **79**, 2869, (1983).
- Mourits 1977 F. M. Mourits and H. A. Rummens, "A critical evaluation of Lennard-Jones and Stockmayer potential parameters and of some correlation methods," *Can. J. Chem.* **55**, 3007, (1977).
- Mudjijono 1994a Mudjijono and W. D. Lawrance, "Is there a light collision partner effect in vibrational energy transfer? Relaxation of *p*-difluorobenzene by He and Ar," *Chem. Phys. Lett.* **223**, 173, (1994).
- Mudjijono 1994b Mudjijono and W. D. Lawrance, "Do state-to-state propensity rules for vibrational energy transfer remain valid in the intermediate state density region?," *Chem. Phys. Lett.* **227**, 447, (1994).
- Mudjijono 1996a Mudjijono and W. D. Lawrance, "Vibrational energy transfer from four levels below 410 cm^{-1} in S_1 *p*-difluorobenzene. 1. A strong collision partner dependence in state-to-state transfer by monatomics," *J. Chem. Phys.* **104**, 7444, (1996).
- Mudjijono 1996b Mudjijono and W. D. Lawrance, "Vibrational energy transfer from four levels below 410 cm^{-1} in S_1 *p*-difluorobenzene. 2. A search for vibration to rotation transfer," *J. Chem. Phys.* **105**, 3019, (1996).
- Mudjijono 1996c Mudjijono and W. D. Lawrance, "Vibrational energy transfer from four levels below 410 cm^{-1} in S_1 *p*-difluorobenzene. 3. Different propensity rules for polyatomic partners," *J. Chem. Phys.* **105**, 9874, (1996).
- Mudjijono 1998a Mudjijono and W. D. Lawrance, "State-to-state vibrational energy transfer in S_1 *p*-difluorobenzene at intermediate state densities: A change in propensity rules," *J. Chem. Phys.* **108**, 4877, (1998).
- Mudjijono 1998b Mudjijono and W. D. Lawrance, "State-to-state vibrational relaxation from levels at state densities up to 2.3 states per cm^{-1} in *p*-difluorobenzene," *J. Chem. Phys.* **109**, 6736, (1998).
- Müller-Dethlefs 1995 K. Müller-Dethlefs "High resolution spectroscopy with photoelectrons: ZEKE spectroscopy of molecular systems," in *High resolution laser photoionization and photoelectron studies*, p 21, eds I. Powis, T. Baer, C.-Y. Ng, Wiley, New York, (1995).

- Mulliken 1955 R. S. Mulliken, "Report on notation for the spectra of polyatomic molecules," *J. Chem. Phys.* **23**, 1997, (1955).
- Mullin 1995 A. S. Mullin, C. A. Michaels, and G. W. Flynn, "Molecular supercollisions: Evidence for large energy transfer in the collisional relaxation of highly excited pyrazine by CO₂," *J. Chem. Phys.* **102**, 6032, (1995).
- Murakami 1981 J. Murakami, M. Ito, and K. Kaya, "The multiphoton ionization spectrum of toluene in a supersonic free jet: internal rotation of the methyl group," *Chem. Phys. Lett.* **80**, 203, (1981).
- Nesbitt 1988 D. J. Nesbitt, "High-resolution infrared spectroscopy of weakly bound molecular complexes," *Chem. Rev.* **88**, 843, (1988).
- Neufeld 1972 P. D. Neufeld, A. R. Janzen, and R. A. Aziz, "Empirical equations to calculate 16 of the transport collision integrals $\Omega^{(l,s)*}$ for the Lennard-Jones (12-6) potential," *J. Chem. Phys.* **57**, 1100, (1972).
- Neuhauser 1997 R. G. Neuhauser, K. Siglow, and H. J. Neusser, "High n Rydberg spectroscopy of benzene: Dynamics, ionisation energy and rotational constants of the cation," *J. Chem. Phys.* **106**, 896, (1997).
- Neuhauser 1998 R. Neuhauser, J. Braun, H. J. Neusser, and A. van der Avoird, "Vibrational overtones in the electronic ground state of the benzene-Ar complex: A combined experimental and theoretical analysis," *J. Chem. Phys.* **108**, 8408, (1998).
- Neusser 1994 H. J. Neusser and H. Krause, "Binding energy and structure of van der Waals complexes of benzene," *Chem. Rev.* **94**, 1829, (1994).
- Nicholson 1995 J. A. Nicholson, W. D. Lawrence and G. Fischer, "Single vibronic level fluorescence spectra from $\tilde{\Lambda}(^1\text{B}_{2u})$ benzene: Fermi resonances and S₀ IVR lifetimes," *Chem. Phys.* **196**, 327, (1995).
- Nimlos 1989 M. R. Nimlos, M. A. Young, E. R. Bernstein, and D. F. Kelley, "Vibrational dynamics of aniline(Ar)₁ and aniline(CH₄)₁ clusters," *J. Chem. Phys.* **91**, 5268, (1989).
- Nishiyama 1985 I. Nishiyama and I. Hanazaki, "Infrared photodissociation of the benzene dimer. Translational energy distributions of dissociation fragments," *Chem. Phys. Lett.* **117**, 99, (1985).
- NOST 1995 NASA/Science Office of Standards and Technology, "Definition of the flexible image transport system (FITS): NOST 100-1.1," (NASA Goddard Space Flight Centre 1995)

- Öhrwall 1998 G. Öhrwall and P. Baltzer, "Angle-resolved photoelectron spectrum of rotational states in H₂⁺," *Phys. Rev. A* **58**, 1960, (1998).
- Oref 1990 I. Oref and D. C. Tardy, "Energy-transfer in highly excited large polyatomic-molecules," *Chem. Rev.* **90**, 1407, (1990).
- Page 1988 R. H. Page, Y. R. Shen, and Y. T. Lee, "Infrared-ultraviolet double resonance studies of benzene molecules in a supersonic beam," *J. Chem. Phys.* **88**, 5362, (1988).
- Parker 1997 D. H. Parker and A. T. J. B. Eppink, "Photoelectron and photofragment velocity map imaging of state-selected molecular oxygen dissociation/ionization dynamics," *J. Chem. Phys.* **107**, 2357, (1997).
- Parmenter 1982 C. S. Parmenter, "Vibrational energy flow within excited electronic states of large molecules," *J. Phys. Chem.* **86**, 1735, (1982).
- Parmenter 1986 C. S. Parmenter and B. M. Stone, "The methyl rotor as an accelerating functional group for IVR," *J. Chem. Phys.* **84**, 4710, (1986).
- Pearce 1973 R. A. R. Pearce, D. Steele, and K. Radcliffe, "The vibrational force field of halogenated aromatic molecules: 2 Out-of-plane vibrations of fluoroaromatics," *J. Mol. Struct.* **15**, 409, (1973).
- Philis 1990 J. G. Philis and L. Goodman, "Torsional vibrations in two-photon resonance spectroscopy of toluene derivatives," *J. Mol. Struct.* **221**, 1, (1990).
- Phillips 1967 D. Phillips, "Fluorescence and triplet state of hexafluorobenzene," *J. Chem. Phys.* **46**, 4679, (1967).
- Pinaré 1998 J. C. Pinaré, B. Baguenard, C. Bordas, and M. Broyer, "Photoelectron imaging of small clusters: Evidence for non-Boltzmannian kinetic-energy distribution in thermionic emission," *Phys. Rev. Lett.* **81**, 2225, (1998).
- Pitzer 1943 K. S. Pitzer and D. W. Scott, "The thermodynamics and molecular structure of benzene and its methyl derivatives," *J. Am. Chem. Soc.* **65**, 803, (1943).
- Poel 1995 K. L. Poel, Z. T. Alwahabi, and K. D. King, "Time-resolved infrared fluorescence studies of the collisional deactivation of CO₂ (00⁰1) by large polyatomic molecules," *Chem. Phys.* **201**, 263, (1995).

- Poel 1996 K. L. Poel, Z. T. Alwahabi, and K. D. King, "Collisional deactivation of N₂O(00⁰1) studied by time-resolved infrared fluorescence," *J. Chem. Phys.* **105**, 1420, (1996).
- Poel 1997 K. L. Poel, C. M. Glavan, Z. T. Alwahabi, and K. D. King, "Collisional deactivation of CO₂(00⁰1) and N₂O(00⁰1) by toluene isotopomers: Near-resonant energy transfer from N₂O(00(0)1)," *J. Phys. Chem. A* **101**, 5614, (1997).
- Press 1992 W. H. Press, S. A. Teukolsky, W. T. Vetterling, and B. P. Flannery, *Numerical Recipes in FORTRAN* (Cambridge University Press, Cambridge, 1992).
- Ramaekers 1983 J. J. F. Ramaekers, H. K. van Dijk, J. Langelaar, and R. P. H. Rettschnick, "Energy conversion in van der Waals complexes of *s*-tetrazine and argon," *Faraday Discuss. Chem. Soc.* **75**, 183, (1983).
- Reid 1995 K. L. Reid and D. Leahy, "Exploiting polarization in the study of molecular photoionization dynamics," in *High resolution laser photoionization and photoelectron studies*, p 247, eds I. Powis, T. Baer, C.-Y. Ng, Wiley, New York, (1995).
- Reid 1999 K. L. Reid, T. A. Field, M. Towrie, and P. Matousek, "Photoelectron angular distributions as a probe of alignment evolution in a polyatomic molecule: Picosecond time- and angle-resolved photoelectron spectroscopy of S₁ para-difluorobenzene," *J. Chem. Phys.* **111**, 1438, (1999).
- Rice 1986 S. A. Rice, "Selectivity of elemental molecular processes associated with energy transfer and chemical reaction," *J. Phys. Chem.* **90**, 3063, (1986).
- Riedle 1996a E. Riedle, R. Sussmann, Th. Webber, and H. J. Neusser, "Rotationally resolved vibronic spectra of the van der Waals modes of benzene-Ar and benzene-Kr complexes," *J. Chem. Phys.* **104**, 865, (1996).
- Riedle 1996b E. Riedle and A. van der Avoird, "Unambiguous assignment of the van der Waals modes of benzene-Ar by analysis of the rotationally resolved UV-spectra and comparison with multidimensional calculations," *J. Chem. Phys.* **104**, 882, (1996).
- Rinaldi 1996 C. A. Rinaldi, J. C. Ferrero, M. A. Vázquez, M. L. Azcárate, and E. J. Quel, "Collisional deactivation of CDCl₃ excited with a TEA CO₂ laser," *J. Phys. Chem.* **100**, 9745, (1996).
- Rogers 1996 L. J. Rogers, M. N. R. Ashfold, Y. Matsumi, M. Kawasaki, and B. J. Whitaker, "The photodissociation of iodine monochloride at 235 nm," *Chem. Phys. Lett.* **258**, 159, (1996).

- Saigusa 1983 H. Saigusa, B. E. Forch, K. T. Chen, and E. C. Lim, "Photoinduced vibrational predissociation of pyrimidine clusters in a supersonic molecular beam: Evidence for statistical energy partitioning," *Chem. Phys. Lett.* **101**, 6, (1983).
- Samartzis 1997 P. C. Samartzis and T. N. Kitsopoulos, "Two-photon dissociation study of CS₂ using ion imaging," *J. Phys. Chem. A* **101**, 5620, (1997).
- Samartzis 1999 P. C. Samartzis, B. L. G. Bakker, D. H. Parker, and T. N. Kitsopoulos, "Photoelectron and photofragment velocity imaging following the excitation of CH₃I to the A-band using fs, ps, and ns laser pulses," *J. Phys. Chem. A* **103**, 6106, (1999).
- Savard 1929 J. Savard, "Comparative spectrum analysis of *o*-, *m*- and *p*-isomerides of certain benzene derivatives," *Ann. de Chimie* **11**, 287, (1929).
- Scherzer 1992 W. Scherzer, H. L. Selzle and E. W. Schlag, "Identification of spectra of mixed structural isomers via mass selective hole-burning in the gas phase," *Chem. Phys. Lett.* **195**, 11, (1992).
- Schmidt 1991a M. Schmidt, M. Mons, J. Le Calvé, "Microsolvation of the benzene molecule by argon atoms: Spectroscopy and isomers," *Chem. Phys. Lett.* **177**, 371, (1991).
- Schmidt 1991b M. Schmidt, M. Mons, J. Le Calvé, and P. Millié, "The second conformer of the benzene-argon₂ van der Waals complex," *Chem. Phys. Lett.* **183**, 69, (1991).
- Sedlacek 1991 A. J. Sedlacek, R. E. Weston Jr, and G. W. Flynn, "Interrogating the vibrational relaxation of highly excited polyatomics with time-resolved diode laser spectroscopy: C₆H₆, C₆D₆, and C₆F₆ + CO₂," *J. Chem. Phys.* **94**, 6483, (1991).
- Shaw 1998 D. A. Shaw, D. M. P Holland, M. A. Macdonald, M. A. Hayes, L. G. Shpinkova, E. E. Rennie, C. A. F. Johnson, J. E. Parker, and W. von Niessen, "An experimental and theoretical study of the spectroscopic and thermodynamic properties of toluene," *Chem. Phys.* **230**, 97, (1998).
- Smalley 1976 R. E. Smalley, D. H. Levy, and L. Wharton, "The fluorescence excitation spectrum of the HeI₂ van der Waals complex," *J. Chem. Phys.* **64**, 3266, (1976).
- Smalley 1983 R. E. Smalley, "Dynamics of electronically excited states," *Annu. Rev. Phys. Chem.* **34**, 129, (1983).
- Speiser 1980 S. Speiser and E. Grunwald, "Vibrational energy redistribution and hot-band spectrum for hexafluorobenzene following infrared multiphoton excitation," *Chem. Phys. Lett.* **73**, 438, (1980).

- Sponer 1942 H. Sponer, "Remarks on the absorption spectra of phenylalanine and tyrosine in connection with the absorption in toluene and *p*-cresol," *J. Phys. Chem.* **10**, 672, (1942).
- Stephenson 1984 T. A. Stephenson and S. A. Rice, "Relaxation dynamics of photoexcited benzene–rare gas van der Waals complexes," *J. Chem. Phys.* **81**, 1083, (1984).
- Strickland 1991 R. N. Strickland and D. W. Chandler, "Reconstruction of an axisymmetric image from its blurred and noisy projection," *Appl. Opt.* **30**, 1811, (1991).
- Sussmann 1995 R. Sussmann, R. Neuhauser, and H. J. Neusser, "Coherent ion dip spectroscopy of the ground state benzene-Ar complex: Vibration to rotation levels up to 130 cm^{-1} intermolecular energy," *J. Chem. Phys.* **103**, 3315, (1995).
- Suzuki 1996 T. Suzuki, H. Katayanagi, Y. Mo, and K. Tonokura, "Evidence for multiple dissociation components and orbital alignment in 205 nm photodissociation of N_2O ," *Chem. Phys. Lett.* **256**, 90, (1996).
- Suzuki 1999 T. Suzuki, L. Wang, and H. Kohguchi, "Femtosecond time-resolved photoelectron imaging on ultrafast electronic dephasing in an isolated molecule," *J. Chem. Phys.* **111**, 4859, (1999).
- Sverdlov 1973 L. M. Sverdlov, M. A. Kovner, and E. P. Krainov, *Vibrational Spectra of Polyatomic Molecules* (Wiley, New York, 1973).
- Tardy 1993 D. C. Tardy, "Collisional efficiencies for vibrational energy relaxation of C_6F_{14} and C_8F_{18} : Dependence on deactivator mass," *J. Chem. Phys.* **99**, 963, (1993).
- Tasumi 1986 M. Tasumi, T. Urano and M. Nakata, "Some thoughts on the vibrational modes of toluene as a typical monosubstituted benzene," *J. Mol. Struct.* **146**, 383, (1986).
- Toselli 1991 B. M. Toselli, J. D. Brenner, M. L. Yerram, W. E. Chin, K. D. King, and J. R. Barker, "Vibrational relaxation of highly excited toluene," *J. Chem. Phys.* **95**, 176, (1991).
- Turner 1970 D. W. Turner, C. Baker, A. D. Baker, and C. R. Brundle, "Molecular photoelectron spectroscopy," Wiley-Interscience, New York, (1970).
- Vacek 1994 J. Vacek, K. Konvicka, and P. Hobza, "A molecular dynamics study of the benzene- Ar_2 complex. Application of the nonempirical ab initio and empirical Lennard-Jones 6-12 potentials," *Chem. Phys. Lett.* **220**, 85, (1994).

- Vacek 1998 J. Vacek, P. Hobza, and J. Jortner "Nuclear dynamics of benzene-(Ar)_n clusters," *J. Phys. Chem. A* **102**, 8268, (1998).
- van der Avoird 1993 A. van der Avoird, "Van der Waals rovibration levels and the high resolution spectrum of the argon-benzene dimer," *J. Chem. Phys.* **98**, 5327, (1993).
- Varsanyi 1974 G. Varsanyi, *Assignments for Vibrational Spectra of Seven Hundred Benzene Derivatives* (Wiley, New York, 1974).
- Vasudev 1979 R. Vasudev and J. C. D. Brand, "The two-photon spectrum of toluene vapour," *Chem. Phys.* **37**, 211, (1979).
- Vernon 1981 M. F. Vernon, J. M. Lisy, H. S. Kwok, D. J. Krajnovich, A. Tramer, Y. R. Shen, and Y. T. Lee, "Vibrational predissociation of benzene dimers and trimers by the crossed laser - molecular beam technique," *J. Phys. Chem.* **85**, 3327, (1981).
- Waclawik 1993 E. R. Waclawik, W. D. Lawrance, and R. A. J. Borg, "State-to-state vibrational energy transfer from 6¹ benzene induced by low-energy collisions with nitrogen: Temperature-dependent propensities," *J. Phys. Chem.* **97**, 5798, (1993).
- Waclawik 1995 E. R. Waclawik and W. D. Lawrance, "Vibrational energy transfer from the 6¹ level of S₁ (¹B_{2u}) benzene in a supersonic expansion. I. Monatomic collision partners," *J. Chem. Phys.* **102**, 2780, (1995).
- Waclawik 1996 E. R. Waclawik, R. A. J. Borg, Mudjijono, J. R. Gascooke, C. G. Hickman, and W. D. Lawrance, "An investigation of vibration to rotation transfer in vibrational relaxation of S₁ aromatics," *Chem. Phys. Lett.* **251**, 95, (1996).
- Wang 1999 L. Wang, H. Kohguchi and T. Suzuki, "Femtosecond time-resolved photoelectron imaging", *Faraday Discuss.* **113**, 37, (1999)
- Watanabe 1990 A. Watanabe, Y. Koga, K. Sugawara, H. Takeo, K. Fukuda, C. Matsumura, P. M. Keehn, "Infrared laser induced decomposition of hexafluorobenzene and some monosubstituted derivatives. Intermediacy of the pentafluorophenyl radical,". *Spectrochim. Acta* **46A**, 463, (1990).
- Weber 1990 Th. Weber, A. von Bargen, E. Riedle, and H. J. Neusser, "Rotationally resolved ultraviolet spectrum of the benzene-Ar complex by mass-selected resonance-enhanced two-photon ionization," *J. Chem. Phys.* **92**, 90, (1990).
- Weber 1991 Th. Weber and H. J. Neusser, "Structure of the benzene-Ar₂ cluster from rotationally resolved ultraviolet spectroscopy," *J. Chem. Phys.* **94**, 7689, (1991).

- Wilmshurst 1957 J. K. Wilmshurst and H. J. Bernstein, "The infrared and Raman spectra of toluene, toluene- α -d₃, *m*-xylene, and *m*-xylene- $\alpha\alpha'$ -d₆," *Can. J. Chem.* **35**, 911, (1957).
- Wilson 1934 E. B. Wilson, "The normal modes and frequencies of vibration of the regular plane hexagon model of the benzene molecule," *Phys. Rev.* **45**, 706, (1934).
- Winterhalter 1999 J. Winterhalter, D. Maier, J. Honerkamp, V. Schyja and H. Helm, "Imaging of charged atomic reaction products: Inversion by a two-dimensional regularization method," *J. Chem. Phys.* **110**, 11187, (1999).
- Wiley 1955 W. C. Wiley and I. H. McLaren, "Time-of-flight mass spectrometer with improved resolution", *Rev. Sci. Instrum.* **26**, 1150 (1955).
- Yerram 1990 M. L. Yerram, J. D. Brenner, K. D. King, and J. R. Barker, "Collisional deactivation of highly excited benzene pumped at 248 nm," *J. Phys. Chem.* **94**, 6341, (1990).
- Yoder 1999 L. M. Yoder, J. R. Barker, K. T. Lorenz, and D. W. Chandler, "Ion imaging the recoil energy distribution following vibrational predissociation of triplet state pyrazine-Ar van der Waals clusters," *Chem. Phys. Lett.* **302**, 602, (1999).
- Zellweger 1985a J.-M. Zellweger, T. C. Brown, and J. R. Barker, "Vibrationally excited populations from IR-multiphoton absorption. I. Absorbed energy and reaction yield measurements," *J. Chem. Phys.* **83**, 6251, (1985).
- Zellweger 1985b J.-M. Zellweger, T. C. Brown, and J. R. Barker, "Vibrationally excited populations from IR-multiphoton absorption. II. Infrared fluorescence measurements," *J. Chem. Phys.* **83**, 6261, (1985).
- Zellweger 1986 J.-M. Zellweger, T. C. Brown, and J. R. Barker, "Vibrationally excited populations from IR-multiphoton absorption. 3. Energy transfer between 1,1,2-trifluoroethane and argon," *J. Phys. Chem.* **90**, 461, (1986).